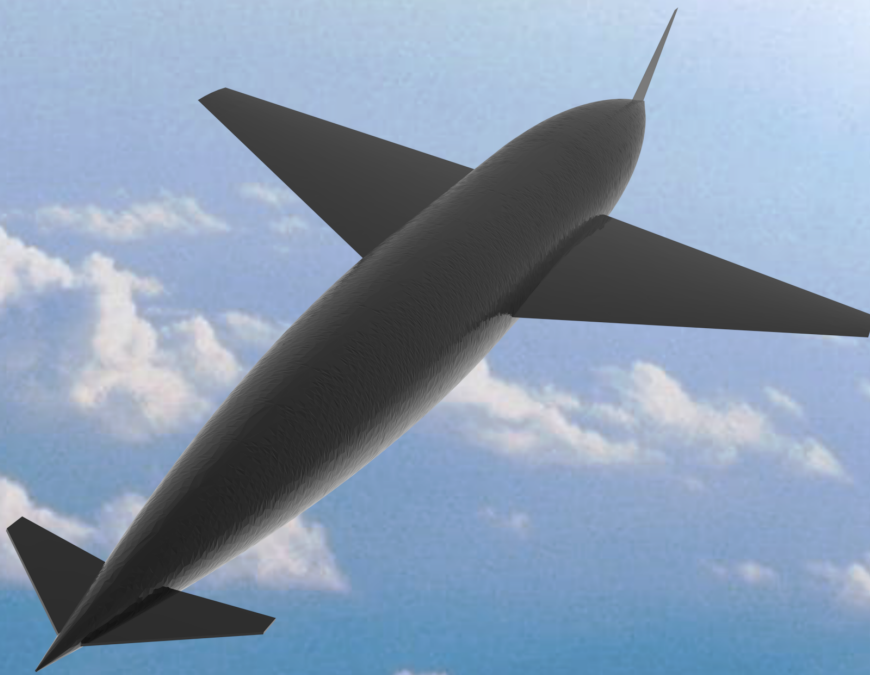


DELFT UNIVERSITY OF TECHNOLOGY

Thesis Report

DEVELOPMENT AND APPLICATION OF A
MULTIDISCIPLINARY DESIGN OPTIMISATION SIZING
PLATFORM FOR THE CONCEPTUAL DESIGN OF HYPERSONIC
LONG-RANGE TRANSPORT AIRCRAFT



Thibault Clar

DELFT UNIVERSITY OF TECHNOLOGY

**Development and application of a
Multidisciplinary Design Optimisation
sizing platform for the conceptual design of
hypersonic long-range transport aircraft**

by

Thibault Clar

To obtain the degree of
MASTER OF SCIENCE
in Aerospace Engineering
At the Delft University of Technology

Student number: 4234707
Submitted on: March, 2019
Thesis committee: Dr. Ir. Fabrizio Oliviero, TU Delft, supervisor
Prof. Dr. Ir. Leo Veldhuis, TU Delft
Dr. Ir. Dominic Dirkx, TU Delft

An electronic version of this thesis is available at <http://repository.tudelft.nl/>.



THE UNIVERSITY OF
SYDNEY

Abstract

With the global increase in passenger traffic and growing popularity of ultra long-haul routes over the Asia Pacific region and Atlantic Ocean, the possibility for hypersonic transport vehicle could become an attractive option to reduce flight time over long distance from 16-20 hours down to around 4-5 hours. Through the use of low-emission, high efficiency liquid hydrogen propulsion systems, hypersonic transport could become a viable option for antipodal flights. While the hypersonic flow regime has been studied extensively since the development of the X-15 research plane and the Space Shuttle in the mid 20th century, this flow regime presents some challenging aspects such as extreme heat transfer and varying flow regimes that can critically impact the design of such vehicles.

In view of the high investment cost which would be required for the manufacturing and development of a hypersonic transport vehicle, Multi-Disciplinary Optimisation (MDO) techniques can prove to be extremely beneficial in understanding the coupling of critical disciplines at an early conceptual design phase and reduce development risks. While applications of MDO have been extensively applied to subsonic aircraft, they are not common for hypersonic vehicle design. In this thesis, an MDO platform has been developed to allow for the optimal sizing of hypersonic transport vehicles using vehicle take-off mass (W_{TO}) as the performance indicator subjected to fuel volume and payload height constraints. To achieve this, the developed platform uses parametric shape variables to automatically generate three dimensional models and computational meshes for a wing-body hypersonic aircraft geometry using MIT Engineering SteckPAD software [49] and EDF's SALOME [34]. Two aerodynamic panel code solver are implemented to cover the subsonic and supersonic/hypersonic flow regimes. The higher-order panel code PANAIR developed by Boeing [37] (low to medium fidelity) is integrated to compute the subsonic inviscid flow over a configuration while a supersonic/hypersonic panel code developed by the author based on the well known Engineering Impact flow methods is used for the high speed inviscid flow. Using the semi-empirical corrections of Ekcerc, Van Dries and Splading and Chi, the viscous flow properties and convective heat transfer for an arbitrary configuration are computed. A Multi-Discipline Feasible (MDF) loop is used in the platform to allow for mass estimation by providing a consistent value of the vehicle take-off mass. In the MDF loop, a mission performance module is used to compute fuel mass flow based on the assumption of steady flight and the GHAME engine model. Additionally a passive thermal protection system (TPS) sizer has been developed and the HASA and WAATs mass estimation correlations are used to compute the aircraft component masses.

The current platform is applied to the LAPCAT A2 hypersonic long-range transport configuration by Reaction Engines [112] to determine the impact of range and cruise Mach number on the design of hypersonic aircraft. Results show that the implemented platform allows for the rapid sizing of hypersonic transport aircraft and is thus appropriate at a conceptual design stage. Additionally, the optimisation results shows that the optimal shape of the configuration is greatly dependent on the aircraft range and fuel volume constraint and that an optimum hypersonic cruise Mach number exists which is dictated by a trade-off between mission time, engine efficiency and TPS mass.

Acknowledgements

With this Master Thesis, I am completing my studies at the Delft University of Technology. During my Thesis I have had to great opportunity of spending a significant portion of my research work at the University of Sydney, Australia. I would first like to thank my supervisor abroad, Professor Dries Verstraete, who has given me the opportunity to work abroad on a subject which I particularly enjoyed. Thank you for all your enthusiasm, the interesting discussions during our meetings, valuable insights and the knowledge you shared with me during my time abroad. I would also like to thank my supervisor here in Delft, Professor Fabrizio Oliviero, for your positivity, the time you took to meet on Skype while I was abroad and here in Delft, your guidance and advice which have allowed me to complete my Thesis research and for sharing your expertise in the field of Multi-Disciplinary Optimisation.

I am also very grateful to have been surrounded by many great friends and colleagues during my studies in Delft. Thank you to my irreplaceable friends: Baris, Dionisios, Jan, Michael, Ruben and Thomas and the ones who have been here since the beginning, you have always been a source of motivation to push myself and enjoy my time in Delft and abroad to the fullest. Hoping the best for you all in the future and let's make sure barbecues continue and our startup project sees the light one day!

Lastly I would like to thank my family who have always been there to support me in the good and bad times, helping bringing the best out of myself and believing in me, your continued encouragements made this possible.

Thibault Clar

Contents

1	Introduction	1
I	Background	2
2	Demand and Motivations of hypersonic flight	2
2.1	Typical vehicle types	5
2.2	Existing hypersonic transport concepts	7
2.2.1	LAPCAT A2 aircraft	8
2.2.2	HyCAT series	8
2.2.3	JAXA vehicle	10
2.2.4	ZEHST Aircraft	11
3	Challenges of hypersonic cruise vehicle design	12
3.1	Aerodynamics	12
3.2	Thermal and dissociation effects	16
3.3	Liquid hydrogen tank design	20
3.4	Multi-disciplinary optimisation	20
4	Thesis Objectives and Overview	22
II	Modelling	24
5	The Aero-Thermo-Structural platform	24
6	The Design Structure Matrix	24
7	Parametrisation of an Aircraft	28
7.1	Wing Parametrisation: Class Shape Transformation Functions	28
7.2	Fuselage Parametrisation: Super Ellipses	29
8	Mission definition	31
8.1	Implementation	31
9	Automatic CAD modelling	33
9.1	Implementation	33
10	Automatic Meshing	35
10.1	Strategy: Geometry partitioning	35
11	Aero-Thermodynamic analysis	38
11.1	High speed analysis: Engineering methods	39
11.1.1	Implementation	39
11.1.2	Lift and Drag coefficient computations	45
11.1.3	Limitations of Hypersonic Engineering methods	46
11.2	Subsonic (“Low speed”) analysis: PANAIR	47
11.2.1	Theoretical background	47
11.2.2	Implementation	48
11.2.3	Limitations of PANAIR	51
11.3	Viscous-Thermal analysis	52

11.3.1	Convective heat transfer computations	52
11.3.2	Heat transfer field decomposition: POD	56
11.3.3	Limitations of convective heat transfer model	60
12	Mission performance	62
12.1	Performance model	62
12.1.1	Limitations of mission performance module:	64
13	Thermal Protection System sizing	66
13.1	TPS concept selection	66
13.2	Unsteady heat transfer TPS sizing	67
13.2.1	TPS materials selection	69
13.2.2	TPS sizing correlations	70
13.2.3	Limitations and recommendations	73
14	Component mass estimation	75
14.1	Mass estimation models	75
14.1.1	Limitations and recommendations	77
III	Validation and model selection	79
15	Validation of Aerodynamic solvers	79
15.1	Low speed: NACA RM L51F07 Wing-Body Configuration	79
15.2	High speed verification: Inviscid flow over an ogive body	86
15.3	High speed: Complete configuration, X-15 and HyCAT aircrafts	90
15.3.1	X-15 Configuration	90
15.3.2	HyCAT Configuration	96
16	Thermal solver	100
16.1	Flow over plates, wedge and cones	100
16.2	TPS Unsteady heat transfer balance verification	104
IV	Results	109
17	Case study: LAPCAT A2 aircraft	109
17.1	Baseline configuration	109
17.2	Optimiser setup	115
17.3	Results and discussion	117
17.3.1	Mesh selection	117
17.3.2	Sensitivity of shape variables	119
17.3.3	Baseline Aircraft sizing	124
17.3.4	Range dependence	138
17.3.5	Mach number effects	145
V	Conclusions and Recommendations	148
18	Conclusions	148
18.1	Case study results summary	150
19	Recommendations	152

Appendices	161
Appendix A Dimensionalisation of subsonic inviscid results (PANAIR)	161
Appendix B Real gas equations for air	162
Appendix C Additional flow diagrams	163
C.1 Viscous thermal analysis computations	163
C.2 Thermal Protection System sizing	164
C.3 Component mass estimation	164
Appendix D Hypersonic solver solution examples	165
Appendix E PANAIR pressure validation along wing span at $M = 0.6$ [-]	169
Appendix F Additional viscous flow validation	170
Appendix G Vertical Tail sizing	173
Appendix H Additional results: Design variable sensitivities	174
Appendix I Additional sensitivities: Lift, Drag and Drag due to lift polar	176
Appendix J Additional results: Range effects	185

List of Figures

1	The LAPCAT A2 conceptual design	1
2	NASA X-43 Hyper-X design	2
3	Flight envelope of three experimental hypersonic aircrafts	2
4	Strong acceleration of long-haul operations by low cost carriers over the last five years, Airbus [10].	3
5	Trajectory proposed for a Mach 5 hypersonic aircraft and comparison with subsonic flights [93].	4
6	Specific impulse for various hydrogen/hydrocarbon based propulsion systems [18].	4
7	Types of Hypersonic vehicles; Left: Re-entry Apollo capsule (NREV) [113], Center: Space Shuttle (WREV) [47], Right: X-15 (CAV) [90].	6
8	Design of hypersonic vehicles [6].	6
9	Planform and section design [124]	7
10	Wave rider vehicle [131]	7
11	NACA type airfoil (left), Biconvex airfoil (right) [7], Double wedge airfoil (bottom)	7
12	Internal structure design [120]	7
13	LAPCAT A2 cruiser aircraft configuration (left) [110] and Scimitar engine (right) [60].	8
14	Basic hyCAT-I configuration [99].	9
15	Top view hyCAT (left) [35] Turbo-Scramjet concept (right) [99]	9
16	JAXA hypersonic vehicle configuration [118]	10
17	Zero Emission High-Speed Transport (ZEHST) EADS [32].	11
18	Hypersonic flow over a flat plate [48].	12
19	Hypersonic Engineering Methods. Newton impact theory (left), Cone theory (centre) and Shock-expansion (right).	13
20	Different shock types for hypersonic vehicles (top: CAV type vehicle X-15 [89], bottom: re-entry capsule)[55].	14
21	Use of hypersonic engineering methods on vehicle sections [7].	15
22	Lift to Drag barrier for hypersonic aircraft [58].	16
23	Average skin temperature at different Mach and Altitudes [101].	17
24	Skin temperature over the blackbird aircraft at Mach 3.2 [46].	17
25	Strength vs service temperature of materials [2].	18
26	Material tensile strength as a function of temperature [56].	18
27	Thermal protection system over the space shuttle [92].	19
28	Chemical reactions occurring at different Mach and altitudes [13].	19
29	Tank structure and insulation [119].	20
30	Single vs Multiple Bubble integral tank arrangements [52].	20
31	Multi-disciplinary optimisation for trajectory of JAXA vehicle [122].	21
32	Disciplines involved in Hypersonic cruise aircraft design	24
33	Design Structure Matrix of MDO platform.	25
34	Basic cross section generated by various exponents N1 and N2 of the class function [68].	28
35	Inboard and Outboard wing planform definition.	29
36	Perspective view of wing definition.	29
37	Normalised superellipse curves ($H = W = 1$) with varying control parameters. . .	30
38	Example of fuselage cross section generated with various control parameters and scaling factors.	30
39	Discretisation of altitude from original mission.	31
40	Discretisation of Mach number from original mission.	31
41	Rate of climb computed at mission plateaux.	32

42	Flight Path angle computed at mission plateaux.	32
43	Fuselage and wing cross sections generated in ESP.	33
44	Wing and fuselage solids.	33
45	Fused water-tight aircraft geometry.	34
46	Tanks and Payload bay.	34
47	Partitioning of fuselage surfaces.	35
48	Definition of wake networks.	36
49	Exploded view of aircraft mesh networks.	36
50	Flow chart of geometry and meshing process.	37
51	Flow chart for hypersonic methods.	39
52	Strip method for flow computations. Example of strips shown with coloured panels.	40
53	Impact and shadow flow along strips.	40
54	Definition of local impact angle and shear vector.	41
55	Panel normal vector computation.	41
56	Equivalent Wedge (left) and Cone methods [59].	41
57	Interpolated cone shock angle.	43
58	Interpolated Mach number at cone.	43
59	Description of conical flow [73].	44
60	Subdivision of a panel in PANAIR [37].	48
61	Wireframe model according to LaWGS format and mesh network groups for boundary conditions.	49
62	Flow diagram for the implementation of PANAIR.	50
63	Heat transfer modes at surface of vehicle [93].	52
64	Typical temperature distribution within an hypersonic boundary layer [13]. . . .	52
65	Original convective heat transfer snapshot field over configuration at $M = 5$ [-], ALT = 25.8 km and $AOA = 0[deg]$	58
66	Original convective heat transfer snapshot field over configuration at $M = 5$ [-], ALT = 25.8 km and $AOA = 12[deg]$	58
67	Accumulated energy of POD modes.	59
68	Interpolated POD mode coefficients as a function of angle of attack at $M = 5$ [-], ALT = 25.8 km.	59
69	First POD mode.	59
70	Second POD mode.	59
71	Third POD mode.	60
72	Fourth POD mode.	60
73	Equilibrium of forces in a steady climb [114].	63
74	GHAME engine specific impulse.	64
75	Integration of the Thermal Protection System [93].	66
76	Different type of TPS concepts [62].	67
77	Schematic of numerical model of TPS.	68
78	Thermal conductivity of TPS types.	70
79	Specific heat of TPS types.	70
80	Heat profiles for TPS unit mass sizing.	71
81	Thickness vs unit mass of insulation types.	72
82	Unit mass of tps types as a function of total heat load at 400 K Back wall tem- perature.	72
83	SiO_2TiO_2 unit mass vs back wall temperature constraint.	72
84	Slimflex unit mass vs back wall temperature constraint.	72
85	Quartz unit mass vs back wall temperature constraint.	72
86	AETB8 unit mass vs back wall temperature constraint.	72
87	The modifying factor.	76

88	Model of NACA RM L51F07 configuration (unit: inches) [132].	79
89	Fuselage shape top view [132].	79
90	Location of pressure orifices along wing span [132].	80
91	Location of pressure orifices around fuselage [132].	80
92	PANAIR mesh for NACA configuration.	81
93	PANAIR pressure results over top of configuration at $M = 0.6$ [-], $AOA = 4$ [deg].	82
94	PANAIR pressure results over bottom of configuration at $M = 0.6$ [-], $AOA = 4$ [deg].	82
95	Pressure distribution along wing span at $M = 0.8$ [-] and $AOA = 2$ [deg], $ST = 0.2b_s, 0.6b_s, 0.95b_s$ (top to bottom).	83
96	Pressure distribution along wing span at $M = 0.8$ [-] and $AOA = 4$ [deg], $ST = 0.2b_s, 0.6b_s, 0.95b_s$ (top to bottom).	83
97	Pressure distribution along fuselage at $M = 0.8$ [-] and $AOA = 2$ [deg], Locations: B, C, D, E (top to bottom).	84
98	Pressure distribution along fuselage at $M = 0.8$ [-] and $AOA = 4$ [deg], Locations: B, C, D, E (top to bottom).	84
99	Lift polar at $M = 0.6$ [-].	85
100	Lift polar at $M = 0.8$ [-].	85
101	Inviscid drag polar at $M = 0.6$ [-].	85
102	Inviscid drag polar at $M = 0.8$ [-].	85
103	Description of ogive-cylinder model [59].	86
104	Mesh for ogive-cylinder configuration.	86
105	Validation pressure distribution along fuselage longitudinal top and bottom strips (top figure) and around circumference at $0.25L$ and $0.75L$ (bottom figure) at $M = 8$ [-] and $AOA = 4$ [deg] [59].	88
106	Implemented Engineering methods pressure distribution along fuselage longitudinal top and bottom strips (top figure) and around circumference at $0.25L$ and $0.75L$ (bottom figure) at $M = 8$ [-] and $AOA = 4$ [deg].	88
107	Validation pressure distribution along fuselage longitudinal top and bottom strips (top figure) and around circumference at $0.25L$ and $0.75L$ (bottom figure) at $M = 12$ [-] and $AOA = 2$ [deg] [59].	89
108	Implemented Engineering methods pressure distribution along fuselage longitudinal top and bottom strips (top figure) and around circumference at $0.25L$ and $0.75L$ (bottom figure) at $M = 12$ [-] and $AOA = 2$ [deg].	89
109	X-15 configuration, top view (unit: inches).	90
110	X-15 configuration, side view (unit: inches).	91
111	Mesh for the X-15 configuration.	92
112	X-15 Lift and Drag polars for fuselage only configuration at $M = 6.83$ [-].	94
113	X-15 drag vs lift dependency for fuselage only configuration at $M = 6.83$ [-].	94
114	X-15 Lift and Drag polars for fuselage + wing configuration at $M = 6.83$ [-].	95
115	X-15 drag vs lift dependency for fuselage + wing configuration at $M = 6.83$ [-].	95
116	Top view of HyCAT A1 configuration [35].	96
117	Mesh for HyCAT configuration.	97
118	Lift polar of HyCAT at $M = 6$ [-], $Re = 23 \cdot 10^6$ [-].	98
119	Drag polar of HyCAT at $M = 6$ [-], $Re = 23 \cdot 10^6$ [-].	98
120	Lift and Drag coefficient vs Mach number for $AOA = 4$ [deg], $ALT = 36$ km.	99
121	Lift and Drag coefficient vs Mach number for $AOA = 8$ [deg], $ALT = 36$ km.	99
122	Laminar (top) and Turbulent (bottom) local friction coefficient c_f over flat plate at $M = 8$ [-] and altitude of 35 km.	102
123	Laminar (top) and Turbulent (bottom) local convective heat transfer q_{conv} over flat plate at $M = 8$ [-] and altitude of 35 km.	102

124	Total laminar (top) and turbulent (bottom) convective transfer $Q_{tot,unit}$ (per unit width) over a flat plate in hypersonic flow as a function of the freestream Mach number and at fixed altitude of 35 km.	103
125	Local turbulent convective heat transfer q_{conv} over a 10 degrees wedge (top) and cone (bottom) at $M = 8$ [-] and altitude of 35 km.	103
126	Case 1: Heat transfer modes (top) and temperature through material thickness (bottom) during simulation.	105
127	Case 1: Temperature at surface and back wall during simulation.	105
128	One meter nose radius, 37 degrees inclination [25].	106
129	Case 2 (Windside): Heat transfers (top) and temperature at surface and back wall (bottom) during simulation.	107
130	Case 2 (Windside): Temperature through material at specific times (top) and exact temperature distribution map in TPS (bottom) during simulation.	107
131	Case 2 (Leeside): Heat transfers (top) and temperature at surface and back wall (bottom) during simulation.	108
132	Case 2 (Leeside): Temperature through material at specific times (top) and exact temperature distribution map in TPS (bottom) during simulation.	108
133	The LAPCAT A2 vehicle (bottom), compared with the Airbus A380 (Steelant,2008).	110
134	LAPCAT A2 vehicle properties from [93].	110
135	Great circle route for Brussels-Sydney (16734km).	111
136	Alternative route for Brussels-Sydney (18728km).	111
137	Schematic of LAPCAT A2 configuration, top view with cryogenic tanks [93].	111
138	Mesh convergence study.	118
139	Mesh computational time.	119
140	Mesh (4) chosen for optimisation.	119
141	Sensitivity of wing surface area on mass distribution (left) and subsonic/hypersonic lift to drag ratio (right).	121
142	Sensitivity of wing aspect ratio.	122
143	Sensitivity of wing thickness to chord ratio.	122
144	Sensitivity of fuselage height factor.	123
145	Sensitivity of fuselage length factor.	124
146	Value of (normalised) objective function during optimal sizing	125
147	Behaviour of fuel volume constraint during optimal sizing.	125
148	Design vector during optimal sizing.	125
149	Geometry comparison between baseline and optimised configurations.	127
150	Variation in empty and fuel mass during optimal sizing process.	128
151	Baseline configuration mass distribution.	129
152	Optimised configuration mass distribution.	129
153	Comparison of estimated structural component masses for baseline LAPCAT A2 configuration with the results of Dr. Sharifzadeh [93].	131
154	Lift polar comparison at subsonic cruise $M = 0.9$ [-], $ALT = 5.9$ km.	132
155	Drag polar comparison at subsonic cruise $M = 0.9$ [-], $ALT = 5.9$ km.	132
156	Drag due to lift comparison at subsonic cruise $M = 0.9$ [-], $ALT = 5.9$ km.	132
157	Lift polar comparison at hypersonic cruise $M = 5$ [-], $ALT = 25.8$ km.	133
158	Drag polar comparison at hypersonic cruise $M = 5$ [-], $ALT = 25.8$	133
159	Lift to drag ratio comparison between baseline and optimised configurations.	134
160	Angle of attack during mission.	134
161	Aerodynamic performance during mission.	134
162	Fuel flow during mission.	134
163	Geometry render comparing baseline and optimised configurations (with fuel tanks included).	135

164	Total heat transfer distribution on baseline configuration.	136
165	Total heat transfer distribution on optimised configuration.	136
166	Thermal protection system unit mass distribution on baseline configuration.	137
167	Thermal protection system unit mass distribution on optimised configuration.	137
168	Scaling of LAPCAT A2 mission using a cruise factor (CF).	138
169	Change in mass distribution of sized configurations with increasing cruise range.	139
170	Lift to drag ratio of optimised configurations for two different cruise factors.	141
171	Exponential rise in fuel mass flow with increasing range.	141
172	Comparison of optimally sized configurations of the LAPCAT A2 vehicle with other aircraft.	142
173	Optimally sized configurations for varying mission range (top view).	143
174	Optimally sized configurations for varying mission range (side view).	144
175	Scaled missions for different Mach number (fixed range of 18771 km).	145
176	Average convective heat transfer (left) and conduction-radiation average surface temperature (right) throughout scaled mission profiles.	146
177	Change in TPS, fuel and take-off mass estimation for varying cruise Mach number of the LAPCAT A2 configuration.	147
178	Change in total mission time and cruise engine specific impulse for varying Mach number.	147
179	Viscous-Thermal computations flow diagram.	163
180	TPS sizing flow diagram.	164
181	Structural component mass estimation flow diagram.	164
182	Impact angles over LAPCAT A2 baseline configuration at AOA = 0 [deg], M = 5 [-] and ALT = 25.8 [km].	165
183	Impact angles over LAPCAT A2 baseline configuration at AOA = 5 [deg], M = 5 [-] and ALT = 25.8 [km].	165
184	Pressure coefficient distribution over LAPCAT A2 baseline configuration at AOA = 0 [deg], M = 5 [-] and ALT = 25.8 [km].	166
185	Pressure coefficient distribution over LAPCAT A2 baseline configuration at AOA = 5 [deg], M = 5 [-] and ALT = 25.8 [km].	166
186	Mach number distribution over LAPCAT A2 baseline configuration at AOA = 0 [deg], M = 5 [-] and ALT = 25.8 [km].	167
187	Mach number distribution over LAPCAT A2 baseline configuration at AOA = 5 [deg], M = 5 [-] and ALT = 25.8 [km].	167
188	Convection-Radiation equilibrium wall temperature distribution over LAPCAT A2 baseline configuration at AOA = 0 [deg], M = 5 [-] and ALT = 25.8 [km].	168
189	Convection-Radiation equilibrium wall temperature distribution over LAPCAT A2 baseline configuration at AOA = 5 [deg], M = 5 [-] and ALT = 25.8 [km].	168
190	Pressure distribution along wing span at M = 0.6 and AOA = 2 [deg], ST = 0.2b _s , 0.6b _s , 0.95b _s (top to bottom).	169
191	Pressure distribution along wing span at M = 0.6 and AOA = 4 [deg], ST = 0.2b _s , 0.6b _s , 0.95b _s (top to bottom).	169
192	Goyne et al. average test conditions on a hypersonic flat plate [45] [93].	170
193	Chien average test conditions on a hypersonic sharp cone [24] [93].	171
194	Stanton number comparison for a flat plate under conditions described by Goyne in Table 192, sets : 1,2,3 (top to bottom).	172
195	Stanton number comparison for a 5 [deg] sharp cone under conditions described by Chien in Table 193, sets : 1,2,3 (top to bottom).	172
196	Effect of changes in wing taper ratio (top), wing tip twist angle (middle) and fuselage width factor (bottom) on estimated mass distribution and subsonic/hypersonic lift to drag polars.	175

197	Effect of wing platform area on Subsonic lift (top left), drag (bottom left) and drag due to lift (right) polars.	176
198	Effect of wing platform area on Hypersonic lift (top left), drag (bottom left) and drag due to lift (right) polars.	177
199	Effect of wing aspect ratio on Subsonic lift (top left), drag (bottom left) and drag due to lift (right) polars.	177
200	Effect of wing aspect ratio on Hypersonic lift (top left), drag (bottom left) and drag due to lift (right) polars.	178
201	Effect of wing taper ratio on Subsonic lift (top left), drag (bottom left) and drag due to lift (right) polars.	178
202	Effect of wing taper ratio on Hypersonic lift (top left), drag (bottom left) and drag due to lift (right) polars.	179
203	Effect of wing tip twist on Subsonic lift (top left), drag (bottom left) and drag due to lift (right) polars.	179
204	Effect of wing tip twist on Hypersonic lift (top left), drag (bottom left) and drag due to lift (right) polars.	180
205	Effect of wing thickness to chord ratio on Subsonic lift (top left), drag (bottom left) and drag due to lift (right) polars.	180
206	Effect of thickness to chord ratio on Hypersonic lift (top left), drag (bottom left) and drag due to lift (right) polars.	181
207	Effect of fuselage width factor on Subsonic lift (top left), drag (bottom left) and drag due to lift (right) polars.	181
208	Effect of fuselage width factor on Hypersonic lift (top left), drag (bottom left) and drag due to lift (right) polars.	182
209	Effect of fuselage height factor on Subsonic lift (top left), drag (bottom left) and drag due to lift (right) polars.	182
210	Effect of fuselage height factor on Hypersonic lift (top left), drag (bottom left) and drag due to lift (right) polars.	183
211	Effect of fuselage length factor on Subsonic lift (top left), drag (bottom left) and drag due to lift (right) polars.	183
212	Effect of fuselage length factor on Hypersonic lift (top left), drag (bottom left) and drag due to lift (right) polars.	184
213	Normalised objective function value at Cruise Factor = 0.2 [-].	185
214	Fuel constraint during optimal sizing, CF = 0.2 [-].	185
215	Design vector during optimal sizing, CF = 0.2 [-].	185
216	Empty and Fuel mass during optimal sizing, CF = 0.2 [-].	185
217	Normalised objective function value at Cruise Factor = 0.4 [-].	185
218	Fuel constraint during optimal sizing, CF = 0.4 [-].	185
219	Design vector during optimal sizing, CF = 0.4 [-].	186
220	Empty and Fuel mass during optimal sizing, CF = 0.4 [-].	186
221	Normalised objective function value at Cruise Factor = 0.6 [-].	186
222	Fuel constraint during optimal sizing, CF = 0.6 [-].	186
223	Design vector during optimal sizing, CF = 0.6 [-].	186
224	Empty and Fuel mass during optimal sizing, CF = 0.6 [-].	186
225	Normalised objective function value at Cruise Factor = 0.8 [-].	187
226	Fuel constraint during optimal sizing, CF = 0.8 [-].	187
227	Design vector during optimal sizing, CF = 0.8 [-].	187
228	Empty and Fuel mass during optimal sizing, CF = 0.8 [-].	187

List of Tables

1	Comparison of fuel properties [1]	5
2	Summary of Aircraft control parameters	31
3	Impact methods implemented in platform	42
4	Boundary conditions applied to mesh networks.	49
5	Properties of TPS under consideration [93]	70
6	Distribution of elements over NACA model.	80
7	Full scale model main wing properties [39].	91
8	Main wing properties hyCAT (100 times scale model) [35]	96
9	Case studies properties [25].	104
10	Geometrical properties of LAPCAT A2 baseline configuration	112
11	Modelling setting parameters for platform	113
12	Constant values associated with Baseline configuration	114
13	Initial value and Bounds of optimisation problem	115
14	Settings for optimisation algorithm and MDF tolerance	117
15	Meshes properties for convergence study.	118
16	Baseline versus Optimal design vector.	126
17	Mass estimation results for baseline and optimised configurations.	128
18	Geometrical properties of baseline and optimised configurations.	128
19	Optimal design vector for sized aircraft at varying cruise factors.	139
20	Estimated mass distribution for sized aircraft at varying cruise factors.	140
21	Derived properties for sized aircraft at varying cruise factors.	140

Nomenclature

List of Symbols

Symbol	Definition	Unit
α	Angle of attack	[deg]
γ	flight path angle	[deg]
δ	Impact angle	[deg]
Δt	Time step	[s]
ε	Emissivity of surface	[–]
θ_s	Shock angle	[deg]
λ	Wing taper ratio	[–]
λ_m	Eigenvalue of POD mode	[–]
Λ_{le}	Wing leading edge sweep angle	[deg]
ϕ_m	Eigenvector of POD mode	[–]
μ	Dynamic viscosity	[Pa · s]
ρ	Density	[kg/m ³]
σ	Stephan Botzmann constant ($5.67 \cdot 10^{-8}$)	[W/(m ² · K ⁴)]
τ	Material thermal diffusivity	[m ² /s]
ϕ	Perturbation potential	[–]
A	Aero-Thermal performance matrix	[–]
A_P	Panel Area	[m ²]
ALT	Altitude	[m]
AR	Wing aspect ratio	[–]
b	Wing full span	[m]
b_s	Wing semi-span	[m]
c_f	Local friction coefficient	[–]
c_p	Coefficient of pressure	[–]
c_{spe}	Heat capacity at constant pressure	[J/(kg · K)]
C_A	Axial force coefficient	[–]
C_D	Drag coefficient	[–]
C_H	Stanton number	[–]
C_L	Lift coefficient	[–]
C_N	Normal force coefficient	[–]
C_p	Specific heat capacity	[J/(kg · K)]
F_c	Friction coefficient compressibility factor	[–]
F_{Re_x}	Reynolds number compressibility factor	[–]
h	Specific enthalpy	[J/kg]
J	Objective function value	[–]
k	Thermal conductivity	[W/(m · K)]
k_m	POD mode coefficient	[–]
M	Mach number	[–]
\vec{n}	Panel normal vector	[–]
Pr	Prandlt number	[–]
q	Dynamic pressure	[Pa]
Q	Heat load	[J/m ²]
q_{cond}	Conduction heat transfer	[W/m ²]
q_{conv}	Convective heat transfer	[W/m ²]
q_{rad}	Radiation heat transfer	[W/m ²]

Symbol	Definition	Unit
r	Recovery factor	$[-]$
R	Snapshot correlation matrix	$[-]$
R	Specific gas constant	$[J/(kg \cdot K)]$
Re	Reynolds number	$[-]$
R_f	Reynold analogy factor	$[-]$
ROC	Rate of Climb	$[m/s]$
S_{ref}	Wing reference area	$[m^2]$
S_{tank}	Tanks total surface area	$[m^2]$
t/c	Wing thickness to chord ratio	$[-]$
T	Temperature	$[K]$
t_{tps}	Thickness of TPS insulation material	$[m]$
U	Snapshot matrix	$[-]$
v	velocity perturbation vector	$[-]$
V	Velocity	$[m/s]$
V_F	Fuel volume	$[m^3]$
V_{pay}	Payload volume	$[m^3]$
W_{avi}	Avionics mass	$[kg]$
W_{elec}	Electrical systems mass	$[kg]$
W_{eng}	Engine Dry mass	$[kg]$
W_{emp}	Empty mass	$[kg]$
W_{equip}	Equipment mass	$[kg]$
W_F	Fuel mass	$[kg]$
W_{hs}	Horizontal stabilizer mass	$[kg]$
W_{hydr}	Hydraulics mass	$[kg]$
W_{lg}	Landing gears mass	$[kg]$
W_{pay}	Payload mass	$[kg]$
$W_{tank,ins}$	Fuel tank insulation mass	$[kg]$
$W_{tank,struct}$	Fuel tank structure mass	$[kg]$
W_{TO}	Take-off mass	$[kg]$
$W_{tot,body}$	Fuselage body structure mass	$[kg]$
W_{tps}	Thermal Protection System mass	$[kg]$
$W_{unit,tps}$	TPS unit mass	$[kg/m^2]$
W_{vt}	Vertical tail mass	$[kg]$
\vec{X}	Design vector	$[-]$

Subscripts

Subscript	Meaning
<i>av</i>	Available
<i>aw</i>	Adiabatic wall
<i>bw</i>	Back wall (substructure interface)
<i>visc</i>	Viscous
<i>c</i>	Cone surface
<i>fus</i>	Fuselage body
<i>incp</i>	Incompressible
<i>inv</i>	Inviscid
<i>mat</i>	Insulation material
<i>nd</i>	Non-dimensional
<i>norm</i>	Normalized
<i>pla</i>	Plateau
∞	Freestream
<i>P</i>	Mesh panel
<i>perf</i>	Perfect Gas
<i>ref</i>	Reference value
<i>req</i>	Required
<i>s</i>	Sample
<i>struct</i>	Structural
<i>w</i>	Wall (surface)

Abbreviations

Abbreviation	Definition
AETB	Alumina Enhanced Thermal Barrier
ATS	Access to Space
BEM	Beam Element Model
CAD	Computer Aided Design
CAV	Cruise and Acceleration Vehicle
CFD	Computational Fluid Dynamics
CST	Class Shape Transformation
DSM	Design Structure Matrix
ESP	Engineering SketchPad
FEA	Finite Element Analysis
GHAME	Generic Hypersonic Aerodynamics Model Example
HASA	Hypersonic Aerospace Sizing Analysis
HEM	Hypersonic Engineering Methods
ISP	Engine Specific Impulse
JAXA	Japanese Aerospace Exploration Agency
MAC	Mean Aerodynamic Chord
LAPCAT	Long-Term Advanced Propulsion Concepts and Technologies
NREV	Non-winged Re-entry Vehicle
MDO	Multi-Disciplinary Optimisation
MLI	Multi-Layer Insulation
POD	Proper Orthogonal Decomposition
PRE	Payload Range Efficiency
RANS	Reynolds Averaged Navier Stokes
RCC	Reinforced Carbon-Carbon
RLV	Reusable Launch Vehicle
SiO_2TiO_2	Silicon Dioxide Titanium Dioxide Light silica based aerogel
SIP	Super-Inclined Panel
SSTO	Single Stage to Orbit
TPS	Thermal Protection System
WAATs	Weight Analysis of Advanced Transport systems
WREV	Winged Re-entry Vehicle
ZEHST	Zero-Emission High-Speed Transport

1. Introduction

Hypersonic flight has been a subject of extensive research where a significant number of projects have seen the light over the last 60 years to investigate the challenges and potential of high-speed controlled re-usable flights. Up until recently, most controlled hypersonic aircraft research have been aimed at short acceleration missions such as for the X-15 aircraft or for re-entry vehicles such as the well known Space Shuttle. However, with the ever growing global passenger traffic and the strong acceleration of long haul operations over the last five years, a new potential market has opened for long distance passenger hypersonic flight. Currently, long-range aircraft are close to pushing the limit of what can be achieved in a subsonic regime but will never be capable of providing the significant flight time reductions of hypersonic flight.

Promising development in the field of hypersonic transport vehicles include the liquid hydrogen powered LAPCAT A2 airliner concept which aims to reduce intercontinental flight between Europe and Asia Pacific from 16 to only 4 hours by flying at a cruise Mach number of 5 while carrying a payload of 300 passengers. While the potential of using high performance liquid hydrogen propulsion and the reduction in flight times are attractive, hypersonic flights present numerous challenges that must be considered early in the vehicle design to successfully understand and predict the performance of such vehicles.



Figure 1: The LAPCAT A2 conceptual design

In the hypersonic regime the presence of extreme aerodynamic heating, the formation of shocks over the vehicle surface, the low achievable lift to drag ratios and the interactions of such aspects on the vehicle structural and fuel mass call for the use of Multi-Disciplinary Optimisation techniques for the appropriate design of such vehicles. As a result, a Multi-Disciplinary platform has been developed in this study in an effort to capture the interaction among relevant disciplines and to optimally size hypersonic cruise vehicles at a conceptual phase.

In this research, the developed Multi-Disciplinary platform is employed using the LAPCAT A2 conceptual configuration and mission as a baseline to first investigate the effects and sensitivity of vehicle shape parameters on the aerodynamic and mass performance of an hypersonic cruise vehicle over a long range mission. An optimisation algorithm is further employed on the LAPCAT A2 baseline configuration to study the potential gains in performance for such an aircraft. The results obtained are compared to previous mass estimation and aerodynamic performance studies of the LAPCAT A2 configuration performed by Reaction Engines and a PhD thesis by Shayan Sharifzadeh [93]. The effects of the mission Mach number and range on optimal vehicle size are furthermore investigated.

Part I.

Background

2. Demand and Motivations of hypersonic flight

Hypersonic flight made its first appearance in the year of 1949 with the flight launch of the V2 rocket. Since this first flight, there has been a significant number of projects which continued to push further the research and development of high speed aircrafts. In the 1960s, the NASA X-15 rocket plane marks the first research effort towards controlled hypersonic flight. In more recent work, the VentureStar program launched by Lockheed martin aimed to provide single-stage to orbit re-usable hypersonic vehicle. Unfortunately, the project was discontinued in 2001 due to failures during structural testing [80]. More recent work in the field include NASA Hyper-X experimental vehicle program, the University of Queensland HyShot program and the NASA Fundamental Hypersonic project [5].

The driving demand for hypersonic vehicles lies in both the need for high speed long distance intercontinental flights and re-usable launch/re-entry vehicles. With the increase in global aircraft traffic, the interest of hypersonic flight is strongly growing. In addition, for space flight, re-usable hypersonic vehicle would enable an enhanced flexibility in operations as well as drastic cost savings [84].

X-43A Hyper-X

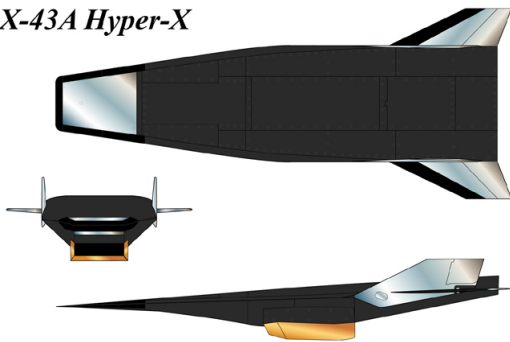


Figure 2: NASA X-43 Hyper-X design

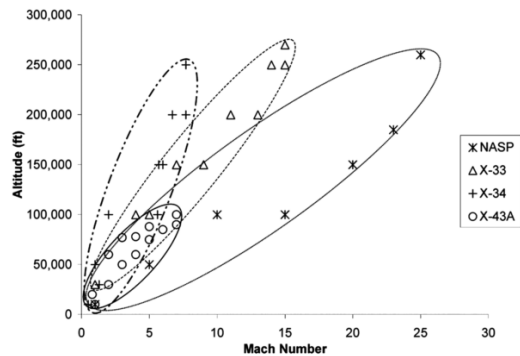


Figure 3: Flight envelope of three experimental hypersonic aircrafts

Hypersonic flight is typically characterised by cruise Mach numbers above 3 as well as high cruise altitudes located within the stratosphere (above 20km) [80]. As seen in figure 3, the flight envelope of different hypersonic aircraft spans a wide range of altitudes (0 to around 300,000 fts) and Mach numbers (0 to around 25) but the majority of flight conditions are located in a “low” hypersonic regime (Mach number more than 3). This flight regime allows for alternative propulsion system such as scramjet engines used by NASA’ X-43 hypersonic aircraft (figure 2) which reached a Mach number of 9.68 during a flight test in 2004 [84]. The use of propulsion systems such as the scramjet allows reduction of mass due to the removal of movable engine parts. The possibility of air-breathing compression engine present a promising alternative to rocket engines which have been typically used to reach hypersonic speeds and which require extra mass originating from the need to carry oxygen on-board the rocket engine system [29].

The overall growth rate of aviation has kept increasing over the years, where in 2017 about 4 billion passenger have flown around the globe. Predictions estimate the number of passengers to reach 7 billion by 2035 [10], almost double the current market. Looking more specifically at the long haul market, a steady growth can be observed over the last five years as given in figure 4. Long haul aircraft routes are concentrated within Asia Pacific and across the Atlantic and are increasing in passenger traffic over time at a strong rate. Ultra long haul aircraft are also becoming more popular with the introduction of the A350 XWB Ultra Long Range aircraft capable of flying up to 18,000 km in 20 hours [11]. This aircraft achieved the longest flight ever recorded between Singapore and New York covering 16,562 km in 17h52. In addition, Qantas has challenged Airbus and Boeing to extend the flying range of their next generation of long haul aircraft to make direct flights from the east coast of Australia to cities including London and New York a reality by 2022 [121]. Current Long-range aircraft are already pushing the limits of what can be achieved in a subsonic regime but will never be able to provide the significant flight time reductions experienced by hypersonic flights.

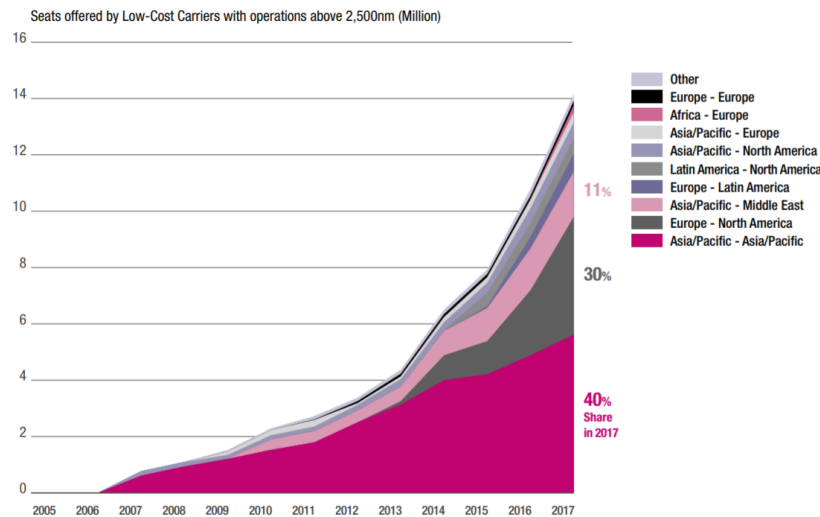


Figure 4: Strong acceleration of long-haul operations by low cost carriers over the last five years, Airbus [10].

Promising development in the field of hypersonic transport vehicles include the LAPCAT (Long-term Advanced Propulsion Concept and Technologies) A2 hypersonic airliner concept which aims to reduce intercontinental flights between Europe and Asia Pacific from 16 to only 4 hours [112] [85]. In figure 5, the expected flight times for a Mach 5 aircraft such as the LAPCAT A2 over different routes are given and compared to a subsonic transport aircraft. Indeed as can be seen, average time savings of 80% can be expected from the use of hypersonic aircraft. The speed of Mach 5 is typically chosen for hypersonic transport vehicles [126] [75] [117] as it provides a significant reduction in flight time in comparison to subsonic aircraft. However any increase in cruise speed is not seen as beneficial as no significant time saving are expected beyond Mach 5 and other issues such as reduction of engine performance and higher heating are encountered at higher speeds. In addition, beyond a 80% in time savings, the increase in estimated market for a faster aircraft would be negligible.

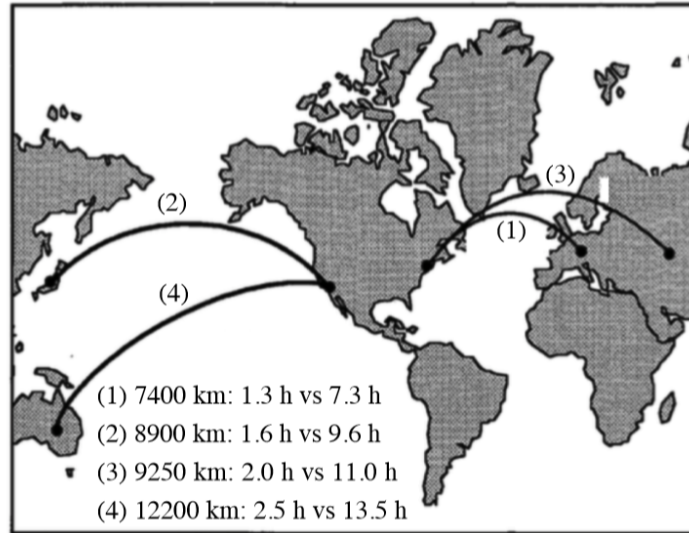


Figure 5: Trajectory proposed for a Mach 5 hypersonic aircraft and comparison with subsonic flights [93].

To achieve ultra long distance flights at reasonable cost and aircraft mass requires an appropriate fuel and propulsion system. One of the key figures when looking at engine performance is the specific impulse which provides an indication of the amount of fuel flow for a given thrust requirement. The higher the impulse, the least fuel required. In figure 6, the specific impulse as a function of Mach number for hydrogen or hydrocarbon fuel based propulsion systems is given. The first aspect that can be noticed is that for any type of fuel, the specific impulse decreases with Mach number and the ideal thermodynamic cycle changes as well. Secondly, the specific impulse of liquid hydrogen fuel is much higher than hydrocarbon based fuels [130] [64]. This is a results of the specific energy of liquid hydrogen in comparison to hydrocarbon fuels. In Table 1, the fuel properties are compared against each other [1]. As can be seen the energy per unit mass (heat of combustion) released for liquid hydrogen is about 2.7 times higher than hydrocarbons yielding to the increase in specific impulse observed in figure 6. The high specific impulse of liquid hydrogen makes it the only feasible fuel type for long-range hypersonic aircraft [9].

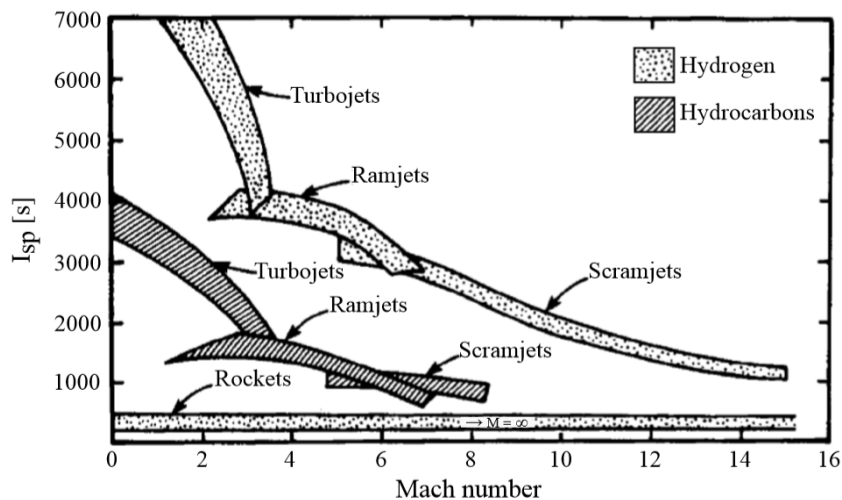


Figure 6: Specific impulse for various hydrogen/hydrocarbon based propulsion systems [18].

If hydrocarbons were used for hypersonic flights, the specific impulse at high Mach number of around 5 would be so low (around 1500s) that the fuel mass required would be extremely high leading to excessively large take-off mass through the snow ball effect for a long-range mission. On the other hand, the specific impulse of liquid hydrogen fuel near Mach five is comparable to the one of a subsonic hydrocarbon fuel. This increase in specific impulse makes liquid hydrogen powered hypersonic aircraft a promising competitor to subsonic aircraft both in terms of speed gain and take-off mass [1]. The primary downside of hydrogen is its low density (about 71 kg/m^3 [3]) in comparison to hydrocarbon fuel. This makes the storage of liquid hydrogen one of the key challenge for this fuel type, where the fuel is typically designed to be stored in the fuselage section of the aircraft and the dimensions of the body are mainly sized to account for the large fuel volumes required by liquid hydrogen [125].

Table 1: Comparison of fuel properties [1]

Property	Hydrocarbons	Liquid Hydrogen
Boiling point at 1 atm [K]	456-508	20
Density [kg/m^3]	800	71
Heat of combustion [MJ/kg]	44	118

This new revived demand for high speed controlled flight drives the purpose of this thesis. For a long time the lack of technology required to tackle the complexity of hypersonic flow has created a bottleneck for the development of hypersonic flow vehicles [80]. However, with today's technology advancements in area such as computational speed, realistic design and optimisation of hypersonic vehicle becomes possible and allows for new breakthroughs in this flight regime [6]. The ability to optimise and provide useful design guidelines at an early conceptual stage of the vehicle design can drastically reduce design and development costs and improve the performance of the final aircraft [84]. These key aspects provide additional motivation for the thesis research.

2.1. Typical vehicle types

Hypersonic vehicles come in a wide variety of shapes depending on their intended mission and the environment they are exposed to. Most hypersonic vehicle types can be sub-classified in three categories: Cruise and Acceleration vehicles (CAV), Winged Re-Entry (WREV) and Non-Winged Re-Entry vehicles (NREV) [54]. Examples of the different types of hypersonic vehicles built throughout history are given in figure 7. Non-winged and winged re-entry vehicles are characterised by very blunt surfaces. During re-entry, Mach numbers of around 30 can be expected leading to extremely high surface heating. Surface heating can be reduced by the generation of strong bow shocks over the vehicle geometry as a result of the reduction in flow kinetic energy behind a strong bow shock. To generate these bow shocks, blunt surfaces are used and are typical of non-winged and winged re-entry vehicles [42]. In addition to the high Mach numbers, re-entry vehicles need to decelerate as quickly as possible (maximum drag) to reach the ground with a low speed. This leads to the need for high angles of attack and thus increased heating and significant flow separation effects. Winged re-entry vehicles such as the space shuttle are intended to be re-usable and designed to land horizontally. As a result control and lift generating surfaces (wings) are required for such objectives to ensure controllability during decent, stability and low speed lift generation. Non-winged re-entry capsules on the other hand are designed for maximum deceleration with less emphasis on control and re-usability and are aided by the deployment of a parachute system for vertical landing.



Figure 7: Types of Hypersonic vehicles; Left: Re-entry Apollo capsule (NREV) [113], Center: Space Shuttle (WREV) [47], Right: X-15 (CAV) [90].

Cruise and acceleration (CA) type hypersonic vehicles on the other hand typically consist of long, “slender” lifting body designs [80] to minimise wave drag (a major drag component at hypersonic speeds). These types of vehicles fly at lower angles of attack to generate enough lift while minimising drag and are subject to lower heating rates. The schematics of three CA type hypersonic aircrafts are presented in figures 2 and 8 for different NASA Hyper X series designs. What is typical of these vehicles is the use of double-delta wings as seen in figures 8 and 9. The double delta shape is inspired from supersonic aircraft [7]. The purpose of this partitioning of the wing is to allow the use of subsonic airfoil section near the root as well as supersonic/hypersonic airfoils near the tip. Using highly swept subsonic airfoils and slightly swept supersonic/hypersonic sections near the tip allows for good balance between subsonic (usually climb) and supersonic/hypersonic performance [124]. Another type of hypersonic vehicle design is the so called wave-rider as shown in figure 10. This particular type of vehicle improves supersonic/hypersonic lift to drag ratio by using the compression shock waves being generated by its own shape to generate lift and has the advantage of improving available internal volume [131].

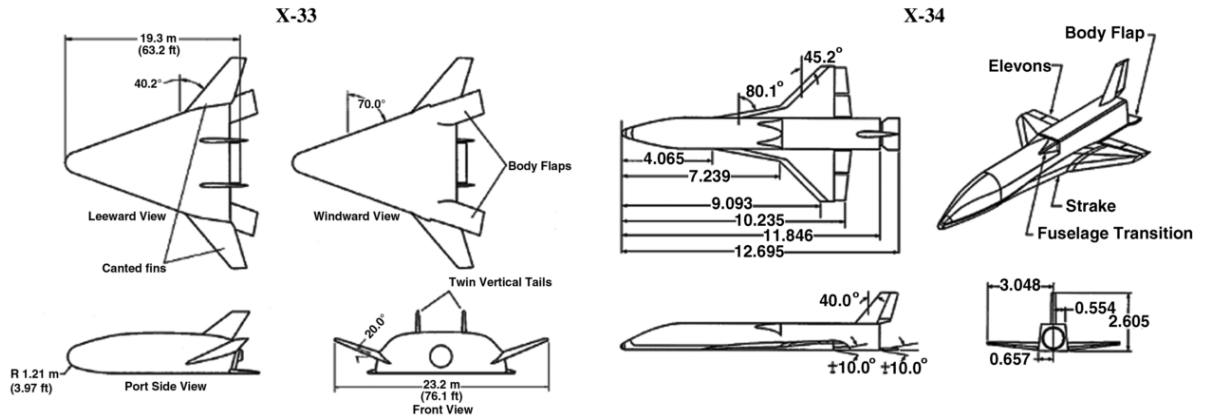


Figure 8: Design of hypersonic vehicles [6].

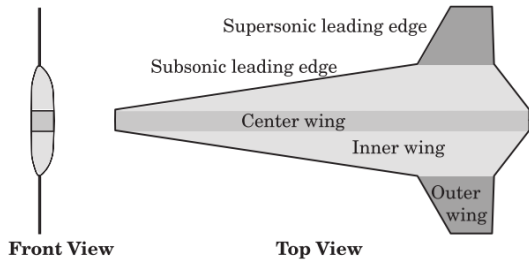


Figure 9: Planform and section design [124]



Figure 10: Wave rider vehicle [131]

In figure 11 three types of airfoil used for hypersonic aircraft wing sections are displayed. Typically, the inner wing will consist of a NACA type airfoil for improved low speed performance. Example of low speed airfoil section include NACA 64A-203 and NACA 0006 airfoil [124]. An example of supersonic/hypersonic airfoil is the biconvex section as shown in figure 11 (right). This airfoil has a sharp leading edge creating weaker shock waves at the leading edge and thus improving the airfoil performance in a supersonic/hypersonic regime [68] through wave drag reduction. This type of airfoil has proven to perform well at high supersonic/hypersonic speeds as proven in CFD studies [17]. Another common supersonic/hypersonic airfoil type is the double wedge airfoil [6] which is represented in figure 11 (bottom).

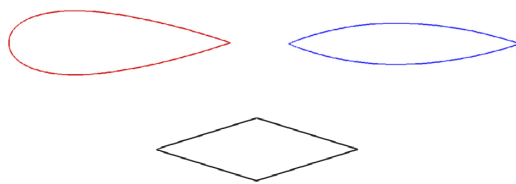


Figure 11: NACA type airfoil (left), Biconvex airfoil (right) [7], Double wedge airfoil (bottom)

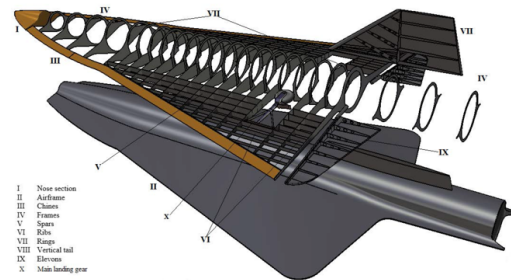


Figure 12: Internal structure design [120]

An example of the internal structure of a conceptual CA hypersonic vehicle is shown in figure 12 [120]. In this figure, it can be seen that the wing internal structure is mainly composed of ribs and spars while loads are transmitted to the fuselage via ring shaped bulkheads (to allow propellant to be stored in the fuselage section [66]). Strong shock waves and temperature gradients are present near the leading edge and thus frames can be used on the leading edge of the wing as thermal protection as shown in figure 12. This type of internal structure can also be observed in other project such as the Hypersonic vehicle Structural Analysis Program (HySAP) [66] which aims at automatising the sizing of the internal structure of hypersonic vehicles via the industrial finite element software ANSYS and a sizing algorithm.

2.2. Existing hypersonic transport concepts

Within the category of cruise and acceleration hypersonic vehicles, most vehicle built such as the X-15 and NASA X-43 are acceleration aircraft which have been designed for short missions under high accelerations. Acceleration vehicles mission are more aimed towards rapid and re-usable single stage to low earth orbit (SSTO) trajectories with horizontal take off and landing. A lot of knowledge has been gained from the design of acceleration aircraft which is now used for the design of cruise type vehicles. Hypersonic cruise transport aircraft as opposed to acceleration vehicles are aimed for long range missions with significant hypersonic cruise periods. As of

today, hypersonic cruiser are still mostly in conceptual or preliminary design phase with few wind tunnel and engine tests having been performed. In this section some of the promising hypersonic cruiser configurations designed by different companies are presented.

2.2.1. LAPCAT A2 aircraft

The LAPCAT A2 configuration is a conceptual liquid hydrogen fuel based hypersonic transport aircraft designed to cruise at a Mach number of 5 [97]. This design has been created as part of the LAPCAT programme of the European Union aiming to study the potential of long range, high capacity, environmentally friendly hypersonic transportation. The actual design of this aircraft is proposed by the British Aerospace company, Reaction Engines, who predict that this concept could be fully developed in 25 years given a promising market is present [112].

The configuration is set to fly from Brussels to Sydney while passing across the North pole and Pacific ocean leading to a total trip distance of around 19,000 km. The aircraft mission is set to fly subsonically over populated areas to prevent the sonic-boom from producing a nuisance in those areas. The designers of the aircraft estimate a take-off mass of 400 tonnes with a payload capacity of 300 passengers [112]. Although significantly longer than an A380 aircraft, with a length of 140 meters, the LAPCAT A2 configuration is estimated to have a lower take-off mass and could land on current runways making it a potential candidate for the high-speed market. An artist view of the LAPCAT A2 concept can be seen in figure 13 (left).

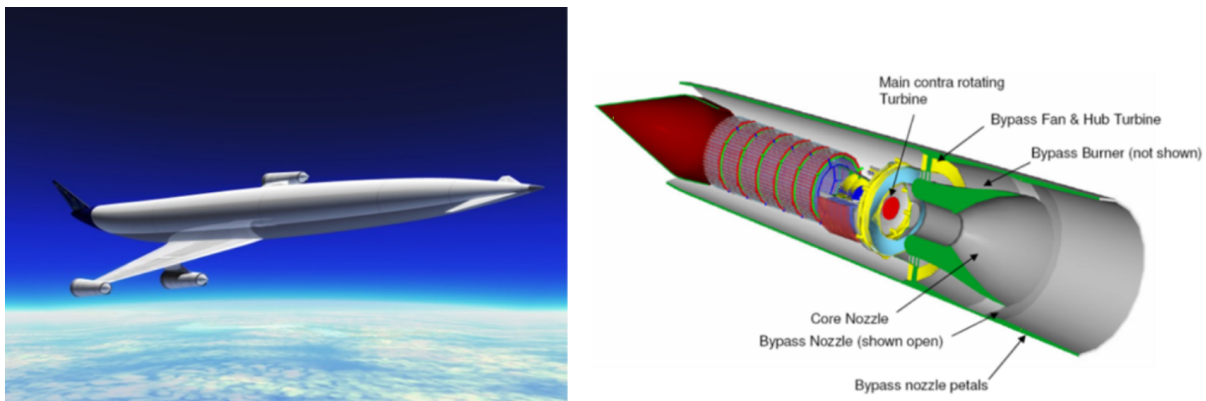


Figure 13: LAPCAT A2 cruiser aircraft configuration (left) [110] and Scimitar engine (right) [60].

The aircraft is designed to be powered by the so called Scimitar engines (figure 13, right). These engines are designed around gas turbine and ramjet technology to maximise the propulsion performance throughout both subsonic and hypersonic flow conditions. The key feature of this engine design is the use of a pre-cooler which allows the air in the compressor to be transferred to the liquid hydrogen fuel allowing the engine to operate at high efficiency during cruise [60]. The inlet is designed to create shock waves to slow down the incoming air, with the diffuser further decelerating the flow to subsonic speeds before combustion. In addition the engine is described as having a high bypass ratio of 4:1 to ensure good efficiency at subsonic speeds.

2.2.2. HyCAT series

The HyCAT configuration series are a set of different hypersonic aircraft designs aimed at long range liquid hydrogen fuelled passenger transport missions. These configurations were designed by Lockheed-California Company on the NASA Hypersonic Cruise Aircraft Propulsion Integration Study, Contract NAS1-15057 in the 1970s [99]. The primary emphasis was to evaluate the

most promising conceptual vehicle and propulsion integration approach for a liquid hydrogen fuelled, Mach 6 transport capable of carrying 200 passengers at a range of 9 260 km [72]. The first iteration of the HyCAT design is presented in figure 14. Lockheed-California predicted a take-off gross mass of 272 160 to 362 880 kg for this configuration and mission [99].

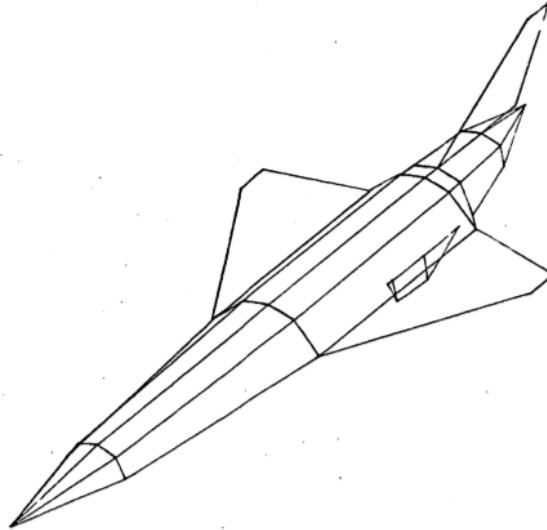


Figure 14: Basic hyCAT-I configuration [99].

For the propulsion system, two types of turbo-scamjet configurations were put under investigation. One of these configurations is presented in figure 15, for a turbo-scamjet engine with retractable inlet. The advantage of this type of engine configuration is the possibility for maximising the engine specific impulse at different flight phases. During take-off, landing and subsonic cruise, the turbojet engine is used while the scramjet is used for the hypersonic cruise phase. For aerodynamic performance estimations, Lockheed made use of a panel code called VORLAX [99] for subsonic flow with a leading edge suction correction to include vortex flow at high angle of attack/low Mach number combinations. For the hypersonic flow aerodynamic performance, Lockheed made use of the Hypersonic Arbitrary Program (HAB) developed by Douglas Aircraft Company [35]. This program makes use of inviscid impact/expansion flow methods corrected by a viscous semi-empirical model to estimate skin-friction. In the research conducted by Lockheed on the HyCAT configurations, the tangent-cone impact method and prandtl meyer expansion method were employed for the computation of inviscid flow. The viscous flow was calculated using the Spalding and Chi method [35]. For the HyCAT-I configuration, a Mach 6 cruise lift to drag ratio of 5.21 [-] is estimated for a wing with biconvex airfoil sections of 3% thickness to chord ratio.

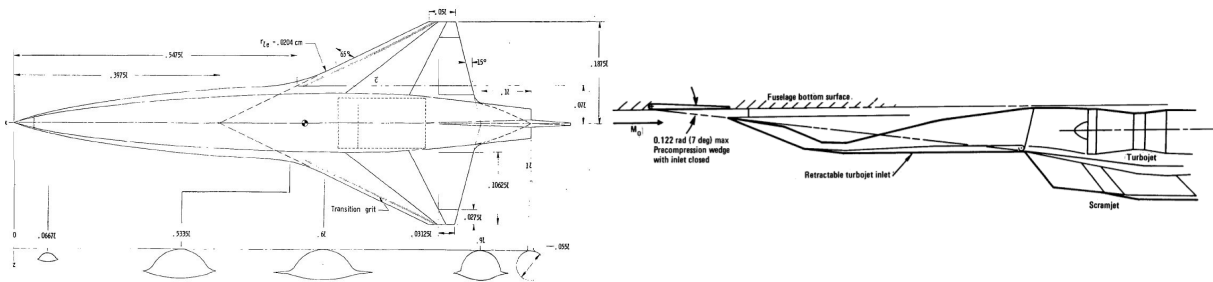


Figure 15: Top view hyCAT (left) [35] Turbo-Scramjet concept (right) [99]

Some of the key conclusions from the research conducted by Lockheed include aerodynamic and propulsive performance. From an aerodynamics point of view, the research concludes that the lift provided by a flattened fuselage is important in improving the overall aerodynamic efficiency (L/D ratio) and providing the necessary width for an underbody propulsion integration. This flattening effect is especially relevant for hydrogen fuelled aircraft where large fuselage to wing area ratios can be expected as a result of the high volume requirements from liquid hydrogen' low density.

On the propulsion side, it is concluded that the propulsion system should be integrated with the fuselage to minimise friction and wave drag generated. Additionally the propulsion system should be located near the center of gravity of the aircraft and as forward as possible for balance purposes, to reduce boundary layer thickness and to facilitate takeoff rotation without excessive ground clearance requirements. Proper location and inclination of the thrust vector can also lead to significant reduction in fuel required during cruise through a reduction in aerodynamic lift required (and thus also resulting drag). Noise constraints could have a very adverse impact on vehicle size [99].

2.2.3. JAXA vehicle

This hypersonic aircraft concept is under development by the Japanese Aerospace Exploration Agency (JAXA). The configuration has been sized to carry a payload of 100 passengers across the pacific ocean in 2 hours at a cruise Mach number of 5 reaching a range of 8700 km [117]. The propulsion system for this configuration is liquid hydrogen based using a pre-cooled turbojet engine with afterburner [118]. The configuration features a flattened lifting fuselage to promote a high lift to drag ratio during hypersonic cruise and to accommodate for the liquid hydrogen volume required. The airframe of the configuration was sized using the HyperSizer software and the FEA code Nastran using a honeycomb sandwich structure placed under heat shield materials. This consists of titanium honeycomb sandwiched between Carbon Fiber Reinforced Polymer (CFRP) panels. Leading edges of the airframe and wings are protected from the air convective heat transfer by tiles made of silicon carbide (*SiC*). Ceramic tiles are placed on the flat surfaces that are parallel to the airstream [118]. Liquid hydrogen tanks are placed in front and behind the cabin to adapt the center of gravity for different flight phases. The preliminary design of the JAXA configuration is given in figure 16.

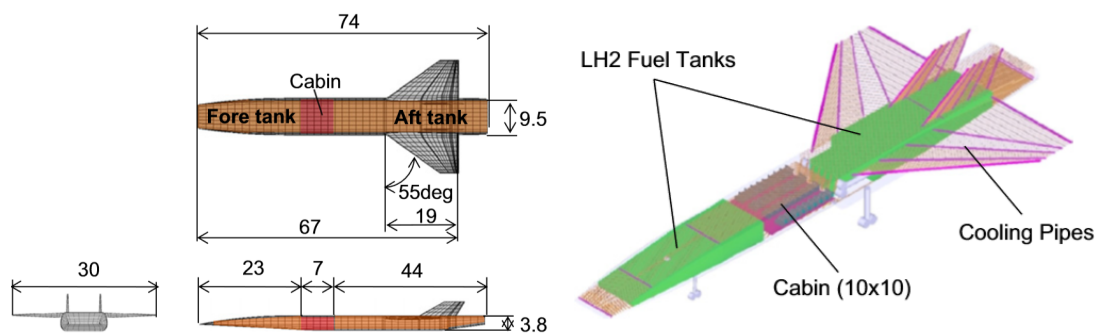


Figure 16: JAXA hypersonic vehicle configuration [118]

For the preliminary design of the JAXA configuration, a Multi-Disciplinary design optimisation approach was employed. In this multidisciplinary model, the coupling of aerodynamics, propulsion, trajectory and mass estimation are taken into consideration. For the preliminary design, the PANAIR panel code is used for subsonic aerodynamic analysis and tangent-cone/prandtl

meyer expansion are used as impact and expansion (shadow flow) models respectively for hypersonic flow [122]. The preliminary methods have been verified and validated using CFD and wind tunnel experiments. The majority of the aircraft mass is estimated using empirical methods such as the Hypersonic Aerospace Sizing Analysis (HASA [51]) model [79]. The overall take off mass of the aircraft is estimated to be around 284 tonnes. This take-off mass is fairly large in comparison to the LAPCAT A2 and HyCAT vehicles but it is believed to be a result of the low specific impulse predicted by JAXA for their pre-cooled turbojet engine, only expected to reach 1833 s in cruise (as opposed to an expected impulse of around 3800s for a hydrogen fuelled ramjet engine according to figure 6) [118].

2.2.4. ZEHST Aircraft

The Zero Emission High-Speed Transport (ZEHST) Aircraft was proposed as part of a French-Japanese cooperation by the European Aeronautic Defence and Space (EADS) [32]. The configuration has been designed for low sonic boom, long range and low emission (zero carbon). Three different propulsion systems are proposed including separate rocket, turbojet and ramjet engines. It also features a narrow fuselage body and small highly swept wings for low-sonic boom and good supersonic flow performance. The configuration is presented in figure 17 with the different propulsion systems.

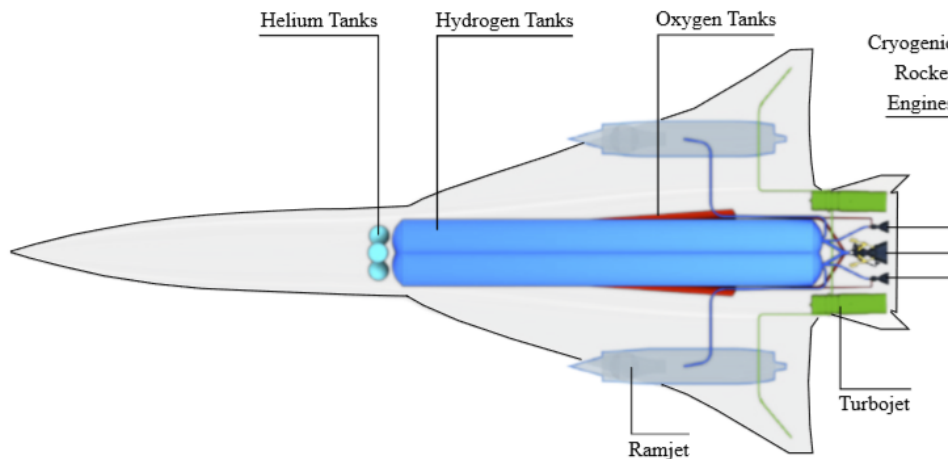


Figure 17: Zero Emission High-Speed Transport (ZEHST) EADS [32].

The turbojet engines are designed to operate for the take-off and subsonic acceleration to Mach 0.8 using seaweed based biofuels. The rocket boosters are included to accelerate the aircraft past the transonic regime to a Mach number of 2.5 using liquid hydrogen and oxygen [30]. Finally liquid hydrogen based ramjet engine are utilised to reach the cruise Mach number of 4 at an altitude of 32 km [93]. This configuration of propulsion systems is aimed at maximising the engine performance by utilising the most appropriate type of thermodynamic cycle per flight phase.

3. Challenges of hypersonic cruise vehicle design

The supersonic/hypersonic flow domain is significantly different from the subsonic environment and requires awareness of the critical phenomena associated with this flow regime for successful vehicle design. In this chapter, the aerodynamics, thermal aspects, tank design and multi-disciplinary nature of supersonic and hypersonic vehicles are explained and summarized.

3.1. Aerodynamics

When an object travels in the hypersonic flow regime, the characteristics of the flow are complex. Since hypersonic flow exceed by more than 3 times the speed of sound, the presence and effects of shock waves is predominant. In figure 18, the characteristics of the flow around a flat plate in hypersonic conditions is displayed. In this figure, the presence of the shockwave and boundary layer can be observed. In this regime, as the Mach number increases, the shock increases in strength and moves closer to the body causing strong interactions with the boundary layer [48]. Due to the proximity and strength of the shock wave, strong viscous interactions are present between the shock wave, inviscid flow and boundary layer [80]. These so called shock-turbulent boundary layer interactions (STBLIs) amplify the turbulent boundary layer causing extreme localised heating [29].

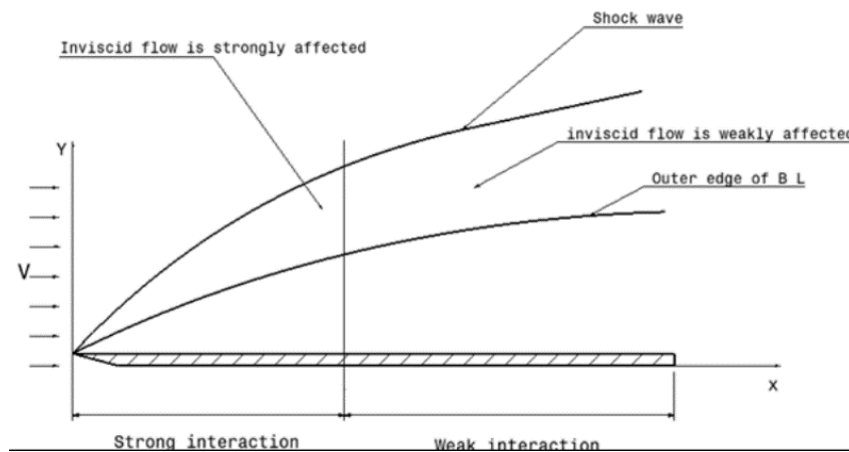


Figure 18: Hypersonic flow over a flat plate [48].

As a result of these effects, it is important to retain the non-linear aspects of governing flow equations to keep an acceptable level of accuracy when resolving the flow [80]. Two approaches are commonly used to resolve hypersonic flows around an object: Computational Fluid Dynamics (CFD) and Hypersonic Engineering Methods (HEM) [7].

Computational Fluid Dynamics (CFD):

Computational Fluid Dynamics (CFD) methods use discretized elements over and around an object surface to solve systems of equations that are based on conservation laws that provide solution of the flow around the object. Common types of CFD model that solve different form of the Navier-Stokes equations include; Reynolds Averaged Navier-Stokes (RANS) , Large Eddy Simulation (LES) and Direct Numerical Simulation (DNS). Direct numerical simulation, although the most accurate type of CFD method, is computationally very demanding and is thus not applicable in the case of coupled system that require multiple flow solutions. RANS based method are more commonly used for hypersonic flow and the accuracy of the method is mainly

dependent on the choice of turbulence model. These include: k-w, k-e, Spalart-Allmaras and Baldwin-Lomax turbulence models which have been verified for supersonic/hypersonic regime in multiple shock-boundary interaction studies [29].

Although Navier-Stokes CFD based solution may be attractive due to the accuracy of the solutions that can be obtained, their high computational cost makes their use prohibitive in optimisation schemes due to the high number of required solution from the aerodynamic solver [7] [29].

Hypersonic Engineering Methods (HEM):

Alternative methods to the computationally expensive computational fluid dynamics have been developed and used over the years to approximate hypersonic flow. The so called Hypersonic Engineering Methods usually solve the inviscid flow to compute resulting pressure distribution and use corrections for viscous flow to account for zero lift viscous drag. These inviscid methods include: Unsteady Hypersonic Shock-Expansion Method, Newtonian Impact theory and Inclined/Tangent cone methods [111] [80] [6]. For viscous corrections, methods such as the Spalding-Chi [7] and Effective shape corrections [6] have been used in literature.

The accuracy of these methods differ in their ability to model non-linearities of the flow and also depends on the shape of the body being analysed. In figure 19, a diagram of different inviscid flow theories is provided.

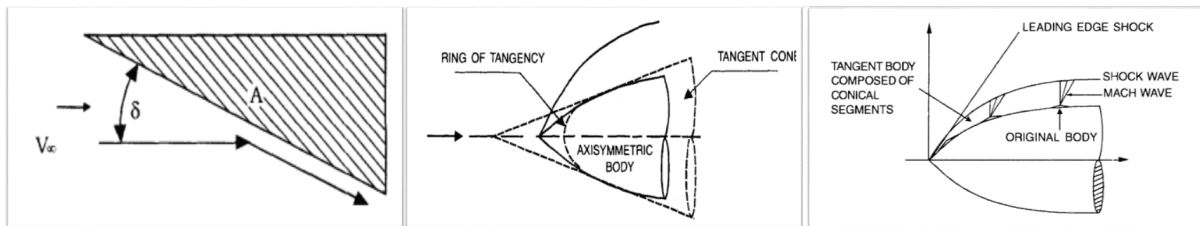


Figure 19: Hypersonic Engineering Methods. Newton impact theory (left), Cone theory (centre) and Shock-expansion (right).

Newton impact theory assumes that when air particles collide with an object, the tangential momentum component is conserved along the surface of the body while normal momentum is lost. In addition, in case of Newtonian theory, the shock is assumed to be detached from the body [6]. Inclined/tangent cone theories are widely used among hypersonic engineering methods. The methods assume that shocks are attached to the body and determines the pressure at each point on the surface by calculating the pressure on an equivalent cone of the same half angle as the local inclination angle at the points [111]. Shock-expansion theory assumes the presence of an adiabatic nose shock followed by isentropic flow expansion [111] [6].

In practice the different theories are applied depending on the shape being modelled in hypersonic flow [95], [7], [131], [63]. Newton impact theory is mostly used for blunt bodies with large inclination angles such as rounded fuselage nose sections as shocks are not attached to the body in such cases. Inclined cones theories are used on bodies with pointed nose and works relatively well for sharp leading edge airfoils [111]. Shock expansion theories are typically applied to slender wing and tail segments [7] due to the ability to model expansion of convex surfaces. In

figure 20, the different shock waves pattern created by varying hypersonic vehicle types is given. Indeed, for cruise and acceleration type vehicles (CAV) such as the X-15, attached and oblique shocks are expected over the vehicle body and wings as a result of sharp surfaces [89]. On the other hand, vehicles such as re-entry capsules and shuttles possess more blunt surfaces that creates strong shock detachment where the flow behind such shocks creates a region of subsonic flow [61]. Blunt surfaces reduce aerodynamic heating due to the reduction in flow kinetic energy behind a detached shock however increase wave drag significantly. For certain applications (such as re-entry capsules), heat transfer is critical whereas aerodynamic performance is not a primary criteria and in this cases blunt surfaces are common [55]. For hypersonic cruise and acceleration vehicles however, aerodynamic performance is critical and heat transfers are lower which results in sharp sections shapes as shown in figure 20 in an effort to minimize wave drag.

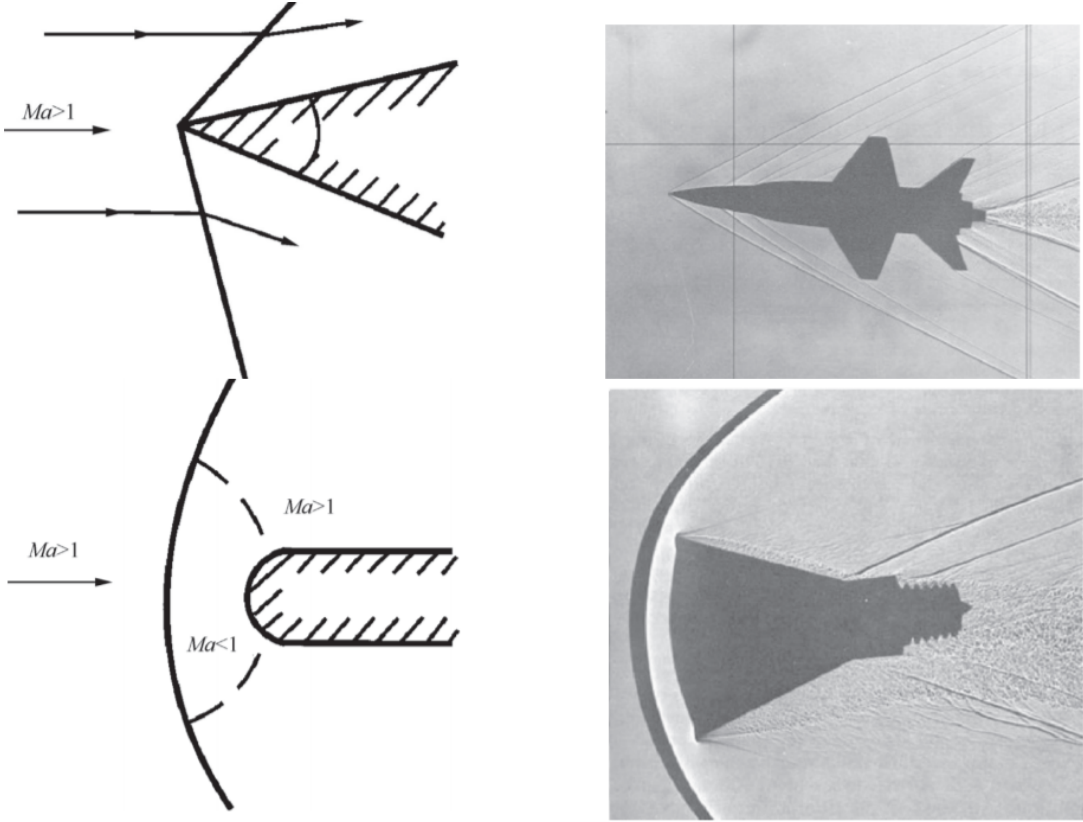


Figure 20: Different shock types for hypersonic vehicles (top: CAV type vehicle X-15 [89], bottom: re-entry capsule)[55].

Figure 21 shows an example of the re-partition of engineering methods imposed to aircraft surfaces to compute the hypersonic flow around a vehicle. Softwares such a CBAERO (Configuration Based Aerodynamics) [63] developed by NASA make use of proven and well understood engineering methods such as modified newtonian, tangent/wedge cone theory to resolve the flow around a vehicle at very low computational costs [63].

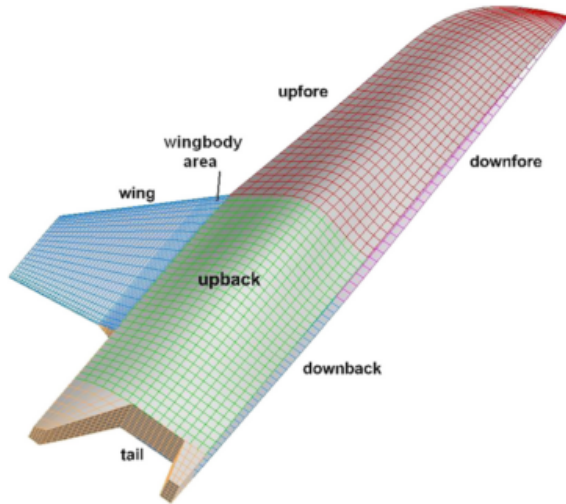


Table 4
Methods for inviscid calculations of flow along various surfaces.

	Properties	Method
Upper fore	expansion flow	inclined cone, modified Newton
Lower fore	3D compressible flow	inclined cone, modified Newton
Upper aft	flow around body	tangent cone
Lower aft	flow around body	tangent cone
Wing	primarily 2D flow	shock-expansion, tangent wedge
Tail	separated flow	Prandtl-Meyer

Figure 21: Use of hypersonic engineering methods on vehicle sections [7].

Viscous corrections are typically applied in engineering methods to account for drag generated by the bodies. These methods are usually based on semi-empirical relations to approximate viscous effects. The most common type of method use flat plate semi-empirical relations to estimate viscous drag on a vehicle [7].

In general, the flow around a hypersonic vehicle rapidly becomes turbulent due to high Reynolds numbers, and approximations of the turbulent boundary layer are formulated with the aid of experimental data and semi-empirical relations. Three of the methods used to compute viscous effects in turbulent hypersonic boundary layers include: Eckert's reference enthalpy method, Van Driest II and Spalding and Chi methods. All three methods use expressions for viscous (friction) drag effects on a flat plate and empirically determined coefficients [91]. To model the drag of a complete vehicle, the surface of the vehicle is modelled with a series of flat plates [7] and the resultant boundary layer is obtained through superposition of boundary layer properties over the different plate sections.

Supersonic and Hypersonic aircraft have a limited aerodynamic performance which is often characterized by the lift to drag barrier as presented in figure 22. As an aircraft Mach number increases past sonic conditions, the high friction and wave drag generated limits the maximum achievable aerodynamic performance. While lift to drag ratio of around 15 can be expected for a subsonic aircraft, L/D ratios of only 4 to 9 can be expected in the hypersonic regime [58] [38]. For hypersonic transport aircraft flying in the Mach range of 4 to 6, maximum aerodynamic efficiencies will approximately range between 6 and 9, with a maximum L/D of 8.4 at Mach 5. The theoretical barrier for wing-body and waverider type vehicles are given by the solid and dashed lines respectively.

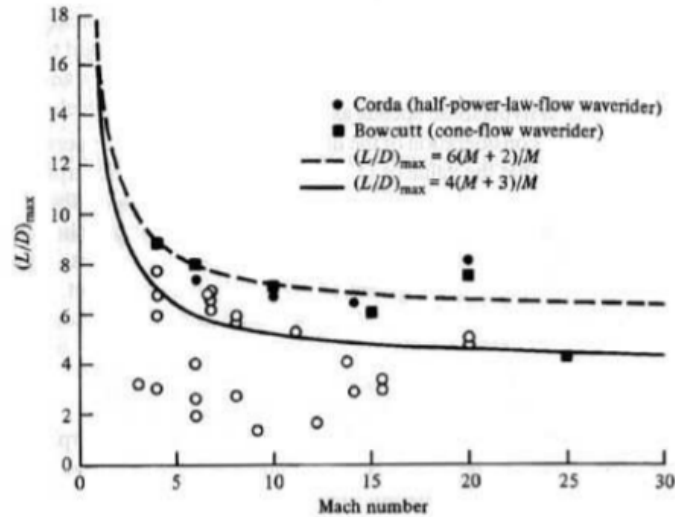


Figure 22: Lift to Drag barrier for hypersonic aircraft [58].

To maximise the aerodynamic potential of hypersonic configuration, slender lifting fuselage bodies configurations are generally used.

Another important aspect to take into consideration when dealing with hypersonic vehicles is the sonic boom generated. Shock waves around supersonic and hypersonic vehicles create acoustic disturbances in air that propagate till the ground surface creating unwanted noise [74]. Regulation exist prohibiting aircrafts from exceeding noise levels which are a nuisance to populations and can cause damage. In order to work around these regulations however, hypersonic aircraft can use alternative trajectories to fly over less populated area such as oceans and the arctic poles [112].

3.2. Thermal and dissociation effects

One of the biggest challenges of hypersonic flight is heat management. Due to the rapid deceleration of high speed flow of the vehicle surface, large amounts of kinetic energy are converted to heat. In figure 23, the typical average surface temperatures which can be expected at varying Mach numbers and altitudes are depicted. As can be seen, in subsonic flow domain the surface temperatures are low (around 310 Kelvins near Mach 1) but rapidly increase with Mach number where average temperatures of around 1200 Kelvins can be expected near Mach 5 [65]. This change in surface temperature really highlights the importance of taking heat aspects of the flow into account in the hypersonic domain.

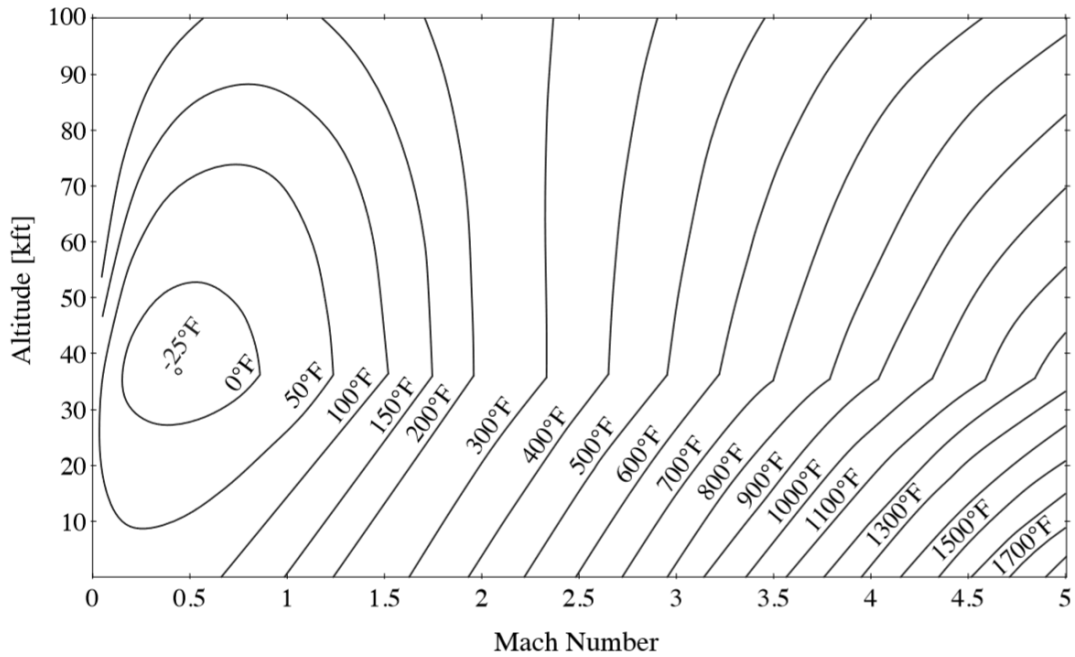


Figure 23: Average skin temperature at different Mach and Altitudes [101].

One of the direct effect of high temperature flow is the reduction in material strength and the need for heat resistant materials. For the Lockheed SR-71 Blackbird supersonic/hypersonic aircraft which made its first flight in 1964, high temperatures over the airframe (up to around 800 Kelvins, figure 24) lead to the use of titanium over the majority of the aircraft [81].

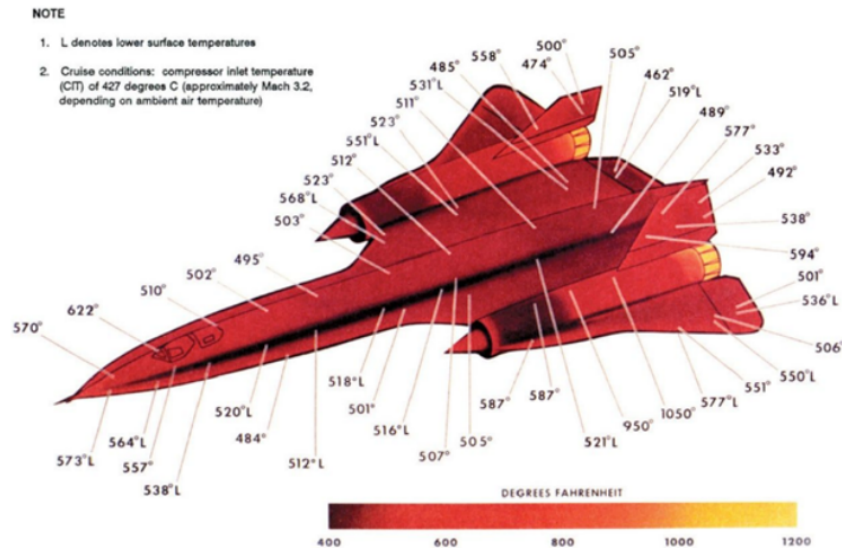


Figure 24: Skin temperature over the blackbird aircraft at Mach 3.2 [46].

In typical subsonic aircrafts, aluminum is used to provide rigidity to the structure. However for high speed aircraft, the increase in surface temperatures yields a rapid decrease in the effective strength and yield stress allowable for materials as can be seen in figures 25 and 26 [2] [56]. Clearly, for high speed aircraft applications, aluminium can no longer be used and materials such as titanium are the preferable choice. At speeds within the low-mid hypersonic range with temperature of around 1200 Kelvins, the applicability of metals and alloys decreases and ceramic

based materials become more relevant [81].

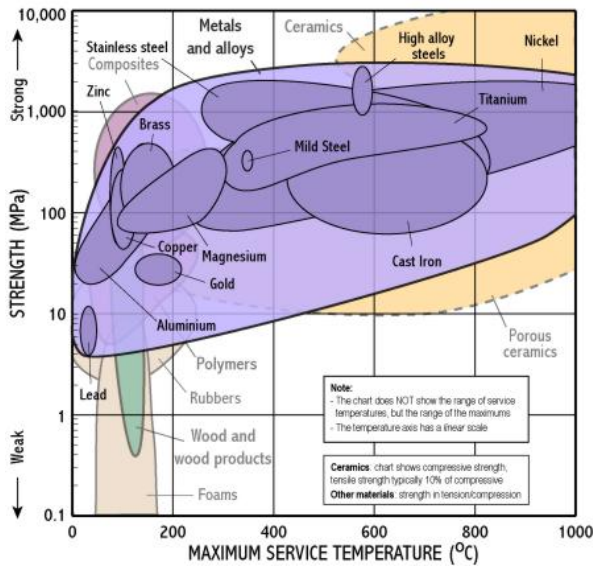


Figure 25: Strength vs service temperature of materials [2].

High temperature not only deteriorate material strength properties but also leads to high deformations as a result of strong temperature gradients within the materials. Excessive thermal stresses can yield to buckling of vehicle panels and to the phenomenon of creep leading to premature structural failures [14]. Creep can occur as a result of elevated loads combined with high thermal stresses for extensive time. At elevated temperature, materials strength is decreased but can also drastically reduce as a function of exposure time leading to premature failures and thus should be taken into account in hypersonic aircraft design [102].

Instead of exposing the airframe load bearing material directly to the outside air flow, a common practice in hypersonic aircraft design is the use of Thermal Protection Systems (TPS) [22] [57]. Vehicles such as the space shuttle orbiter from NASA have used thermal protection systems for hypersonic earth re-entry (figure 27) [92]. The purpose of the TPS is to protect an internal load bearing structure from the high convective heat transferred by the high speed flow. Different types of TPS types exists including passive, semi-passive and active systems with different benefits and drawbacks [43]. Protection system selection mainly depends on the type of application, re-usability, associated cost, unit mass, thicknesses and manufacturability [26]. Typical protection systems such as the one used on the space shuttle make use of an insulating material (depleting or non-depleting) which absorbs the incoming convective heat flow to maintain the load bearing “cold” sub-structure to an acceptable temperature. The type of TPS used over different sections of the surface depends on the heat exposure, with leading edges and the vehicle lower surface being exposed to the highest amount of convective heat [22]. Protection systems can also provide structural strength and resistance against thermal deformations and present a promising options for re-usable hypersonic cruisers where “hot” structures are not likely to be feasible. TPS are investigated in more depth in the methodology chapter of the report.

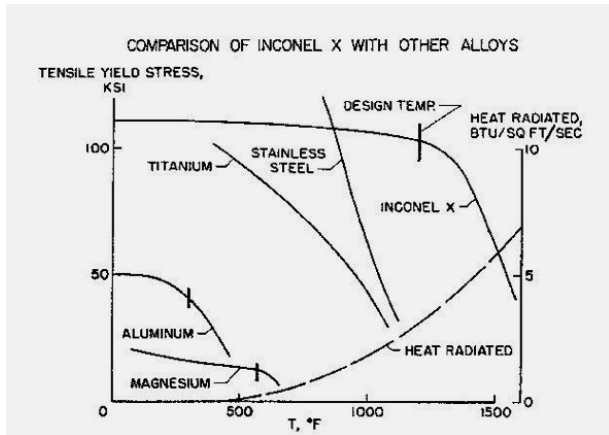


Figure 26: Material tensile strength as a function of temperature [56].

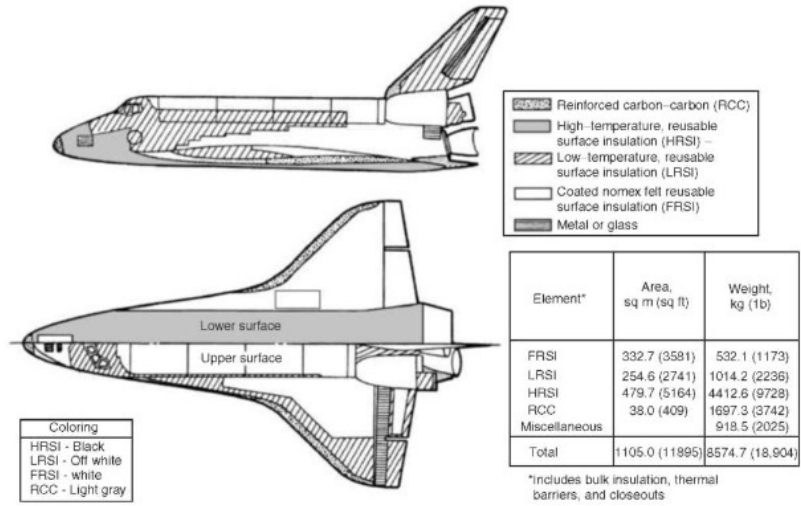


Figure 27: Thermal protection system over the space shuttle [92].

The high temperature within the boundary layer of a hypersonic vehicle can also lead to chemical reactions at the vehicle surface. Under high temperature, the high kinetic energy of the air particles can lead to molecular dissociation or even ionization of the gas [13]. In figure 28, the various chemical reactions taking place as a function of altitude and velocity is shown. As can be seen, increases in vehicle speed lead to additional chemical reactions where oxygen dissociation starts to occur at speeds ranging from 2 to 3 km/s. This corresponds to Mach numbers starting at around 6.3 for an altitude of 60 km. Real gas effects can affect the properties of the flow quite significantly and should be taken into account if present. Dissociation effects are most notable for re-entry type vehicles such as the space shuttle as shown in figure 28. For hypersonic cruise and acceleration vehicles however, the Mach numbers are generally lower and suffer less from dissociation effects. In any case, these effects should be taken into account to some extent within the boundary layer flow [83].

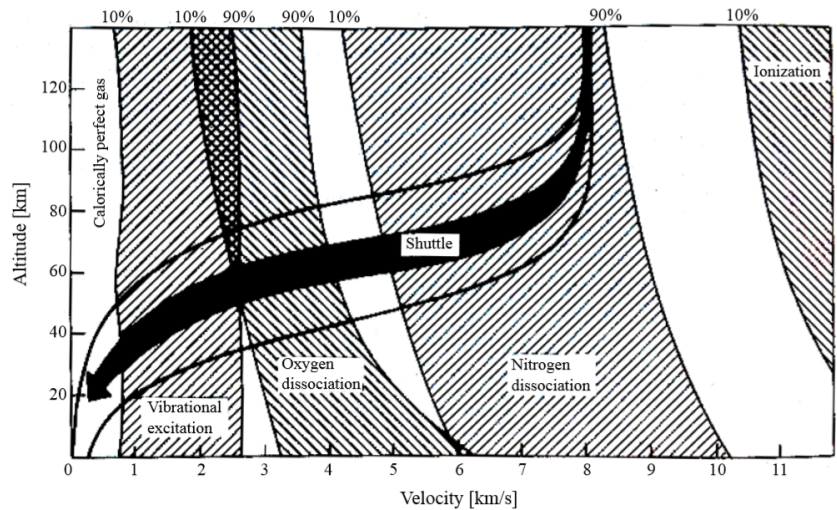


Figure 28: Chemical reactions occurring at different Mach and altitudes [13].

Another aspect relevant to the design of hypersonic vehicles is the boundary layer transition. For high speed vehicles, transitional flow will occur over the surface. Turbulent flow at high speed generate more heat transfer than laminar flow. As a result to ensure that no weight

penalties occur as a result of conservative designs, the transition of hypersonic flow should be predicted. It has been shown however that transition predictions for high speed flow is still very challenging. No accurate models for flow transition currently exist in literature [98] [53] and it is a common practice for now to assume that the flow over the entire vehicle is turbulent for a conservative design approach.

3.3. Liquid hydrogen tank design

Liquid hydrogen tanks are heavy components which can constitute a considerable fraction of an aircraft take off mass [51]. Liquid hydrogen tanks are composed of a load bearing structure and insulation layers as shown in figure 29. The load bearing must be able to sustain the high pressure loads that are required to keep the fuel in liquid form or cryogenic state. Additionally external loads such as accelerations must be taken into account in the design of liquid hydrogen tanks to size the load structure. To prevent excessive boil-off of the hydrogen fuel, insulation is used to protect low temperature fuel from the outside environment [119].

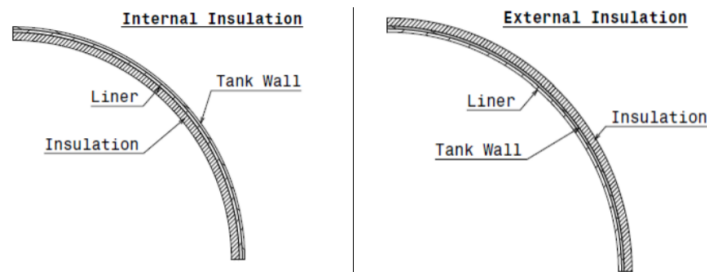


Figure 29: Tank structure and insulation [119].

Fuel tanks can be stored within an aircraft as an integral tank or outside the airframe as separate external tanks. Internal tanks are non-removable and are typically placed inside the fuselage for liquid hydrogen fuel as a result of the fuel's low density. Different packing arrangements exist for tanks aimed at maximising the volume of fuel stored by the tanks while minimising surface area. The insulation mass of the tanks is proportional to the surface area and thus minimising the surface to volume ratio of a tank decreases its mass [44]. In figure 30, two types of integral fuselage tank arrangements are shown, single and multi-bubble types. The best tank configuration will be dependent on their structural efficiency, volume and surfaces.



Figure 30: Single vs Multiple Bubble integral tank arrangements [52].

3.4. Multi-disciplinary optimisation

For the appropriate design of hypersonic vehicles, the coupling among disciplines should be captured at an early design stage. For the design of the JAXA hypersonic transport vehicle introduced in subsection 2.2.3, the multi-disciplinary coupling given in figure 31 was employed [109] [122]. In this multi-disciplinary optimisation, the gross mass is minimised subject to equality and inequality constraint.

In the platform presented, the design vector contains geometry, flight performance and trajectory parameters. In this platform two iteration loops are present; the mass estimation primary loop and trajectory sub-loop. For each design variable iteration, the component mass of the aircraft is first estimated in the primary loop and used as input to the secondary loop. In the sub-loop, the aerodynamic and engine performance throughout a trajectory are used to estimate the fuel required for the aircraft. To achieve this, the aircraft take-off mass estimated from the primary loop is used as input to the trajectory analysis. Then based on each of the trajectory points, the propulsion analysis provides an estimate of the fuel flow of the engine and thus the change in aircraft mass. Since a change in mass and flight conditions affects the aerodynamic performance of the aircraft (which in turn effects the propulsion performance), the aerodynamic analysis must be updated throughout the trajectory analysis. At the end of the trajectory analysis, a new estimated fuel mass is obtained and used as input to the primary loop to update the estimated take-off mass. Once both loops have reached convergence, the objective function and constraints can be evaluated and a new design iteration can start until an optima is reached.

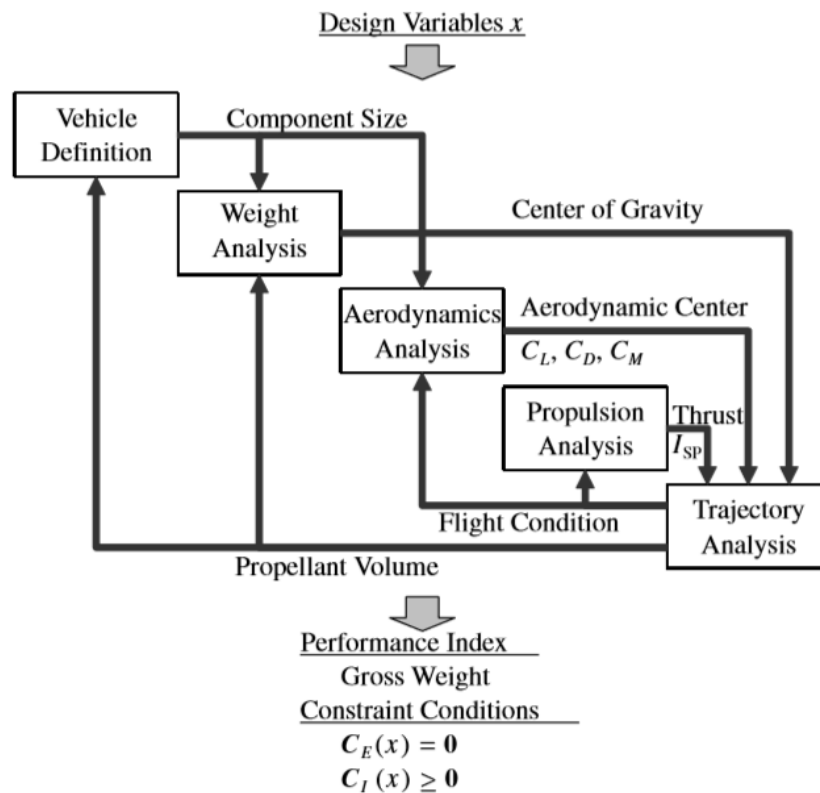


Figure 31: Multi-disciplinary optimisation for trajectory of JAXA vehicle [122].

The multi-disciplinary scheme presented here for the JAXA vehicle is believed to be quite inefficient in the author's opinion due to the use of two convergence loops (primary and sub-loops). Having sub-convergence loops in Multi-disciplinary optimisation platforms is quite inefficient due to the large number of discipline calls required for complete convergence. Additionally, the scheme presented here does not account for heat transfers and thermal management sizing (eg: thermal protection system) [122] [118] which is a critical component of high-speed transport vehicles [26].

4. Thesis Objectives and Overview

While Multi-disciplinary optimisation techniques are widely present in the context of subsonic aircraft design, their application to the conceptual design of hypersonic transport aircraft is not common. In comparison to conventional aircraft, hypersonic transports must consider the extreme heat transfers and different flow regime the vehicle undergoes during a mission. Thermal management is thus an essential aspect of the successful design of such vehicles and must be considered early on. While techniques such as Computational Fluid Dynamics (CFD) coupled to Finite Element Analysis (FEA) codes have previously been used to compute pressure, thermal loads and structural deformations for hypersonic aircraft sizing [93], these methods are computationally prohibitive and do not enable for the exploration of a large configuration design space. To elevate these limitations, this thesis aims at the development of a Multi-Disciplinary Optimisation platform for the sizing of hypersonic long-range transport aircraft via the control of the configuration outer shape. Formally, the main objective of the thesis can be formulated as follows:

How can a Multi-Disciplinary Optimisation approach be used to improve the conceptual design of long-range hypersonic transport vehicles?

In order to achieve the main goal of the thesis research, a set of sub-goals are formulated as follows:

- What techniques and tools can be used to generate a parametric model, automatic geometry builder and mesh generator for the analysis of complete aircraft configurations?
- How can Aero-Thermal panel code solvers be developed and integrated to the platform to allow for the rapid performance evaluation of a hypersonic transport aircraft?
- Which strategy and modules can be developed to estimate the mass of a generic configuration and ensure consistency among disciplines?
- To what extent do geometrical and mission properties of a long-range hypersonic transport aircraft impact the design of such vehicles?

In part II, the construction of the multi-disciplinary platform implemented in this thesis is described. In Sections 5 and 6, the disciplines considered and design structure matrix highlighting the integration and multi-disciplinary strategy for the sizing of a hypersonic long-range transport aircraft are introduced. Subsequentially, the implemented parametrisation, mission definition, automatic geometry and meshing of an arbitrary hypersonic vehicle are explained in Sections 7.1 to 10. The developed high-speed aerodynamic solver (Engineering Impact Methods) and integrated low speed solver (PANAIR) as well as the method for computing viscous flow and convective heat transfer using semi-empirical engineering methods are given in Section 11. Finally, the implemented mission performance module, thermal protection system sizer and mass estimation correlations used to estimate component mass characteristics of a configuration are provided in Sections 12 to 14.

An extensive validation of the aerodynamic solvers and thermal computations is provided in part III and provides a basis for the selection of appropriate models for the estimation of aerodynamic and thermal characteristics of a hypersonic aircraft. Starting with the integrated subsonic solver from Boeing (PANAIR), the results obtained on the NACA RM L51F07 wing body configuration are compared against wind tunnel experiments for a variety of Mach number and angle of

attack combinations. The high speed (hypersonic) solver developed in this thesis is validated by comparing the results from different hypersonic engineering methods to wind-tunnel experiments carried out on an ogive body and wing-body configurations such as the famous X-15 and HyCAT aircraft. The thermal solver is validated by comparing the convective heat transfer, Stanton number and friction coefficients computed over flat plates, wedges and cones to CFD and wind-tunnel experiments. The thermal protection system sizer developed in this thesis is verified by comparing the unsteady heat transfer balance throughout a hypersonic vehicle mission to that of a similar thermal protection model present in literature.

Finally in part IV, the optimal sizing platform developed in this thesis research is applied to the LAPCAT A2 hypersonic cruise vehicle configuration. In Sections 17.1 to 17.2, the characteristics of the baseline configuration, the control parameters selected for the platform, formal optimisation problem formulation and optimiser settings are provided. In Section 17.3 the results obtained using the developed optimal sizing platform on the LAPCAT configuration are provided. This section starts with a mesh convergence study followed by a sensitivity study of the control shape parameters on the mass estimation of the complete aircraft. The results from the application of the sizing optimisation algorithm on the baseline configuration are then provided and the effects of mission range and Mach number on the configuration sizing are analysed and discussed. Finally conclusions and recommendation are given in Section V.

Part II.

Modelling

5. The Aero-Thermo-Structural platform

The design of Hypersonic cruise vehicles involves interaction between numerous disciplines. Each of these disciplines can have an influence on the other which makes the design of such a vehicle a multi-disciplinary problem. Figure 32 displays the different disciplines that are most relevant to the design of a hypersonic cruise vehicle. In this work the disciplines taken into account are shown in green. The platform developed focuses on the preliminary design aspect of the cruise vehicle and aspects such as noise, emissions, costs and stability and control are not directly considered at this stage.

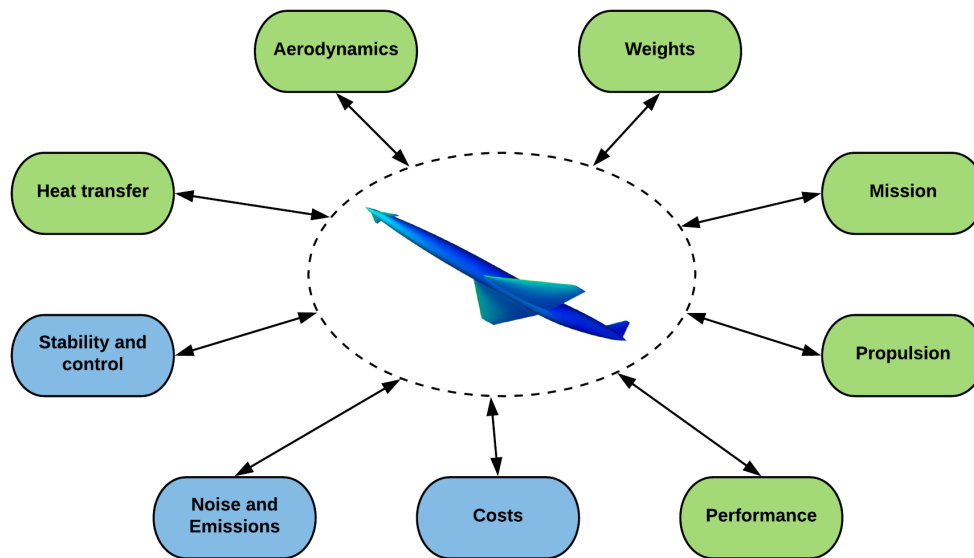


Figure 32: Disciplines involved in Hypersonic cruise aircraft design

6. The Design Structure Matrix

The platform has as aim to optimally size an aircraft based on the maximum take off mass W_{to} performance index. As a result in order to size an aircraft, the overall strategy employed is described in the design structure matrix as shown in figure 6.

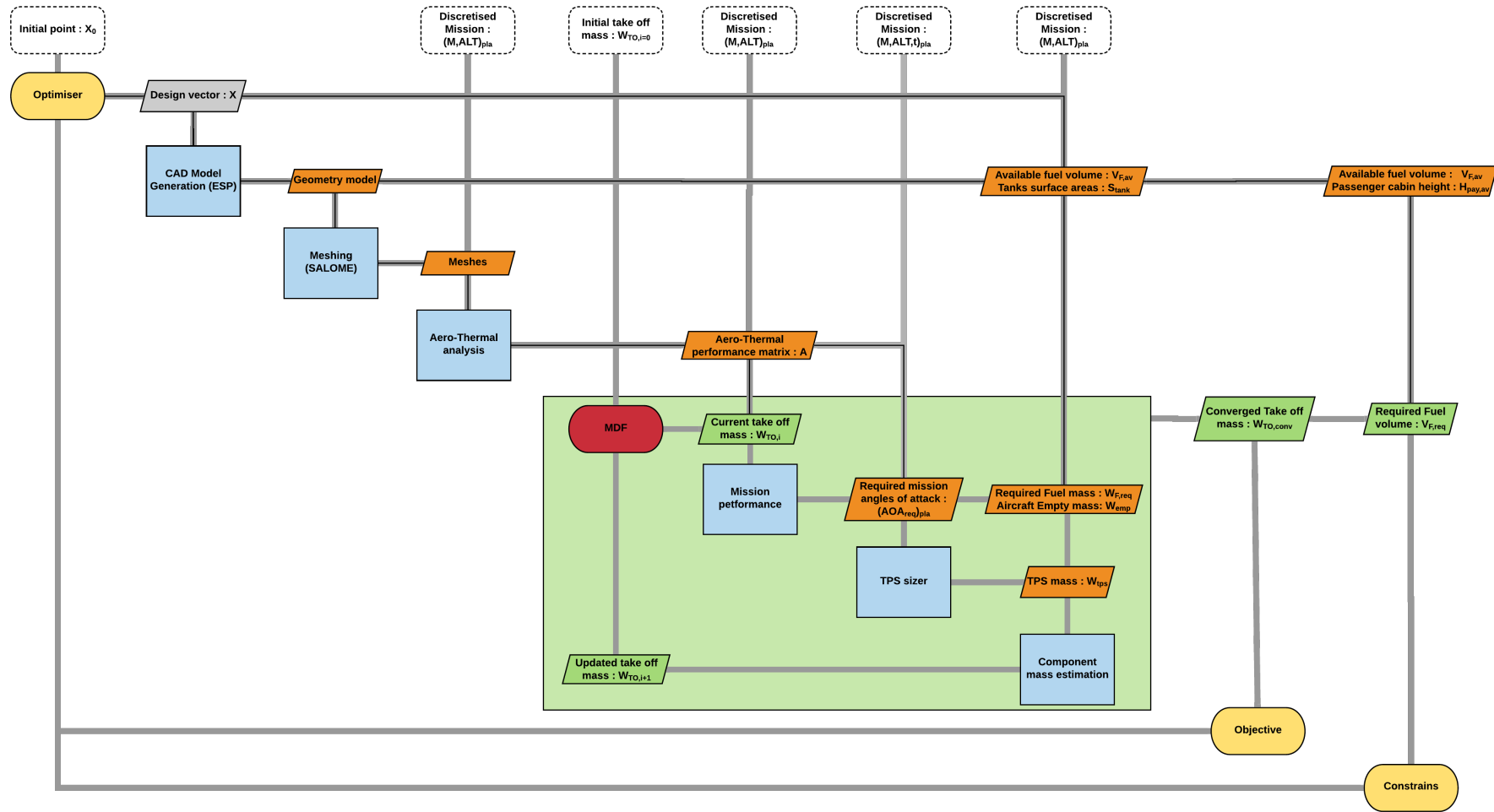


Figure 33: Design Structure Matrix of MDO platform.

Overall, the optimisation platform is composed of six modules, three of which need to be iterated to obtain a consistent system. The general aim of the platform is to search for optimal aircraft geometries that minimise the performance index subjected to constraints. In the following paragraphs, a summary of the working principles of the platform is given.

Inputs:

The inputs to the platform (shown in grey) are an set of initial parametrisation parameters (\vec{X}_0) and a mission profile. The parametrisation parameters serve as the design variables to the optimiser; \vec{X} . Parametrisation variables are used to control the shape of the wing cross sections (CST) and planform as well as the shape and scaling of the fuselage (Super-ellipses). The mission profile is an additional input that is kept constant during the optimisation process. The mission profile is defined a set of discretised plateaux and is subsequently used in the platform to evaluate the aircraft performance.

Modules:

The modules developed in the platform (in light blue in Figure 6) perform all the necessary steps and calculations to obtain an evaluation of the objective function. The modules can be sub-characterised into single evaluation and iteration modules as follows.

Single evaluation modules:

The modules described here consist of the first three modules of the platform and are evaluated only once for a given design variable vector \vec{X} . The working principle of each of the single evaluation modules can be described as follows:

- CAD model generation: This module is used to generate a three dimensional model of the complete aircraft through lofting and boolean operations based on the parametrisation design variables X . The CAD model generation engine used is called Engineering Sketch-Pad from MIT [50]. The output of this modules is a boundary representation of the aircraft (Brep). The outputted Brep files describe the outer surfaces (or outer mould) of the three dimensional aircraft geometry. Additionally, information regarding the fuel volume and payload height ($V_{F,av}$ and $H_{pay,av}$) available within the fuselage geometry are outputted for use in the optimiser constraints. Additionally the fuel tanks surface area (S_{tank}) are outputted by the geometry module for use in the structural mass estimations.
- Meshing: The meshing module takes as input the Brep files from the CAD model. Through a partitioning method, the aircraft outer mould surfaces are used to create a network of structured computational grids for further calculations. The module uses the SALOME platform [34] code to generate structured meshes of the aircraft.
- Aero-Thermal analysis: This module makes use of the meshes generated by SALOME [34] to compute a performance matrix A of the aircraft. The performance matrix contains the lift and drag polars of the given aircraft at each of the discretised mission plateaux. In addition, the performance matrix contains the interpolation of the convective heat transfers over the entire aircraft surface as a function of angle of attack at each of the mission plateaux by means of the Proper Orthogonal Decomposition method (POD).

For the aero-thermal computations, the calculations are divided within the module as inviscid and viscous flow. Depending on the Mach number at a given plateau, the low-speed code PANAIR [37] or high-speed impact methods are used to compute the inviscid

flow over the aircraft. For viscous flow and thermal computations, the semi-empirical methods of Eckert, Van Dries or Spalding and Chi are used based on the results of the inviscid analyses.

Iteration modules:

The iteration modules need to be evaluated multiple times in order to arrive at a consistent system. Consistency among modules in this part of the platform is ensured via the multi-discipline feasible (MDF) method. The MDF modules converge for the take off mass of the aircraft $W_{to,conv}$ which is the performance index of the platform.

In order to start the iteration loop, the MDF scheme takes as input the performance matrix A from the aero-thermal analysis and an initial (estimated) take off mass $W_{to,0}$. Afterwards the steps undertaken by the different iteration modules can be summarised as follows:

- Mission performance: This module takes an estimated take off mass as input. Using the steady flight assumption, the performance matrix A and the discretised mission, the module calculates the angles of attack required throughout the mission. Using an engine model, the fuel mass W_F required, empty mass W_{emp} and an engine mass W_{eng} are also computed.
- TPS sizer: This module sizes the thermal protection system W_{tps} of the hypersonic aircraft. Using the angles of attack required from the mission performance module and the interpolated convective heat transfer POD modes from the performance matrix A , the protection system is sized using a parametric curve approach relating TPS unit mass to total heat load.
- Component mass estimation: The mass estimation module takes as input the empty and fuel mass estimated by the mission performance module as well as the TPS and engine masses computed. This module uses empirical based relations from the Hypersonic Aerospace Sizing Analysis (HASA) and Weight Analysis of Advanced Transport systems (WAATs) methods to estimate the take-off mass and absolute mass of the different aircraft structural components such as aerodynamic surfaces, fuselage and subsystems masses. The component empirical relations are mostly based on the geometry of the aircraft and the take-off mass. As a result iterations are required within this module to arrive at a (new) estimated take off mass $W_{to,i+1}$.

The iteration process continues from the updated estimated take off mass $W_{to,i+1}$ obtained from the mass estimation module. Using the updated take-off mass, the mission performance module outputs new and different empty, fuel and engine masses as well as a new set of required angle of attacks for steady flight. This also induces a new TPS mass and a new take-off mass estimated from the mass estimation module. This process goes on till the take-off mass between two iterations is lower than a tolerance value such that $|W_{TO,i+1} - W_{TO,i}| < \Delta_{MDF}$. The converged take-off mass $W_{to,conv}$ is subsequently used to evaluate the objective function. The constraints are finally evaluated and both performance index and constraints are returned to the optimiser. The optimiser then changes the value of the design variables until an optimum is found.

In the following sections, the different modules constructed are described in more detail before validation of each of the major modules is given in the following part of the report.

7. Parametrisation of an Aircraft

Within the MDO framework, the purpose of the parametrisation step is to define a set of design variables \vec{X} that are used to modify the geometry of the aircraft and optimise the configuration. The configuration geometry is controlled via both parametrisation of wing and fuselage cross sections as well as planform parameters for the wing and scaling parameters for the fuselage. Two types of cross section parametrisation techniques have been implemented: The Class Shape Transformation Function and Super Ellipse parametrisation. These have been selected due to their wide use in aircraft design and their ability to represent a wide array of shapes with a small number of control variables.

7.1. Wing Parametrisation: Class Shape Transformation Functions

The Class Shape Transformation functions have been used to parametrise the wing cross sections. The method consist in parametrising any shape using a combination of class and shape functions [67] [68]. The class function is used describe the basic shape of a section while the shape function controls local perturbations around the basic shape. Class functions are very handy in the sense that they are able to capture certain basic properties of aircraft shapes such as round leading edges and sharp trailing edge for aircraft wings. The CST method can be expressed for a two dimensional section as given by equation 7.1 in normalised space ($\zeta = y/c$, $\psi = x/c$). In this equation, C represent the class function, S are the shape functions and $\zeta_T = \zeta_{te}/c$ is a dimensionless trailing edge thickness [68].

$$\zeta(\psi) = C_{N_2}^{N_1}(\psi) \cdot S(\psi) + \psi \cdot \zeta_T \quad (7.1)$$

The class function is further defined using equation 7.2 where the exponents N_1 and N_2 allow control over the basic shape being modelled. The class function exponents can be changed to represent virtually any type of cross section possible. In figure 34, examples of basic cross section shapes that can be modelled by adjusting the coefficients of the class function are shown.

$$C_{N_2}^{N_1}(\psi) = (\psi)^{N_1}(1 - \psi)^{N_2} \quad (7.2)$$

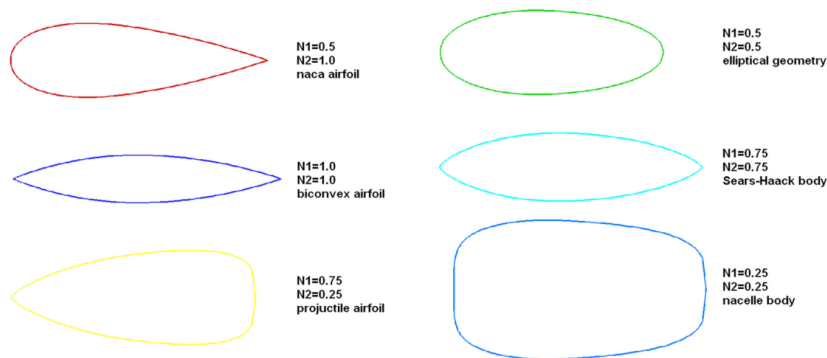


Figure 34: Basic cross section generated by various exponents N_1 and N_2 of the class function [68].

The second component of the class shape method is the shape function. In the CST method developed by Kulfan [67], the Bernstein polynomials are used as the shape functions which are defined by equation 7.3 where K_i is the binomial coefficient given by equation 7.4 and n is the

order and also number of individual berstein polynomials functions used. Finally the overall resulting shape function is obtained using equation 7.5 where the A_i coefficients are the control parameters that scale each of the shape functions to represent the overall shape.

$$S_i(\psi) = K_i \psi^i (1 - \psi)^{n-i} \quad (7.3)$$

$$K_i = \binom{n}{i} = \frac{n!}{i!(n-i)!} \quad (7.4)$$

$$S(\psi) = \sum_{i=0}^n A_i \cdot S_i(\psi) \quad (7.5)$$

In their original form (equation 7.1), the CST functions are expressed in non-dimensional space. In order to dimensionalise the functions and create a wing, a planform definition must be defined. Currently the wing can be parametrised as two separate planform each associated with four planform variables namely, taper ratio $\lambda = \frac{c_t}{c_r}$, wing span b , aspect ratio $AR = \frac{b^2}{S}$ and leading edge sweep Λ_{le} . The full parametrisation of the aircraft wing planform is described in figures 35 and 36 where each of the airfoil cross section are defined using the CST method.

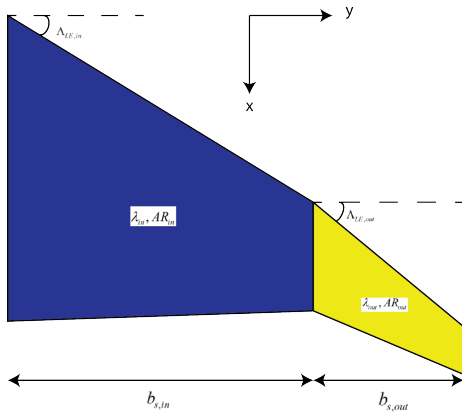


Figure 35: Inboard and Outboard wing planform definition.

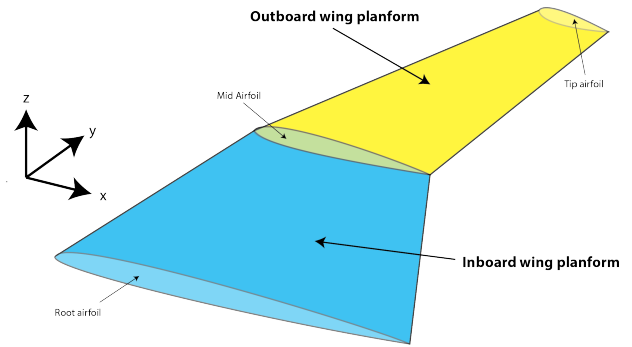
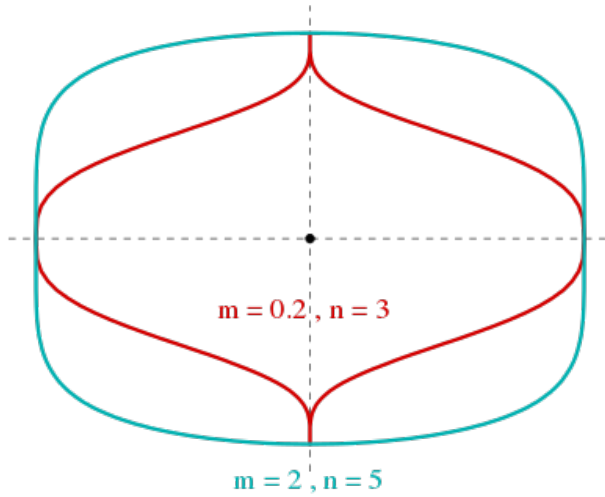


Figure 36: Perspective view of wing definition.

7.2. Fuselage Parametrisation: Super Ellipses

Super Ellipses have been used in this tool to parametrise fuselage cross sections. The general form of the super-ellipse is given by equation 7.6 [103] [104]. In this equation W and H represent the height of the dimensionalised cross section. On the other hand n and m represent the control variables of the superellipse. They allow the control of the upper and mid section of the ellipse shape. In figure 37, the different types of elliptical shapes that can be achieved using the super-ellipse technique is shown where negative values of the control variable yield concave local curvature and positive values result in convex local curvature.



$$\left| \frac{x}{W} \right|^m + \left| \frac{y}{H} \right|^n = 1 \quad (7.6)$$

$$\begin{aligned} y_{up} &= H_{up} \left(1 - \left(\frac{x}{W} \right)^{m_{up}} \right)^{\frac{1}{n_{up}}} \\ y_{lo} &= -H_{low} \left(1 - \left(\frac{x}{W} \right)^{m_{lo}} \right)^{\frac{1}{n_{lo}}} \end{aligned} \quad (7.7)$$

Figure 37: Normalised superellipse curves ($H = W = 1$) with varying control parameters.

To allow greater control of the local curvature of both upper and lower curves of the fuselage cross sections, four control parameters have been set to control separately both curves according to equation 7.7. In the developed platform an arbitrary number of fuselage cross sections can be used to represent a fuselage body. For each cross section the control parameters m_{up} , m_{lo} , n_{up} and n_{lo} must be specified as well as the scaling parameters H_{up} , H_{low} and W . This extension of the superellipse equation allows a much wider spectrum of cross sectional shapes to be generated as shown in figure 38.

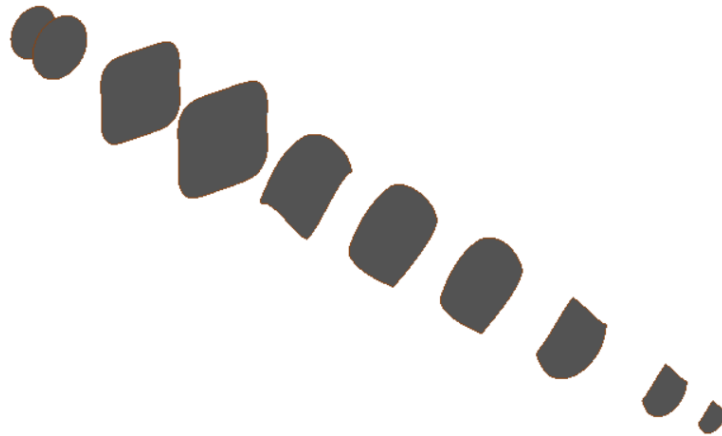


Figure 38: Example of fuselage cross section generated with various control parameters and scaling factors.

A summary of the control parameters that have been configured to modify the shape of an aircraft geometry is shown in Table 2.

Table 2: Summary of Aircraft control parameters

Section	Control Parameters
Inboard Wing	$CST_{inb}, AR_{inb}, \lambda_{inb}, b_{s,inb}, \Lambda_{le,inb}$
Outboard Wing	$CST_{out}, AR_{out}, \lambda_{out}, b_{s,out}, \Lambda_{le,out}$
Fuselage (Cross sections)	$W, H_{up}, H_{lo}, n_{up}, n_{low}, m_{up}, m_{low}$

8. Mission definition

The mission definition is an input and constant to the MDO platform. Through the discretisation of an input mission into a set of plateaux, the Mach number M_{pla} , altitude ALT_{pla} , rate of climb ROC_{pla} , flight path angle γ_{pla} and dynamic pressure q_{pla} at each of the plateaux is derived. These values are further used in the platform to compute the aero-thermal performance of the aircraft at each of the plateaux and in the mission performance module to estimate the fuel mass required throughout the mission.

8.1. Implementation

In the MDO platform, a mission profile is loaded into the platform. This original mission profile contains the altitude and Mach number profile of a hypersonic aircraft mission as a function of time. In the platform, the original mission profile is discretised as a set of N plateaux as described in figures 39 and 40. On each of the plateaux, the altitude ALT_{pla} and Mach number M_{pla} are kept constant for a set time $t_{pla} = t_{end} - t_{start}$. The altitude and Mach number of each plateau is taken as the average value between the value of Mach and altitude of the original mission at the start and end of the plateaux time segment as given by equation 8.2 and 8.1.

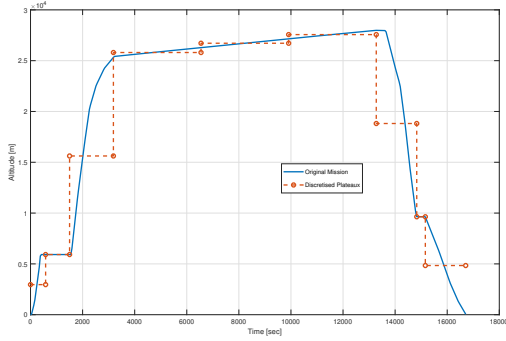


Figure 39: Discretisation of altitude from original mission.

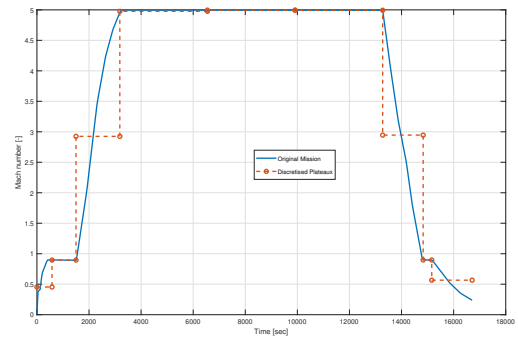


Figure 40: Discretisation of Mach number from original mission.

$$ALT_{pla} = \frac{ALT_{org,t_{start}} + ALT_{org,t_{end}}}{2} \quad (8.1)$$

$$M_{pla} = \frac{M_{org,t_{start}} + M_{org,t_{end}}}{2} \quad (8.2)$$

Next, the plateaux velocity and density can be computed using the Standard Atmosphere values of density and speed of sound on the original mission at the start and end time of each plateaux

as given by equations 8.3 and 8.4.

$$V_{pla} = \frac{(V_{org,t_{start}} + V_{org,t_{end}})}{2} = \frac{(a_{org,t_{start}} \cdot M_{org,t_{start}} + a_{org,t_{end}} \cdot M_{org,t_{end}})}{2} \quad (8.3)$$

$$\rho_{pla} = \frac{(\rho_{org,t_{start}} + \rho_{org,t_{end}})}{2} \quad (8.4)$$

Finally, the rate of climb, flight path angle and dynamic pressure at each plateau can be computed from their definitions using equation 8.5 to 8.7. An example of the plateaux rate of climb and flight path angle computed from the original mission (figures 39 and 40) is given in figures 41 and 42.

$$ROC_{pla} = \frac{ALT_{org,t_{start}} + ALT_{org,t_{end}}}{t_{end} - t_{start}} \quad (8.5)$$

$$\gamma_{pla} = \frac{ROC_{pla}}{V_{pla}} \quad (8.6)$$

$$q_{pla} = \frac{1}{2} \rho_{pla} V_{pla}^2 \quad (8.7)$$

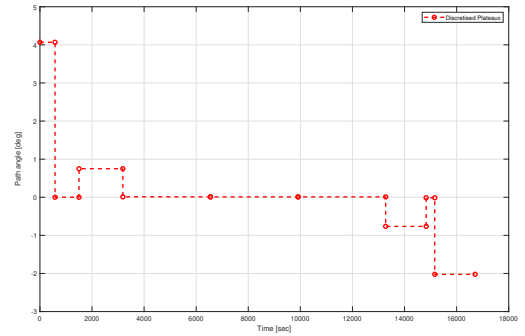
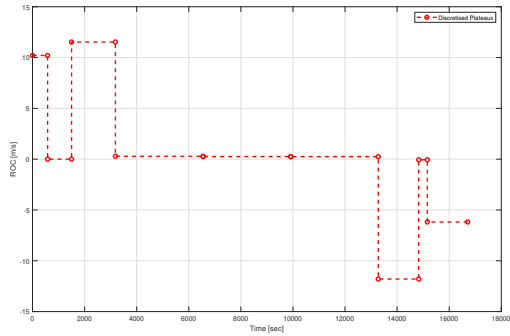


Figure 41: Rate of climb computed at mission plateaux. Figure 42: Flight Path angle computed at mission plateaux.

9. Automatic CAD modelling

The aim the CAD modelling module is to use the parametrised design variables and create a solid geometry representation of the aircraft configuration. In addition, the modelling module is used to compute the available fuel tanks volumes and payload bay height that are used as constraints within the optimisation framework.

9.1. Implementation

In order to automatically generate a three dimensional representation of an aircraft, the software *Engineering SketchPAD* (ESP) developed at the Massachusetts Institute of Technology is employed [50] [49]. This software has been selected due to it's ability to perform the rapid generation of three dimensional watertight geometries.

Using the built in Class Shape Transformation function, the cross sections of the wing surface are created, scaled and and positioned according to the planform variables. The fuselage cross sections defined by the super-ellipse definition are similarly positioned and scaled in the longitudinal direction (along the x axis). Following the generation of points for the cross sections using the parametric equations previously described, a spline interpolating function is fitted internally by ESP. An example of the cross sections generated for the wing planform and fuselage is displayed in figure 43.

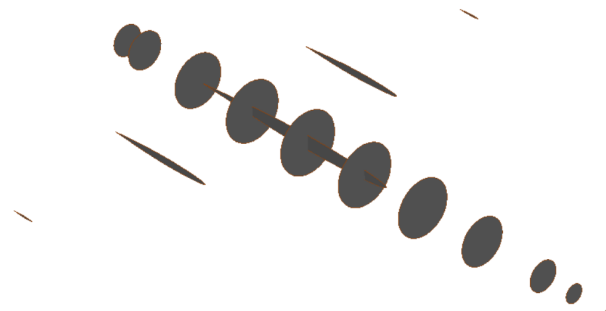


Figure 43: Fuselage and wing cross sections generated in ESP.

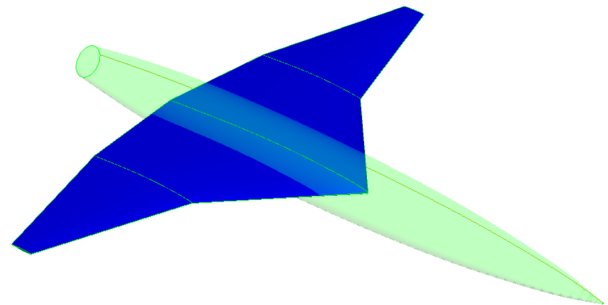


Figure 44: Wing and fuselage solids.

To generate solids, the generated cross section are subsequently lofted using ESP's "Blend" function. For the two wing planforms, the lofting function is applied between two defined cross sections resulting in a C^1 continuity of each planform. The fuselage cross section are composed of more than two cross section and thus as a result ESP ensures C^2 continuity for the fuselage solid geometry. In figure 44, an example of the resulting lofted geometry for the wing and fuselage is shown.

In order to perform aerodynamic computation of an aircraft geometry, it is essential to obtain a water-tight model. A water-tight geometry ensures that the aircraft can be represented as a single solid with no holes present. To achieve this the boolean operation "Union" of ESP is used to fuse together the wing and fuselage solids. This results in a unified aircraft geometry as shown in figure 45.

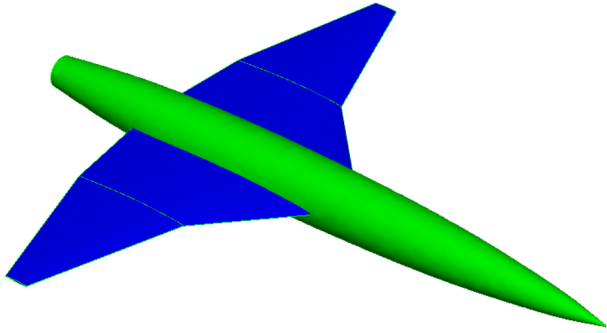


Figure 45: Fused water-tight aircraft geometry.

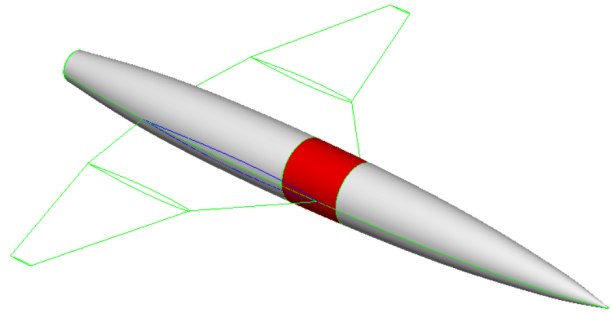


Figure 46: Tanks and Payload bay.

In addition to the aircraft geometry, internal fuel tanks and payload bays solids are computed through the intersection of the fuselage solid and rectangular cuboids to obtain the volume available for the fuel and the payload bay height ($V_{F,av}$ and $H_{pay,av}$). Finally the generated geometry is exported as a boundary representation format (Brep) which outputs the vertices, edges and faces of the aircraft solid.

10. Automatic Meshing

The meshing module aims to use the generated CAD geometry to construct and output a network of computational grids (meshes) on which further aero-thermal calculations (via the use of panel codes) can be performed.

In this platform, the open source python based software SALOME Platform [34] is integrated to the tool to generate meshes from an aircraft geometry created in ESP. The software is used to automatically generate meshes and has been implemented using a python script which is based on the python programming interface of SALOME.

10.1. Strategy: Geometry partitioning

For the aerodynamic panel codes used in this platform, it is required to provide structured meshes composed of quadrilateral elements. To ensure structured quad meshes can be generated on surfaces, it is necessary to obtain four edge surfaces. To achieve this it is essential to build meshes on surfaces which do not contain any holes.

The first step of the operation performed in SALOME consists in partitioning the fuselage body. When imported into SALOME, the fuselage section contains a hole on the surface created by the presence of the wing intersection. Using intersection of the fuselage with planes defined at the leading and trailing point of the wing-fuselage intersection edge, the fuselage is partitioned into a set of six surface networks as shown in figure 47.

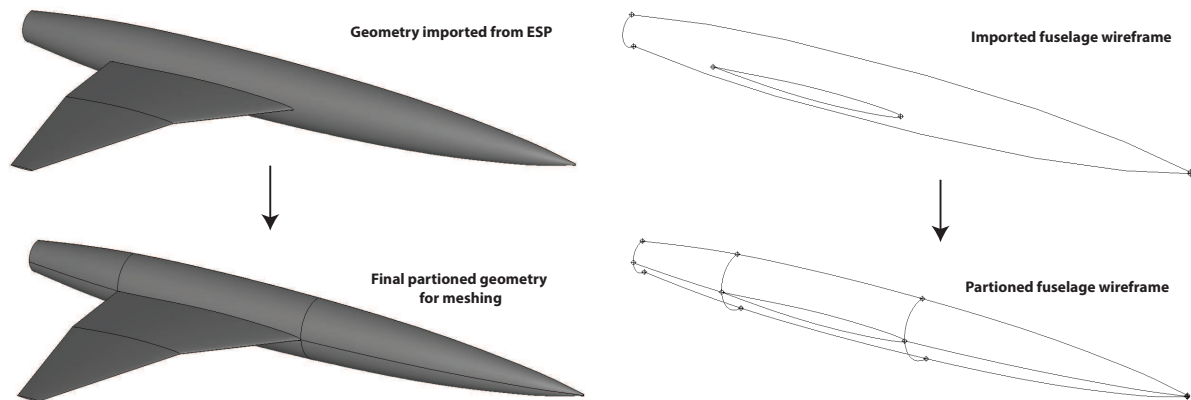


Figure 47: Partitioning of fuselage surfaces.

Additionally, for the low speed aerodynamic panel code, the wakes attached to the trailing edge of any surface must be generated. To create the wakes, surfaces are automatically generated by the SALOME python script as depicted in figure 48. The wakes are generated through a translation of the trailing edge of the respective surfaces.

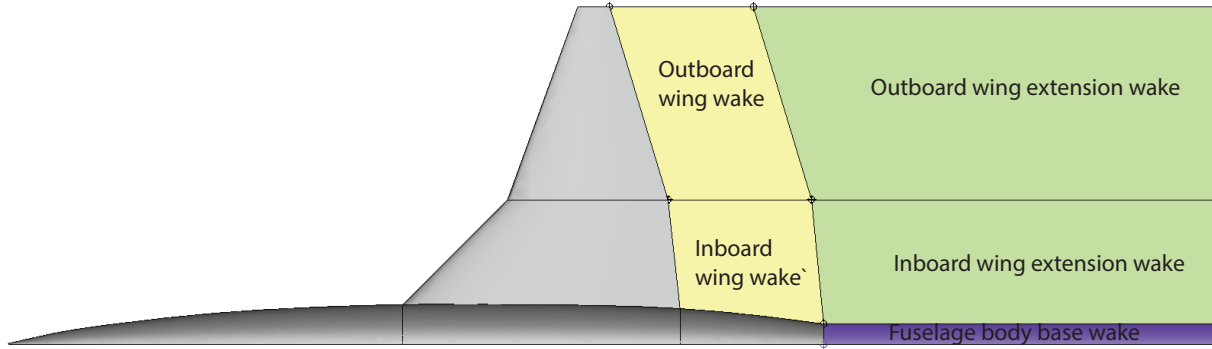


Figure 48: Definition of wake networks.

Having completed the different partitioning operations and creation of wake networks, the individual surfaces are meshed using the “Automatic Quadrangulation” function in SALOME. This results in a set of 16 mesh networks as shown in figure 49. The mesh refinement can be controlled via the number of nodes running along the longitudinal and lateral direction of the network’s edges. The distribution of nodes can also be adjusted in both directions.

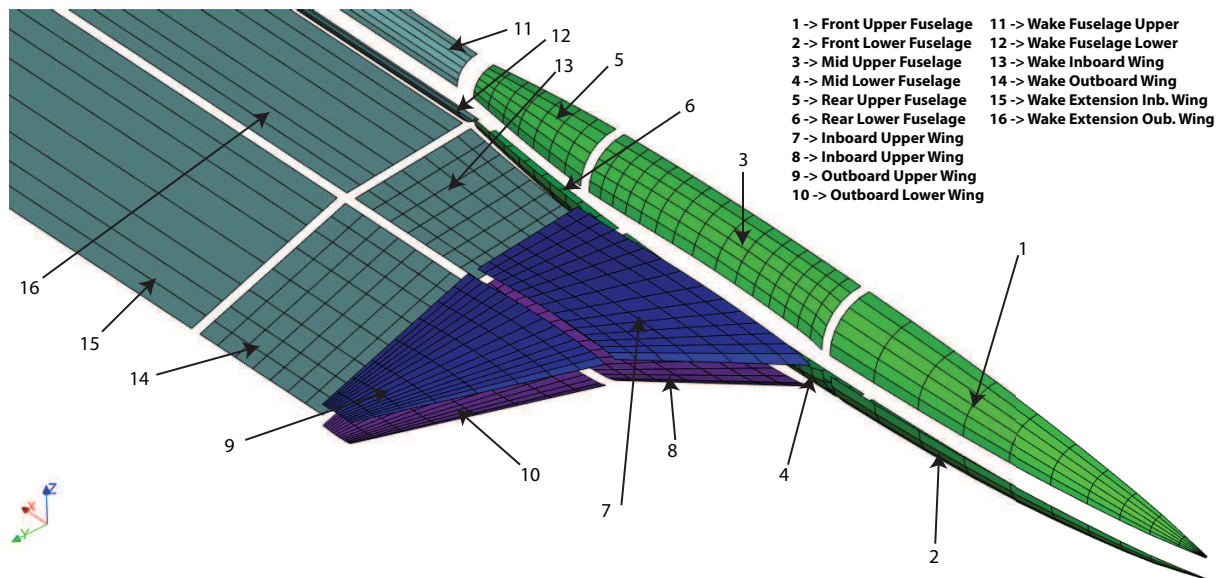


Figure 49: Exploded view of aircraft mesh networks.

To ensure that each of the mesh nodes coincide, the parameters chosen for the mesh control include:

- The number of nodes and distribution along the longitudinal direction of the wing planform and the fuselage front and rear sections.
- The number of nodes and distribution along the lateral direction of the inboard, outboard wing planforms and the fuselage.

A summary of the step taken to generate a geometry and perform the meshing operations within the platform is shown in figure 50.

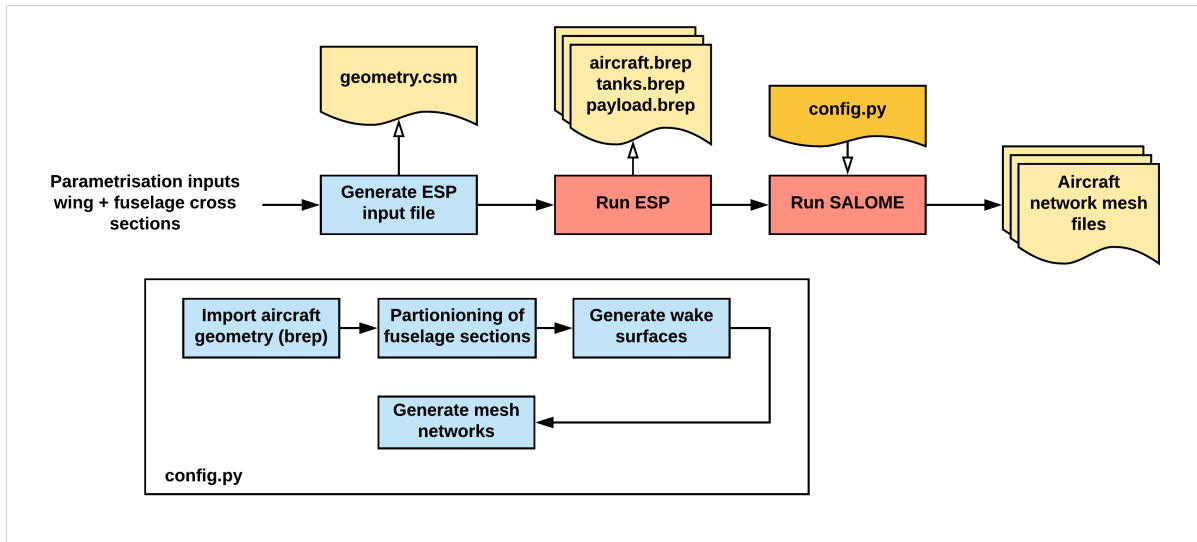


Figure 50: Flow chart of geometry and meshing process.

11. Aero-Thermodynamic analysis

The purpose of the Aero-Thermodynamic module in the MDO platform is to analyse the aerodynamic and thermal performance of the aircraft at each of the discretised plateaux of the mission definition. The aero-thermodynamic module uses the meshes computed from SALOME to perform the flow computations. The module is divided into two main parts; the inviscid flow analysis and the viscous-thermal analysis. At each plateau defined in the mission, the Mach number and altitude is used as an input to the Aero-Thermodynamic module.

For the inviscid analysis, depending on the magnitude of the Mach number at a given plateau, the module will either perform a “low-speed” subsonic analysis (if $M_{pla,i} < 1$) or a high speed analysis (if $M_{pla,i} > 3$). From the inviscid analysis, at each of the plateaux, the lift coefficient C_L and inviscid drag coefficient $C_{D,inv}$ are computed as a function of the angle of attack α .

Using the inviscid local flow properties derived from the inviscid low/high speed analyses at each angle of attack and plateau Mach number/altitude combination, the viscous-thermal flow analysis is performed. The aim of the viscous-thermal analysis is firstly to compute the friction induced viscous drag coefficient that is added to the inviscid drag coefficient to obtain the total drag coefficient $C_D = C_{D,inv} + C_{D,visc}$ as a function of the angle of attack at each plateau. Finally the heat transfer distribution over the entire vehicle is computed at each of the plateaux and the Proper Orthogonal Decomposition (POD) method is used to reduce the heat transfer distribution into a function of the angle of attack.

Overall, the Aero-Thermodynamic module results in a performance matrix A as shown in equation 11.1. This aero performance matrix contains the lift and drag coefficient and heat transfer distributions of the vehicle as a function of the angle of attack at each of the mission plateau Mach numbers ($M_{pla,1}, M_{pla,2}, \dots, M_{pla,N}$) and altitudes ($ALT_{pla,1}, ALT_{pla,2}, \dots, ALT_{pla,N}$).

$$A = \begin{bmatrix} C_L(\alpha)_{(M)_{pla_1}} & C_D(\alpha)_{(M,ALT)_{pla_1}} & q(\alpha)_{(M,ALT)_{pla_1}} \\ C_L(\alpha)_{(M)_{pla_2}} & C_D(\alpha)_{(M,ALT)_{pla_2}} & q(\alpha)_{(M,ALT)_{pla_2}} \\ \vdots & \vdots & \vdots \\ C_L(\alpha)_{(M)_{pla_N}} & C_D(\alpha)_{(M,ALT)_{pla_N}} & q(\alpha)_{(M,ALT)_{pla_N}} \end{bmatrix} \quad (11.1)$$

At each plateau, the lift and drag coefficient are described as a linear and quadratic function respectively. This is achieved through a linear interpolation of the lift (only dependent on inviscid flow) and a quadratic interpolation of the drag (dependent on inviscid and viscous flow) coefficients. Both interpolations are performed at each plateau over a range of sampled angles of attack as shown in equations 11.2 and 11.3.

$$C_L(\alpha)_{(M)_{pla}} = \left[C_{L,\alpha=0} + \frac{dC_L}{d\alpha} \alpha \right]_{(M)_{pla}} \quad (11.2)$$

$$C_D(\alpha)_{(M,ALT)_{pla}} = \left[C_{D,\alpha=0} + K_1 C_L + K_2 C_L^2 \right]_{(M,ALT)_{pla}} \quad (11.3)$$

11.1. High speed analysis: Engineering methods

To compute inviscid high speed flow over complete configurations, the so-called Hypersonic Engineering methods have been widely utilised [18] [111] [21]. Relevant codes include the Hypersonic Arbitrary Body Programme (HABP) for which development started in the 60's by Gentry & Mc Douglas [41] [116]. The HABP programme has been extensively used in the 1990s being the “most widely used tool in the preliminary design and analysis of hypersonic vehicles” [59]. Unfortunately, the HABP source code is written in FORTRAN 66 language which cannot be compiled on modern operating systems. The Public Domain Aeronautical Software contains an open-source version of HABP [4] written in modern FORTRAN, however this version has been found to be critically incomplete and thus not applicable to the platform. Other hypersonic panel codes include CBAERO by NASA [63] and ZONAIR by Zona Tech [133]. However, these codes are licenced and could not be accessed in the framework of this thesis. As a result of this, a tool has been developed to analyse the hypersonic flow over an arbitrary configuration based on the well-known hypersonic engineering methods present in literature.

11.1.1. Implementation

The code developed for the computation of local flow properties is based on strip theory. This method has been used over decades [59] to solve supersonic and hypersonic flows over arbitrary geometries. The strip theory consists in subdividing the surfaces of the geometry into a set of two dimensional strips in the configuration's longitudinal axis [59]. The flow diagram summarizing the operations performed in the hypersonic (high-speed) solver is shown in figure 51.

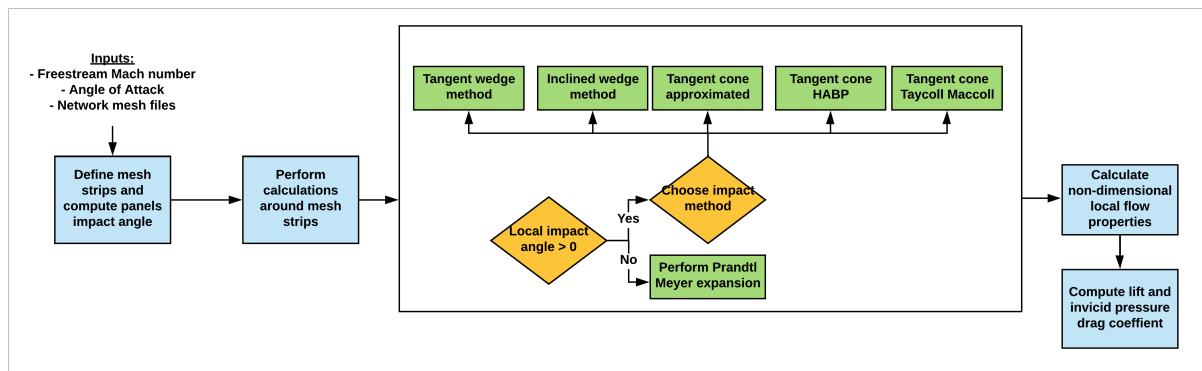


Figure 51: Flow chart for hypersonic methods.

In the solver, the first step defines each strip along the longitudinal direction of the vehicle as is shown in figure 52. For each strip, the flow computations are performed starting at the first panel and then along the other panels following the direction shown in figure 52.

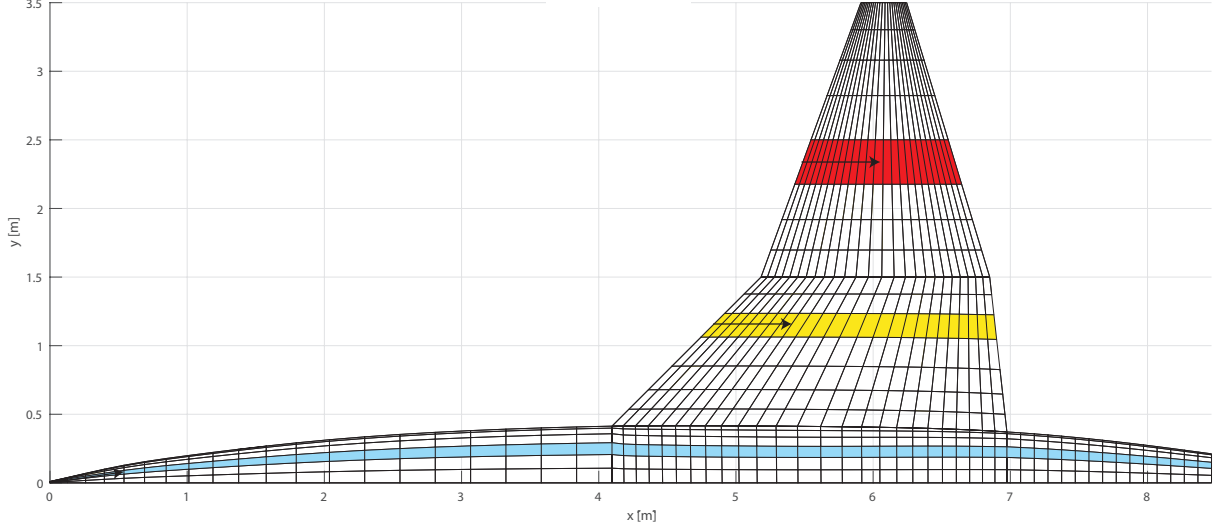


Figure 52: Strip method for flow computations. Example of strips shown with coloured panels.

Along each strip, the flow is characterised by impact flow or expansion (or “shadow”) flow. In figure 53, a schematic of the flow behaviour along a strip is shown. In hypersonic flow, if a panel surface is inclined with respect to the freestream ($\delta > 0$), the flow over the panel is modelled as a compression surface where a shockwave is formed. For panels at a negative impact angle with respect to the freestream ($\delta < 0$), the flow undergoes an expansion and is modelled using an expansion fan [59]. For compression flow, the flow over each panel is independent of other panel’s flow properties ($f_{i,comp}(M_\infty, \delta_i)$) whereas expansion flow is dependent on the flow over the panel prior to it ($f_{i,exp}(M_{i-1}, \delta_{i-1}, \delta_i)$).

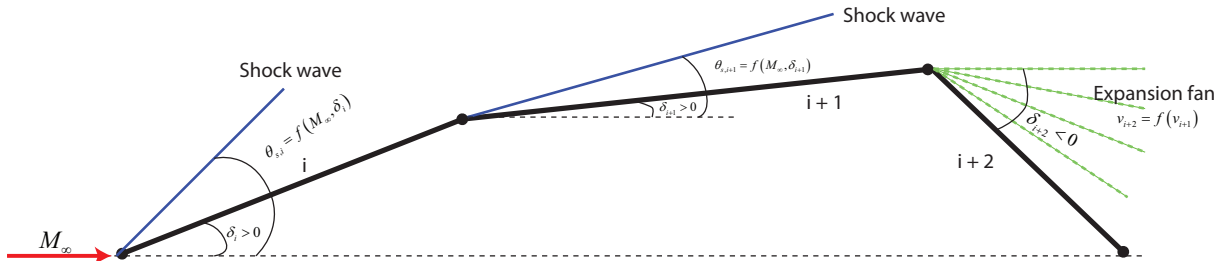


Figure 53: Impact and shadow flow along strips.

To determine the local impact angle at each panel along the strips the dot product of the incoming freestream velocity vector with the panel normal is used (see equation 11.5), where the freestream unit vector represents the directions of the freestream vector ($\vec{V}_{unit,\infty} = [\cos(\alpha), 0, \sin(\alpha)]$) [41]. The panel’s normal vector is obtained using the cross product of the diagonal vectors linking the vertices of each panel according to equation 11.4 (see figure 55).

$$\vec{n} = \vec{T}_2 \times \vec{T}_1 \quad (11.4)$$

$$\delta = \cos^{-1} \left[\frac{(\vec{n} \cdot \vec{V}_{unit,\infty})}{|\vec{n}| |\vec{V}_{unit,\infty}|} \right] - \frac{\pi}{2} \quad (11.5)$$

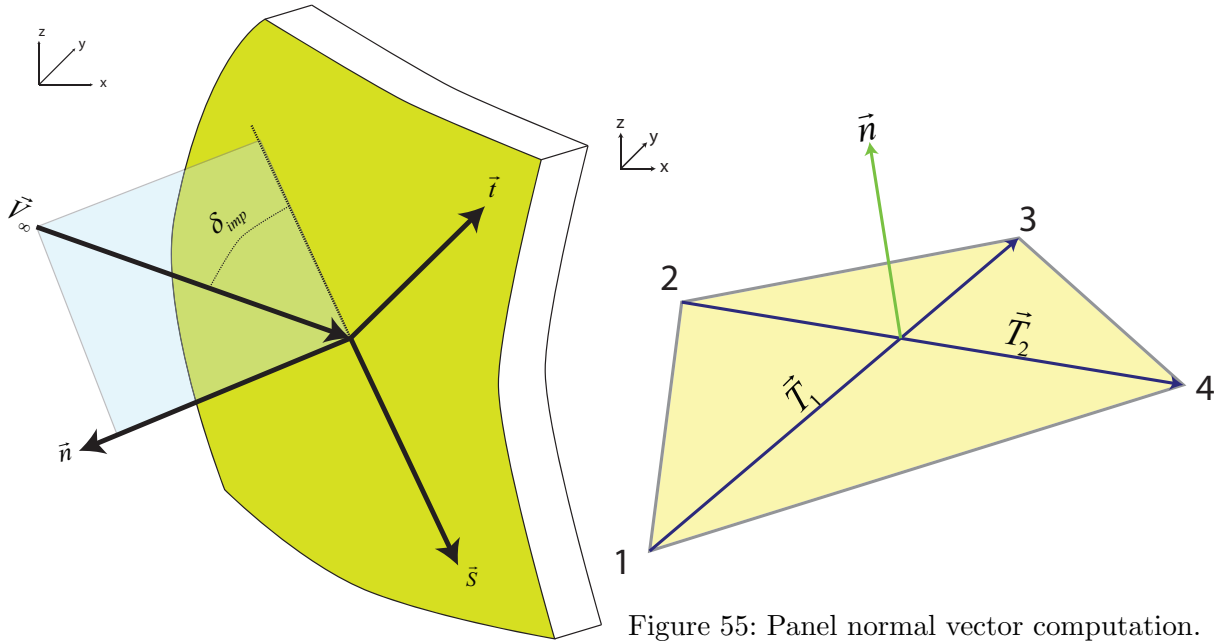


Figure 54: Definition of local impact angle and shear vector.

Figure 55: Panel normal vector computation.

11.1.1.1 Impact flow ($\delta > 0$): Cone and Wedge solutions

In the case of impact flow, a wide variety of shock models can be found in literature [41] [116]. In this report four impact flow models have been implemented. All the models assume an adiabatic shock wave whereby the total temperature is conserved across the shock $T_{0,\infty} = T_{0,s}$. The implemented flow models can be sub-categorised into two types of impact models: Wedge and Conical models.

In the wedge models, each panel is represented as an equivalent wedge with the local impact angle δ set as the equivalent wedge angle with respect to the freestream. Conical solutions model the local panel as an equivalent conical section with semi-apex angle equal to the local impact angle δ . The main difference between wedge and cone solution lies in assumption of the flow behind the shock.

Wedge models assume that the local shock angle θ_s is small when compared to the impact angle and thus the flow immediately behind the shock wave is equal to the flow on the surface of the panel [73]. On the other hand, cone models assume that the flow undergoes an isentropic re-compression between the back of the shock wave and the panel surface [73].

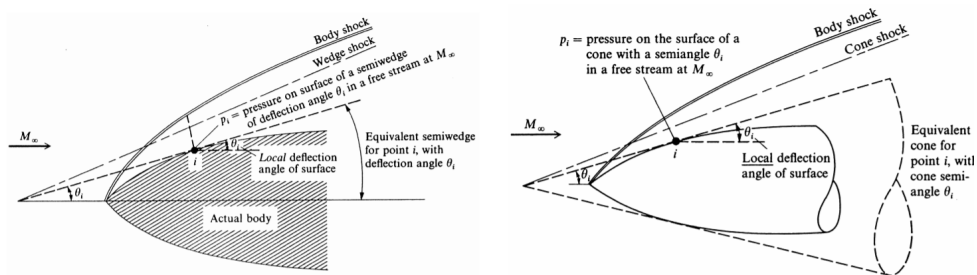


Figure 56: Equivalent Wedge (left) and Cone methods [59].

Table 3, summarises the impact methods (and associated assumptions) developed within the platform for the computation of impact flow. Other impact models exists in literature such as the Modified Newtonian method and other Conical methods [40]. Most of these models are however not adapted to the platform as they simply give an estimation of the pressure coefficient at the surface of the geometry but do not estimate shock wave angles and thus local flow properties such as local temperature and density cannot be derived from such methods.

Table 3: Impact methods implemented in platform

Impact model	Name of model	Main assumption
Wedge	-Tangent Wedge	Flow at surface is the same as behind the shock
	-Inclined Wedge	
Cone	-Tangent Cone Taylor Maccoll	Flow undergoes isentropic re-compression behind shock
	-Tangent Cone Approximate	

Tangent-Wedge Method:

The tangent-wedge method assumes that the flow over an inclined panel produces a two-dimensional oblique shock wave. Also the flow is assumed to be steady, inviscid and adiabatic across the shock wave [8]. To apply this method, a check is first performed to determine whether the shock is attached to the body using the equations described in [87]. For the case of detached shock, the shock angle is modelled as a normal shock $\theta_s = 90[deg]$. On the other hand if the shock is attached, the oblique shock-wave angle θ_s is determined by solving the implicit equation 11.6 for the shock angle.

$$\tan(\delta) = 2 \cot(\theta_s) \cdot \frac{M_\infty^2 \sin^2(\theta_s) - 1}{M_\infty^2 (\gamma + \cos(2\theta_s)) + 2} \quad (11.6)$$

The inviscid flow properties at the surface can be computed from the remainder of the oblique shock relations and the equation of state according to equations 11.7 to 11.10.

$$M_{inv} = \frac{1}{\sin(\theta_s - \delta)} \sqrt{\frac{1 + \left(\frac{\gamma-1}{2}\right) M_\infty^2 \sin^2(\theta_s)}{\gamma M_\infty^2 \sin^2(\theta_s) - \left(\frac{\gamma-1}{2}\right)}} \quad (11.7)$$

$$\frac{P_{inv}}{P_\infty} = \frac{2\gamma M_\infty^2 \sin^2(\theta_s) - (\gamma - 1)}{\gamma + 1} \quad (11.8)$$

$$\frac{T_{inv}}{T_\infty} = \frac{[2\gamma M_\infty^2 \sin^2(\theta_s) - (\gamma - 1)] [(\gamma - 1) M_\infty^2 \sin^2(\theta_s) + 2]}{(\gamma + 1)^2 M_\infty^2 \sin^2(\theta_s)} \quad (11.9)$$

$$\frac{\rho_{inv}}{\rho_\infty} = \frac{P_{inv}}{P_\infty} \cdot \left(\frac{T_{inv}}{T_\infty}\right)^{-1} \quad (11.10)$$

Inclined-Wedge Method:

This method was developed by Emanuel [36] to compute the shock angle on an inclined wedge without having to solve the implicit equation of the tangent-wedge method. Using this method, the shock angle θ_s can be computed explicitly as a function of the freestream Mach number M_∞ and the local impact angle δ according to equations 11.11 to 11.13. Since the equation is applied

to external flows, the weak shock solution $\epsilon = 1$ is used. Shock attachment is assumed in this method as long as $|X| < 1$ [36].

$$\theta_s = \tan^{-1} \left[\frac{(M_\infty^2 - 1) + 2\lambda \cos \left(\frac{4\pi\epsilon + \cos^{-1}(X)}{3} \right)}{3 \left(1 + \frac{\gamma-1}{2} M_\infty^2 \right) \tan(\delta)} \right] \quad (11.11)$$

$$X = \frac{(M_\infty^2 - 1)^3 - 9 \left(1 + \frac{\gamma-1}{2} M_\infty^2 \right) \cdot \left(1 + \frac{\gamma-1}{2} M_\infty^2 + \frac{\gamma+1}{4} M_\infty^4 \right) \cdot \tan^2(\delta)}{\lambda^3} \quad (11.12)$$

$$\lambda = \sqrt{(M_\infty^2 - 1)^2 - 3 \left(1 + \frac{\gamma-1}{2} M_\infty^2 \right) \cdot \left(1 + \frac{\gamma+1}{2} M_\infty^2 \right) \tan^2(\delta)} \quad (11.13)$$

Once the shock angle is computed, the rest of the flow conditions is computed using equations 11.7 to 11.10 for an oblique shock.

Tangent-Cone Taylor Maccoll (Interpolated):

This method was formulated by G.I. Taylor and J.W. Maccoll in 1933 [69]. In this method, the flow over a symmetrical cone is described by a complicated implicit differential equation but yields exact solutions of the shock angle and Mach number at the cone surface. The solutions to the Taylor Maccoll equations have however been tabulated [16]. The tabulated solutions are used in the platform and linearly fitted to obtain the cone shock-wave angle $\theta_{s,c}$ and the Mach number at the cone surface $M_{inv,c}$ as a function of the freestream Mach number M_∞ and the impact angle δ . Figures 57 and 58 shows the resulting interpolations from the tabulated values.

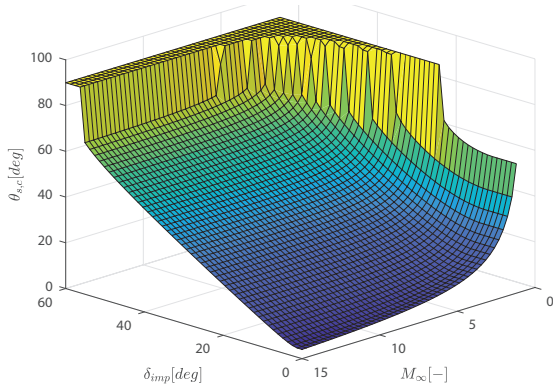


Figure 57: Interpolated cone shock angle.

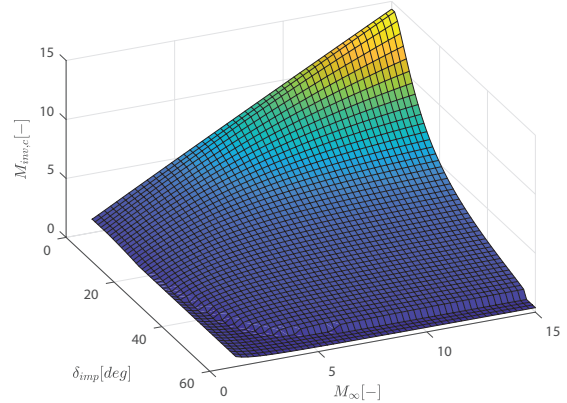


Figure 58: Interpolated Mach number at cone.

As it was previously stated, conical solutions assume that the flow conditions at the cone surface is not equal to the conditions directly behind the shock-wave. As shown in figure 59, the flow is assumed to undergo an isentropic re-compression behind the shock wave (between points 2 and c). As a result, the ratio of inviscid flow properties between the cone surface and freestream condition is given by equations 11.14 to 11.16. In these equations, the Mach number M_2 , pressure ratio P_2/P_∞ and temperature ratio T_2/T_∞ immediately behind the shock wave are obtained using the oblique shock relations previously given in equations 11.7, 11.8 and 11.9 [73].

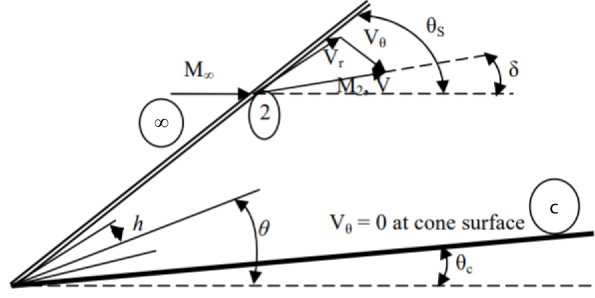


Figure 59: Description of conical flow [73].

$$\frac{P_{inv,c}}{P_\infty} = \frac{P_c}{P_2} \cdot \frac{P_2}{P_\infty} = \left[\frac{1 + \frac{\gamma-1}{2} M_2^2}{1 + \frac{\gamma-1}{2} M_{inv,c}^2} \right]^{\frac{\gamma}{\gamma-1}} \cdot \frac{P_2}{P_\infty} \quad (11.14)$$

$$\frac{T_{inv,c}}{T_\infty} = \frac{T_c}{T_2} \cdot \frac{T_2}{T_\infty} = \left[\frac{1 + \frac{\gamma-1}{2} M_2^2}{1 + \frac{\gamma-1}{2} M_{inv,c}^2} \right] \cdot \frac{T_2}{T_\infty} \quad (11.15)$$

$$\frac{\rho_{inv,c}}{\rho_\infty} = \frac{P_{inv,c}}{P_\infty} \cdot \left(\frac{T_{inv,c}}{T_\infty} \right)^{-1} \quad (11.16)$$

Tangent-Cone Approximate:

The approximated tangent cone solution from A.G. Hammitt and K.R.A. Murthy [87] is essentially an approximation of the exact Taylor Maccoll equation. The approximation is formulated to give the cone shock angle $\theta_{s,c}$ and Mach number $M_{inv,c}$ at the cone surface as an explicit function of the freestream properties and the impact angle δ given by equations 11.17 and 11.18. In equation 11.17, the correct sign (\pm) is the one given by the smallest positive value of $\theta_{s,c} - \delta$.

$$\theta_{s,c} - \delta = -\frac{\sin(2\delta)}{2 - (\gamma + 5) \sin^2(\delta)} \pm \sqrt{\frac{\sin(2\delta)}{2 - (\gamma + 5) \sin^2(\delta)} + \frac{(\gamma - 1) \sin^2(\delta) + \frac{2}{M_\infty^2}}{2 - (\gamma + 5) \sin^2(\delta)}} \quad (11.17)$$

$$M_{inv,c} = \sqrt{\frac{M_\infty^2 \cos^2(\theta_{s,c}) \cdot [1 + 2(\theta_{s,c} - \delta)^2]}{1 + \frac{\gamma-1}{2} M_\infty^2 \cdot [\sin^2(\theta_{s,c}) - 2(\theta_{s,c} - \delta)^2 \cos^2(\theta_{s,c})]}} \quad (11.18)$$

Once again the local inviscid conditions at the cone can be obtained using equations 11.14 to 11.16.

11.1.1.2 Expansion flow ($\delta < 0$): Prandtl Meyer expansion

For expansion flow (also know as shadow flow), the Prandtl Meyer expansion fan equation is used. The expansion fan is modelled as an infinite number of isotropic Mach waves around a convex corner [8]. The expansion fan is dependent on the properties of the flow on the panel prior ($i - 1$) to the expansion panel (i).

To solve the flow over an expansion panel, the Prandtl Meyer function is used. Firstly, the Prandtl Meyer angle at the previous panel on the strip is computed using equation 11.19. The Prandtl angle at the expansion panel can then be computed by adding the flow deflection $\Delta\delta = |\delta_i - \delta_{i-1}|$. Finally, the Mach number at the expansion panel surface can be computed by solving the implicit equation 11.21 for M_i .

$$v_{i-1} = \sqrt{\frac{\gamma+1}{\gamma-1}} \tan^{-1} \left(\sqrt{\frac{\gamma-1}{\gamma+1}} (M_{i-1}^2 - 1) \right) - \tan^{-1} \left(\sqrt{M_{i-1}^2 - 1} \right) \quad (11.19)$$

$$v_i = v_{i-1} + \Delta\delta = v_{i-1} + |\delta_i - \delta_{i-1}| \quad (11.20)$$

$$v_i = \sqrt{\frac{\gamma+1}{\gamma-1}} \tan^{-1} \left(\sqrt{\frac{\gamma-1}{\gamma+1}} (M_i^2 - 1) \right) - \tan^{-1} \left(\sqrt{M_i^2 - 1} \right) \quad (11.21)$$

The local flow properties can be derived using the obtained Mach number M_i and the isentropic relations according to equations 11.22 to 11.24. As can be seen from these equations, the flow properties at the expansion panel i are dependent on the previous panel $i - 1$.

$$\frac{T_{inv}}{T_\infty} = \frac{T_i}{T_{i-1}} \frac{T_{i-1}}{T_\infty} = \frac{1 + \frac{\gamma-1}{2} M_{i-1}^2}{1 + \frac{\gamma-1}{2} M_i^2} \cdot \frac{T_{i-1}}{T_\infty} \quad (11.22)$$

$$\frac{P_{inv}}{P_\infty} = \frac{P_i}{P_{i-1}} \frac{P_{i-1}}{P_\infty} = \left(\frac{T_i}{T_{i-1}} \right)^{\frac{\gamma}{\gamma-1}} \cdot \frac{P_{i-1}}{P_\infty} \quad (11.23)$$

$$\frac{\rho_{inv}}{\rho_\infty} = \frac{\rho_i}{\rho_{i-1}} \frac{\rho_{i-1}}{\rho_\infty} = \frac{P_i}{P_{i-1}} \left(\frac{T_i}{T_{i-1}} \right)^{-1} \cdot \frac{\rho_{i-1}}{\rho_\infty} \quad (11.24)$$

11.1.2. Lift and Drag coefficient computations

To compute the lift and inviscid drag coefficients of the configuration, the pressure coefficient (equation 11.25) is firstly integrated over the panels P to obtain the axial and normal force coefficients (equations 11.26 and 11.27). Since only half of the configuration is analysed the normal and axial coefficients are non-dimensionalised using the semi-wing area $S_{semi} = S_{ref}/2$.

$$c_{p,inv} = \frac{2}{\gamma M_\infty^2} \left(\frac{P_{inv}}{P_\infty} - 1 \right) \quad (11.25)$$

$$C_N = -\frac{1}{(S_{ref}/2)} \sum_P c_{p,inv} A_P n_{z,P} \quad (11.26)$$

$$C_A = -\frac{1}{(S_{ref}/2)} \sum_P c_{p,inv} A_P n_{x,P} \quad (11.27)$$

Using the angle of attack, the lift and inviscid drag coefficients are computed with respect to the freestream flow direction according to equations 11.28 and 11.29.

$$C_L = C_N \cos(\alpha) - C_A \sin(\alpha) \quad (11.28)$$

$$C_{D,inv} = C_N \sin(\alpha) + C_A \cos(\alpha) \quad (11.29)$$

11.1.3. Limitations of Hypersonic Engineering methods

Hypersonic Engineering Methods have been implemented to solve the inviscid flow over an aircraft configuration. The methods used are semi-empirical in nature and use similarity methods to estimate the flow over a configuration. The implemented methods allow the flow over the entire aircraft to be computed at a very low computational cost, which is desirable in an MDO platform. However the simplifications pose some limitations:

- Strip method: The strip method employed to solve the flow over the configuration assumes that the flow over the aircraft can be analysed using a set of two dimensional sections. It is often assumed in hypersonic conditions that the flow momentum is very high and thus three dimensional effects are small [59]. It can however be expected that three dimensional effects become more predominant as a result of streamline curving at higher angle of attacks. As a result, the implemented methods should be used at low angles of attack where three dimensional effects are small.
- No wing-body interference: In the strip method implemented, the flow over the wing and fuselage surfaces are computed independently. As a result wing-body interference effects are not taken into account. While interference effects have a large contribution in subsonic flow, in hypersonic flow these effects are assumed to be near negligible [40].
- Impact flow: The flow is modelled separately for each panel inclined with respect to the flow. This assumption originates from the Newtonian flow model whereby the majority of the freestream flow momentum is converted to tangential momentum at the surface of a panel [116]. This assumption becomes valid at high Mach numbers $M \gg 3$ and limits the application of this method from high supersonic to hypersonic Mach numbers.
- Shock-Boundary layer interactions: In hypersonic flow interactions occur between the shock-wave, inviscid layer and boundary layer [18]. In this method, the inviscid layer is de-coupled from the viscous layer. This assumption has been made consistently in previous preliminary design codes [40] [59].

Overall, due to the previously stated limitations, the engineering methods used in this platform can be used for high supersonic to hypersonic Mach numbers $M_\infty \geq 3$. In addition, the angle of attack is restricted to not exceed 10 [deg] to minimise the error which could arise due to three dimensional effects.

11.2. Subsonic (“Low speed”) analysis: PANAIR

In order to compute the properties of the subsonic flow over a generated aircraft configuration, the “higher order” PANAIR panel code developed by Boeing is employed [37].

11.2.1. Theoretical background

The theoretical basis of the PANAIR code is based on the Prandtl-Glauert equation. This equation is achieved through the simplification of the continuity, momentum, energy and state equations. In order to arrive at the Prandtl-Glauert equation, a few assumptions regarding the nature of the flow must be applied, these include:

- Inviscid flow: The stress tensor $\tau_{i,j}$ of the momentum and energy equations is assumed to be zero. As a result any viscous effects related to viscosity of the fluid are neglected.
- Isentropic flow: It is assumed that no heat is added to the fluid, $q = 0$. Without the presence of shock wave in the flow, the entropy of the fluid is kept constant leading to a reversible process.
- Irrotational: The fluid particles do not undergo a net rotation about a chosen coordinate system, $\nabla \times \vec{V} = 0$. This means the flow path may be circular however the fluid particles do not rotate about a chosen axis themselves. Rotational flow is more common in viscous flow due to the strong velocity gradient present that induce a difference in shear force on the elements which results in distortions and rotation of fluid particles.
- Steady: The fluid particles velocity do not change magnitude or direction with time, $\frac{\partial}{\partial t} = 0$.

After linearization of the steady-linear potential flow equation, the Prandtl Glauert equation is obtained as given in equation 11.30. The linearization of the potential flow equation implies that the change in flow magnitude over a surface is small ($M_\infty^2 |\vec{v}| \ll 1 - M_\infty^2$ and $M_\infty^2 |\vec{v}| \ll 1$) and thus surfaces with strong changes in local flow properties or panel orientation (such as a sharp corner) cannot be correctly predicted. The perturbation potential ϕ is related to the local (non-dimensional) velocity \vec{V}_{nd} through equation 11.31 where $\vec{V}_{unit,\infty}$ is the freestream (unit magnitude) vector.

$$(1 - M_\infty^2) \phi_{xx} + \phi_{yy} + \phi_{zz} = 0 \quad (11.30)$$

$$\vec{V}_{nd} = \vec{V}_{unit,\infty} + \nabla \phi = \begin{bmatrix} \cos(\alpha) \\ 0 \\ \sin(\alpha) \end{bmatrix} + \vec{v} \quad (11.31)$$

The Prandtl Glauert equation is formulated over a body S_B using Green’s theorem which results in a integral given by equation 11.32 where the *source strength* (σ) and *doublet strength* (μ) are defined through equation 11.33.

$$\phi(P) = -\frac{1}{4\pi} \int_{S_B} \left[\frac{\sigma}{R} - \mu \vec{n} \cdot \nabla \frac{1}{R} \right] dS \quad (11.32)$$

$$\begin{aligned} \sigma(Q) &= \vec{n} \cdot \nabla \phi(Q) \\ \mu(Q) &= \phi(Q) \end{aligned} \quad (11.33)$$

Furthermore, the Prandtl Glauert equation is solved using discretised points on a set of panels where each panel is sub-divided into a set of sub-panels (figure 60) which allow the doublet strength over a panel to be represented as a quadratic function and the source terms as a linear function. This allows both doublet and source terms to be continuous over the panel which greatly enhances the accuracy of the solver and characterises PANAIR as a higher order panel code.

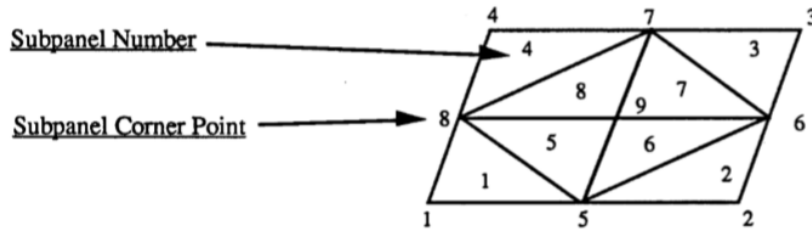


Figure 60: Subdivision of a panel in PANAIR [37].

The discretisation of equation 11.32 results in a matrix of aerodynamic influence coefficients given by equation 11.34 which is solved for the perturbation coefficients ϕ using a set of boundary conditions (b) on the mesh panels.

$$[AIC] \{\phi\} = \{b\} \quad (11.34)$$

11.2.2. Implementation

The steps undertaken for the implementation of PANAIR within the platform are depicted in the flow chart of figure 62. As shown, the inputs to the PANAIR analysis include the freestream flow characteristics, freestream Mach number M_∞ and angle of attack α as well as the mesh files previously generated in SALOME.

The PANAIR input pre-processor PANIN [94] is employed to create the input file for PANAIR (*A502.inp*). To use the PANIN pre-processor, a wireframe format of the geometry and wakes must be used (*geometry.wgs*). The wireframe format is written according to the Langley format [28] which requires points to be written for each cross section, respecting the normals given by the right hand rule. An example of the wireframe of a geometry containing the wakes is given in figure 61.

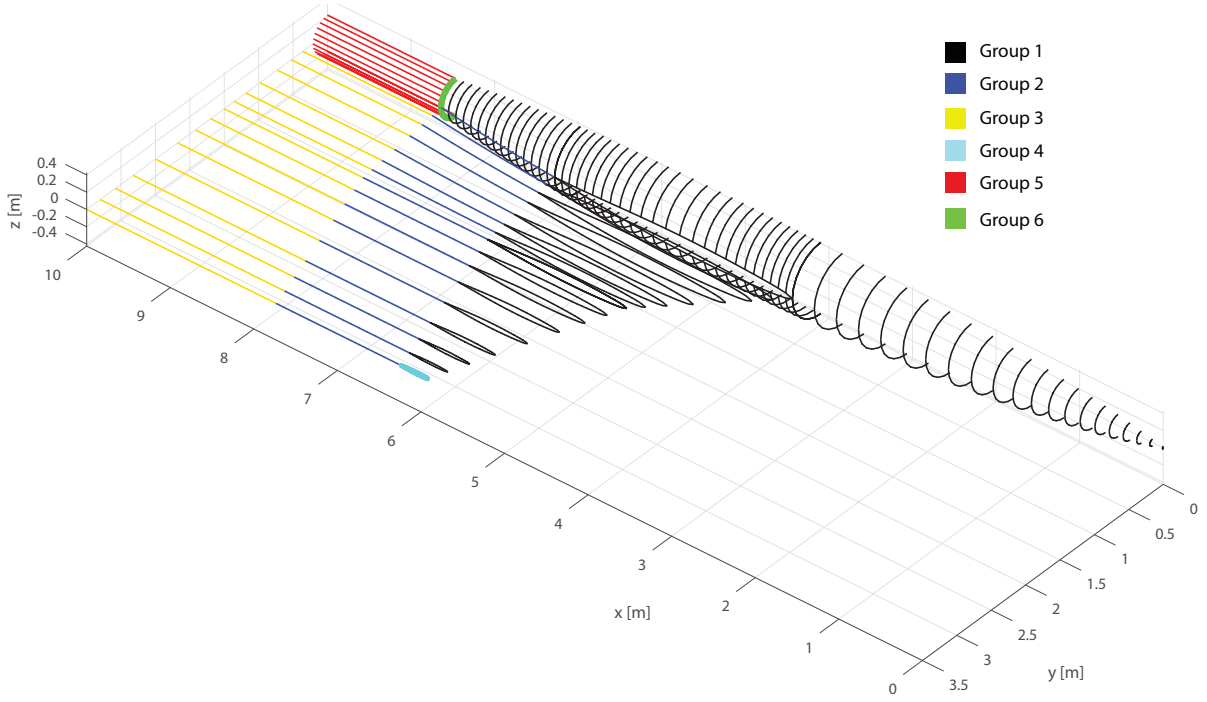


Figure 61: Wireframe model according to LaWGS format and mesh network groups for boundary conditions.

As part of the PANIN pre-processor input file (*panin.inp*), the boundary conditions applied to each mesh network must be prescribed. In figure 61, the different groups of mesh networks to which boundary conditions have been applied are shown in different colours. In Table 4, the corresponding boundary conditions applied to each group are shown.

The direct condition on an impermeable surface represent the fluid' inability to go through a solid surface. This boundary condition is enforced by setting the normal component of velocity on the surface to be equal to zero $\vec{V} \cdot \vec{n} = 0$. The wake boundary condition enforces the Kutta condition, which sets the flow velocity originating from both upper surface and lower surface at the sharp trailing edge to be equal $(\phi_U - \phi_L)|_{T.E.} = \Delta\phi|_W$.

Table 4: Boundary conditions applied to mesh networks.

Mesh Group	Mesh network(s)	Description	PANAIR boundary condition
1	Fuselage (Front, Mid, Rear) Wing (top, bottom)	Direct condition on an impermeable thick surface	8
2	Wing wakes	Vorticity matching kutta condition	18
3	Wing extension wakes	Doublet matching condition	18 (matchw = 1)
4	Wing tip	Direct condition on an impermeable thick surface	8
5	Fuselage body wakes	Doublet matching condition	18 (matchw = 1)
6	Fuselage base	Base surface condition	5

Upon running the PANAIR program with the associated input file (*A502.inp*), the output file (*panair.out*) lists the source and the gradient of the doublet strength (in x,y,z directions) at the center of each panel of the mesh networks. Using equation 11.35, the local perturbation velocity \vec{v} over the panels can be computed [37]. Furthermore, the local pressure coefficient at the panels is computed using the second-order pressure coefficient formulation which is dependent on the

local perturbation velocities according to equation 11.36 [105].

$$\vec{v} = \begin{bmatrix} u \\ v \\ w \end{bmatrix} = \nabla\mu + \sigma\vec{n} = \begin{bmatrix} \frac{\partial\mu}{\partial x} \\ \frac{\partial\mu}{\partial y} \\ \frac{\partial\mu}{\partial z} \end{bmatrix} + \sigma\vec{n} \quad (11.35)$$

$$c_{p,2nd} = -2u - [(1 - M_\infty^2)u^2 + v^2 + w^2] \quad (11.36)$$

Using the computed perturbation velocity vector from PANAIR, the (inviscid flow) velocity ratio at the panels can be obtained using equation 11.37.

$$\frac{V_{inv}}{V_\infty} = \frac{|\vec{V}_{nd}|}{V_\infty} = \sqrt{[\cos(\alpha) + u]^2 + v^2 + [\sin(\alpha) + w]^2} \quad (11.37)$$

The lift and (inviscid) pressure drag coefficient are computed using the same equations as for the hypersonic panel method given in equations 11.26 and 11.29 for angle of attack α .

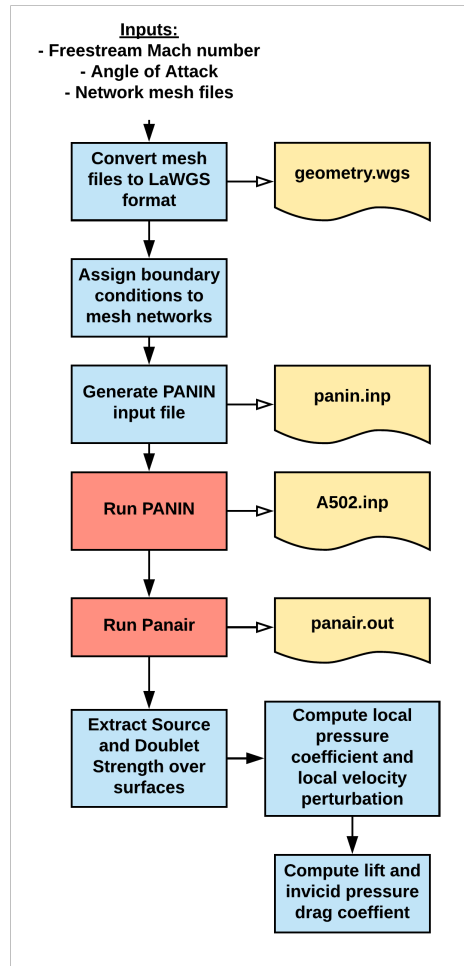


Figure 62: Flow diagram for the implementation of PANAIR.

11.2.3. Limitations of PANAIR

PANAIR is a great tool to compute flows about arbitrary configurations however it comes with limitations due in part to the simplification involved in the Prandtl-Glauert equation but also related to the modelling of the flow problem. The limitations of the PANAIR program can be resumed as follows:

- Small disturbance assumption: This assumption becomes invalid for high angles of attack and thick configurations. Under these cases, the perturbation velocity can be large and as a result small disturbance theory may become invalid.
- Viscous, heat transfer and rotational effects neglected: This assumption restricts the application of PANAIR to certain flow regimes. In transonic flow ($M_\infty \approx 1$), viscous effects cannot be neglected and in hypersonic flow ($M_\infty \gg 1$) heat transfer and viscous effects are also predominant. This limits the application of PANAIR to the subsonic regime ($M_\infty \leq 0.9$) and low supersonic regime ($1.2 < M_\infty < \approx 3$). In addition, at high angles of attack separation can occur. This is dictated by viscous effects that PANAIR cannot capture.
- Wake positioning: In the implementation of the wake networks in PANAIR, the direction of the wakes is defined along the streamwise direction (x-axis). This modelling method of wakes is generally used in panel codes. However, for highly swept wings at high angles of attack, a leading edge vortex can appear which creates a strong suction at the leading edge. PANAIR is not able to iteratively determine the location and shape of the leading edge vortex. As a result, this limits the application to small angles of attack whereby the effect of the leading edge vortex is not predominant.
- Superinclined panels: The superinclined panel (SIP) issue occurs at supersonic Mach numbers where the local impact angle of the panel is more or equal to the Mach wave angle ($\mu = \sin^{-1}(1/M)$) [23]. Under the SIP condition the results of the panel code cease to be valid and PANAIR crashes. This SIP limit is a critical limitation of PANAIR in supersonic flow and becomes more critical as the freestream Mach number increases (due to reduction in Mach wave angle) and the angle of attack increases (due to increased impact angle of the surface panels).

Overall, the limitations of the PANAIR program narrow the range of application of the program. In the framework however, the application of PANAIR has been restricted to analyse subsonic flow ($M_\infty < 0.9$ [-]) to circumvent the issues related to the superinclined panel in supersonic flow as well as the viscous and heat transfer effects which are expected in transonic and hypersonic flow. In addition, the angle of attack is restricted to moderately low angles ($0 \leq \alpha \leq 10$ [deg]) to ensure that viscous effects due to separation are not encountered and small disturbance theory remains valid. Finally, the shapes analysed are smooth and slender in the streamwise direction for which the small perturbation assumption is acceptable.

11.3. Viscous-Thermal analysis

The viscous-thermal part of the aerodynamic analysis is used to compute the viscous drag coefficient and convective heat transfer at the panels of the aircraft mesh. To compute the friction drag and heat transfers within the boundary layer, the results from the inviscid analyses of the low-speed and high-speed flow are used as inputs to the viscous solver.

When a vehicle is travelling at hypersonic speeds, the temperature increases in the boundary layer as a result of the flow friction and viscous dissipation [33]. This transforms kinetic energy of the flow to thermal energy. As a result, a gradient in the temperature profile is created within the boundary layer as shown in figure 64. The high temperature gradient present in the boundary layer produces a significant convective heat transfer to the surface (wall) of a vehicle [93]. From the air convective heat transfer, a heat balance between convective q_{conv} , radiative q_{rad} and conductive q_{cond} heat transfers occurs at the surface of the vehicle as shown in figure 63. Computational Fluid Dynamic codes can be used to accurately compute the convective heat transfer at the surface of a vehicle. However the use of CFD is computationally prohibitive for a conceptual design application. Other methods derived by Eckert, Van Dries and Spalding and Chi [98] [53] [40] have been widely used in the past to estimate convective heat transfer and friction over configurations by means of semi-empirical engineering methods. The methods use information about the properties of the flow in the inviscid layer to estimate the conditions within the boundary layer. In the platform, the semi-empirical methods are implemented to estimate the convective heat transfer and friction on the aircraft configuration surface.

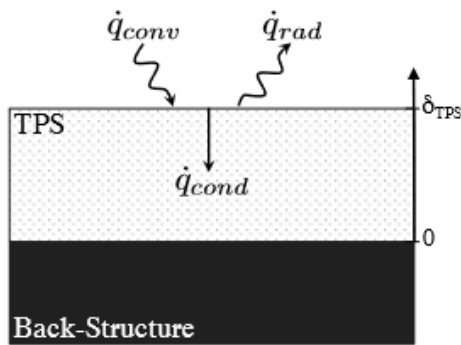


Figure 63: Heat transfer modes at surface of vehicle [93].

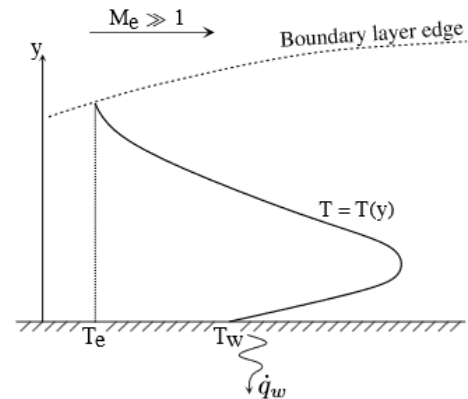


Figure 64: Typical temperature distribution within an hypersonic boundary layer [13].

11.3.1. Convective heat transfer computations

In the semi-empirical engineering methods, the convective heat transfer (at each of the surface panels) is expressed as a function of the adiabatic wall enthalpy h_{aw} (also called recovery enthalpy), the wall enthalpy h_w (vehicle surface) and the heat transfer factor H according to equation 11.38.

$$\dot{q}_{conv} = H (h_{aw} - h_w) \quad (11.38)$$

The heat transfer factor is dependent on the flight condition and is a function of the properties of the flow at the boundary layer edge (inviscid layer). The introduced non dimensional Stanton number C_H represents a measure of the fraction of total energy flux from the flow that will actually heat the surface. Using the definition of enthalpy $h = c_{spe}T$, the convective heat flux equation can therefore be formulated as given in equation 11.39.

$$\dot{q}_{conv} = \rho_{inv}V_{inv}C_H \left(c_{spe,aw}T_{aw} - c_{spe,w}T_w \right) \quad (11.39)$$

The inviscid layer flow properties are obtained from the panel code results of the low-speed or high-speed analysis dimensionalised using the altitude of the mission plateau under consideration. In order to dimensionalise the results of the inviscid analyses, the freestream flow properties (P_∞ , T_∞ and ρ_∞) obtained from the standard atmosphere model are used.

For the high-speed analysis, since all flow properties are expressed as a ratio with respect to the freestream, the dimensionalised flow properties in the inviscid layer are simply computed by multiplying the local pressure ratio P_{inv}/P_∞ , temperature ratio T_{inv}/T_∞ and density ratio ρ_{inv}/ρ_∞ by the freestream properties (and using $V_{inv} = M_{inv}\sqrt{\gamma RT_{inv}}$ for the inviscid velocity). For the result of the low-speed analysis (PANAIR), the local properties at the inviscid layer can be dimensionalised using the equation of state and the isentropic relations as shown in Appendix A.

Stanton number:

The Stanton number is related to the Reynolds analogy factor according to equation 11.40. The Reynolds analogy is an empirically derived factor which allows the link between convective heat transfer and friction coefficients. Depending on the state of the flow, the Reynolds analogy takes on a different value. For laminar flow, the factor is typically set to: $R_f = Pr_{inv}^{-2/3}$ [53] where Pr_{inv} is the Prandtl number defined at the edge of the boundary layer according to equation 11.41. In the case of turbulent flow, in literature, the Reynolds analogy ranges between $0.9 \leq R_f \leq 1.1$ [53] [93].

$$C_H = \frac{R_f c_f}{2} \quad (11.40)$$

$$Pr_{inv} = \frac{\mu_{inv} c_{spe,inv}}{k_{inv}} \quad (11.41)$$

It should be noted that due to the high-temperatures present in the boundary layer, air properties such as heat capacity at constant pressure c_{spe} , dynamic viscosity μ and thermal conductivity k are dependent on temperature and are thus computed using the real gas equations of Appendix B.

Adiabatic wall enthalpy:

The adiabatic wall enthalpy represents the enthalpy of the flow if it was to be slowed down to zero velocity with an adiabatic process. Equation 11.42 [98] gives the adiabatic wall temperature resulting from such a process and is dependent on the recovery factor r .

$$T_{aw} = T_{inv} \left[1 + r \frac{\gamma - 1}{2} M_{inv}^2 \right] \quad (11.42)$$

The recovery factor is dependent on the nature of the flow (laminar or turbulent) and is computed based on the Prandtl number according to equations 11.43 and 11.44.

$$r = Pr_{inv}^{1/2} \quad \text{For laminar flow} \quad (11.43)$$

$$r = Pr_{inv}^{1/3} \quad \text{For turbulent flow} \quad (11.44)$$

Compressibility transformations:

In the engineering methods, the friction coefficient given in equation 11.40 is evaluated using transformation functions (F_c and F_{Re_x}) which correct the incompressible friction coefficient over a flat plate to account for compressibility effects. The transformation functions are given by equations 11.45 and 11.46 where the subscript *incp* indicates incompressible flow conditions. Thus to evaluate the friction coefficient c_f , it is necessary to compute the compressibility factors (F_c and F_{Re_x}) and the Reynolds number $Re_x = \frac{\rho_{inv} V_{inv} x}{\mu_{inv}}$ based on the boundary layer edge flow (inviscid layer) conditions.

$$c_f = \frac{c_{f,incp}}{F_c} \quad (11.45)$$

$$Re_{x,incp} = F_{Re_x} Re_x \quad (11.46)$$

The incompressible flow friction coefficient is computed based on the incompressible Reynolds number (equation 11.46) and can be evaluated using the empirical correlations given by equations 11.47 and 11.48 for a flat plate. Three types of compressibility functions have been implemented, these include; the Eckert, Van Dries and Splading and Chi functions.

$$c_{f,incp} = 0.664 Re_{x,incp}^{-0.5} \quad \text{for a laminar boundary layer} \quad (11.47)$$

$$c_{f,incp} = \frac{0.088 \cdot [\log(R_{x,inc}) - 2.3686]}{[\log(R_{x,inc}) - 1.5]^3} \quad \text{for a turbulent boundary layer} \quad (11.48)$$

For the case of three-dimensional flow (around a fuselage section for example), effects such as streamline spreading and cross-flow are taken into account via the Mangler transformation factor where c_f is multiplied by $\sqrt{3}$ or 1.176 for laminar or turbulent flow respectively [53] [128].

Eckert

The Eckert method is valid for both laminar and turbulent boundary layers. The method is based on the evaluation of a reference temperature T^* and enthalpy h^* . For this method, the compressibility functions are evaluated using equations 11.49.

$$F_c = \frac{T^*}{T_{inv}} \quad F_{Re_x} = \frac{\mu_{inv} T_{inv}}{\mu^* T^*} \quad (11.49)$$

The reference temperature in this methods is computed using the reference enthalpy method as given in equation 11.50 whereby the adiabatic wall enthalpy h_{aw} is computed using the

recovery factor r^* based on the Prandtl number Pr^* evaluated at the reference temperature $Pr^* = \frac{\mu^* c_{spe}^*}{k^*}$.

$$T^* = \frac{h_{inv} + 0.5 \cdot (h_w - h_{inv}) + 0.22 \cdot (h_{aw} - h_{inv})}{c_{spe}^*} \quad (11.50)$$

Since both h_{aw} and c_{spe}^* are themselves dependent on the reference temperature T^* , an iteration process (starting with a guess value, $T^{*,0}$) is required to converge to a final value of T^* .

Van Dries

This method is only valid for turbulent boundary layers. The transformation functions are given by equations 11.51 to 11.52.

$$F_c = \frac{\frac{T_{aw}}{T_{inv}} - 1}{[\sin^{-1}(\kappa) + \sin^{-1}(\tau)]^2} \quad F_{Re_x} = \frac{\mu_{inv}}{\mu_w} \frac{1}{F_c} \quad (11.51)$$

$$\kappa = \frac{\frac{T_{aw}}{T_{inv}} + \frac{T_w}{T_{inv}} - 2}{\left[\left(\frac{T_{aw}}{T_{inv}} + \frac{T_w}{T_{inv}} \right)^2 - 4 \frac{T_w}{T_{inv}} \right]^{1/2}} \quad \tau = \frac{\frac{T_{aw}}{T_{inv}} - \frac{T_w}{T_{inv}}}{\left[\left(\frac{T_{aw}}{T_{inv}} + \frac{T_w}{T_{inv}} \right)^2 - 4 \frac{T_w}{T_{inv}} \right]^{1/2}} \quad (11.52)$$

Spalding and Chi

This method is only valid for turbulent boundary layers. The transformation functions are given by equations 11.53.

$$F_c = \frac{\frac{T_{aw}}{T_{inv}} - 1}{[\sin^{-1}(\kappa) + \sin^{-1}(\tau)]^2} \quad F_{Re_x} = \frac{\left(\frac{T_{aw}}{T_{inv}} \right)^{0.772} \left(\frac{T_w}{T_{inv}} \right)^{-1.474}}{F_c} \quad (11.53)$$

Solution process:

In order to solve the convective heat transfer q_{conv} and local friction coefficient c_f at the surface of an aircraft an iterative process is required. In the platform, the heat transfer is computed over each of the panels of the mesh along the strips (figure 52) such that the local Reynolds number is based on the distance x from the leading edge of the strip. The inviscid properties (boundary layer edge) obtained from the low-speed and high-speed inviscid methods are used as input to the thermal solver.

To start the solution process at each panel, an initial value of the wall temperature $T_{w,0}$ is assigned. Based on the given wall temperature, the convective heat transfer and local skin friction coefficient are estimated using the methods previously described. From the obtained convective heat transfer, the convective-radiation heat balance ($q_{conv} = q_{rad}$) is used to update the estimated wall temperature according to equation 11.54. This convection-radiation heat balance is used frequently to compute the convective heat transfer at the surface [98] [40] as

they are the main heat transfer modes (the magnitude of the conduction heat is negligible in comparison).

$$T_{w,i} = \left(\frac{q_{conv,T_{i-1}}}{\varepsilon\sigma} + T_{\infty}^4 \right)^{1/4} \quad (11.54)$$

This process is repeated up until the difference between the estimated wall temperature between two iterations is less than a prescribed tolerance value $|T_{w,i} - T_{w,i-1}| < \Delta_{tol}$. The matlab function *fsolve* is used to solve this iteration process. A summary of the solution process is described in a flow diagram provided in Appendix C.1. The computed local friction drag coefficients are summed over the elements in the direction of the local flow vectors, non-dimensionalised using the semi-wing area $S_{semi} = S_{ref}/2$ and added to the inviscid drag coefficient to compute the total drag coefficient such that $C_D = C_{D,inv} + C_{D,visc}$. An example of the flow properties over a complete configuration in hypersonic flow ($M = 5$ [-], $ALT = 25.8$ km) computed using the methods described in this section is provided in Appendix C.3.

11.3.2. Heat transfer field decomposition: POD

The proper orthogonal decomposition (POD) method is a very convenient method to break down large amounts of information into a linear set of basis functions. In this platform, the direct POD method described in [96] and [70] is used to decompose the convective heat transfer fields obtained over the mesh panels q_{conv} into sets of linear basis functions. These functions are further used for the interpolation of the heat transfer fields at each of the mission plateau and constitute the last column of the aero-performance matrix A (equation 11.1).

The end goal of the POD here is to be able to represent the heat transfer over the aircraft configuration as a function of the angle of attack $q(\alpha)_{pla}$ at each plateau of the mission $(M, ALT)_{pla}$.

To achieve this, the convective heat transfer obtained over the panel elements $e = 1, 2, \dots, N_{el}$ for each sampled angle of attack $s = 1, \dots, N_{samp}$ at the given mission plateau $((M, ALT)_{pla})$ is inserted into a snapshot matrix U of the form given by equation 11.55.

$$U = \begin{bmatrix} q_{e=1,\alpha_{s=1}} & q_{e=1,\alpha_{s=2}} & \cdots & q_{e=1,\alpha_{s=N_{samp}}} \\ q_{e=2,\alpha_{s=1}} & q_{e=2,\alpha_{s=2}} & \cdots & q_{e=2,\alpha_{s=N_{samp}}} \\ \vdots & \vdots & \ddots & \vdots \\ q_{e=N_{el},\alpha_{s=1}} & q_{e=N_{el},\alpha_{s=2}} & \cdots & q_{e=N_{el},\alpha_{s=N_{samp}}} \end{bmatrix} \quad (11.55)$$

Next, the correlation matrix R is computed from the snapshot matrix (equation 11.56). The eigenvalues (λ) and eigenvectors (ϕ) of the correlation matrix are computed. In the POD method, the eigenvalues (equation 11.57) are arranged such that the eigenvalues of highest value are put first in the vector such that: $\lambda_{m=1} > \lambda_{m=2} > \dots > \lambda_{m=M}$. The eigenvectors given in equation 11.58 represent the POD modes and are arranged with the corresponding eigenvalue. The subscript m stands for the POD basis orthogonal modes and can be truncated such that $1 < m \leq N_{samp}$. To obtain an exact representation of the original field, all POD modes should be used such that $m = M = N_{samp}$.

$$R = UU^T \rightarrow \lambda, \phi \quad (11.56)$$

$$\lambda = [\lambda_{m=1} \quad \lambda_{m=2} \quad \cdots \quad \lambda_{m=M}] \quad (11.57)$$

$$\phi = [\vec{\phi}_{\lambda_{m=1}} \quad \vec{\phi}_{\lambda_{m=2}} \quad \cdots \quad \vec{\phi}_{\lambda_{m=M}}] \quad (11.58)$$

Now any of the sampled convection heat fields can be written as a combination of the eigenvectors and a set of coefficients according to equation 11.59. In this equation, the coefficient matrix is computed by projecting the snapshot matrix onto the POD modes according to equation 11.60. The coefficient matrix contains vectors of coefficients for each sampled field α_s with rows corresponding to the POD modes scaling factors.

$$q_{POD, \alpha_s} = \sum_{m=1}^M \vec{\phi}_{\lambda_m} k_{m, \alpha_s} \quad (11.59)$$

$$K = (U^T \phi)^T \quad (11.60)$$

$$K = \begin{bmatrix} k_{m=1, \alpha_{s=1}} & k_{m=1, \alpha_{s=2}} & \cdots & k_{m=1, \alpha_{s=N_{samp}}} \\ k_{m=2, \alpha_{s=1}} & k_{m=2, \alpha_{s=2}} & \cdots & k_{m=2, \alpha_{s=N_{samp}}} \\ \vdots & \vdots & \ddots & \vdots \\ k_{m=M, \alpha_{s=1}} & k_{m=M, \alpha_{s=2}} & \cdots & k_{m=M, \alpha_{s=N_{samp}}} \end{bmatrix} \quad (11.61)$$

Finally, for each plateau $(M, ALT)_{pla}$, the convective heat transfer over the aircraft can be computed from equation 11.62 where the values of the coefficients k_m are obtained from a spline interpolations of the rows of the coefficient matrix K over the sampled angles of attack. In the current platform, all the modes are selected $m = N_{samp}$ such that the sampled fields can be exactly reproduced by the POD method.

$$q_{conv}(\alpha)_{(M, ALT)_{pla}} = \left(\sum_{m=1}^M \vec{\phi}_{\lambda_m} k_m(\alpha) \right)_{(M, ALT)_{pla}} \quad (11.62)$$

The energy metric for POD given in equation 11.63, gives a measure of the information stored by each of the POD modes when compared to the original snapshots [70].

$$\varepsilon_{energy} = 100 \cdot \left(1 - \frac{\sum_{m=1}^M \lambda_m}{\sum_{m=1}^{N_{samp}} \lambda_m} \right) \quad (11.63)$$

An example of the decomposition of the convective heat flow over an aircraft at Mach number of 5 and altitude of 25.8 km is given in figures 65 to 72. For this configuration, 12 angles of attack are sampled ranging from $0 < AOA < 12[deg]$. The original snapshots of the configuration at angles of attack of 0 and 12 degrees are provided in figures 65 and 66 respectively. After Proper Orthogonal Decomposition of the sampled heat fields, the POD modes are obtained where modes 1 to 4 are given in figures 69 to 72. The corresponding (spline) interpolated modes coefficients are provided in figure 68. In addition the energy accumulated by each of the modes in this

decomposition are given in figure 67.

As can be seen from figure 67, most of the energy is obtained from the first two POD modes with an accumulated energy near 100%. As the angle of attack with respect to the flow increases, the heat transfer over the bottom part of the configuration increases while the top part decreases. This is reflected in the first POD modes where it can clearly be seen that the heat transfer over the lower part of the vehicle is higher than the upper part. The second mode captures the heat transfer that is present over the top surface at low angles of attack. This is again reflected when looking at the associated POD coefficients in figure 68. In this figure it can clearly be seen that the first pod mode increases in magnitude with increasing angle of attack leading to increased bottom surface heating. The second pod mode on the other hand decreases with angle of attack due to the expected decrease in top surface heating. The remainder of the POD modes (3 to 12) have negligible impact on system as can be observed from the low magnitude of the associated POD coefficients in figure 68.

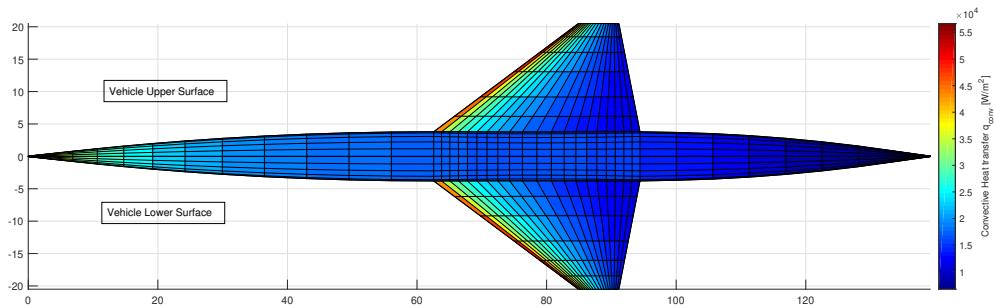


Figure 65: Original convective heat transfer snapshot field over configuration at $M = 5$ [-], $ALT = 25.8$ km and $AOA = 0[deg]$.

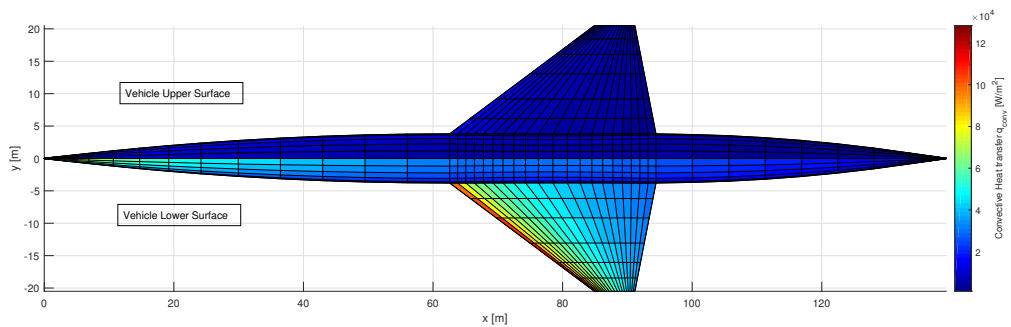


Figure 66: Original convective heat transfer snapshot field over configuration at $M = 5$ [-], $ALT = 25.8$ km and $AOA = 12[deg]$.

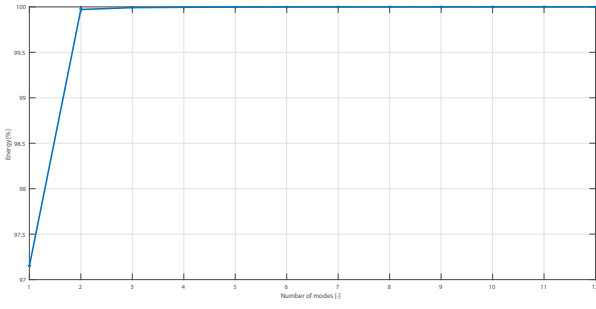


Figure 67: Accumulated energy of POD modes.

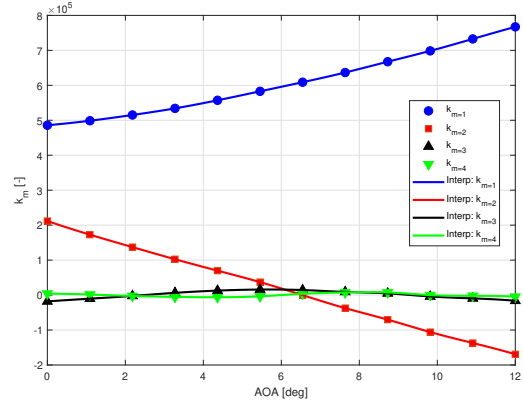


Figure 68: Interpolated POD mode coefficients as a function of angle of attack at $M = 5 [-]$, $ALT = 25.8$ km.

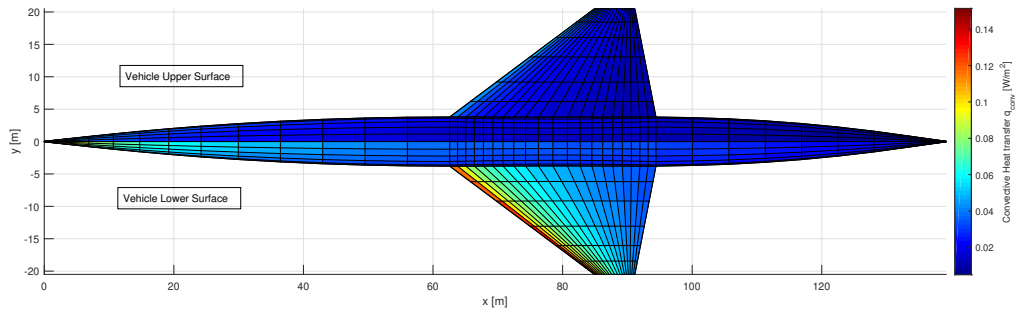


Figure 69: First POD mode.

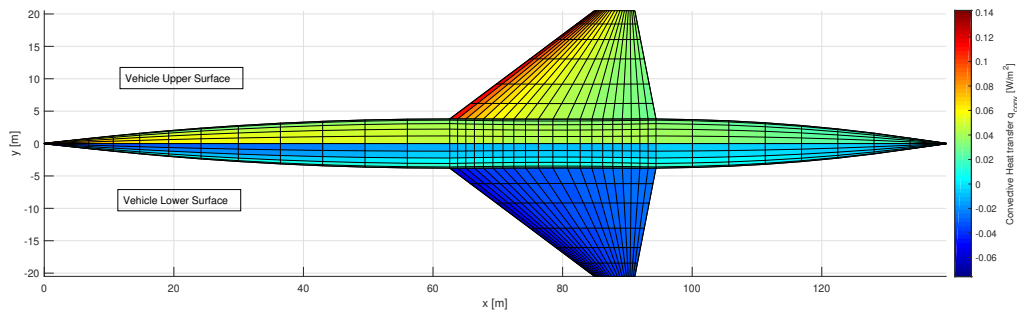


Figure 70: Second POD mode.

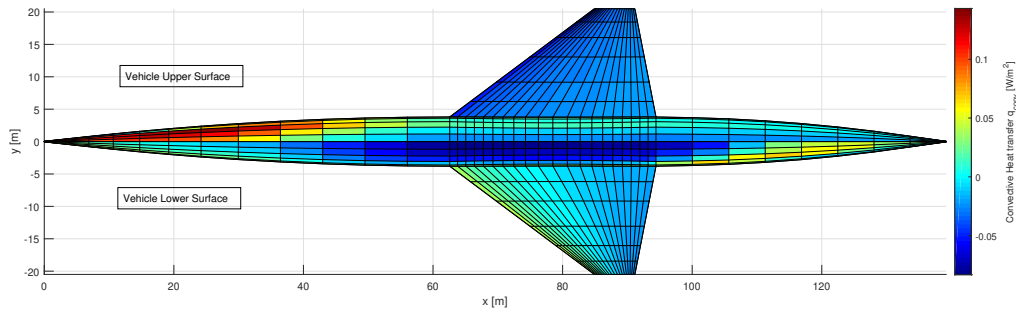


Figure 71: Third POD mode.

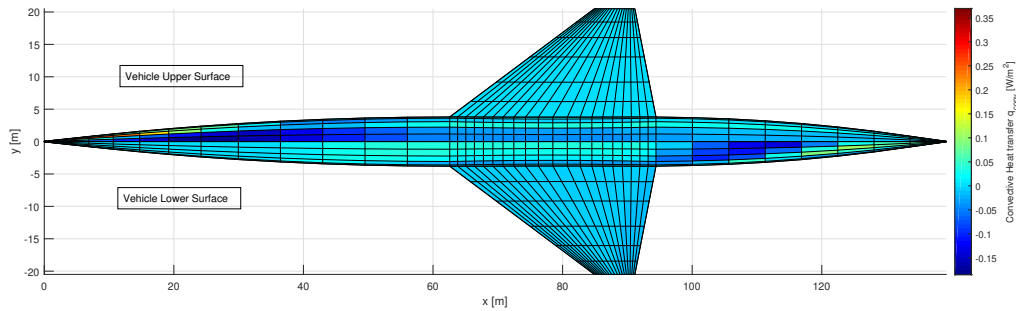


Figure 72: Fourth POD mode.

11.3.3. Limitations of convective heat transfer model

- Semi-Empirical models: The empirical models used here are based on similarity correlations with the viscous flow over flat plates at low and high speeds through the use of compressibility corrections. Although these models have been extensively validated [45] [24] [98] [53], they work under the assumption of zero or small pressure gradients [53]. As a result of this, flows with large pressure gradients such as separation flow or regions with sudden and large geometry changes (such as corners) cannot be predicted correctly. In addition, the semi-empirical models assume that the boundary layer can be decoupled from the inviscid flow and that the properties of the flow in the inviscid layer can be used to directly predict the flow in the viscous layer. While this assumption has been used extensively [40] [53] [98], in reality interactions between the shock wave, inviscid and viscous layers occur and cannot be completely decoupled.
- Prediction of flow transition: Flow transition prediction is one of the most challenging problem in modern aerodynamics; “prediction of boundary layer transition is still more of an art than a science” [98]. Some transition models exist and are based on the local Reynolds, Mach number and shape under investigation (fuselage or wing) [98], however a more common approach is the assumption that the flow is turbulent over the entire aircraft [93] [71]. Since friction drag and heat transfer are higher in turbulent flow, this yields more conservative predictions of the boundary layer flow.

- Stagnation flow: The semi-empirical methods of Eckert, Van Dries and Spalding and Chi developed in the platform cannot predict the properties of the boundary layer at a stagnation point. Other models such as the one derived by Fay and Riddle [98] are able to capture the stagnation local convective heat transfer and friction coefficient. These models are also semi-empirical but are limited to vehicles with round leading edge noses and apply to very small regions of the vehicle and have therefore not been implemented in the platform.
- Streamlines in the strip direction: For the calculation of the local Reynolds number the flow direction has been assumed to follow the strips of the geometry's mesh. This assumption is completely valid at zero angle of attack, however as the angle of attack increases, the streamlines start to curve around the geometry and separate from the surface. This assumption has been used in literature ([59] and [40]) however requires angles of attack to be kept small to ensure streamline curving and separation is not predominant.

12. Mission performance

The primary purpose of the mission performance module is to determine the fuel mass W_F required during a mission. On top of this, the mission performance module calculates the required angles of attack at each of the mission plateaux $\alpha_{req,pla,i}$ based on the steady climb equations. The module uses an estimated take off mass W_{to} , the mission defined plateaux $(M, ALT)_{pla,i}$ and aero-thermal performance matrix A as input.

12.1. Performance model

For the performance model, the steady climb force balance (figure 73) is used to determine the lift required throughout the mission profile. The model takes as input the mission profile plateaux defined in Section 8 and the aero-thermal performance matrix A defined in Section 11. Throughout each of the mission plateaux defined $i = 1, 2, \dots, N_{pla}$, the force equilibrium is applied starting with the aircraft take off mass such that $W_{pla,i=1} = W_{TO}$.

Starting from the first plateau until the last one, the following computations are applied. At each plateau, the lift provided by the aircraft must equal the weight component parallel to the lift vector according to equation 12.1. From there, the lift coefficient can be obtained from the dynamic pressure at the plateau according to equation 12.2. The angle of attack required to achieve the required lift coefficient can then be calculated from the lift coefficient equation at the plateau (11.2) given in the performance matrix A using equation 12.3.

$$L_{req,pla,i} = gW_{pla,i} \cos(\gamma_{pla,i}) \quad (12.1)$$

$$C_{L,reqpla,i} = \frac{L_{req,pla,i}}{q_{pla,i}S_{ref}} \quad (12.2)$$

$$\alpha_{req,pla,i} = \frac{C_{L,reqpla,i} - (C_{L,\alpha=0})_{pla,i}}{\left(\frac{dC_L}{d\alpha}\right)_{pla,i}} \quad (12.3)$$

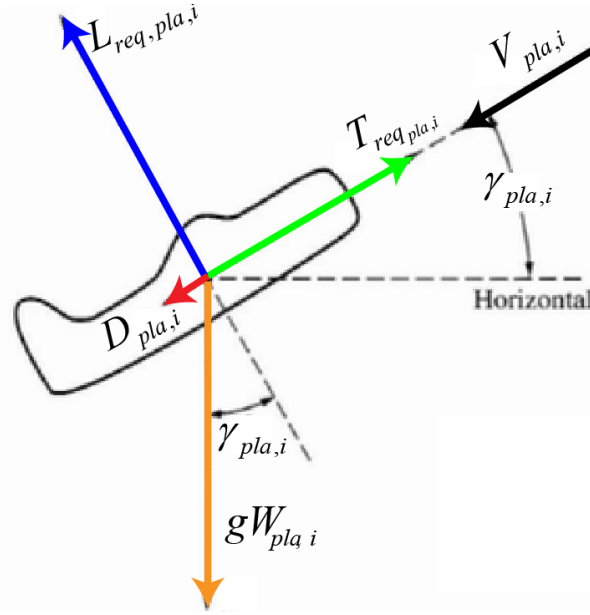


Figure 73: Equilibrium of forces in a steady climb [114].

The drag coefficient associated with the required lift coefficient can then be computed from the drag coefficient equation 11.3 at the plateau using equation 12.4. Using the dynamic pressure and wing reference area, the value of drag can be obtained (equation 12.5) and the thrust required for steady climb is computed from the equilibrium of forces according to equation 12.6.

$$C_{D_{pla,i}} = (C_{D,\alpha=0})_{pla,i} + (K_1)_{pla,i} C_{L,req_{pla,i}} + (K_2)_{pla,i} C_{L,req_{pla,i}}^2 \quad (12.4)$$

$$D_{pla,i} = C_{D_{pla,i}} q_{pla,i} S_{ref} \quad (12.5)$$

$$T_{req_{pla,i}} = D_{pla,i} + gW_{pla,i} \sin(\gamma_{pla,i}) \quad (12.6)$$

From the thrust required, it is possible to compute the fuel flow required at each plateau using an engine model. In this platform, the Generic Hypersonic Aerodynamics Model Example (GHAME) developed by White et al. [86] [77] is used.

The GHAME engine model is based on the use of liquid hydrogen fuel and has been developed to capture the entire flight envelope of a generic hypersonic vehicle. For this model, the engine is assumed to switch automatically from one thermodynamic cycle to the next and has a variable inlet [77]. The model takes into account a turbojet cycle for $0 < M < 2$, ramjet for $2 < M < 6$ and scramjet cycle for $M > 6$. The GHAME model has often been used in hypersonic vehicle mission analysis because it provides aerodynamic, propulsion, and aerothermodynamic models for a generic hypersonic air-breathing Single Stage To Orbit (SSTO) vehicle [77].

In the model, the engine specific impulse ISP is modelled as a function of the freestream Mach number and angle of attack of the aircraft based on a set of lookup tables (see [86] for model). The engine model specific impulse obtained from the GHAME engine model is shown in figure 74. Using the model, the specific impulse of the aircraft at a given plateau is thus computed

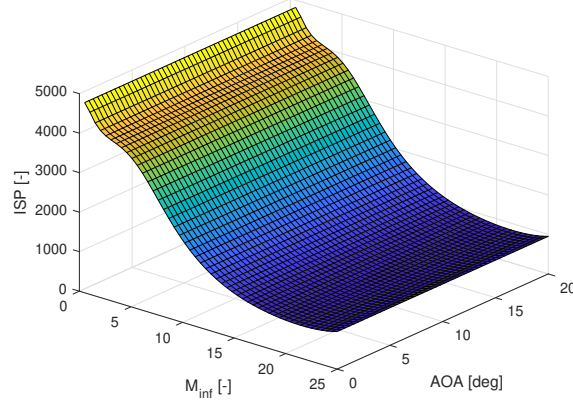


Figure 74: GHAME engine specific impulse.

from equation 12.7.

$$ISP_{pla,i} = f_{eng}(M_{pla,i}, \alpha_{req,pla,i}) \quad (12.7)$$

From the obtained specific impulse, the fuel flow can be computed using the definition of specific impulse according to equation 12.8. Using the fuel flow, the weight of the aircraft at the following plateau can be obtained from equation 12.9. This process is repeated throughout all the plateaux ($i = 1, 2, \dots, N_{pla}$) in the defined mission to obtain the total fuel and empty mass of the aircraft (equations 12.10 and 12.11).

$$\left(\frac{dW_f}{dt}\right)_{pla,i} = \frac{T_{req,pla,i}}{g \cdot ISP_{pla,i}} \quad (12.8)$$

$$W_{pla,i+1} = W_{pla,i} - \left(\frac{dW_f}{dt}\right)_{pla,i} (t_{start} - t_{end})_{pla,i} \quad (12.9)$$

$$W_F = \sum_{i=1}^{N_{pla}} \left[\left(\frac{dW_f}{dt}\right)_{pla,i} (t_{start} - t_{end})_{pla,i} \right] \quad (12.10)$$

$$W_{emp} = W_{to} - W_f \quad (12.11)$$

12.1.1.1. Limitations of mission performance module:

- Discretisation of mission: Due to the discretisation of the mission into a set of plateau, not all flight conditions encountered during the flight are captured. The drag of an aircraft in the transonic flight increases significantly which can yield to a high thrust requirement. Due to the fact that the mission is discretised and transonic flow cannot be accurately predicted by the panel method implemented in the platform, the fuel and engine requirements during this phase may be underestimated by this method. It is recommended for the future to incorporate a panel code such as ZONAIR [133] which is capable of capturing transonic and low superonic flow regimes more accurately.

- Steady flight: To compute the required angle of attack at each mission plateau, steady flight is assumed. In reality during the ascent phase, the aircraft is accelerating and should thus be described as a dynamic system. However in the case of hypersonic cruiser design for passenger carrying purpose, accelerations during climb are assumed to be low such that the assumption of steady flight remains valid. For example the LAPCAT A2 cruiser aircraft' mission (figures 39 and 40) undergoes an average acceleration of only about $0.7[m/s^2]$ during the secondary ascent phase.
- Generic engine model: Engine design for hypersonic cruise aircraft is complicated due to different types of flow regimes during which an hypersonic aircraft must operate. The design of feasible variable inlet engines with varying thermodynamic cycle is still in it's infancy and no fully reliable and computationally cheap models are yet available for the use in an MDO platform. The engine model given here has been used to model engine performance in previous research [86] [77] and captures the performance of a generic hypersonic engine and has thus been deemed appropriate for the current platform.

13. Thermal Protection System sizing

The purpose of the Thermal Protection System (TPS) sizing module is to use the convective heat transfer computed during the mission to estimate the mass of TPS (W_{tps}) required to protect the aircraft airframe.

Overall the TPS is sized according to the total convective heat accumulated at each panel during the mission to provide W_{tps} . It has been developed to provide rapid mass estimation of the TPS while still capturing the effects of changes in local convective heat transfer over the vehicle.

13.1. TPS concept selection

The primary purpose of the TPS is to provide heat protection to an internal load bearing structure by minimising the heat reaching the internal structure [31]. High temperatures on the internal structure can yield excessive deformations and premature failure. TPS systems have shown to constitute from 6 to 16 percent of a hypersonic vehicle dry mass and thus proper sizing of the protection system is very important in high speed flows [26]. The TPS is generally placed above the internal structure as shown in figure 75 to absorb the convective heat from the air.

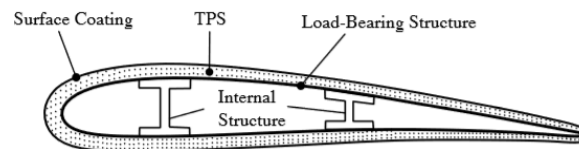


Figure 75: Integration of the Thermal Protection System [93].

Three types of TPS concepts can be found in literature, these include; Passive, Semi-Passive and Active systems. Passive systems rely exclusively on a single or stack of insulation materials to absorb heat from the external environment. Semi-passive concepts make use of a fluid circulating below the vehicle surface through an evaporation-condensation process (heat pipe) or through the use of an ablator (depleting) material to ensure the internal structure is protected. Finally, active systems make use of non-reusable coolant fluids to either directly cool down the flow incoming to the surface (via transpiration or film cooling) or within the structure by convective cooling [62] [19].

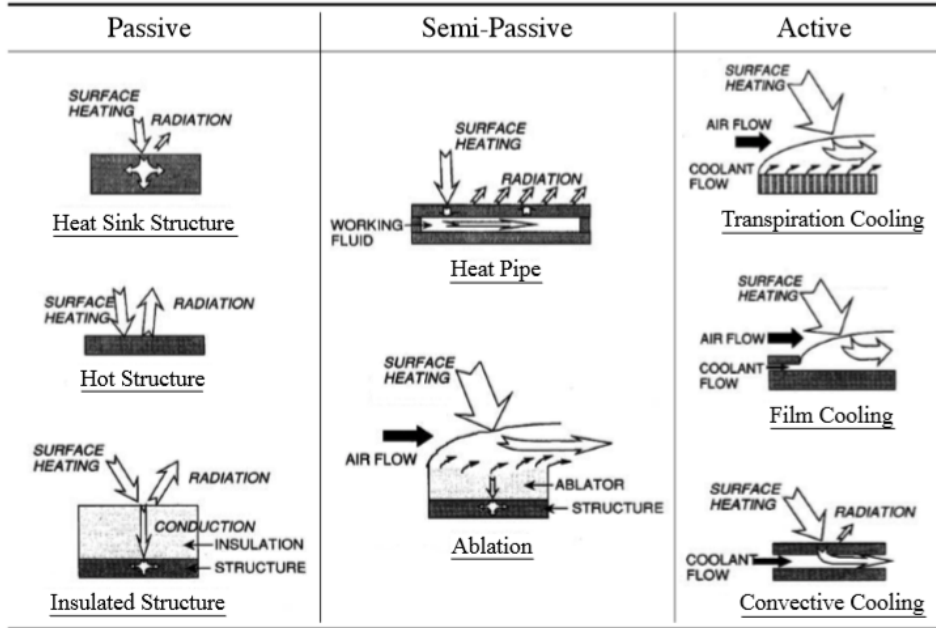


Figure 76: Different type of TPS concepts [62].

In the case of a reusable launch vehicle such as a hypersonic cruiser, passive concepts are preferable since these systems can operate without the need for non-reusable external coolant or the re-installation of an ablator material [27] [21]. Within the passive concepts, the insulated structure is selected since other concepts such as the heat sink and hot structure expose the load bearing structure directly to the incoming heat thereby leading to extreme structural deformations and non-linear aeroelastic effects [19]. For the insulated design concept, a low conductivity material is used to minimise the heat transfer to the internal structure.

13.2. Unsteady heat transfer TPS sizing

The TPS sizer module is implemented mostly based on the methods presented in [31] [26] [27] [25] and [21] for a passive insulated concept. In this method, the TPS system is modelled using the one-dimensional unsteady heat equation 13.1. Since insulated TPS concepts do not contain an effective heat sink, it is necessary to model the heat fluxes as a transient process. In equation 13.1, the material thermal diffusivity τ is dependent on the temperature inside the material and is defined with respect to the material specific heat capacity $C_{p,mat}$, thermal conductivity k_{mat} and density ρ_{mat} according to equation 13.2.

$$\frac{\partial T}{\partial t} = \tau \frac{\partial^2 T}{\partial x^2} \quad (13.1)$$

$$\tau(T) = \frac{k_{mat}(T)}{\rho_{mat} C_{p,mat}(T)} \quad (13.2)$$

In order to solve the unsteady heat equation, boundary conditions must be applied to the problem. At the surface of the insulation material, the convective-conduction-radiation heat balance $q_{conv} = q_{rad} + q_{cond}$ is applied for which the boundary condition is formulated according to equation 13.3. At the back-wall (lower surface of the insulation material), an adiabatic condition is

imposed according to equation 13.4. The adiabatic wall condition is a conservative condition used in a large number of TPS sizing methods [31] [26] [27] and ensures that no heat is transferred to the substructure.

$$q_{conv} - \varepsilon\sigma (T_w^4 - T_\infty^4) + k_{mat} \frac{dT}{dx} = 0 \quad (13.3)$$

$$\frac{dT}{dx} = 0 \quad (13.4)$$

In order to implement the unsteady heat transfer equation, the insulation material is discretised throughout the thickness using $j = 1, 2, \dots, N$ nodes equidistant from one another (Δx) as shown in figure 77. Using a finite difference scheme, the unsteady equation is discretised using a second order scheme in space (x) and first order in time (t).

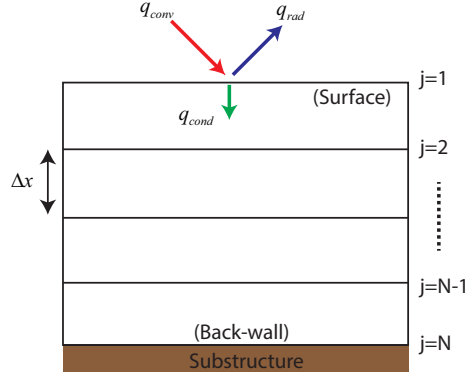


Figure 77: Schematic of numerical model of TPS.

After application of the boundary conditions, discretised equations can be written as implicit (time) functions. For the surface condition, the discretised boundary condition is given by equation 13.5. The interior nodes are described by equation 13.6 and the back-wall adiabatic condition is formulated according to equation 13.7. It should be noted in these equations that the thermal diffusivity coefficient is itself dependent on the temperature at the nodes such that

$$(\tau)_{T_j^{n+1}} = \frac{k_{mat}(T_j^{n+1})}{\rho_{mat}C_{p,mat}(T_j^{n+1})}.$$

$$T_1^n = \left(1 + \frac{2(\tau)_{T_1^{n+1}}\Delta t}{\Delta x^2}\right) T_1^{n+1} - \left(\frac{2(\tau)_{T_1^{n+1}}\Delta t}{\Delta x^2}\right) T_2^{n+1} - \left(\frac{2(\tau)_{T_1^{n+1}}\Delta t}{k_1\Delta x}\right) \cdot (q_{conv} - \varepsilon\sigma [(T_1^{n+1})^4 - T_\infty^4]) \quad (13.5)$$

$$T_j^n = \left(1 + \frac{2(\tau)_{T_j^{n+1}}\Delta t}{\Delta x^2}\right) T_j^{n+1} - \left(\frac{(\tau)_{T_j^{n+1}}\Delta t}{\Delta x^2}\right) T_{j+1}^{n+1} - \left(\frac{(\tau)_{T_j^{n+1}}\Delta t}{\Delta x^2}\right) T_{j-1}^{n+1} \quad (13.6)$$

$$T_N^n = \left(1 + \frac{2(\tau)_{T_N^{n+1}}\Delta t}{\Delta x^2}\right) T_N^{n+1} - \left(\frac{2(\tau)_{T_N^{n+1}}\Delta t}{\Delta x^2}\right) T_{N-1}^{n+1} \quad (13.7)$$

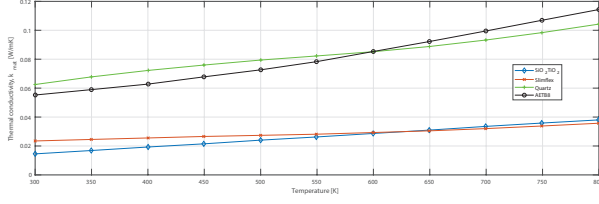


Figure 78: Thermal conductivity of TPS types.

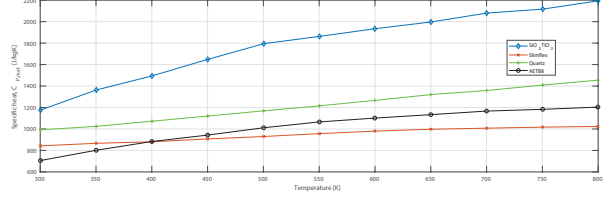


Figure 79: Specific heat of TPS types.

NASA has also investigated promising TPS insulation materials for their use in reusable launch vehicles [88] [20]. These include metallic and ceramic based insulations which are sized using a one dimensional unsteady heat transfer model similar to the one developed in this platform. The study correlated the TPS unit mass to the total convective heat transfer (heat load) during typical Access to Space (ATS) and Reusable Launch Vehicle (RLV) missions. It has also been determined from the studies of that TPS unit weight can be directly correlated to the total convective heat transfer accumulated during a mission (heat load), for a given constrained back wall temperature T_{BW} , independent of the convective heat flux history of the trajectory [88] [20]. The TPS weight correlations given in [88] [20] however have been computed for rather short missions of about 3000 seconds (50 minutes). For the design of long range vehicles (such as the LAPCAT A2 aircraft) the flight time is about 4 hours leading to much higher heat loads and thus significantly higher TPS unit masses can be expected. Due to the lack of correlations for high heat loads associated with long range vehicles, the TPS sizer in this thesis has been developed to correlate the expected TPS unit mass over a high range of heat loads.

Table 5: Properties of TPS under consideration [93]

Thermal Protection System	Emissivity [-]	Density [kg/m^3]
SiO_2TiO_2	0.8	200
Slimflex	0.8	260
Quartz	0.8	72
AETB-8	0.8	128

13.2.2. TPS sizing correlations

As stated in [88], the TPS unit mass $W_{unit,tps}$ is dependent on the total heat transfer Q_{tot} accumulated during a mission. As a result, in order to obtain the correlations between TPS mass and total heat load, convective heat transfer q_{conv} profiles similar to ones which would be expected in a typical long range hypersonic cruiser mission are used. The heat profiles generated for the computation of TPS unit mass are shown in figure 80 and are varied between a maximum convective heat input of $5 \cdot 10^2$ to $1 \cdot 10^5$ [W/m^2]. The duration of the heat profile is fixed to 4 hours and 38 minutes, corresponding to the duration of the LAPCAT A2 long range cruiser nominal mission. The maximum heat input of $1E5$ results in a maximum surface temperature of 1260 Kelvin (for convection-radiation equilibrium at emissivity of 0.7), which is below the maximal operational temperatures of all the TPS insulation materials under investigation and surface temperatures expected for a Mach 5 cruiser.

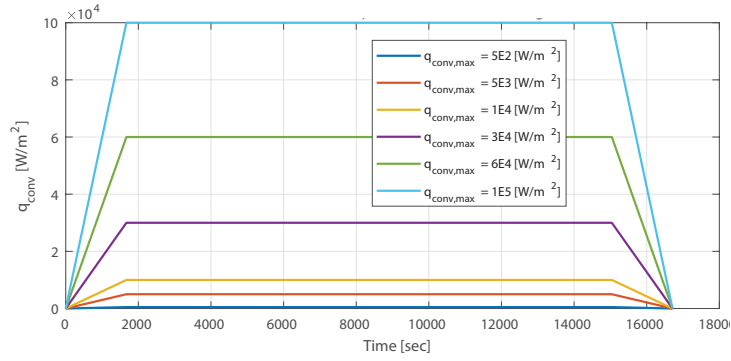


Figure 80: Heat profiles for TPS unit mass sizing.

Using the convective heat profiles of figure 80, the TPS thermal properties and the sizing method of sub-section 13.2, the optimal unit mass of the TPS as a function of total heat transfer ($Q_{tot} = \int_{t_{start}}^{t_{end}} q_{conv}(t)$) for each insulation type under investigation is computed. A summary for the TPS sizing process is given in the flow diagram provided in Appendix C.2.

For a back-wall temperature constrained to 400 Kelvins and freestream radiation temperature of 220 Kelvins (temperature at 25km altitude), the optimal TPS unit masses obtained as a function of heat load for the four different insulation materials are displayed in figure 82. In addition, the associated optimal TPS thicknesses vs unit mass are shown in figure 81.

As can be seen from figures 81 and 82, the choice of TPS is dependent on a trade-off between unit mass and thickness. For example, the SiO_2TiO_2 insulation has the lowest unit mass with increasing heat load but also possesses a lower density than the Slimflex insulation and thus a higher thickness. High TPS thickness is not desirable in hypersonic vehicles since it can either result in the reduction of the effective height of the load bearing internal structure or negatively impact the aerodynamic performance of the aircraft. As a result if TPS thickness and unit mass are given the same importance, the SiO_2TiO_2 and Slimflex protection systems may be most attractive. Overall, when looking solely at unit mass and thickness, the SiO_2TiO_2 insulation provides the lowest unit mass and the second highest density leading to a small thickness thereby making it the most ideal insulation type considered here.

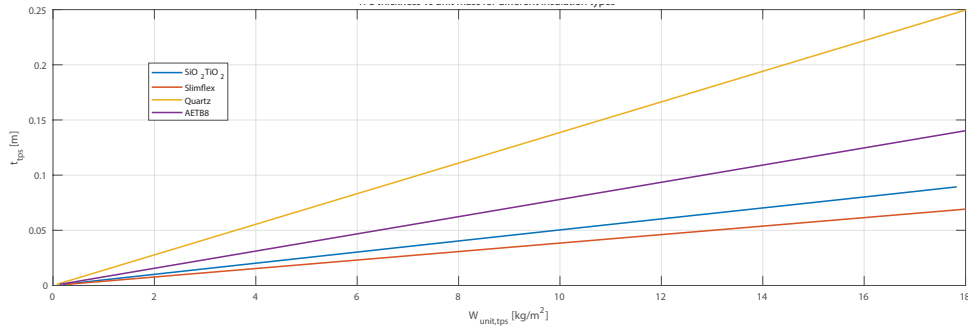


Figure 81: Thickness vs unit mass of insulation types.

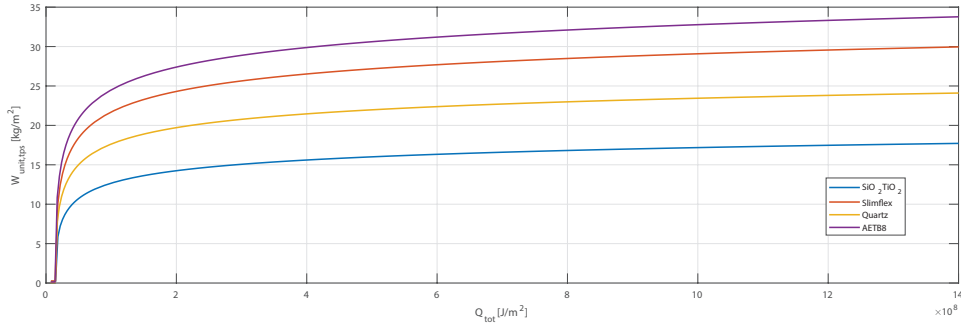


Figure 82: Unit mass of tps types as a function of total heat load at 400 K Back wall temperature.

The unit mass for a given protection system is highly dependent on the back-wall temperature constraint imposed. Figures 83 to 86 show the impact of the back-wall temperature constraint on the unit mass of the different protection systems. The allowed back-wall temperature is dependent on the load bearing substructure material. For an aluminium 6061-TI load bearing substructure, the yield strength of the material rapidly drops after a temperature of 200°C (473K) [115]. Titanium based sub-structures may sustain higher temperature but are much heavier and as a result the author recommends a maximum back wall temperature of 475K for the use of an aluminium based sub-structure.

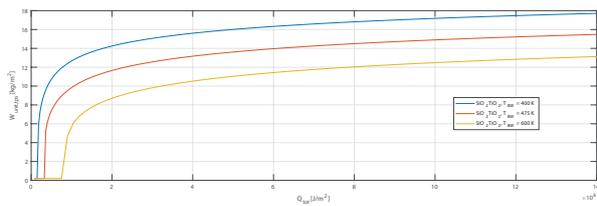


Figure 83: SiO_2TiO_2 unit mass vs back wall temperature constraint.

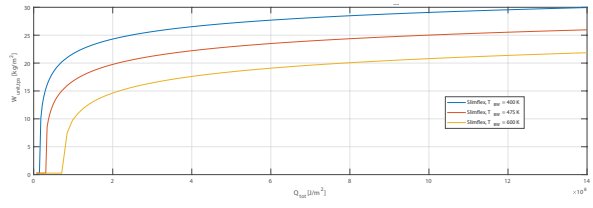


Figure 84: Slimflex unit mass vs back wall temperature constraint.

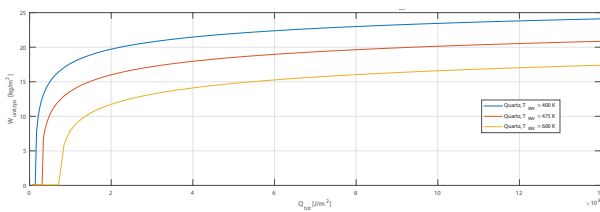


Figure 85: Quartz unit mass vs back wall temperature constraint.

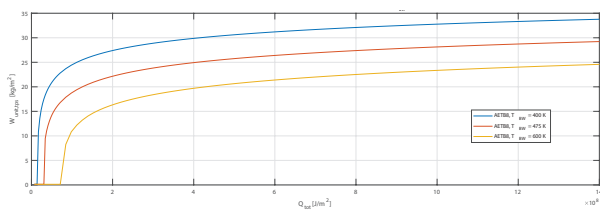


Figure 86: AETB8 unit mass vs back wall temperature constraint.

Using the parametric curves computed (figures 83 to 86), the TPS mass can be estimated for a given mission profile and for a chosen protection system insulation material. Using the performance matrix A defined in Section 11 and equation 11.62 evaluated at the required plateau angles of attacks given by equation 12.3, the total convective heat transfer during the mission (for a given mesh panel) is computed using equation 13.12. Finally using the parametric curves, the total estimated TPS mass $W_{tot,tps}$ is computed by integrating the TPS unit mass over all the mesh panels according to equation 13.13.

$$Q_{tot,P} = \sum_{i=1}^{N_{pla}} \left[q_{conv,pla,i_P}(\alpha_{req,pla,i}) \cdot (t_{start} - t_{end})_{pla,i} \right] \quad (13.12)$$

$$W_{tot,tps} = \sum_P [f(Q_{tot,P}) \cdot A_P] \quad (13.13)$$

13.2.3. Limitations and recommendations

- One dimensional heat analysis: The TPS sizing method used in this module assumes that the heat transfer through the insulation material can be analysed using a 1D numerical scheme. This assumption has been validated by [88] and used in many TPS sizing codes [31] [26] [27] [21]. One of the downside of this assumption however is that the heat dispersion effect between neighbouring panels is not taken into account. Since the effect of heat dispersion is not taken into account, this yields a slightly conservative approach to the protection system sizing. Indeed as [88] shows, the one dimensional sizing correlates very closely to a two dimensional heat analysis making it a fair assumption.
- Each panel' TPS sized separately: In the module the TPS thickness required on each of the mesh panels is computed independently. This yields a non-smooth distribution of the TPS thickness over the aircraft surfaces. In reality the TPS thickness will be made as to create a smooth distribution.
- Reduction in effective structural height: The TPS thickness yields a reduction in the effective height and thus moment of inertia of the internal load bearing structure which in turn creates a heavier internal structure. This reduction in effective height is not taken into account in this platform as it is expected that the thickness of TPS is relatively small in comparison to the total effective height of wing and fuselage internal structures.
- Fixed radiation to space temperature: In the TPS parametric correlations computed, a temperature of $220K$ is used as the radiation to space temperature. This value is chosen according to the freestream air temperature at $25km$ altitude. Although this temperature changes in reality throughout the flight, it's effect is small since radiation heat is dependent on the difference between surface and freestream temperature to the power of four. Since the freestream temperature is much lower than the surface temperature, the radiation temperature is assumed to have little effect on the TPS sizing.
- Adiabatic back wall condition: The adiabatic back wall condition is applied for the TPS sizing as given in equation 13.4. The condition is applied to prevent heat transfer from reaching the substructure and a maximum constraint back wall temperature is applied. In reality if the substructure is in close contact with the TPS, some heat will leak into the substructure due to the differences between the TPS back-wall temperature and the temperature bellow the substructure. This effect is however deemed small if the back wall temperature is chosen to be a low enough value (within the operational temperature of the subsurface material) to prevent significant thermal stresses in the sub-structure.

- No thermal expansion: The effects of the thermal expansion of the structure are neglected. Thermal expansion effects can lead to additional structural deformation which can in turn effect the properties of the flow over the vehicle surface. This assumption is considered reasonable due to the low coefficients of expansion found for TPS materials. If a hot-structure concept was selected (no TPS insulation case) however, significant expansion of the load bearing structure could be expected which would have to be taken into account [93].

14. Component mass estimation

The purpose of the weight estimation module is to estimate the aircraft structural component masses and the take off mass W_{to} based on the aircraft geometry, mission, estimated thermal protection system mass W_{tps} (obtained from TPS sizing module), engine mass W_{eng} , empty mass W_{emp} and fuel mass W_F (obtained from the mission performance module). The module is based on class II type empirical relations for the preliminary sizing of a hypersonic aircraft. The equations used in this section are based on the Hypersonic Aircraft Sizing Analysis (HASA) tool [51] and the Weight Analysis of Advanced Transportation Systems [44] from NASA. These papers re-group an ensemble of empirical relations for component sizing specific to single-stage and two-stage-to-orbit hypersonic aircraft which ensures their applicability to the current platform. The HASA platform has been applied to four hypersonic transport aircraft with a $\pm 10\%$ accuracy in estimated take-off mass [51]. These include the HyCAT configuration, a famous hypersonic long range Mach 6 cruiser conceptual aircraft.

14.1. Mass estimation models

The HASA and WAATs mass estimation models are both based on an iterative process whereby the take off mass is iteratively determined until a converged mass is obtained. To start the iteration process, the empty mass W_{emp} and fuel mass W_F obtained from the mission performance module are used to set the initial take off mass at iteration 1 such that $W_{TO,j=1} = W_{emp} + W_F$. The empirical relations used to evaluate the absolute mass of each structural component divide the aircraft mass into three main components; structural mass, fuel mass and payload mass. The structural mass is comprised of the aerodynamic surfaces, fuselage body, thermal protection system, propulsion system and landing gear mass. Note that all the mass relations described in the following section are written in empirical units but have been converted to SI units within the platform.

For the aerodynamic surfaces, the total mass of the surfaces can be evaluated as the summation of main wing, horizontal stabiliser and vertical fin mass such that $W_{tot,aero,j} = W_{w,j} + W_{hs,j} + W_{vf,j}$. The equation from HASA is used to calculate the wing mass (equation 14.1) as it offers a slightly more conservative mass estimation than the estimation from WAATs. The wing mass equation includes the wing-box structure, control surfaces and wing carry-through structure [51]. As can be seen, this equation contains a modifying factor mf to account for changes in material technology and is dependent on the wing load structure material and structural temperature according to figure 87. The horizontal stabiliser and vertical fin masses are computed according to equations 14.2 and 14.3 (same equations in HASA and WAATs) where the maximum dynamic pressure q_{max} is derived from the mission definition (Section 8) using $q_{max} = \max(q_{pla})$.

$$W_{w,j} = 0.2958 \cdot mf \cdot \left[\left(\frac{(W_{TO,j} - W_F) ULF}{1000} \right)^{0.52} (S_{ref})^{0.7} (AR)^{0.47} \left(\frac{1 + \lambda}{t/c} \right)^{0.4} \left(0.3 + \frac{0.7}{\cos(\Lambda_{1/2})} \right) \right]^{1.017} \quad (14.1)$$

$$W_{hs,j} = 0.0035 \cdot \left[\left(\frac{W_{TO,j}}{S_{ref}} \right)^{0.6} (S_{hs})^{1.2} (q_{max})^{0.8} \right]^{1.0} \quad (14.2)$$

$$W_{vf,j} = 5 \cdot (S_{vf})^{1.09} \quad (14.3)$$

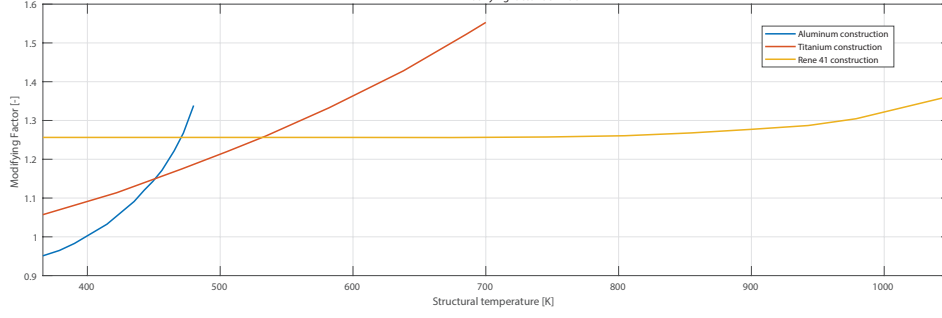


Figure 87: The modifying factor.

For the fuselage mass, the total structural mass is given by equation 14.4. The basic body mass is described by the same equation in both HASA and WAATs and is used to estimate the mass of the major structural components of the fuselage applicable to structural temperature up to about 1350 kelvin [51]. In equation 14.4, the length of the body L_b is derived directly from the parametric definition of the fuselage and the height H_b is calculated from the maximum sectional height defined by the body cross sections in Section 7.1.

$$W_{tot,body,j} = 0.341 \cdot mf \cdot \left[\left(\frac{L_b U L F}{H_b} \right)^{0.15} (q_{max})^{0.16} (S_{w,b})^{1.05} \right]^{1.0} \quad (14.4)$$

The landing gear mass relation (equation 14.5) includes the nose gear, main gear and controls [51]. Since a hypersonic cruise type vehicle is modelled with horizontal take-off, the landing gear mass is set dependent on the take off mass [51].

$$W_{lg,j} = 0.00916 \cdot (W_{TO,j})^{1.124} \quad (14.5)$$

The propulsion system mass is estimated from the summation of engine and fuel tank masses such that $W_{tot,prop,j} = W_{tank,j} + W_{eng}$. The tanks masses are calculated based on the tank structural and insulation masses such that $W_{tank,j} = W_{tank,struct} + W_{tank,ins}$. Tank structural mass is a function of the tank density ρ_{tank} and available fuel volume (obtained from geometry module) according to equation 14.6. Insulation mass is dependent on the tank surface area (from geometry module) and fuel tank insulation unit mass factor according to equation 14.7. The insulation unit mass factor is a function of the tanks surface temperature and mission time such that $W_{ins,unit} = f(T_{surf,tank}, t_{miss})$ as provided by [44].

$$W_{tank,struct} = \rho_{tank} \cdot V_{F,av} \quad (14.6) \quad W_{tank,ins} = W_{ins,unit} \cdot S_{tank} \quad (14.7)$$

Subsystem masses include hydraulics, avionics, electronics and equipment and constitute approximately 5% to 10% of the take off mass. The total subsystem mass is defined such that $W_{tot,sub,j} = W_{hydr,j} + W_{avi,j} + W_{elec,j} + W_{equip,j}$. For the hydraulic, avionics and electronic masses the same relations are present for both HASA and WAATs [51] [44] whereas the equipment mass is defined in HASA. Note that for the hydraulic mass, the structural span of the wing b_{struct} is defined as the distance along the mid chord of the wing from root to tip (multiplied by 2 for complete span).

$$W_{hydr,j} = 2.64 \cdot \left[\left(\frac{(S_{ref} + S_{hs} + S_{fv}) \cdot q_{max}}{1000} \right)^{0.334} (L_b + b_{struct})^{0.5} \right]^{1.0} \quad (14.8)$$

$$W_{avi,j} = 66.37 \cdot (W_{TO,j})^{0.361} \quad (14.9)$$

$$W_{elec,j} = 1.167 \cdot \left[(W_{TO,j})^{0.5} (L_b)^{0.25} \right]^{1.0} \quad (14.10)$$

$$W_{equip,j} = 10000 + 0.01 \cdot (W_{TO,j} - 0.0000003) \quad (14.11)$$

Using the equations described previously, a new estimated take off mass (iteration $j + 1$) can be calculated from the summation of structural component masses, fuel and payload masses according to equation 14.12. It should be kept in mind that the fuel W_F and W_{tps} masses are kept constant during the iteration process since these parameters are dependent on the mission performance (Section 12) and are input to the mass estimation module.

$$W_{TO,j+1} = W_{tot,aero,j} + W_{tot,body,j} + W_{tps} + W_{lg,j} + W_{tot,prop,j} + W_{tot,sub,j} + W_F + W_{payload} \quad (14.12)$$

The iteration process is continued with the updated take-off mass $W_{TO,j+1}$ until convergence between two iteration occurs as given in equation 14.13. For the converge process, a tolerance of $\Delta_{tol} = 0.1kg$ is used to ensure a precise prediction of the final estimated take off mass. A summary of the component mass estimation calculation process is given in the flow diagram of Appendix C.3.

$$|W_{TO,j+1} - W_{TO,j}| < \Delta_{tol} \quad (14.13)$$

14.1.1. Limitations and recommendations

- Simplified fuselage geometry: The fuselage body structural mass relation given by WAATs and HASA only considers the height and length of the fuselage geometry. As a result, the relation cannot capture the structural effect of local changes in fuselage cross sectional shapes. This limits the use of this relation to simple circular or rectangular fuselages with fixed cross sectional shapes.
- Wing relation defined for single planform: The wing mass relation is based on a single planform wing. As a result the effects of cranked or double delta wings on the wing structural mass cannot be measured by this relation. Although the platform has been developed with the possibility of defining two wing planforms, in order to correctly capture the effect on the structural mass, one planform should be used.
- Based on a database of existing aircraft: The empirical relations used here and given in the HASA and WAATs reports are based on a collection of existing supersonic and hypersonic aircraft as well as preliminary sized aircraft. As a result of this, the relations should be used with caution for configurations with geometrical parameters and take off masses considerably different from the database.
- No aeroelastic effects taken into account: Aeroelastic effects are not taken into account in this platform. Due to the nature of the empirical relations used, the structural deformations and the impact of these deformations on the airflow over the aircraft cannot be measured. Aero-elastic deformation tend to reduce the effective lift of the aircraft and can

lead to aerodynamic flutter. Structural deformations of components such as the wing are however expected to be relatively small due to the low-aspect ratio of wings observed for hypersonic vehicles (as opposed to high aspect ratio wings of low-speed aircraft).

In the future the use of finite element (FEA) sizing codes are advised to take into account aero-structural interaction and more accurately predict the mass of structural components. The use of FEA would also capture the structural sensitivity of more parametric design variable such as the cranked or double wing and changes in fuselage cross sectional shapes. However, in the framework of a preliminary design platform, FEA codes could be prohibitively expensive from a computational point of view and thus the relations used here are deemed appropriate at the preliminary design stage. As a next step, prior to the use of a FEA sizing code, the more appropriate method in a preliminary design optimisation code would be the use of Beam Element Models (BEMs) to describe the structural problem in one dimension by using smeared thicknesses and local cross sectional inertia to describe the structural weight distribution of the aircraft. A BEM model is proposed by Mark D. Ardema [76] to estimate the fuselage structural mass for a hypersonic aircraft.

Part III.

Validation and model selection

A crucial part of the construction of any model is validation. It helps understand the limitations and applicability of the implemented models, verify that they have been correctly applied and can be used as part of a larger multidisciplinary platform. To achieve this, in this part of the report, an extensive verification and validation study is performed on all the principal computational models of the platform. For this, the inviscid aerodynamic codes, viscous-thermal solver and the thermal protection system sizing code are validated through the reproduction of experimental tests or the verification of results from other numerical codes such as computational fluid dynamics. Throughout this section, certain models are also selected based on how well they match the verification or validation data.

15. Validation of Aerodynamic solvers

For the aerodynamic solvers, the subsonic low-speed (PANAIR, subsection 11.2) and supersonic/hypersonic high-speed (Engineering methods, subsection 11.1) inviscid flow solvers are verified and validated.

15.1. Low speed: NACA RM L51F07 Wing-Body Configuration

For the validation of the subsonic panel code (PANAIR) implementation, the experimentally tested NACA RM L51F07 configuration [132] is chosen. This configuration is made up of wing and body sections as shown in figure 88. The wing has an aspect ratio of 0.6, a taper ratio of 0.6 and quarter chord sweep angle of 45 degrees (corresponding to a leading edge sweep of 46.7 degrees).

A NACA 65A006 airfoil section is used for the wing with no dihedral [132]. The fuselage sections are circular and the longitudinal shape of the fuselage is given in figure 89 with a sixth of the length cut out for the model to be attached with a sting.

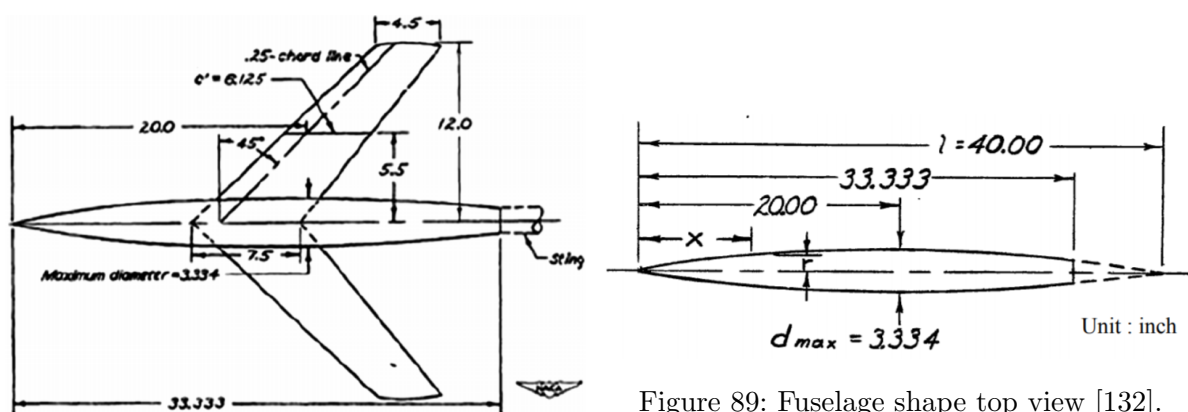


Figure 88: Model of NACA RM L51F07 configuration (unit: inches) [132].

Figure 89: Fuselage shape top view [132].

In the experimental data, one hundred static pressure orifices have been placed on the fuselage

body [132]. These pressure orifices are distributed along six longitudinal rows of the fuselage and placed along circumferential locations as shown in figure 91. For the wing, pressure orifices are placed along the stream direction at five spanwise locations along the wing semi-span as shown in figure 90. The experimental wind tunnel tests on this configuration were conducted with Mach numbers ranging from $M=0.6$ [-] to $M=1.2$ [-] and are available in [132].

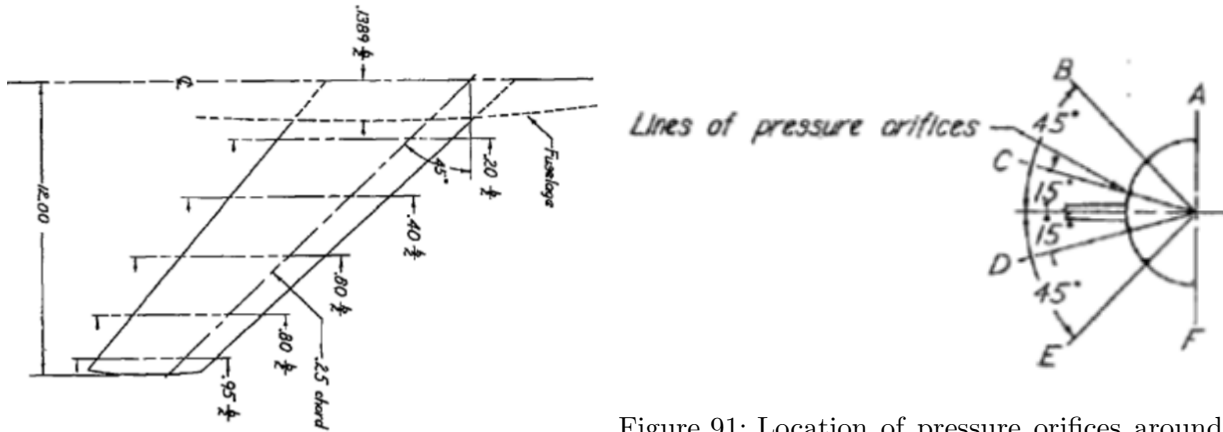


Figure 90: Location of pressure orifices along wing span [132].

Figure 91: Location of pressure orifices around fuselage [132].

For the PANAIR validation model, a total of 1420 panels compose the mesh, where the number of elements distributed along the different mesh directions are defined in Table 6. The resulting mesh obtained for the PANAIR simulation is shown in figure 92 where the blue and red mesh networks correspond to the wing and fuselage wakes respectively. Only half of the geometry is analysed in PANAIR as a result of symmetry about the vertical $x - z$ plane.

Table 6: Distribution of elements over NACA model.

Property	Number of elements [-]
Wing lateral	28
Wing longitudinal	25
Fuselage circumference	12
Fuselage front section	20
Fuselage rear section	15

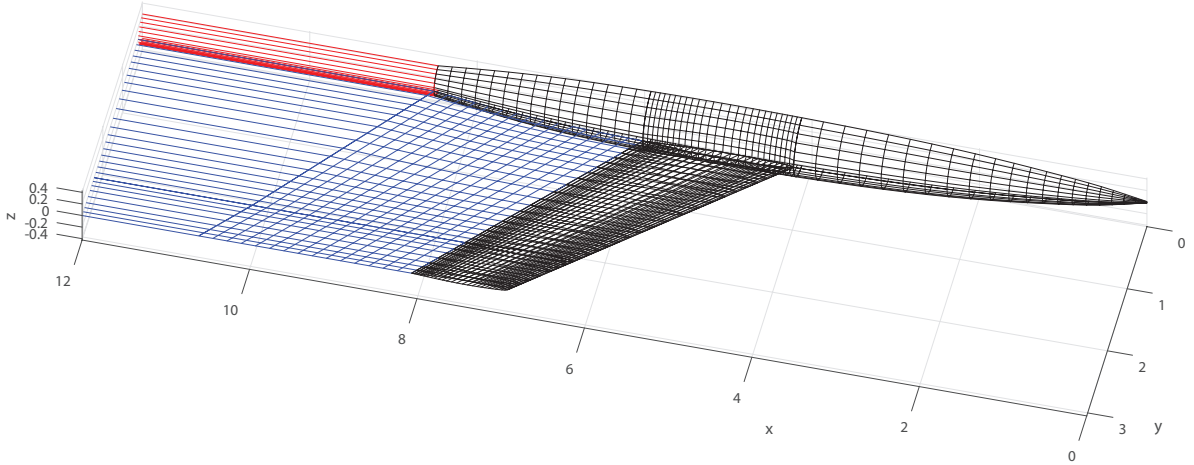


Figure 92: PANAIR mesh for NACA configuration.

All the validation data for this configuration can be found in [132]. In this section, the results obtained from PANAIR are compared to the wind tunnel results for Mach numbers of 0.6 [-] and 0.8 [-]. To demonstrate the typical pressure distribution obtained over the configuration, the pressure coefficients over the mesh at a freestream Mach number of 0.6 [-] and angle of attack of 4 [deg] are plotted in figure 93 and 94. As can be seen from this picture, most of the suction occurs at the wing leading edge and in general over the top surface. On the other hand, flow compression occurs on the bottom surfaces, as expected.

For a more accurate validation study, the pressure coefficient along the chord at three of the defined wing semi span positions ($0.2b_s$, $0.6b_s$ and $0.95b_s$) defined in figure 90 at a freestream Mach number of 0.8 [-] and angles of attack of 2 and 4 [deg] are reported and compared to the wind tunnel data in figures 95 and 96. In addition the local pressure coefficient along the fuselage length is compared against wind tunnel data in figures 97 and 98. Note that the results along the wing span at Mach number of 0.6 [-] are included in Appendix C.3.

As can be seen from the pressure distributions over the configuration, PANAIR provides an excellent match with wind tunnel data for both wing and fuselage sections. Looking at the results around the fuselage section (especially locations C and D), the impact of the wing-body interference are clearly observed. A clear suction can be observed along location C, where the wing leading edge creates a localized suction in the flow. On the other hand, at location D, the compression effect on the lower part of the wing can also be observed. The pressure distribution at other locations around the fuselage section (A and B) also change in the wing-body region, but are much less pronounced.

At the different wing span locations (figures 95 and 96), it can be observed that the mid-span region ($0.6b_s$) of the wing produces the most lift. Due to interference with the fuselage, the suction at the leading edge of the wing near the root section ($0.2b_s$) is reduced. In addition, it can be seen that the Kutta condition is met at the trailing edge of each airfoil section.

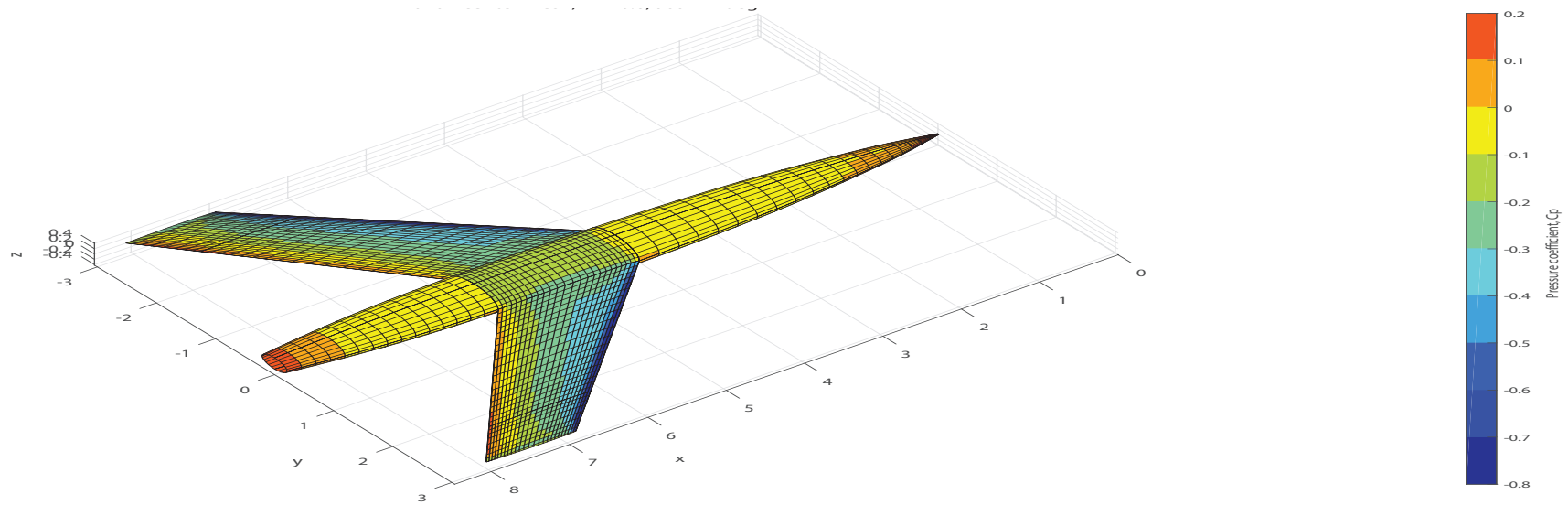


Figure 93: PANAIR pressure results over top of configuration at $M = 0.6$ [-], $AOA = 4$ [deg].

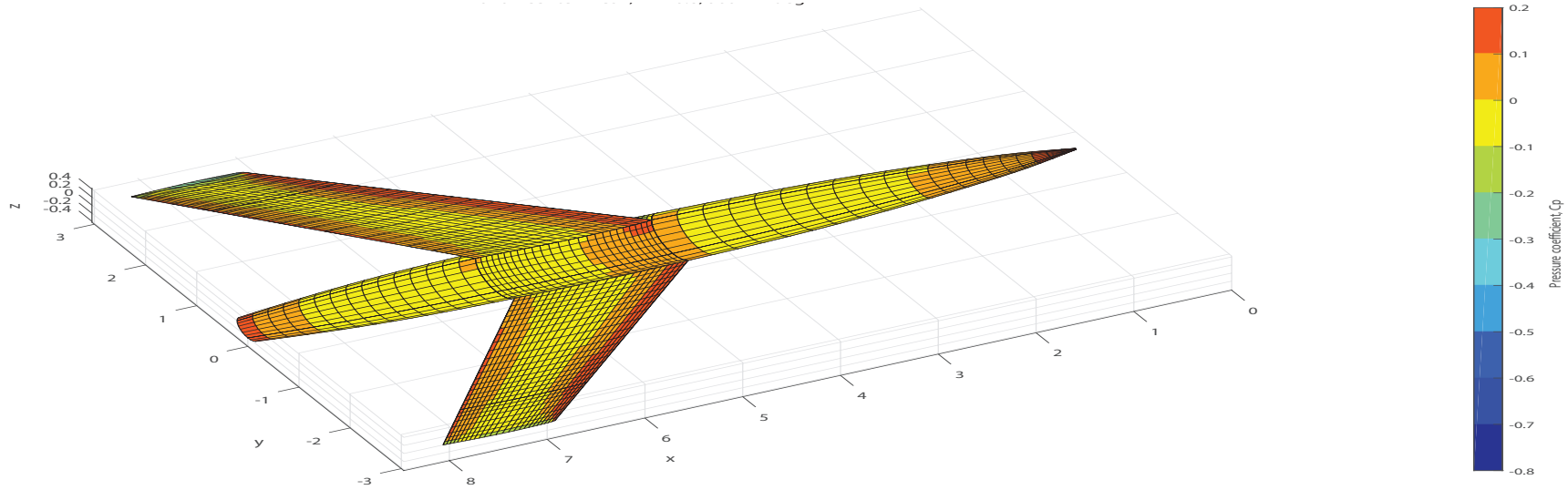


Figure 94: PANAIR pressure results over bottom of configuration at $M = 0.6$ [-], $AOA = 4$ [deg].

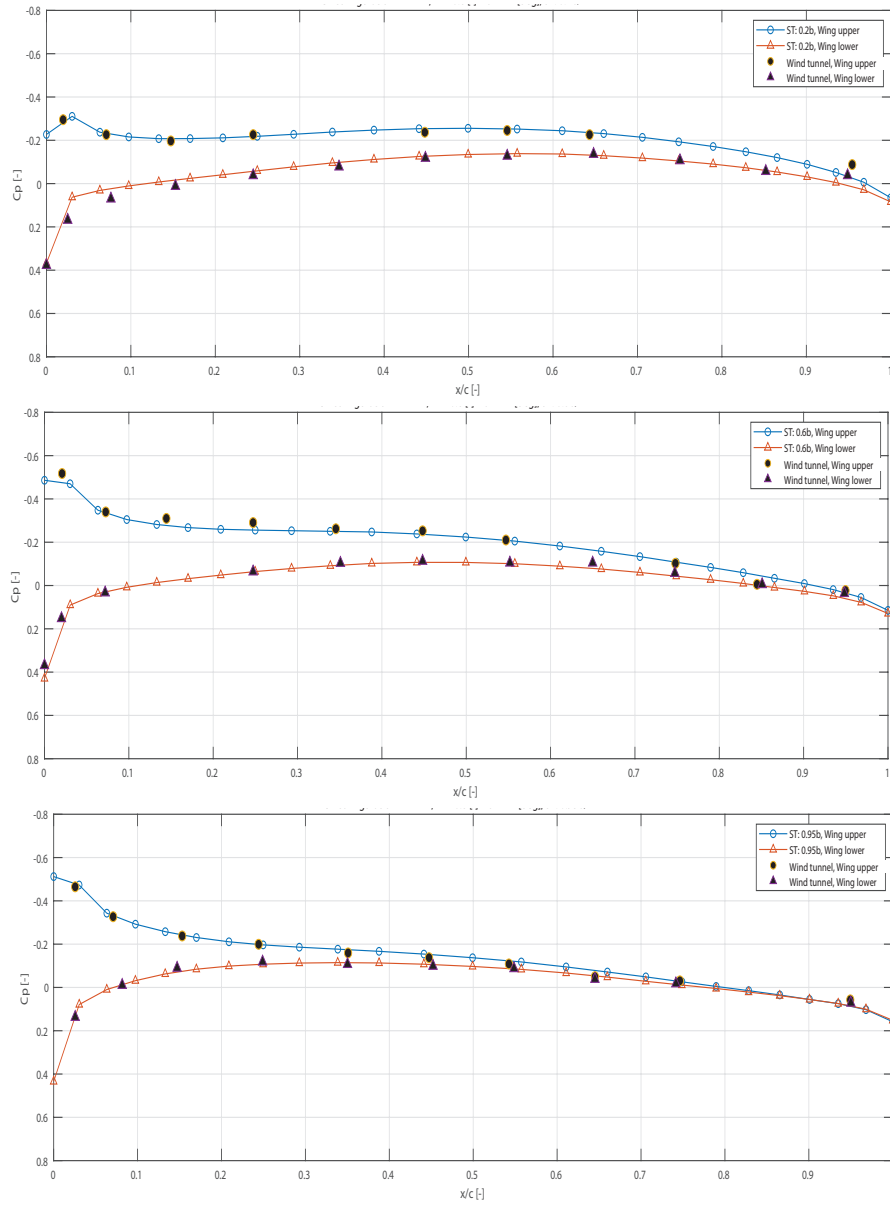


Figure 95: Pressure distribution along wing span at $M = 0.8$ [-] and $AOA = 2$ [deg], $ST = 0.2b_s, 0.6b_s, 0.95b_s$ (top to bottom).

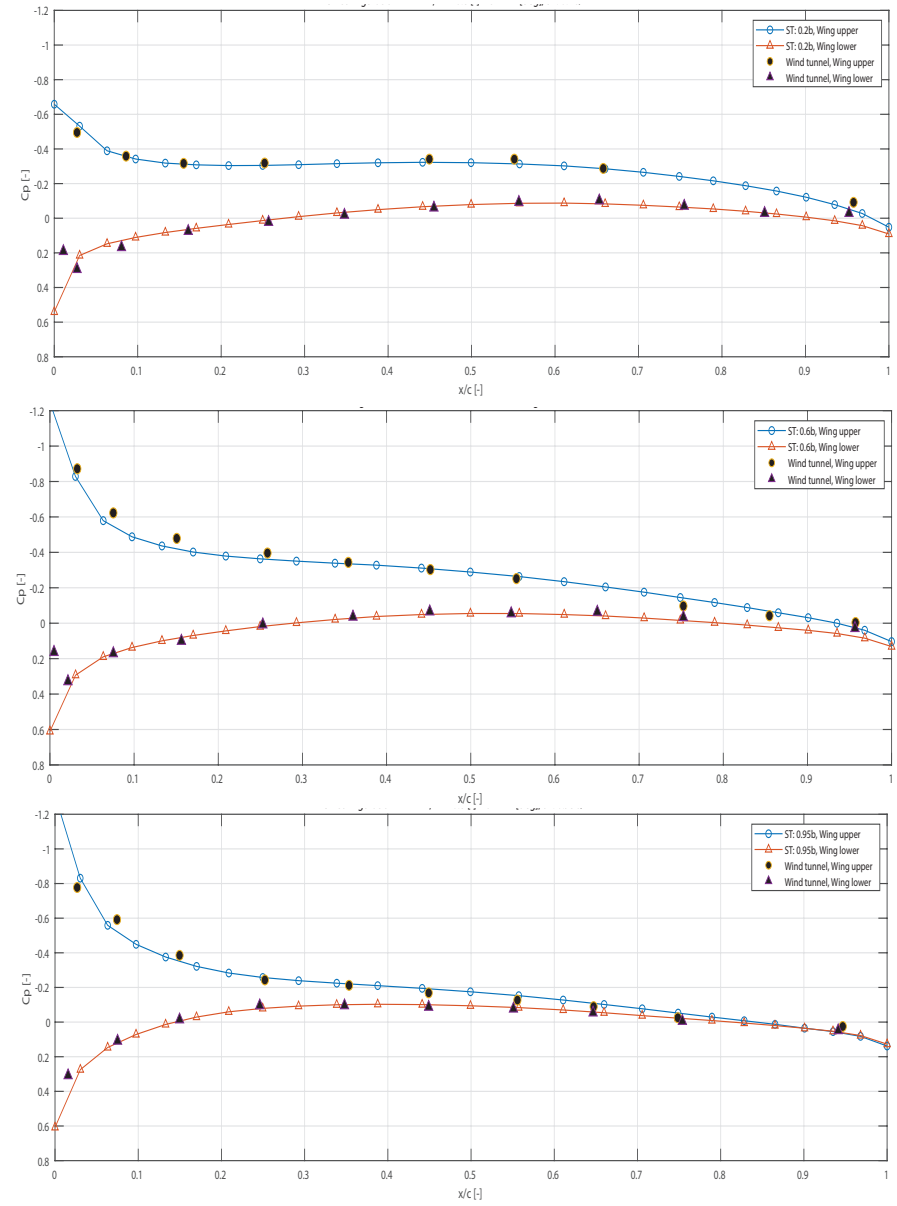


Figure 96: Pressure distribution along wing span at $M = 0.8$ [-] and $AOA = 4$ [deg], $ST = 0.2b_s, 0.6b_s, 0.95b_s$ (top to bottom).

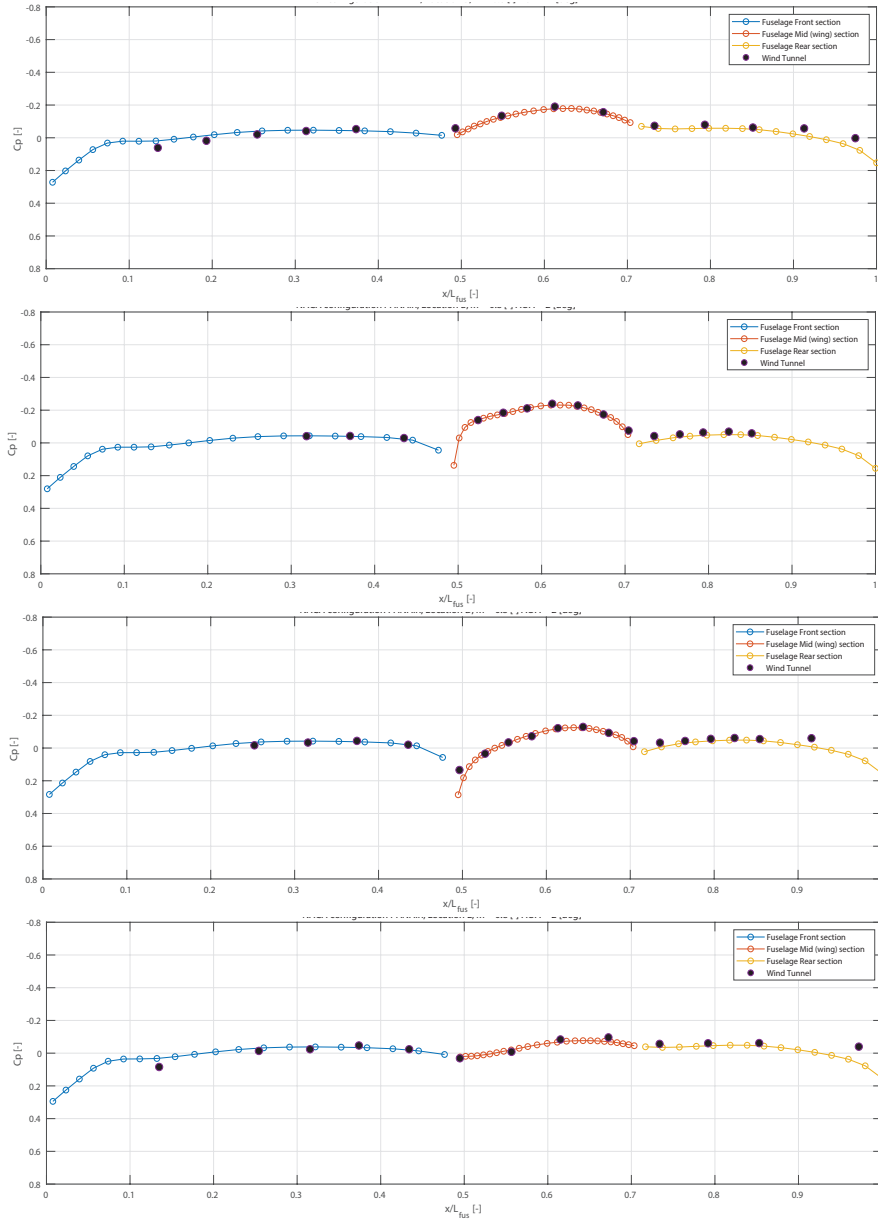


Figure 97: Pressure distribution along fuselage at $M = 0.8$ [-] and $AOA = 2$ [deg], Locations: B, C, D, E (top to bottom).

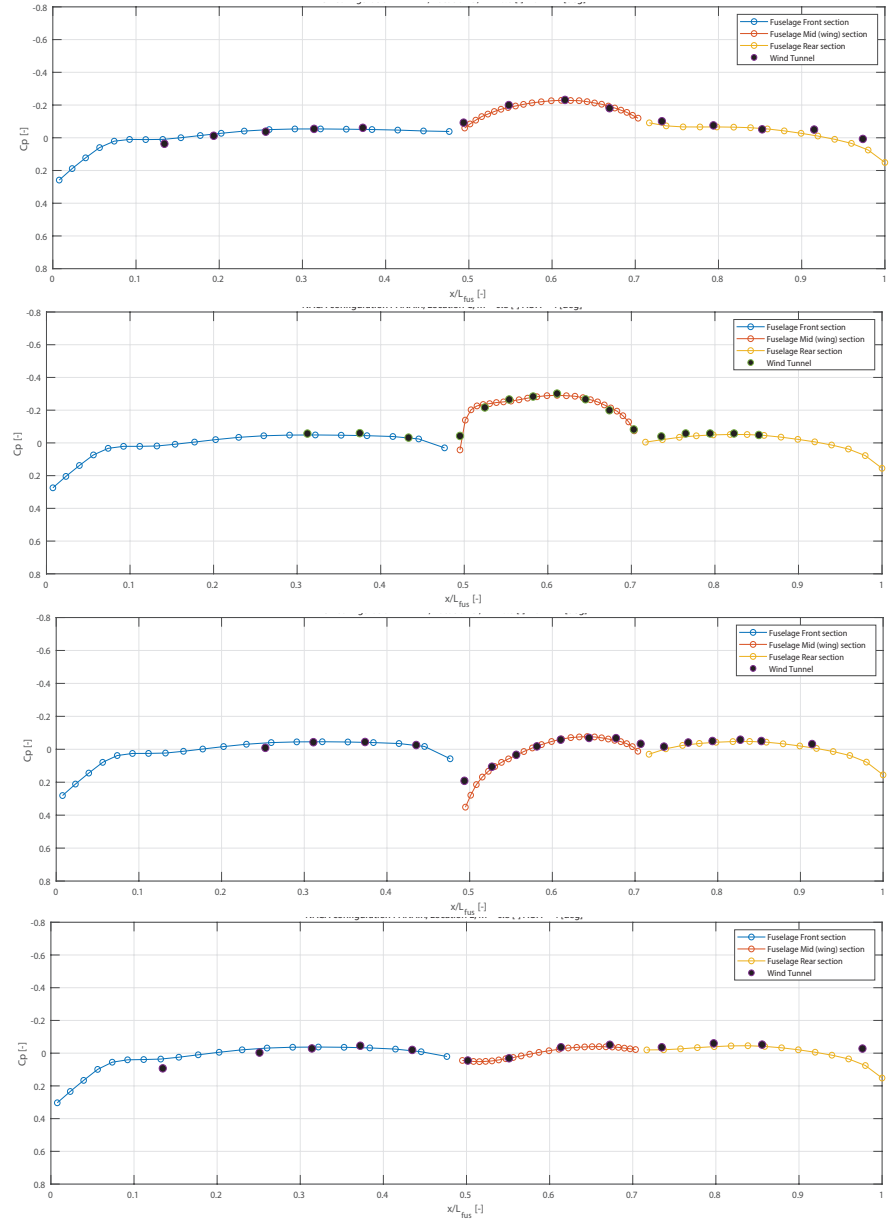


Figure 98: Pressure distribution along fuselage at $M = 0.8$ [-] and $AOA = 4$ [deg], Locations: B, C, D, E (top to bottom).

The comparison between the lift and inviscid drag polars at Mach numbers of 0.6 and 0.8 obtained from PANAIR and the wind tunnel experiments are presented in Figures 99 to 102. As can be seen from the results of PANAIR, a very good agreement is achieved for the lift polars for both flight conditions. The results of PANAIR slightly overestimate the lift curve, as expected, due to the lack of viscous effects in the panel code. After angles of attacks of about 8 [deg], the gradient of the lift curve for the wind tunnel data starts to decrease indicating that viscous effects are becoming significant and local flow separation may be occurring (especially noticeable in figure 100). The possibility for flow separation can clearly be observed in the drag polars starting at an angle of attack of 8 [deg] (Figures 101 and 102), where a sharp increase in drag occurs. PANAIR is not capable of capturing viscous effects and flow separation, however the overall fit of the lift and inviscid drag coefficient is very good at angles of attack below 8 [deg] for a wing with relatively high sweep. This validates the correct implementation of the PANAIR code in the platform and its applicability to subsonic flow.

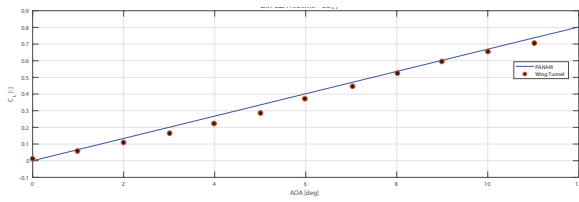


Figure 99: Lift polar at $M = 0.6$ [-].

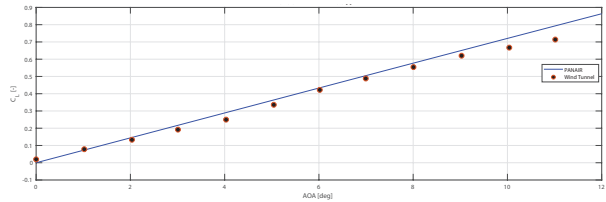


Figure 100: Lift polar at $M = 0.8$ [-].

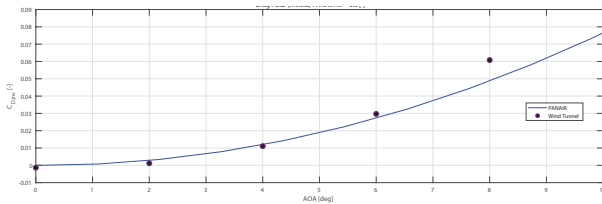


Figure 101: Inviscid drag polar at $M = 0.6$ [-].

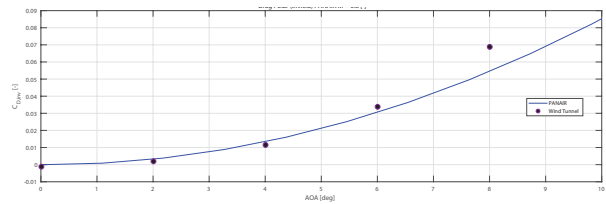


Figure 102: Inviscid drag polar at $M = 0.8$ [-].

15.2. High speed verification: Inviscid flow over an ogive body

In the paper “Development of an Aerodynamics Code for the Optimisation of Hypersonic Vehicles” by Thomas Jazra and al [59], a hypersonic impact and shock-expansion code is verified against the results of a Computation Fluid Dynamics (CFD) analysis on an Ogive-Cylinder configuration in high speed flow. The ogive-cylinder configuration is representative of a typical hypersonic fuselage body shape and is thus useful to verify the validity of the impact methods implemented in the MDO platform. The configuration under which CFD computations were performed by [59] is provided in figure 103.

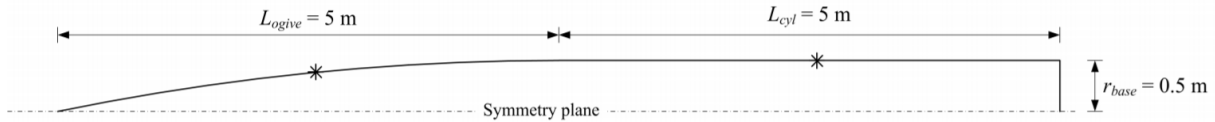


Figure 103: Description of ogive-cylinder model [59].

To replicate the model in the platform, the mesh given by figure 104 is produced. The ogive-cylinder mesh is comprised of 80 longitudinal and 50 circumferential elements and half of the configuration is analysed under symmetry about the $x - z$ axis.

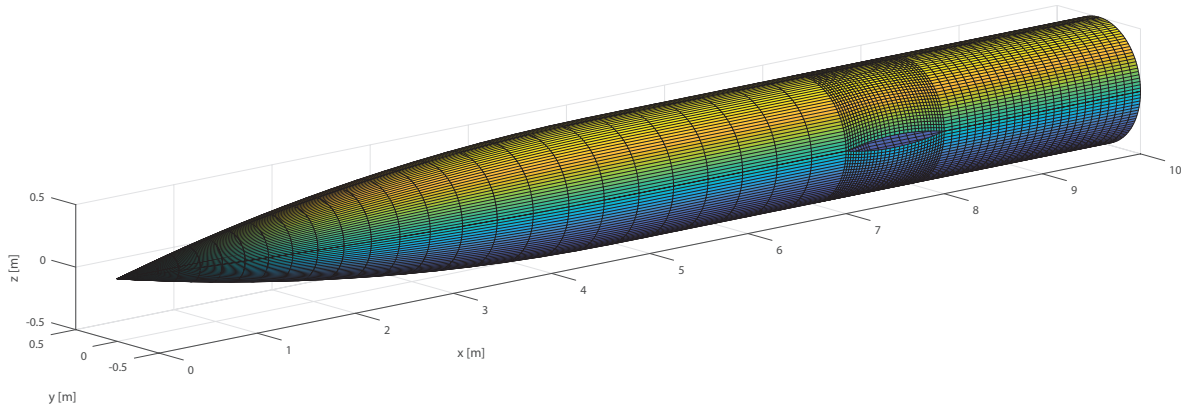


Figure 104: Mesh for ogive-cylinder configuration.

For the configuration, the CFD analysis was conducted by [59] using the RANS solver VULCAN, with a mesh composed of 3.2 million cells. The results of the CFD analysis on the configuration are reported for freestream conditions of $M = 8[-]$, $AOA = 4$ [deg] and $M = 12[-]$, $AOA = 2$ [deg].

The results of the CFD analyses and engineering methods given by [59] are provided in figures 105 and 107. In the verification results, the pressure distribution along the fuselage longitudinal (along the top and bottom strips) and circumferential (at $0.25L$ and $0.75L$) directions (starting from the top 0 [deg] to the bottom 180 [deg] strip) are given. The validation results provided by [59] include the CFD analyses, tangent cone and shock-expansion methods developed by the authors. In this section those results are compared to the tangent-cone Taylor Maccoll interpolated and approximated Engineering Methods implemented in this platform as given in Section 11.

When observing the results at $M = 8$ [-], $AOA = 4$ [deg] (Figures 105 and 106), it can be observed that both engineering methods implemented in the current platform follow the general

trend of pressure distribution along the fuselage length and circumference. The interpolated tangent-cone results follow a very similar behaviour to the tangent-cone method applied by [59].

First, looking at the longitudinal pressure distributions, along the configuration bottom strip (windward side) both tangent-cone methods implemented follow the verification data closely and the differences between the two methods are very small. However, along the top strip (leeward side), the approximated Taylor Maccoll method over predicts the suction on the top strip for $x/L > 0.2$ when compared to the CFD results. The interpolated Taylor Maccoll method creates a plateau in pressure distribution on the top strip in the region $0.2 < x/L < 0.3$, which is believed to be due to the interpolation of the Taylor Maccoll solutions at low impact angles. Indeed, since the configuration is inclined with respect to the flow (AOA = 4 [deg]), the top strip is exposed to very small impact angles over the ogive section of the configuration before switching to expansion flow after $x/L > 0.3$. The interpolation of the Taylor Maccoll equations at very small impact angles could lead to the plateau observed.

Now observing the circumferential distributions at $0.25L$ of the configuration (halfway along the ogive section), the interpolated Taylor Maccoll method once again outperforms the approximated solution near the leeward side of the configuration ($0 < \phi < 60[deg]$) when compared to the CFD solutions. This is again due to the small impact angles expected on the leeward side of the configuration whereby the approximated Taylor Maccoll solution struggles to capture the correct pressures. Closer to the windward side ($\phi > 60[deg]$), both interpolated and approximated tangent cone methods are closely matched. At $0.75L$ (halfway along the cylinder section), the differences between interpolated and approximated Taylor Maccoll methods are quite significant over the range $0 < \phi < 120[deg]$. Over this part of the configuration, very small impact angles are expected thereby resulting in the discontinuous pressure distribution observed. Overall, the interpolated tangent-cone method outperforms the approximated method when compared to the CFD solutions provided by [59]. It can also be noted that the tangent-cone methods (especially the interpolated Taylor Maccoll method) developed in this platform closely match the behaviour of the tangent-cone method developed in [59] thereby providing proof of the correct implementation of these methods.

For $M = 12 [-]$, AOA = 2 [deg] (Figure 107 and 108), the results from the interpolated and approximated tangent cone methods implemented in the platform once again closely correlate to the CFD results of [59]. At this freestream condition, the deviations between both implemented methods reduce and the overall match to the CFD data is improved. Overall, from the comparisons performed against the CFD data from [59], it can be concluded that the interpolated Taylor-Maccoll method provides the best fit in pressure distributions over a typical fuselage body shape and is therefore the preferred method.

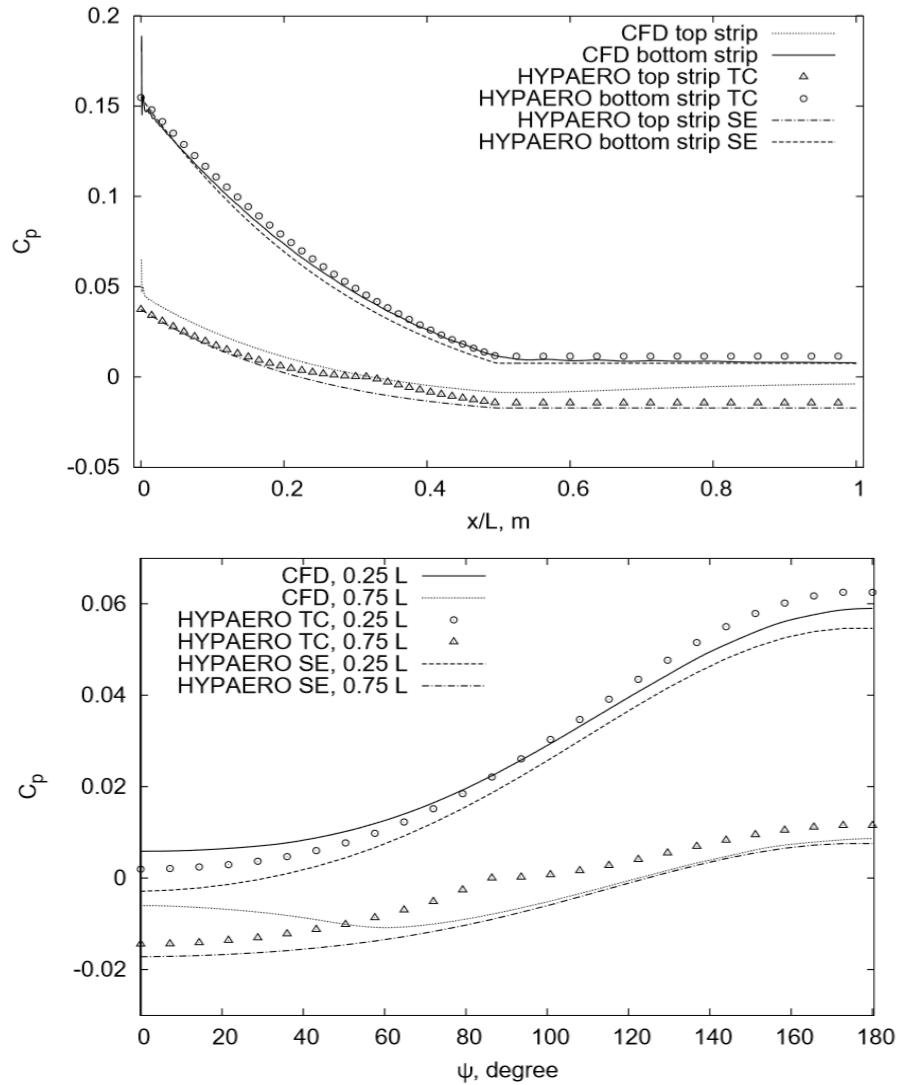


Figure 105: Validation pressure distribution along fuselage longitudinal top and bottom strips (top figure) and around circumference at $0.25L$ and $0.75L$ (bottom figure) at $M = 8$ [-] and $AOA = 4$ [deg] [59].

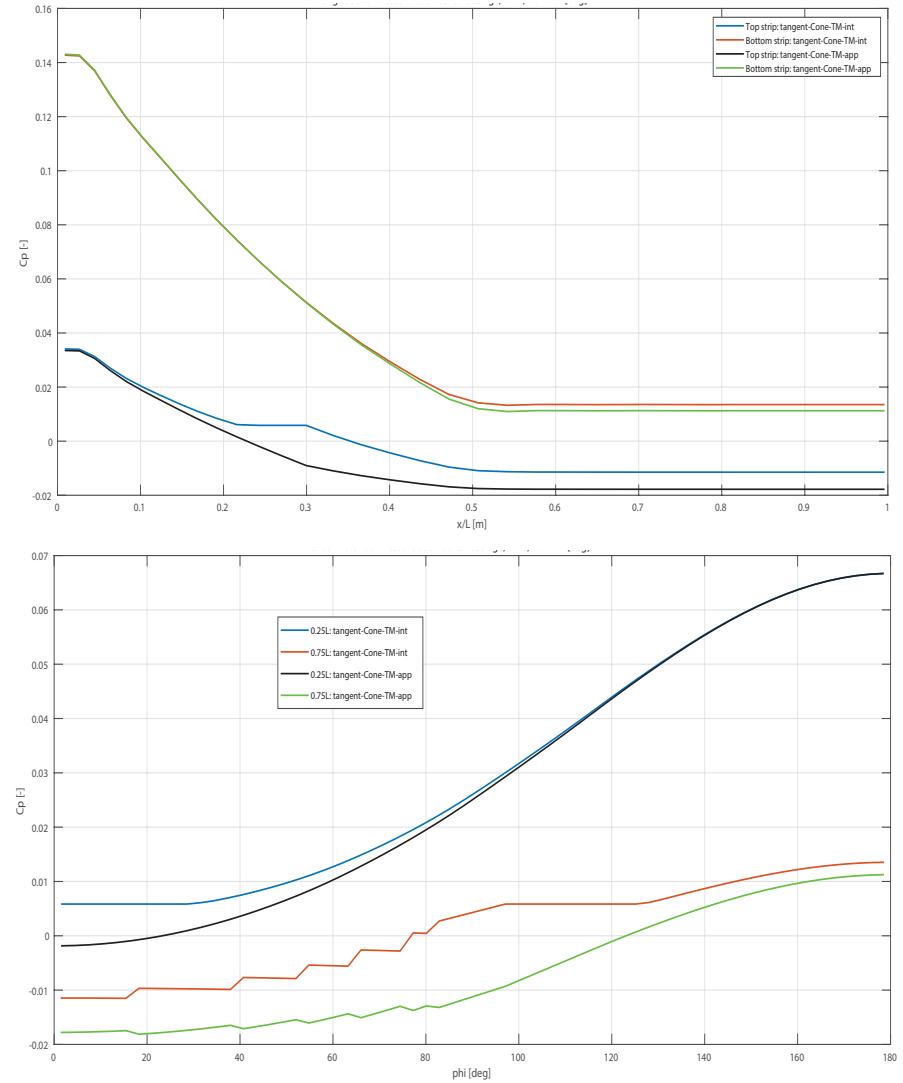


Figure 106: Implemented Engineering methods pressure distribution along fuselage longitudinal top and bottom strips (top figure) and around circumference at $0.25L$ and $0.75L$ (bottom figure) at $M = 8$ [-] and $AOA = 4$ [deg].

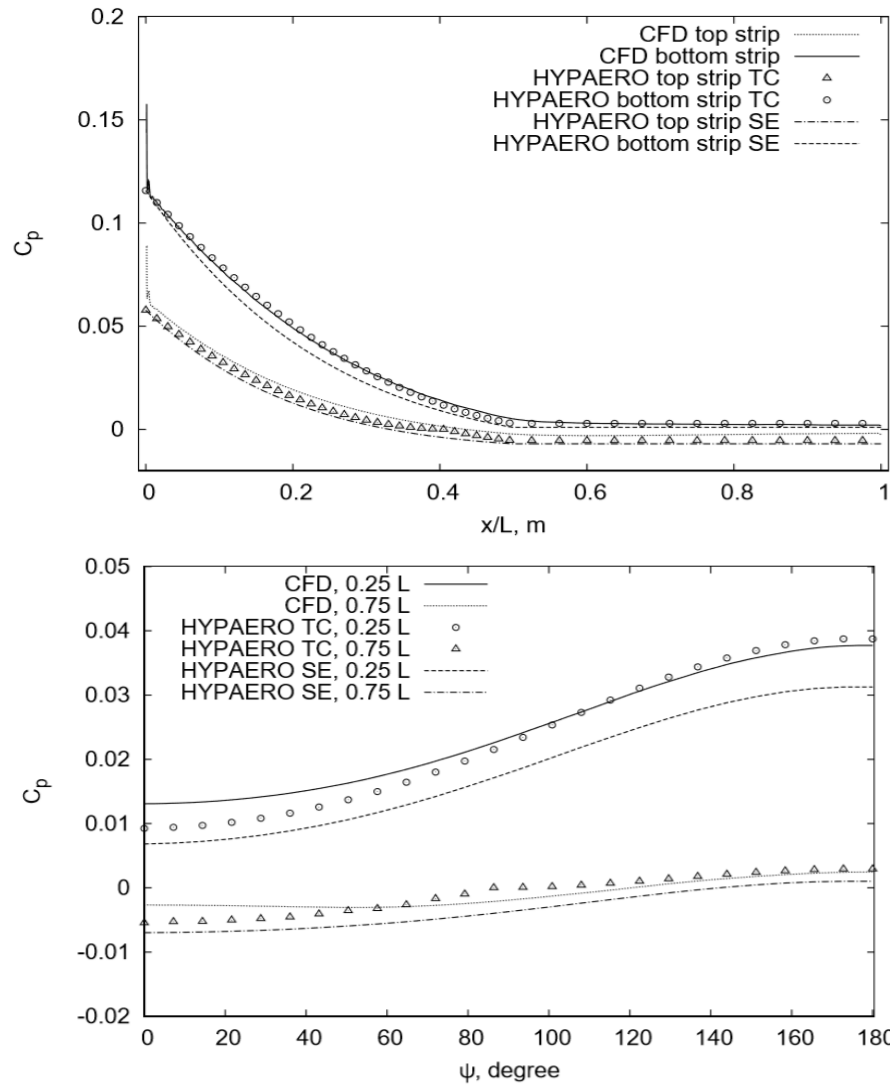


Figure 107: Validation pressure distribution along fuselage longitudinal top and bottom strips (top figure) and around circumference at $0.25L$ and $0.75L$ (bottom figure) at $M = 12$ [-] and $AOA = 2$ [deg] [59].

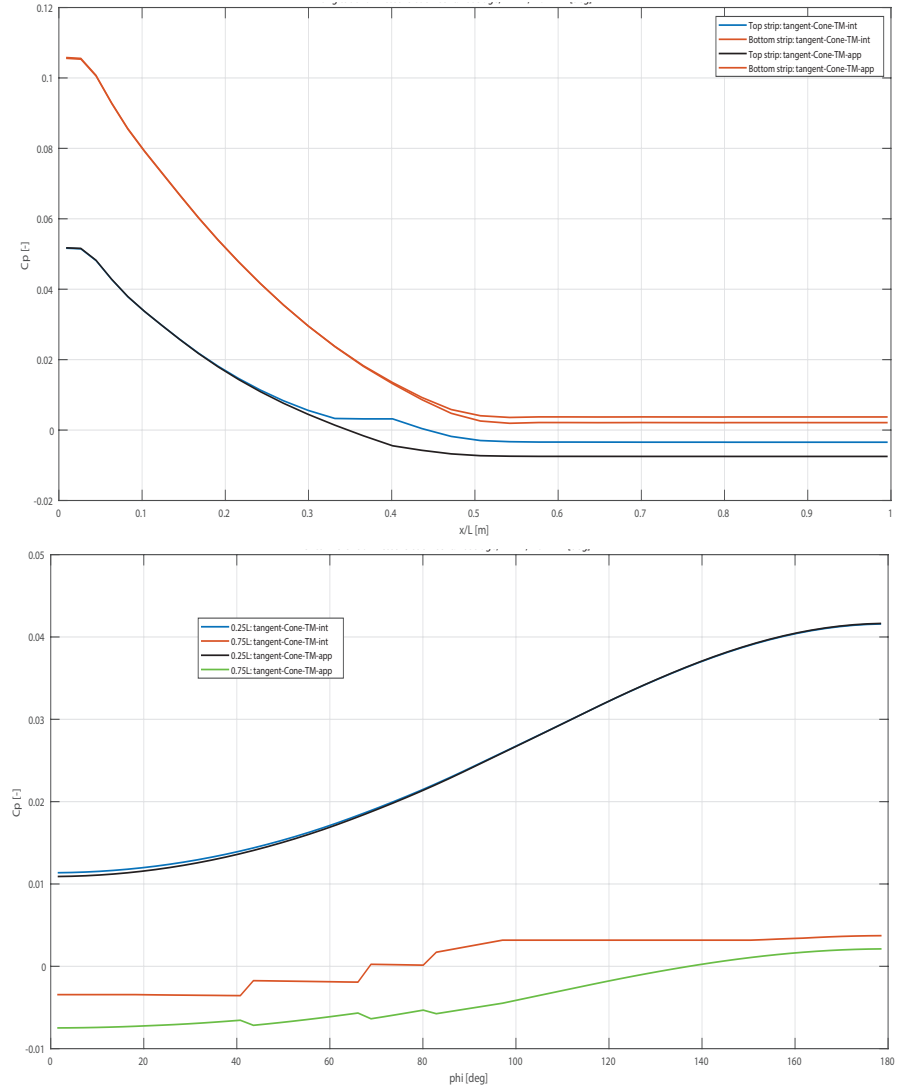


Figure 108: Implemented Engineering methods pressure distribution along fuselage longitudinal top and bottom strips (top figure) and around circumference at $0.25L$ and $0.75L$ (bottom figure) at $M = 12$ [-] and $AOA = 2$ [deg].

15.3. High speed: Complete configuration, X-15 and HyCAT aircrafts

In the previous section, the inviscid flow about an ogive-cylinder configuration was verified. In this section, the results of the hypersonic engineering methods implemented in the platform are validated against full configuration aircraft. Two well-known hypersonic aircraft; the X-15 and HyCAT configurations have been used to provide validation for the engineering methods developed. For both configurations, the aircraft geometries have been reproduced as closely as possible and the impact methods listed in Section 11 are used to evaluate the most appropriate methods to be used in the platform.

15.3.1. X-15 Configuration

The North American X-15 configuration was a hypersonic aircraft operated by the United States Air Force and the National Aeronautics and Space Agency. The configuration saw its maiden flight in 1959 and was developed as part of a series of experimental aircraft. The aircraft has undergone extensive wind tunnel testing [106] [39] which makes it an ideal candidate for the validation of the hypersonic methods implemented.

The X-15 configuration has been tested on a 0.02 scale model of the aircraft at a Mach number of 6.83 [-] and Reynolds number of 640,000 [-] based on the mean aerodynamic chord [39]. In the wind tunnel experiments from [39], a component breakdown analysis was performed to obtain the impact of each component on the aircraft aerodynamic and longitudinal stability performance. The configuration is described in figures 109 and 110. In addition, the main wing and horizontal tail have modified NACA 66-005 airfoil cross sections and the main wing planform properties are listed in Table 7 (for full scale model).

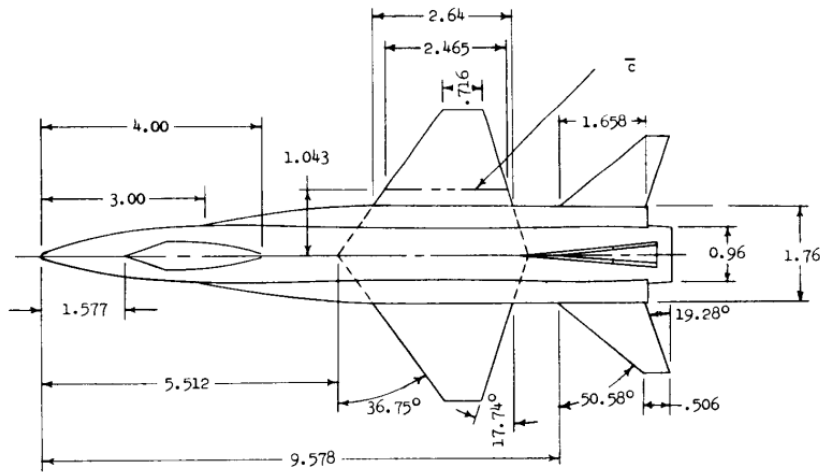


Figure 109: X-15 configuration, top view (unit: inches).

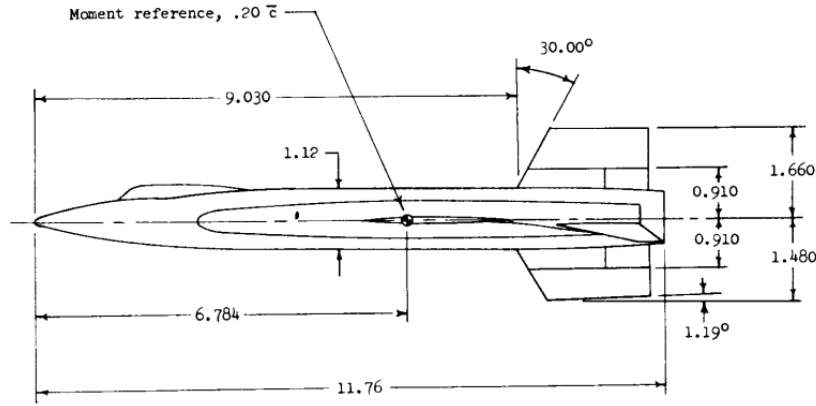


Figure 110: X-15 configuration, side view (unit: inches).

In this validation study, all the impact methods listed in Section 11 are evaluated and compared with the validation data. To account for viscous drag, the Eckert reference enthalpy method (Section 11) is used in this analysis, assuming turbulent flow over the entire configuration and a Prandtl number of $P_r = 0.9[-]$. The full scale configuration is analysed at an altitude of 46 km which corresponds to a Reynolds number of 672,000 [-].

Table 7: Full scale model main wing properties [39].

Property	Value	Unit
Leading edge sweep (Λ_{le})	36.9	[deg]
Aspect ratio (AR)	2.55	[-]
Taper ratio (λ)	0.19	[-]
Span (b)	6.83	[m]
Mean aerodynamic chord (\bar{c})	3.13	[m]
Reference area (S_{ref})	18.29	[m ²]

The validation data for the X-15 presented in [39] provides the lift and drag polars of the configuration based on a component breakdown. The wind-tunnel experiments provide the lift and drag properties of the fuselage only (main body + sidepods) as well as the fuselage + main wing configuration (the impact of other components such as horizontal/vertical tail and canopy are also included in the validation report but are not considered for this analysis). For this analysis, the mesh generated for the aircraft model can be seen in figure 111, where the fuselage (+ sidepods) and main wing of the X-15 configuration have been modelled. Note that in the mesh generated, a high number of elements have been placed near the leading edge of the wing. This is done because the NACA 66-005 airfoil possess a blunt nose and thus to capture the geometrical changes at the wing leading edge, a high number of panels have been placed in this region of the geometry.

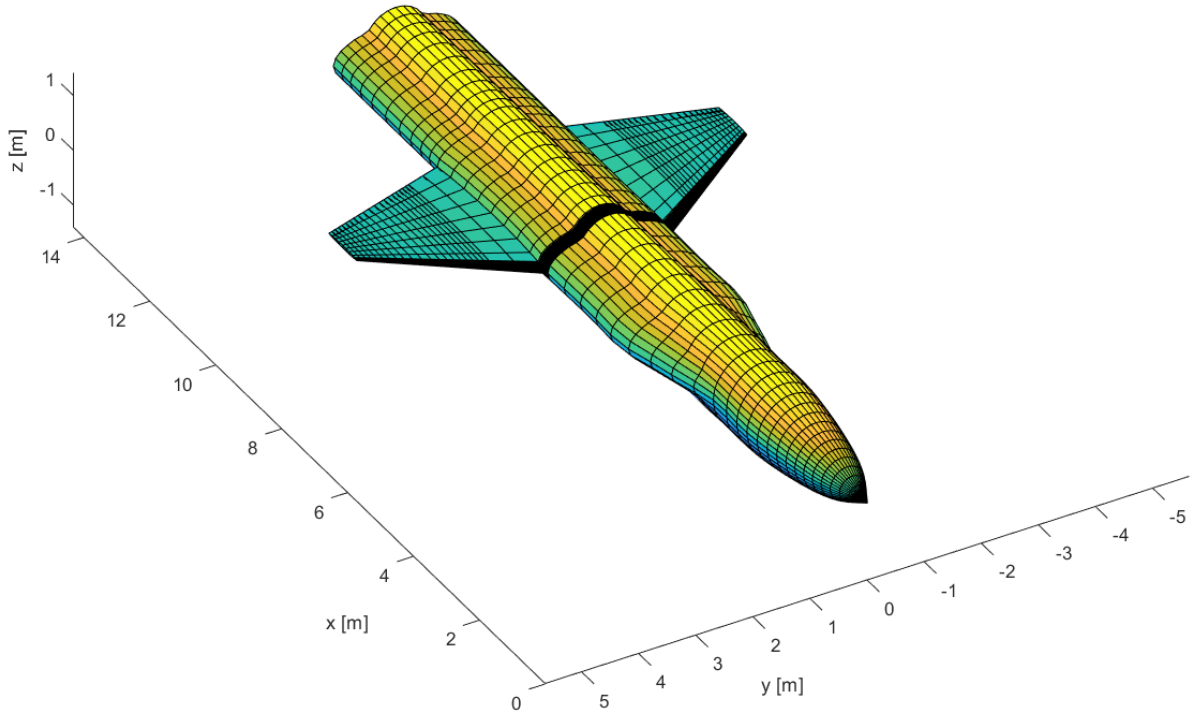


Figure 111: Mesh for the X-15 configuration.

In figures 112 to 115, the lift and drag polars obtained from the different impact methods presented in Section 11 are compared to the X-15 validation data for the fuselage only and fuselage + wing configurations at $M = 6.83 [-]$ and $Re = 672,000[-]$. In addition, for both configurations, a drag-lift dependency plot is given. In this plot the drag coefficient is plotted against the lift coefficient squared (C_D vs C_L^2) and allows a measure of the drag due to lift ($C_D = C_{D,0} + K \cdot C_L^2$).

First, observing the results of the fuselage only lift and drag polars (figure 112), it can be seen that overall each of the impact methods are capable of capturing the expected (near) linear and quadratic behaviour of the lift and drag polars. The tangent-wedge and inclined-wedge methods produce near identical lift and drag curves, however both engineering methods overestimate the lift and drag polars quite significantly. This is most likely due to the lack of a re-compression model behind the shock generated by a wedge. For fuselage bodies, impact angles can be large and thus the re-compression model of the Taylor Maccoll equations provides a much better fit. Indeed both approximated and interpolated tangent cone methods provide a better fit when compared to the validation data. The interpolated Taylor Maccoll method provides a slightly better fit, although both tangent-cone methods slightly overestimate both lift and drag polars. Looking at the drag versus lift dependency curve (figure 113), both tangent-cone methods provide an excellent fit, showing that the drag polar behaves as expected with respect to the lift polar. Overall, the differences can be explained due to the approximations linked to the use of impact methods and the small differences between the aircraft geometry model representation and the true configuration. The zero-lift viscous drag $C_{D,0}$ predicted by Eckert's method is excellent in this case with $C_{D,0, val} = 0.0135[-]$ for the validation data and $C_{D,0, Eckert} = 0.0134[-]$ for Eckert's method using the interpolated Taylor Maccoll impact method, only a 0.7% difference in this case.

Now looking at the fuselage + wing configuration (figures 114 and 115), the tangent-wedge and inclined wedge methods once again are near indistinguishable and overestimate the lift and

drag polars. If tangent-cone methods are applied to both the wing and fuselage bodies, the lift and drag polars are underestimated. The best fit is achieved by combining the inclined wedge method for the wing and the tangent-cone method for the fuselage body. As can be seen in the lift and drag polars, the combination of these methods provide an excellent fit for angles of attack ranging between $0 < AOA < 15[deg]$. For angles $AOA > 15[deg]$, the inclined wedge (wing) + tangent-cone (fuselage) methods start to deviate, likely due to separation over the aircraft. The inclined wedge (wing) + interpolated tangent-cone (fuselage) method gives the best overall fit. The inclined wedge method is most appropriate for the wing due to the smaller impact angles (and thus induced shock waves angles) resulting in a near negligible re-compression over the wing behind the shock. Looking at the drag versus lift curve, once again the inclined wedge (wing) + tangent-cone (fuselage) methods provide a good fit. The zero-lift viscous drag $C_{D,0}$ predicted by Eckert's method is fairly good in this case with $C_{D,0,val} = 0.0227[-]$ and $C_{D,0,Eckert} = 0.0170[-]$, a difference of approximately 30%.

Overall, this validation section has shown the applicability of impact methods for predicting hypersonic flow as well as confirming the correct implementation of these methods. From this analysis, the inclined wedge (wing) + interpolated tangent-cone (fuselage) methods seem most appropriate to calculate the pressures over a configuration.

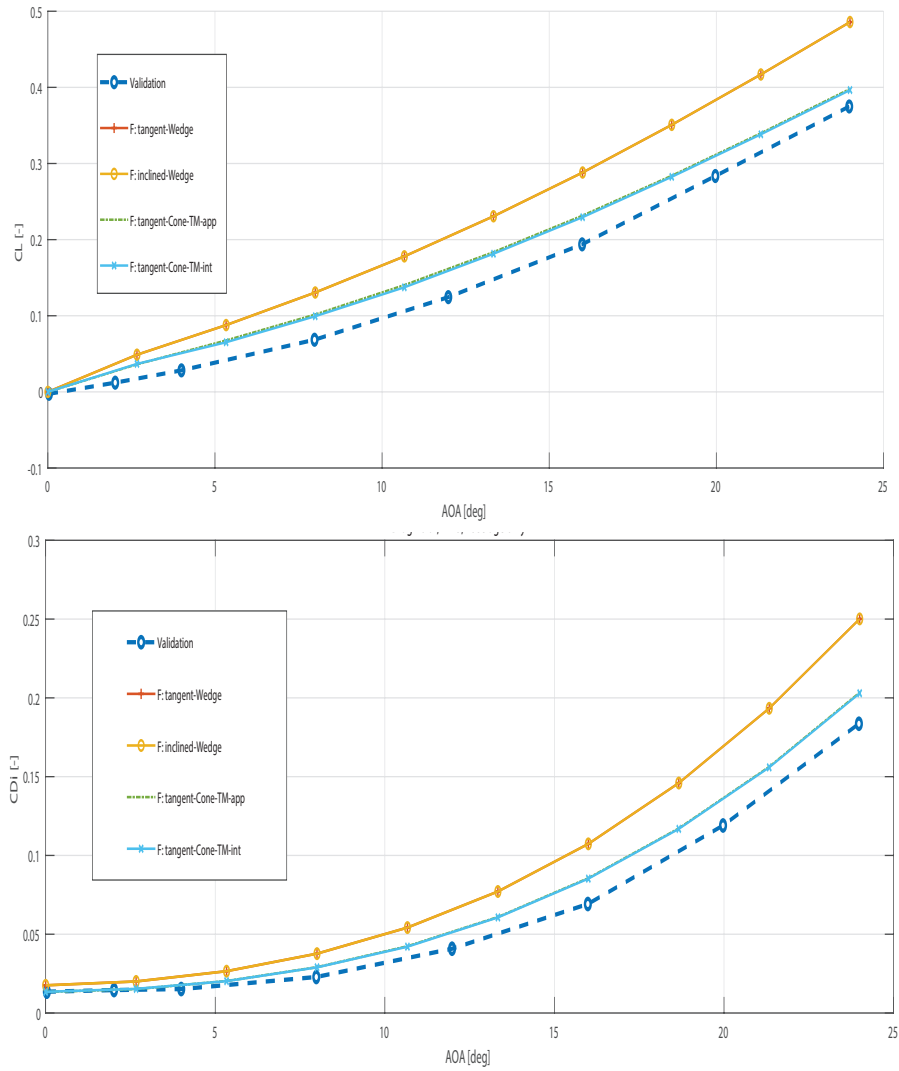


Figure 112: X-15 Lift and Drag polars for fuselage only configuration at $M = 6.83$ [-].

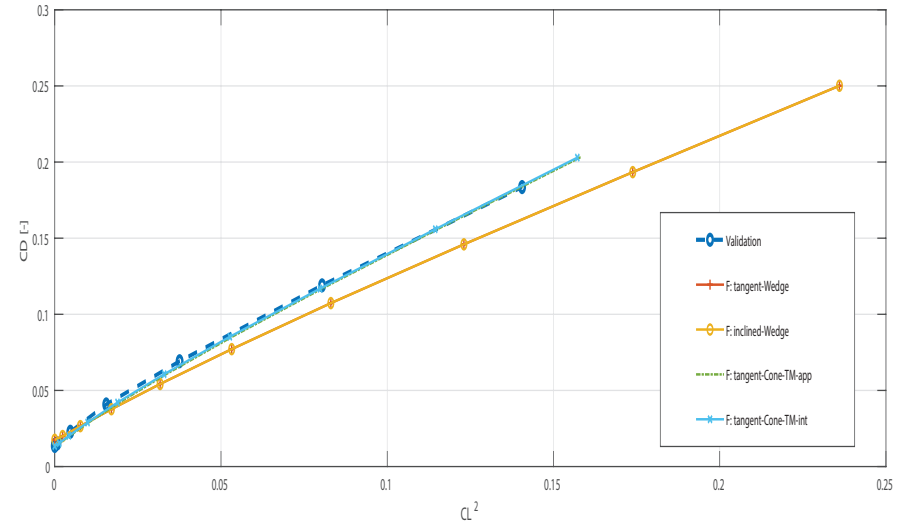


Figure 113: X-15 drag vs lift dependency for fuselage only configuration at $M = 6.83$ [-].

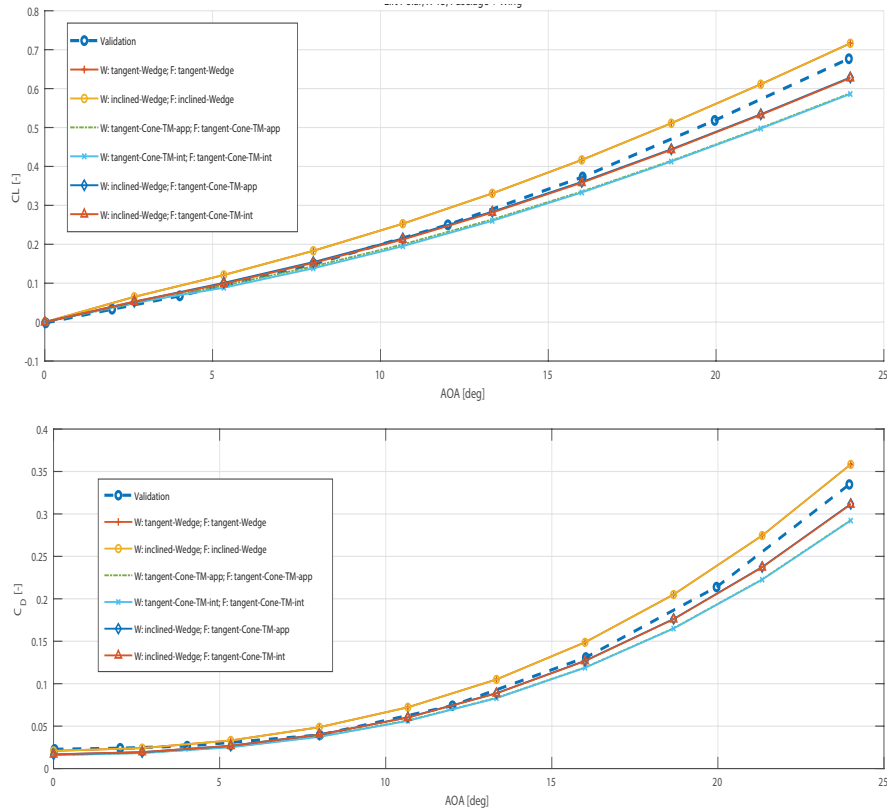


Figure 114: X-15 Lift and Drag polars for fuselage + wing configuration at $M = 6.83$ [-].

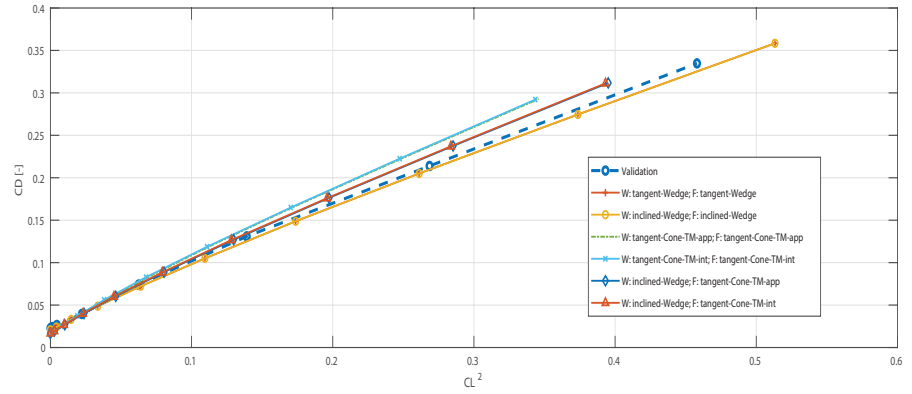


Figure 115: X-15 drag vs lift dependency for fuselage + wing configuration at $M = 6.83$ [-].

15.3.2. HyCAT Configuration

The HyCAT-A1 configuration was one of the most promising hypersonic cruiser in the 1970's. This configuration was designed by Lockheed-California Company for the NASA Hypersonic Cruise Aircraft Propulsion Integration study under contract NAS1-15057 [99]. Extensive study has been performed on this conceptual vehicle designed to be a liquid hydrogen fuelled, Mach 6 transport capable of carrying 200 passengers over 9260 km [99]. The configuration has also been extensively tested in wind tunnel experiments in [35], where the performance of the vehicle for Mach numbers of 0.36, 1.5, 2.0, 2.36, 2.86 and 6 has been investigated.

The top view of the configuration is given in figure 116, where a 0.02 scale model was tested in the wind-tunnel experiments [35]. The configuration is composed of fuselage and wing bodies, where the wing airfoil is a biconvex airfoil with thickness to chord ratio of 0.03. The properties of the wing planform are given according to Table 8. The configuration has been tested at Reynolds numbers ranging from $6.67 \cdot 10^6$ [-] (Mach 0.36 [-]) to $21.6 \cdot 10^6$ [-] (Mach 6 [-]) based on the mean aerodynamic chord and depending on the freestream Mach number. The aircraft model produced for the validation of the impact methods has a size set to 100 times the scale model and analysed at an altitude of 36 km resulting in a Reynolds number of $23 \cdot 10^6$ [-].

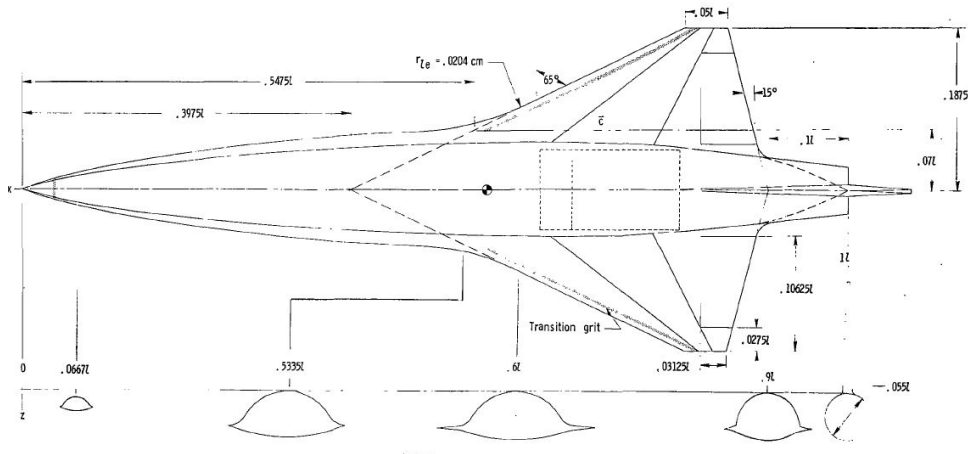


Figure 116: Top view of HyCAT A1 configuration [35].

Table 8: Main wing properties hyCAT (100 times scale model) [35]

Property	Value	Unit
Leading edge sweep (Λ_{le})	65	[deg]
Aspect ratio (AR)	1.4	[-]
Taper ratio (λ)	0.0875	[-]
Span (b)	30.46	[m]
Mean aerodynamic chord (\bar{c})	27.56	[m]
Reference area (S_{ref})	662.72	[m ²]

Once again, for this configuration, all the impact methods listed in Section 11 are compared to the validation data for the HyCAT configuration given in [35]. For the viscous model, Eckert' reference enthalpy method is once again used, assuming a fully turbulent configuration with a Prandtl number of $P_r = 0.9$ [-]. The mesh for the HyCAT configuration is shown in figure 117.

It can be seen in mesh generated that the sharp fuselage side chines have been smoothed out to provide more rounded fuselage cross sections.

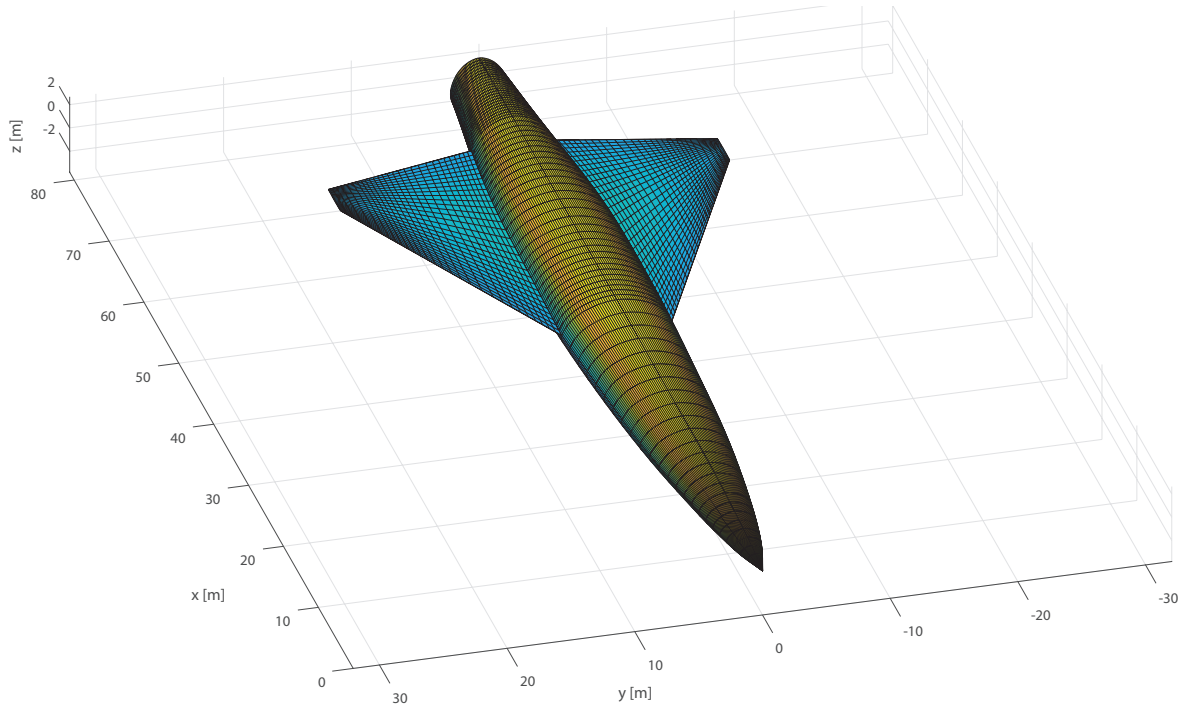


Figure 117: Mesh for HyCAT configuration.

The results of the different impact methods for the aircraft at cruise condition ($M = 6$ [-]) are first compared to the validation data. The lift and drag polar obtained at $M = 6$ [-] are displayed in figures 118 and 119. Observing the results of the impact methods, it is clear that once again, if the tangent-wedge or inclined wedge methods are applied to both wing and fuselage bodies, the lift and drag polars are overestimated (significant for $AOA > 4[deg]$). On the other hand, if tangent-cone methods are applied to both wing and fuselage bodies, the lift and drag polars are underestimated. Once again, using the inclined-wedge method for the wing and the tangent-cone methods for the fuselage yields the best overall fit, with a slightly smaller lift coefficient compared to the validation data at small angles of attack ($0 < AOA < 4[deg]$). This time, the inclined-wedge (wing) and approximated Taylor Maccoll methods (fuselage) performs slightly better than the interpolated tangent-cone method especially for the lift polar at lower angles of attack ($0 < AOA < 4[deg]$). The original HyCAT configuration posses fuselage cross sections with a sharp chine. These sharp sections are used to improve the lifting capability of the fuselage. Since the chine is not modelled in the model used for this analysis (see figure 117), this difference could partially explain the lift coefficient deficit of the inclined-wedge (wing) tangent-cone (fuselage) methods at low angles of attack ($0 < AOA < 4[deg]$). Regarding the zero lift drag coefficient, for the validation data, $C_{D,0,val} = 0.0056[-]$ while $C_{D,0,Eckert} = 0.005[-]$ for Eckert's method using the inclined-wedge (wing) interpolated tangent-cone (fuselage) methods, resulting in a difference of approximately 11%.

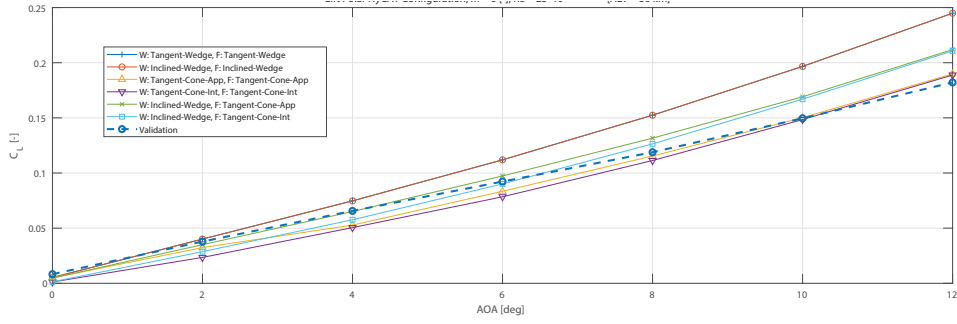


Figure 118: Lift polar of HyCAT at $M = 6$ [-], $Re = 23 \cdot 10^6$ [-].

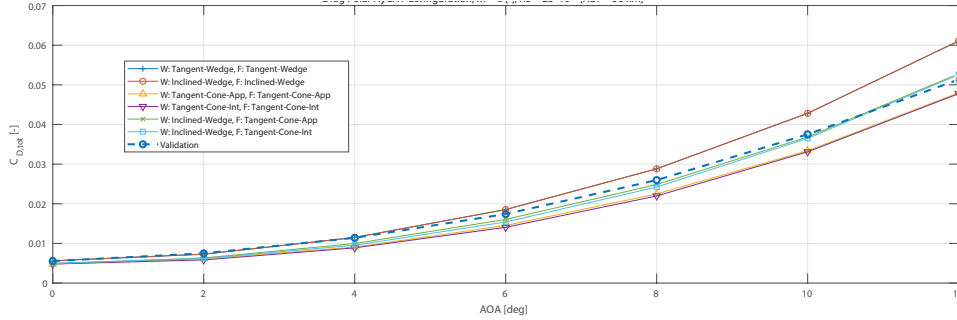


Figure 119: Drag polar of HyCAT at $M = 6$ [-], $Re = 23 \cdot 10^6$ [-].

Using the validation results of the HyCAT configuration at Mach numbers of 1.5, 2.0, 2.36, 2.86 and 6, the behaviour of the impact methods as a function of the freestream Mach number can be analysed. In figures 120 and 121, the lift and drag coefficients obtained from the different impact methods at angles of attack of 4 and 8 [deg] are compared to the validation data for Mach numbers ranging from 1.5 to 6. As expected, both lift and drag coefficients increase as the Mach number is reduced for all impact methods. For Mach numbers higher than 2.5, the inclined wedge (wing) and interpolated tangent-cone (fuselage) methods yield the best fit for both lift and drag coefficients as a function of Mach number for angles of attack of 4 and 8 [deg]. The inclined wedge (wing) + approximated Taylor-Maccoll (fuselage) method starts to significantly overestimate both lift and drag at lower Mach numbers, most likely due to limitations of the approximation function used for the Taylor Maccoll equation. Other impact methods either overestimate (inclined wedge W+F) or underestimate (tangent cone W+F) the lift and drag coefficient at lower Mach numbers. Overall, the inclined wedge (wing) and interpolated tangent-cone (fuselage) methods are most appropriate with varying Mach numbers. Below Mach 2.5, all impact methods start to diverge significantly from the validation data, whereby both lift and drag coefficients start to be significantly overestimated. This is due to the limitations of impact theory and impact models. At lower supersonic Mach numbers, the flow can no longer be described by impact flow and the lift and drag coefficients of each of the impact models tend to infinity at $Mach = 1$ [-].

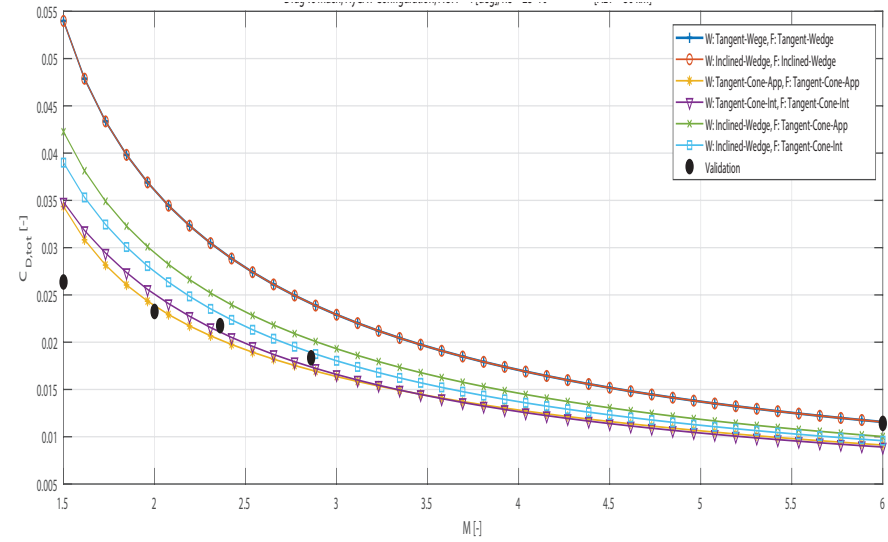
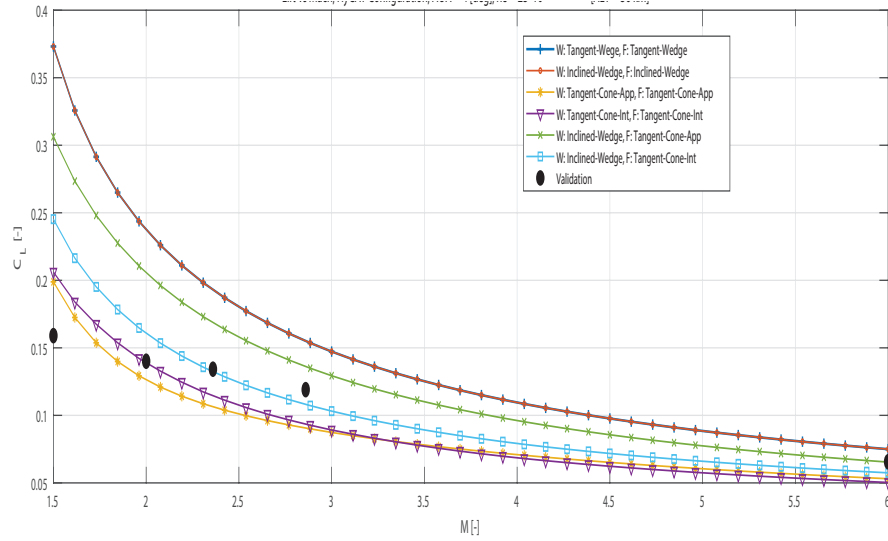


Figure 120: Lift and Drag coefficient vs Mach number for AOA = 4 [deg], ALT = 36 km.

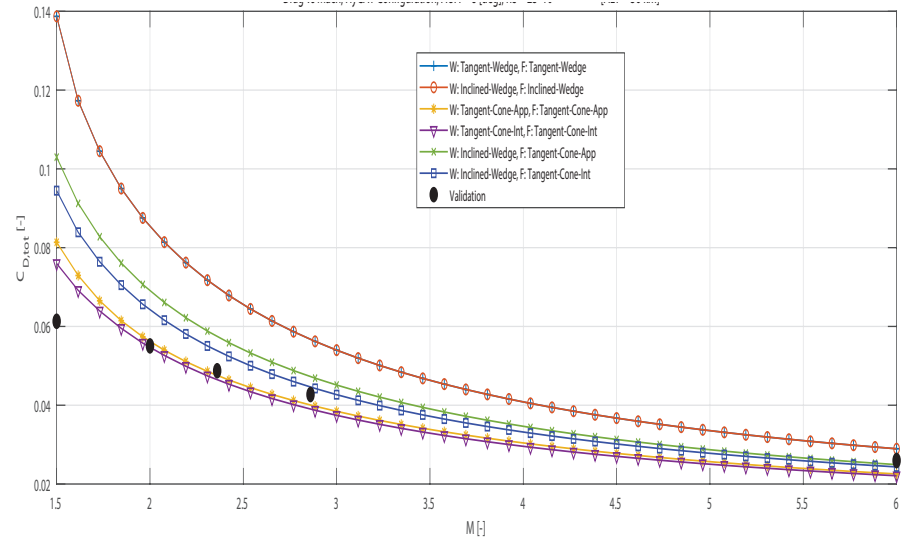
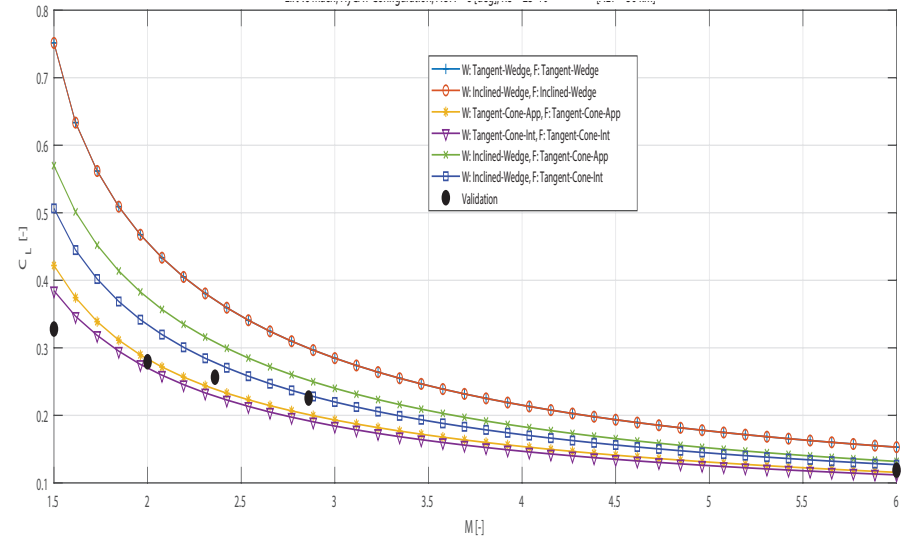


Figure 121: Lift and Drag coefficient vs Mach number for AOA = 8 [deg], ALT = 36 km.

16. Thermal solver

In this section, the viscous-thermal solver implemented in this thesis is validated using experimental data for hypersonic flow over plates, wedge and cones geometries.

16.1. Flow over plates, wedge and cones

For the validation of the viscous flow computations, the results from the paper “Comparison of Engineering Correlations for Predicting Heat Transfer in Zero-pressure-gradient Compressible Boundary Layers with CFD and Experimental Data” by K. Higgins [53] are used. In Appendix F, the local Stanton number C_H over a flat plate and conical section in hypersonic flow are compared to the experimental validation data from Goyne et al. and Chien [45] [24]. From this initial validation, it is concluded that the Eckert and Van Dries models are the most accurate for computing viscous flow over flat plates and cone sections.

In this section, the validation of the semi-empirical models are further expanded on using the results of [53] for viscous flow on a flat plate, wedge and cone. In the analyses reported by [53], laminar and turbulent CFD models are used on a flat plate, 10[deg] wedge and 10[deg] semi-apex angle cone at a Mach number of 8 [-] and an altitude of 35 km. These particular freestream conditions were implemented by [53] as they provide conditions that could be encountered in a typical hypersonic flight and specifically for the Hypersonic International Flight Research Experimentation (HIFiRE) program from the University of Queensland, Australia.

For these models, a 1 meter long flat plate, wedge and cone are modelled with 100 panels distributed along their length. A Reynolds analogy factor of $R_f = 1.1$ is used for the turbulent flow and in all cases the wall temperature is fixed at a value of 300K according to [53]. For the turbulent flow predictions, the CFD results from [53] use the Menter-SST turbulence model to predict convective heat transfers and local friction coefficient at the wall.

The results of the CFD analyses from [53] and the implemented semi-empirical viscous flow models for both laminar and turbulent flow conditions over a flat plate in hypersonic flow are presented in Figures 122 and 123. These plots compare the differences between CFD and semi-empirical methods in terms of the local friction coefficient c_f and convective heat transfer q_{conv} at the wall of the flat plate. Looking at the laminar flow results, it can be seen that the semi-empirical (laminar) Eckert method fits very well with the CFD data for both local friction coefficient and convective heat transfer. For turbulent flow, the Spalding and Chi model underestimates the local friction coefficient in comparison to the CFD data but provides an excellent fit for the local convective heat transfer. The turbulent Eckert and Van Dries methods on the other hand overestimate both friction coefficient and heat transfer over the plate. The Van Dries method predictions show the greatest overestimation of friction and heat transfer over the plate. As a result for a flat plate in this case, the Eckert method is preferable as it provides a conservative estimation of local friction coefficient and heat transfer while keeping a reasonable overestimation of both terms over the plate.

Additionally the CFD results from [53] provide an estimation of the total heat transfer per unit width (equation 16.1) over the flat plate in laminar and turbulent flow for Mach numbers ranging from 5 to 10 at an altitude of 35 km. The results of the CFD are compared to the implemented semi-empirical models as given in figure 124. Once again, the laminar Eckert model provides a good fit over all Mach numbers, especially at lower Mach numbers (from 5 to 8). For the turbulent flow, both turbulent Eckert and Van Dries models overestimate the total

heat transfer. The Spalding and Chi method provides a very good fit at lower Mach numbers ($5 \leq M \leq 8$) but underestimates the total heat transfer at higher Mach numbers. Overall, the turbulent Eckert model provides a conservative total turbulent heat transfer over a flat plate without excessive overestimation and would thus be the preferable model.

$$Q_{tot,unit} = \int_{x=0}^{x=1} q_{conv}(x) dx \quad (16.1)$$

Finally, [53] provides the turbulent heat transfer over a 10 [deg] wedge and cone obtained from CFD analyses at Mach number of 8 [-] and 35 km altitude. The CFD and implemented semi-empirical results for this case are given in figure 125. To compute the inviscid flow properties for the wedge and cone models, the inclined wedge and interpolated Taylor Maccoll equations presented in Section 11.1 are used. As was previously observed, the turbulent Eckert and Van Dries methods over-estimate the local turbulent convective heat transfer over both the wedge and cone. The Spalding and Chi model provides a much better fit in both cases, even-though it underestimates the heat transfer near the leading edge of the cone ($x < 0.1[m]$). The turbulent Eckert model overestimates the heat transfer over both wedge and cone but slightly less than the Van Dries model.

From the analysis of all the validation studies presented, the Eckert model is deemed most appropriate for the computation of both local friction coefficient, c_f , and local convective heat transfer, q_{conv} . In general, the Eckert model provides a conservative estimation of the viscous flow over plates, wedges and cones while keeping an acceptable overestimation of local properties in comparison to the Van Dries method. Since the prediction of laminar to turbulent flow transition is very hard to estimate in reality, for a conservative estimate of viscous flow, the turbulent Eckert semi-empirical model (over the complete configuration) is chosen as the preferred model.

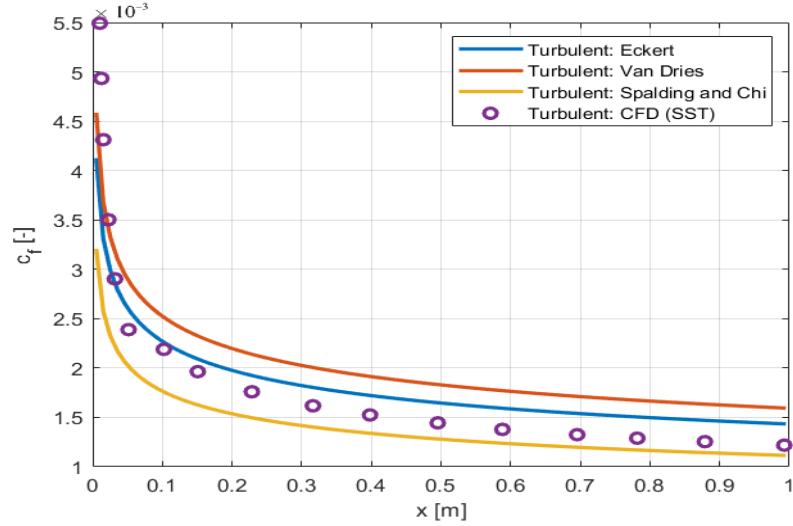
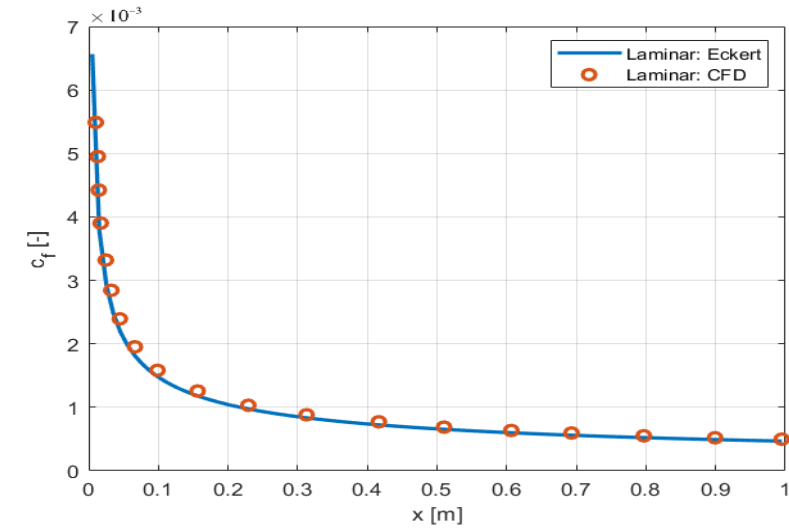


Figure 122: Laminar (top) and Turbulent (bottom) local friction coefficient c_f over flat plate at $M = 8$ [-] and altitude of 35 km.

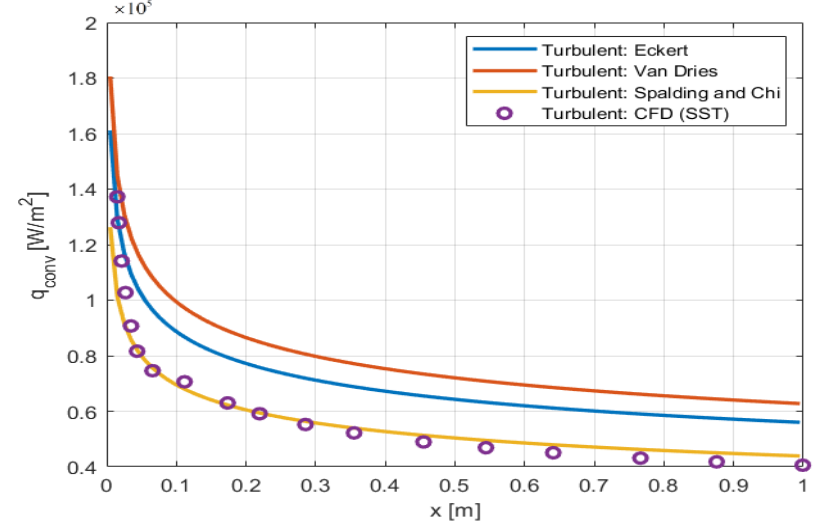
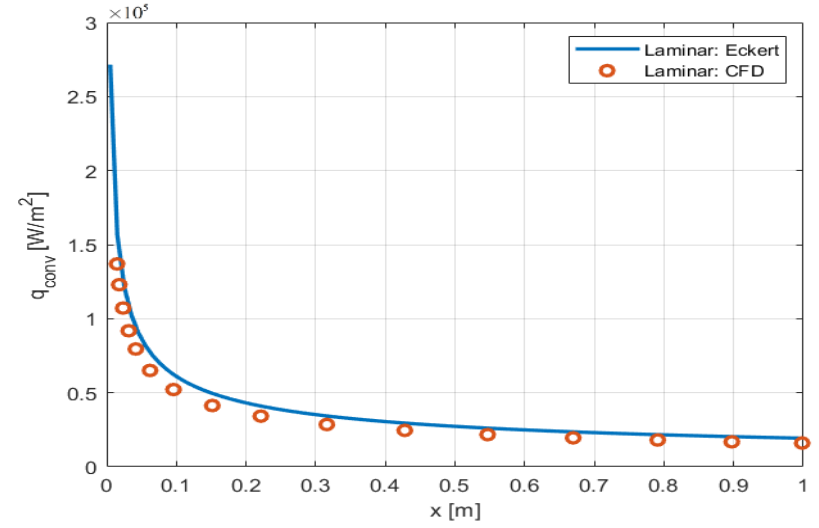


Figure 123: Laminar (top) and Turbulent (bottom) local convective heat transfer q_{conv} over flat plate at $M = 8$ [-] and altitude of 35 km.

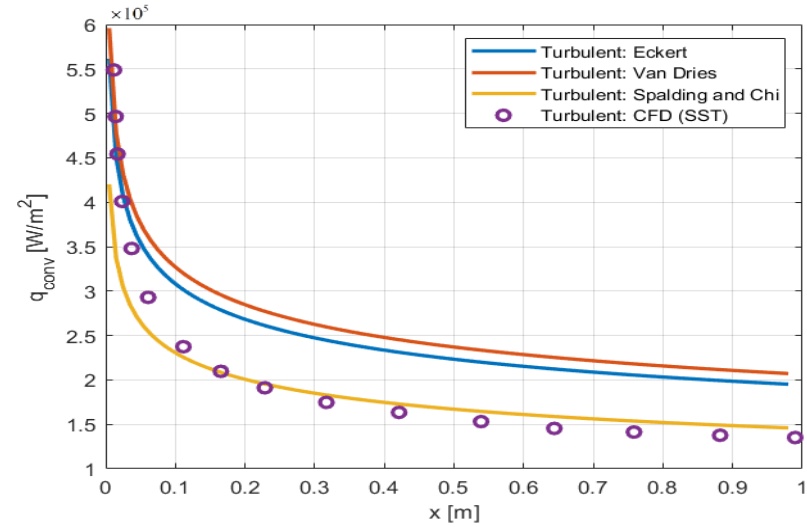
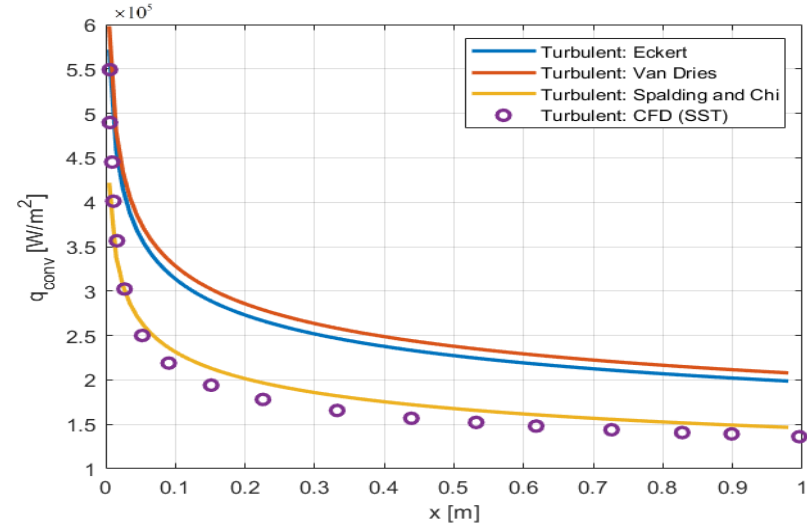
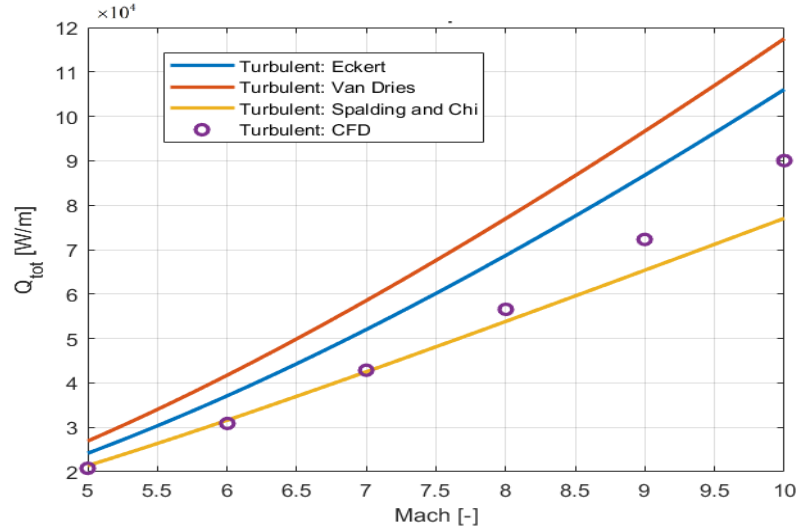
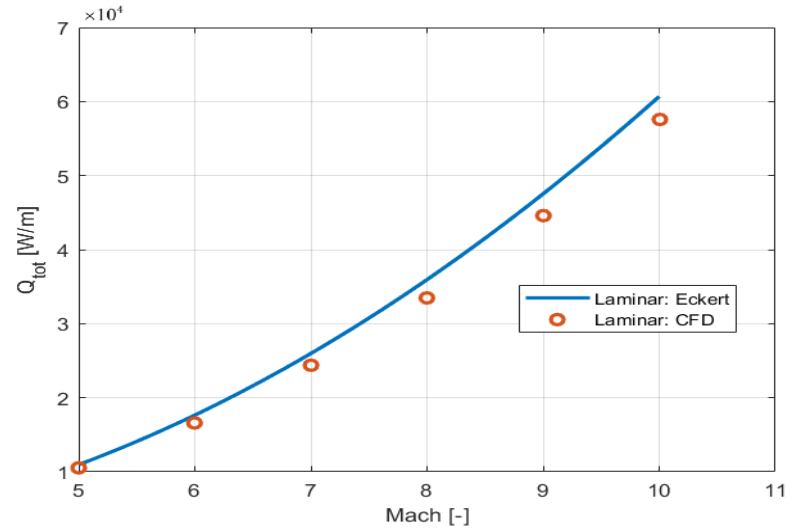


Figure 124: Total laminar (top) and turbulent (bottom) convective transfer $Q_{tot,unit}$ (per unit width) over a flat plate in hypersonic flow as a function of the freestream Mach number and at fixed altitude of 35 km.

Figure 125: Local turbulent convective heat transfer q_{conv} over a 10 degrees wedge (top) and cone (bottom) at $M = 8$ [-] and altitude of 35 km.

16.2. TPS Unsteady heat transfer balance verification

For the validation of the TPS sizing code, the case studies undertaken in the paper: “Integrating Aeroheating and TPS into Conceptual Reusable Launch Vehicle design” [25] have been replicated. The code developed by [25] for dynamic TPS sizing is very similar to the one implemented in the MDO platform in the sense that the same boundary conditions have been applied at the surface and back wall. The code also aims to size (1D) TPS thicknesses for minimum TPS unit mass subjected to maximum surface and back wall temperatures. For convective heat transfer, the tool presented in [25] makes use of the Eckert reference enthalpy method over a surface and Fay-Riddell model for stagnation heating.

Out of the case studies undertaken by [25], two have been replicated here for verification purposes. The first case study aims at verifying that steady state can be achieved if radiation is allowed on the material back face. The second case study provides a proof of concept for a trajectory based transient analysis on a spherical-cone in a hypersonic descent trajectory. For both cases, the material under consideration is a Reinforced Carbon-Carbon (RCC) tile, for which the material and model properties are given according to Table 9.

Table 9: Case studies properties [25].

Property	Value	Unit
Material	RCC	[-]
Density (ρ)	1580	[kg/m ³]
Specific Heat (C_{spe})	0.77	[kJ/kgK]
Thermal Conductivity (k)	4.3	[W/mK]
Emissivity (ϵ)	0.8	[-]
Radiation temperature (T_∞)	0	[K]
Initial material temperature (T_0)	300	[K]
Maximum operating temperature (T_{max})	1900	[K]

For the first case study, a 0.1016 m thick RCC tile is exposed to a 200,000 [W/m^2] convective heat input for 2000 seconds. In this case, a radiation equilibrium back wall condition is applied as given by equation 16.2, instead of the adiabatic wall condition (previously given in equation 13.4). This is done to investigate whether the TPS model can reach steady state. The numerical form of the back wall condition applied in this case is given by equation 16.3.

$$\left(-k_{mat} \frac{dT}{dx}\right)_{BW} = \epsilon \sigma (T_{BW}^4 - T_\infty^4) \quad (16.2)$$

$$T_N^n = \left(1 + \frac{2(\tau)_{T_N^{n+1}} \Delta t}{\Delta x^2}\right) T_N^{n+1} - \left(\frac{2(\tau)_{T_N^{n+1}} \Delta t}{\Delta x^2}\right) T_{N-1}^{n+1} + \left(\frac{2(\tau)_{T_N^{n+1}} \Delta t}{k_N \Delta x}\right) \cdot \epsilon \sigma \left[(T_N^{n+1})^4 - T_\infty^4\right] \quad (16.3)$$

The results of the first case study simulation are given in Figures 126 and 127 for a time step of 1 second and 100 nodes equispaced throughout the TPS insulation thickness. As can be seen in figure 127, both surface and back wall temperatures reach steady state near the end of the simulation, reaching temperatures of 1400 K and 800 K respectively. Also, as can be observed in

Figures 126 (bottom) and 127, the back wall temperature lags behind the surface temperature which can be expected due to the time needed for heat to reach the lower surface of the TPS. Looking at the different heat transfers, it can be observed that all transfer modes reach steady state near the end of the simulation. Surface conduction decreases with time whereas surface radiation increases due to the rise in surface temperature of the tile. Since the top surface is exposed to the incoming convective heat, surface radiation (about $175,000 [W/m^2]$ at $t = 2000s$) is much higher than the back wall radiation (about $20,000 [W/m^2]$ at $t = 2000s$). If compared to the verification study presented in [25], the result obtained are near identical.

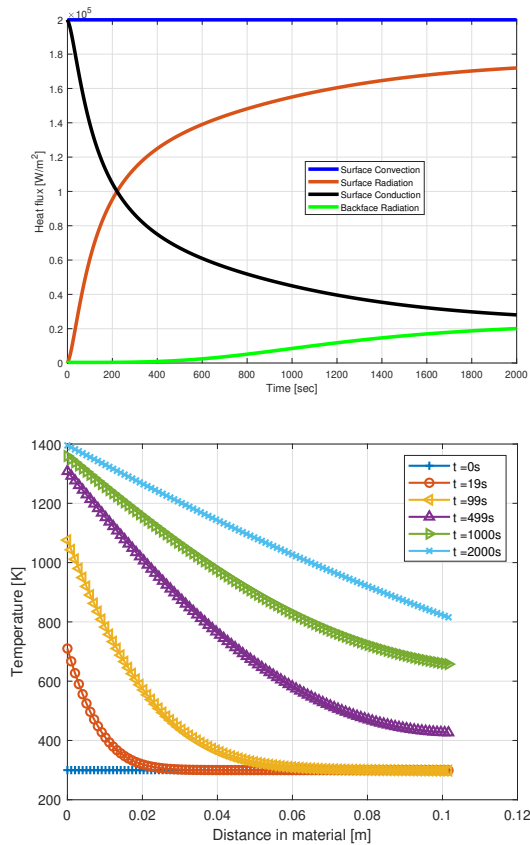


Figure 126: Case 1: Heat transfer modes (top) and temperature through material thickness (bottom) during simulation.

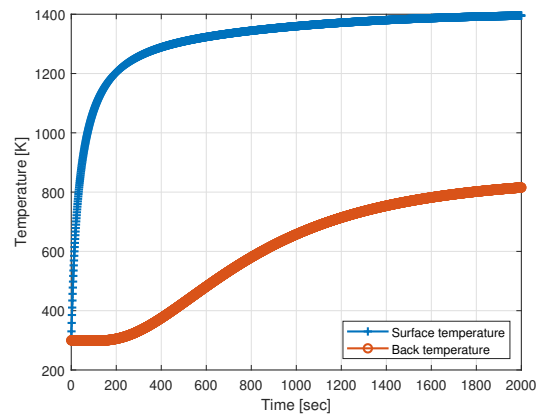


Figure 127: Case 1: Temperature at surface and back wall during simulation.

For the second case study, the typical convective heat transfer over a spherical-cone (figure 128) during a hypersonic descent trajectory is used as input to the simulations. In this case, the convective heat transfers on the Windward side ($S = 0.925$ m from the leading edge on the bottom surface of the spherical-cone) and Leeward side ($S = 0.925$ m along the top surface) are used as inputs. To replicate the case study of [25], the convective heat transfers on the windward and leeward tiles were sampled and used as input to the simulations. This time the usual adiabatic wall condition is employed (equation 13.4) with a time step of 5 seconds and 11 nodes running through a TPS thickness of 0.155 m.

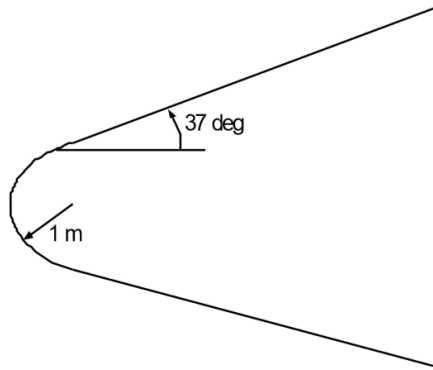


Figure 128: One meter nose radius, 37 degrees inclination [25].

The results of the simulations are displayed in Figures 129 and 130 for the Windward tile and figure 131 and 132 for the Leeward tile. The first thing to be noted is that the results obtained are near identical to the ones from [25] for the same convective heat inputs, thereby confirming that the TPS model has been correctly implemented.

When observing the results from the windward and leeward tile, it can be observed that around $t=1400s$, the surface conduction drops below zero. This behaviour is normal as it indicates that at this point of the simulation the material surface temperatures are higher than the flow field, thereby leading to radiation surpassing the incoming convective heat flux, resulting in the surface rejecting some heat back to the outside environment. The surface temperature in both simulations adapts almost instantaneously to changes in convective heat transfer, whereas as expected, the back wall temperature lags behind. The back-wall temperature continuously increases in these simulations and does not reach steady state due to the lack of a heat sink model as a result of the conservative adiabatic wall condition.

For the windside, maximum surface and back wall temperatures reach approximately 1300 K and 600 K respectively. On the other hand, the maximum temperatures on the leeward tile only reach approximately 575 K and 360 K for the top surface and back wall respectively. This is expected since the leeside, which is mostly in expansion flow, undergoes much lower convective heat transfers throughout the trajectory. These results indicate that if a back-wall temperature of around 400 K is desired, the windward tile thickness should be increased whereas the leeward tile should be made thinner. This highlights the strong need for the implementation of the TPS sizer in the current platform to ensure proper sizing of the protection system.

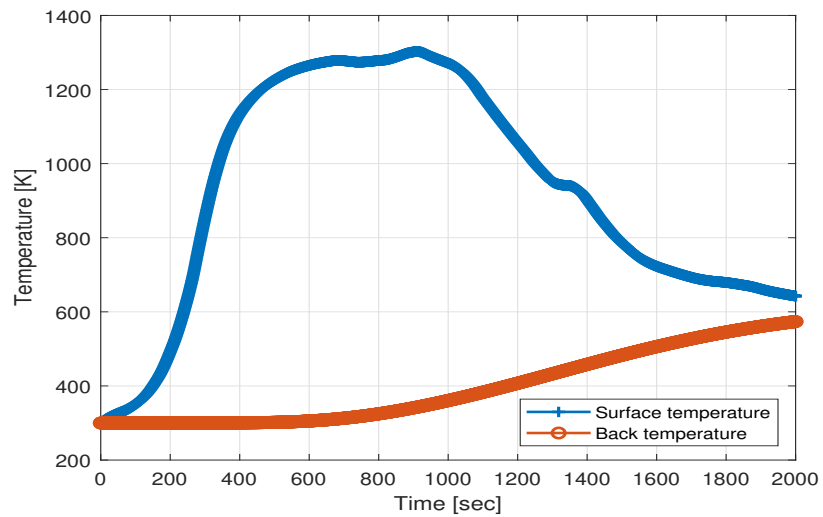
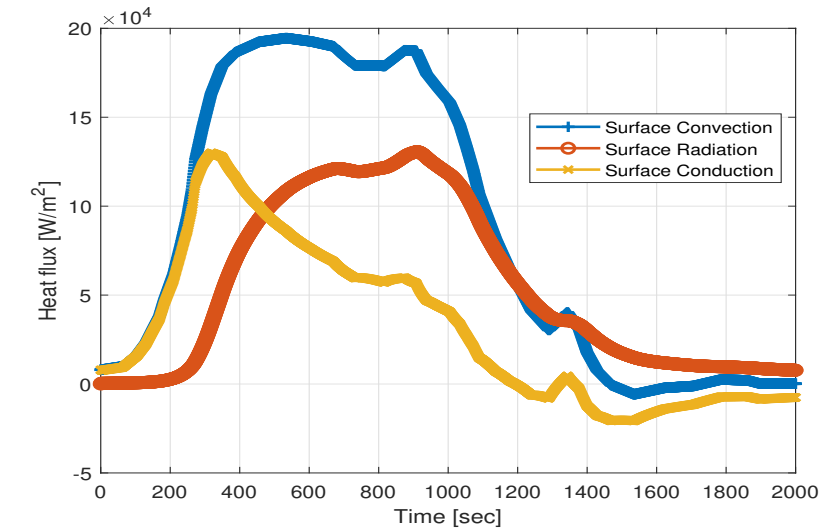


Figure 129: Case 2 (Windside): Heat transfers (top) and temperature at surface and back wall (bottom) during simulation.

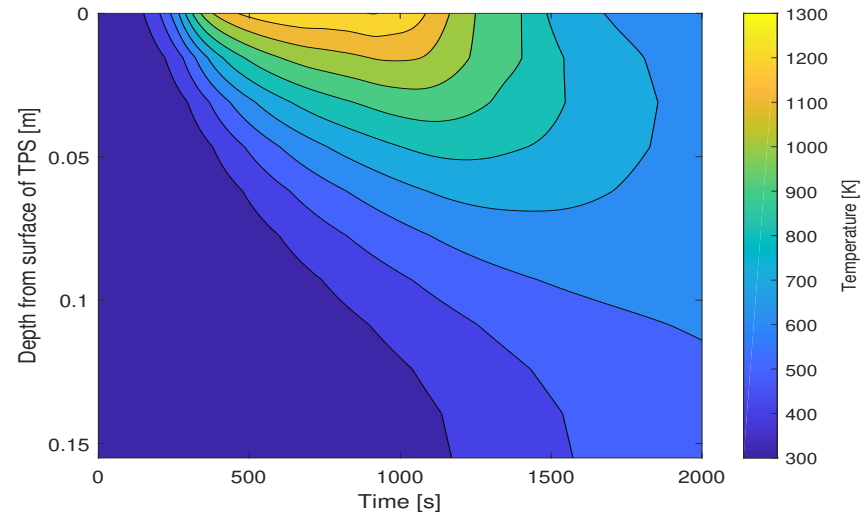
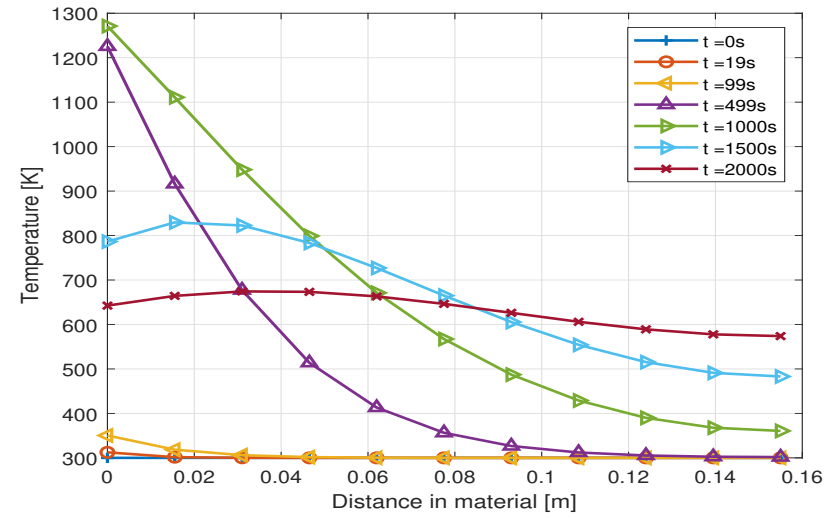


Figure 130: Case 2 (Windside): Temperature through material at specific times (top) and exact temperature distribution map in TPS (bottom) during simulation.

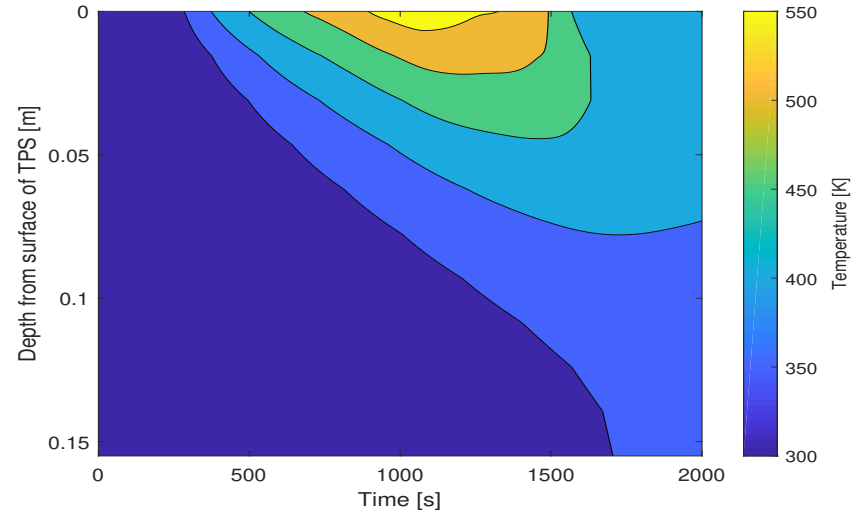
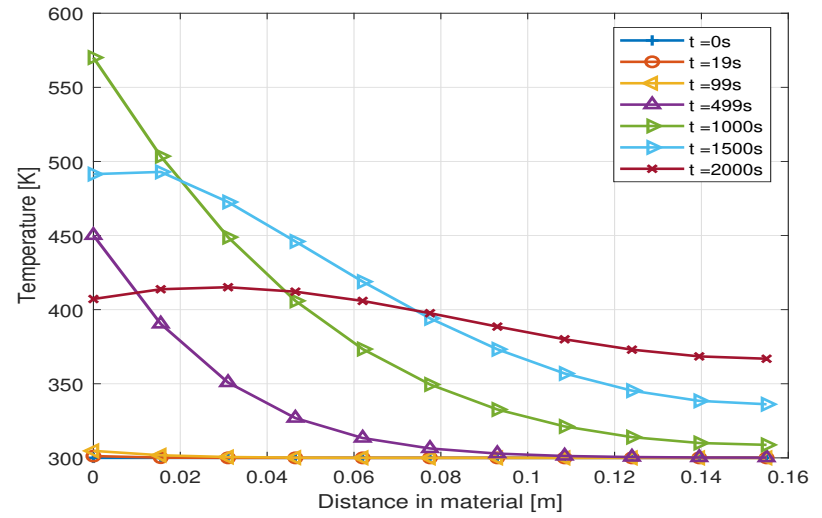
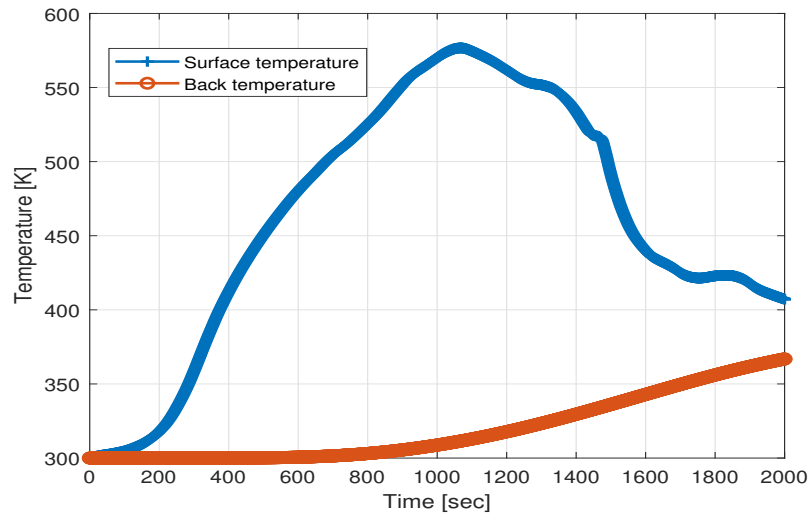
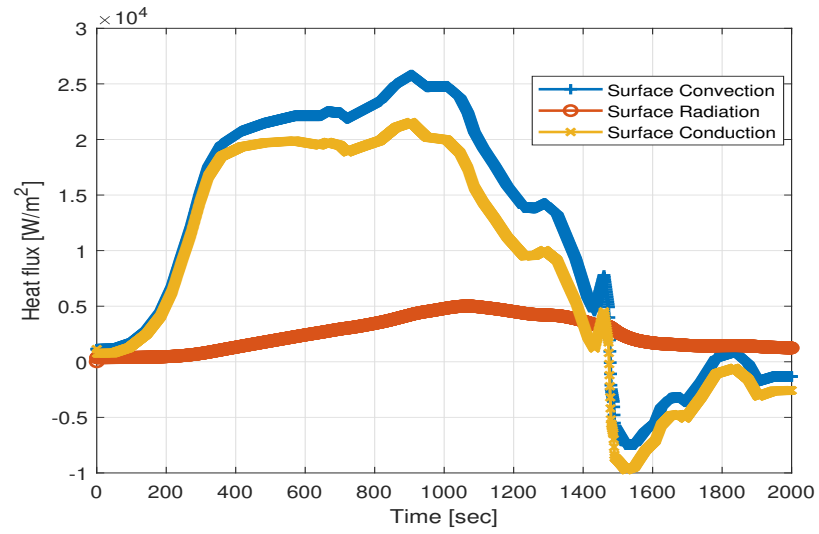


Figure 131: Case 2 (Leeside): Heat transfers (top) and temperature at surface and back wall (bottom) during simulation.

Figure 132: Case 2 (Leeside): Temperature through material at specific times (top) and exact temperature distribution map in TPS (bottom) during simulation.

Part IV.

Results

In this part, the results obtained using the developed optimal sizing platform are given. Firstly, the LAPCAT A2 wing-body configuration used as the baseline design for sizing is described. The settings and optimisation problem formulation are described in this first section along with the optimal sizing of the baseline configuration. The effects of range on the optimally sized configuration and impact of the cruise Mach number for a fixed range on the baseline configuration are then studied.

17. Case study: LAPCAT A2 aircraft

17.1. Baseline configuration

In order to test the hypersonic cruiser aircraft sizing platform developed in this thesis research, the LAPCAT A2 Mach 5 configuration is used as a baseline. The Long-Term Advanced Propulsion Concepts and Technologies (LAPCAT) projects started in 2005 and consist of 12 partners with the European Space Research and Technology Centre (ESTEC), responsible of coordinating research activities [93] [97]. The aim of the project involves the assessment of propulsion and aircraft concepts required for hypersonic long range flights. Out of the different hypersonic vehicles proposed in the LAPCAT-I project phase, only a few were kept in the second phase (LAPCAT-II).

Out of the second phase of the LAPCAT projects, one of the most promising long range configurations is the LAPCAT A2. This conceptual vehicle was designed for a cruise Mach number of 5 and a capacity of 300 passengers. The A2 is proposed as a horizontal take-off and landing vehicle designed to fly from Brussels to Sydney in about 4 hours using liquid hydrogen-fuelled engines [112].

The LAPCAT A2 configuration is shown in Figure 133 and compared to the Airbus 380 aircraft. The configuration is composed of a slender fuselage and a trapezoidal wing of low aspect ratio positioned near the fuselage mid section. Additionally, the LAPCAT A2 possesses canard and vertical tail surfaces. The canard present near the fuselage nose is controlled as an all-movable surface in pitch and provides control over the aircraft longitudinal attitude. All aerodynamic surfaces use a 3% thick airfoil [126]. Due to the low energy density of liquid hydrogen, a very large internal volume is required to store the fuel required. This explains the very long length of the configuration in comparison to an aircraft such as the A380. A fuselage diameter of 7.5 meters has been assigned in the LAPCAT A2 configuration as an attempt to reduce fuselage mass with an acceptable value of wave drag. The LAPCAT A2 uses four precooled turbojet engines for its propulsion system called Scimitar [97].

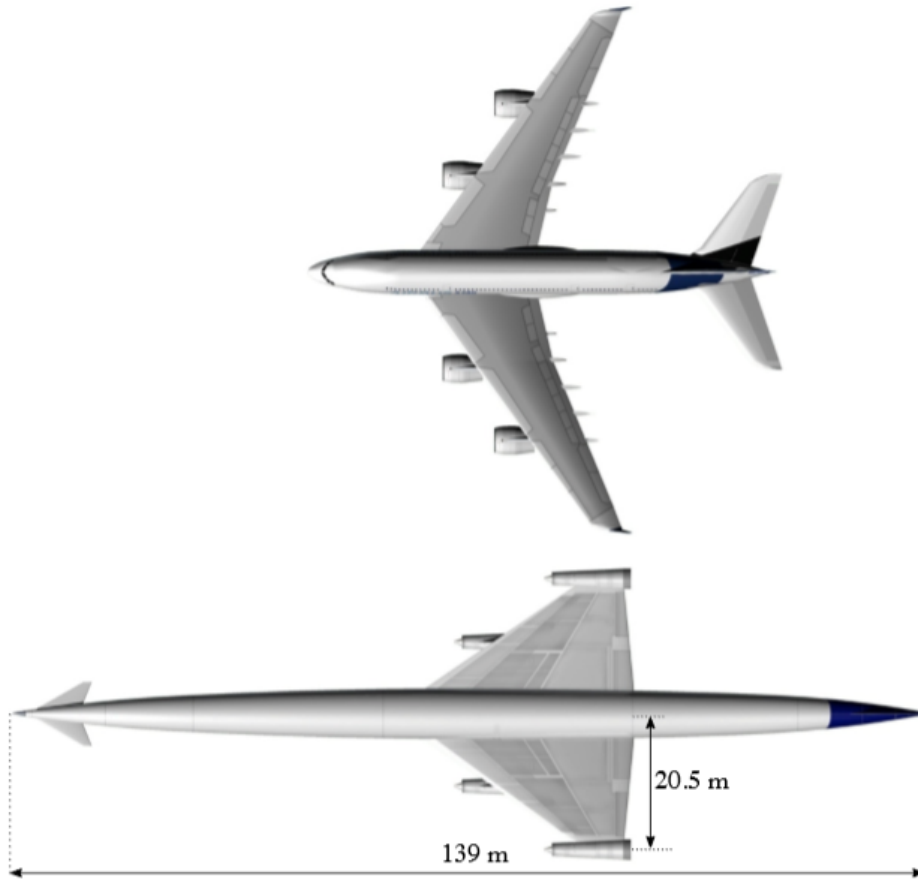


Figure 133: The LAPCAT A2 vehicle (bottom), compared with the Airbus A380 (Steelant,2008).

Figure 134 summarises the configuration main features as estimated by [112] [93]. The estimated take-off mass for the configuration is 400 tonnes with an empty mass of 202 tonnes leading to a fuel fraction of 49.5%. The aircraft is designed for a range of 18700 km and cruises at Mach 5 between altitudes of 25 to 28 km. A payload of 300 passengers was selected for this configuration as it is thought to be the minimum capacity required to achieve a competitive seat-km cost for a hypersonic cruiser [93].

Characteristic	Value
MTOW [ton]	400
Empty weight [ton]	202
Overall Length [m]	139
Wing span [m]	41
Gross wing area [m ²]	900
Passengers [-]	300
Design range [km]	18700
Cruise altitude [km]	25 – 28

Figure 134: LACPAT A2 vehicle properties from [93].

The great circle route was initially selected for the LAPCAT A2 design mission. The great

circle trajectory between Brussels and Sydney covers a distance of 16734 km and is displayed in figure 135. The LAPCAT studies however indicated overpressures of 85 Pa and 70 Pa on the ground track during ascent and cruise phases respectively. A limit overpressure of 50 Pa is set for typical flights over populated areas which led to the choice of an alternative mission route for the LAPCAT A2 configuration [112]. The alternative route devised for the LAPCAT A2 is 18728 km in length and is displayed in figure 136. This new route avoids populated areas and is found to be the minimum alternative distance between Brussels and Sydney [112]. By passing over the north pole and pacific ocean, the aircraft is capable of travelling at hypersonic speed during most of its mission, leading to shorter flight times.

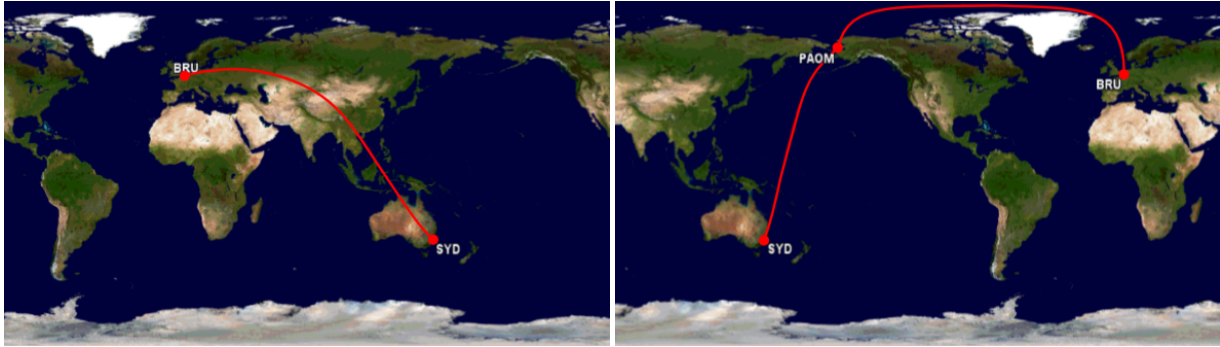


Figure 135: Great circle route for Brussels-Sydney (16734km). Figure 136: Alternative route for Brussels-Sydney (18728km).

A schematic of the LAPCAT A2 cryogenic tanks and passenger bay is given in figure 137. The internal volume of the aircraft is occupied by two tanks (in blue) separated by a passenger cabin. The first tank starts at 9.3% of fuselage length while the second tank ends at 91% of the length. The passenger cabin occupies a length of 31.6 meters in the baseline configuration and is located in the cylindrical part of the aircraft. The fuselage front and back sections have the shape of an ogive and constitute 44.8% and 32.5% of the fuselage length. All cross sections of the fuselage are circular in the baseline configuration.

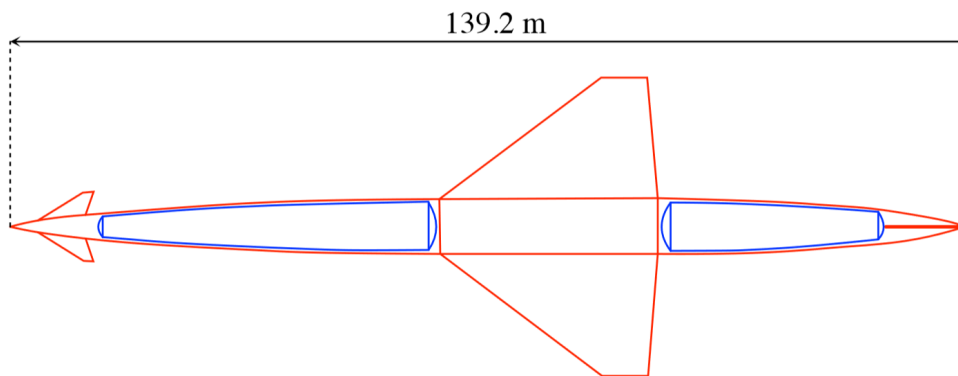


Figure 137: Schematic of LAPCAT A2 configuration, top view with cryogenic tanks [93].

The properties of the main wing, vertical fin and fuselage for the baseline configuration are given in Table 10. The vertical fin properties have been approximated from the three-view drawing of the LAPCAT configuration. The moment arm length for the vertical tail is taken as the distance between the quarter chord of the vertical tail and main wing mean aerodynamic chords. The process for vertical tail surface area estimation and sizing is described in more detail in Appendix G.

Table 10: Geometrical properties of LAPCAT A2 baseline configuration

Property	Value	Unit
Main wing		
Semi span	20.5	[m]
Taper ratio	0.166	[-]
Aspect ratio	1.868	[-]
Leading edge sweep	55	[deg]
Surface Area	900	[m^2]
Twist (tip)	0	[deg]
Vertical fin		
Leading edge sweep	59.85	[deg]
Aspect ratio	1.102	[-]
Taper	0.1829	[-]
Moment arm length (l_{vt})	60.49	[m]
Vertical tail sizing coefficient (C_{vt})	0.076	[-]
Surface area	46.34	[m^2]
Fuselage		
Total Length	139.2	[m]
Front nose ogive fraction	44.8	[%]
Cylinder section fraction	22.7	[%]
Rear ogive fraction	32.5	[%]
Maximum Diameter	7.5	[m]
Start of fuel tank	9.3	[%]
End of fuel tank	91	[%]

In order to run the sizing platform on the baseline aircraft, several settings must be provided. Table 11 provides a summary of the settings used in the optimisation platform for the LAPCAT A2 configuration. Firstly, the mission altitude and Mach number as a function of time are set to the mission profile given by [93] for the LAPCAT A2. These profiles have been previously given in Figures 39 and 40 of Section 8. The mission lasts for 4.6 hours and results in a total of 18771 km range (according to the alternative Brussel-Sydney route). For the viscous-thermal flow model, the semi-empirical Eckert reference enthalpy method is used. This model is set because it provides the best conservative estimates of local friction coefficient and convective heat transfer as was concluded from the validation in Section 16. The flow over the model is assumed to be turbulent over the entire configuration to yield a conservative estimate of viscous flow and since no accurate transition model exists as was discussed in Section 16.

The fuel is stored in the fuselage body and is fixed to start and end at 9.3% and 91% of the fuselage length according to the baseline configuration. The TPS type chosen in the platform is the silica based aerogel SiO_2TiO_2 , where the TPS unit mass to heat load correlation is given according to Figure 83 as given in Section 13.2. An aluminium load bearing sub-structure is selected with a temperature of 400 Kelvin (TPS back wall temperature constraint), leading to a modifying factor of about 1 (see figure 87). For the hypersonic inviscid flow analysis ($M_\infty > 3$), the inclined wedge method is used for the wing and the interpolated Taylor Maccoll tangent-cone method is employed for the fuselage body (see Sections 11.1). These methods have been selected since they provide the best estimate of lift and drag coefficients as well as local pressure coefficient for varying freestream Mach numbers and angles of attack as was concluded in the validation Section 15.3. For the engine model, the liquid hydrogen Generic Hypersonic Aircraft

engine model (GHAME) is used and was defined in Section 12. The baseline LAPCAT A2 configuration possess a 3% thick airfoil section [126]. The airfoil sections in the platform are modelled as biconvex airfoils.

Table 11: Modelling setting parameters for platform

Setting	Value
Input Mission	Given in figures 39 and 40 (see Section 8)
Viscous semi-empirical model	Eckert reference enthalpy
Transition model	Flow assumed turbulent over entire surface
Fuel storage	Fuselage
TPS type	SiO_2TiO_2
Sub-structure material	Aluminum
Hypersonic impact method (wing)	Inclined Wedge
Hypersonic impact method (fuselage)	Interpolated Taylor Maccoll
Fuel Type	Liquid Hydrogen (no oxidizer)
Engine type	GHAME
Wing Airfoil	Biconvex (3% thickness/chord ratio)
Fuselage cross sections	Circular

In Table 12, the constant values set for the optimal sizing are given. The number of passengers is set to 300 according to the LAPCAT A2 baseline configuration, leading to a payload mass of 31,350 kg (based on an assumed passenger unit mass of 82 kg and luggage mass of 22.5 kg according to [100]). The LAPCAT A2 baseline configuration assumes a payload mass of 32,000 kg [112] (2% difference). The fuel density for liquid hydrogen is taken at a pressure of one bar according to the value given in [93]. The tank density for liquid hydrogen is taken from WAATs [44] which is based on the X-15 hydrogen tanks.

An ultimate load factor of 2.5 is applied for the fuselage and wing structural mass computations (equations 14.1 and 14.4). This load factor value has been chosen according to the one previously used to model the LAPCAT A2 internal structure [93]. The emissivity used to calculate the convective heat transfers and TPS masses is set of 0.8 as recommended by [93]. A payload density of $50[kg/m^3]$ is used and has been set according to the value of the 200 passenger horizontal take off hypersonic transports presented in HASA. In HASA, four 200 passenger hypersonic transport aircraft are presented, namely the HyCAT-1, HyCAT-1A, HyCAT-4 and Rockwell vehicle, each with a payload density of about $50[kg/m^3]$ [51]. This payload density value yields a required payload volume of $V_{pay,req} = 626[m^3]$. Finally, to generate a smooth geometry, a total of 30 equispaced circular cross sections were generated along the length of the fuselage.

Table 12: Constant values associated with Baseline configuration

Property	Value	Unit
Number of Passengers	300	[-]
Fuel density (Liquid Hydrogen @1bar)	70.847	[kg/m^3]
Emissivity	0.8	[-]
Sub-structure temperature	400	[K]
Payload density	50	[kg/m^3]
Ultimate Load factor	2.5	[-]
Tank density (Liquid Hydrogen)	8.49	[kg/m^3]
Number of mission plateaux defined	9	[-]
Number of Fuselage cross sections	30 (equispaced)	[-]

Additional assumptions:

Due to the nature of the implemented platform, a few additional assumptions have been specified in the sizing problem to adequately deal with the limitations of the current model and can be summarised as follows:

- The wing quarter chord is placed automatically at the same fuselage fraction as the baseline configuration quarter chord. This is done to ensure that stability is not significantly affected by changes in wing and fuselage shape during optimal sizing.
- The mission is discretised using 9 plateaux (Figures 39 and 40) and the supersonic climb phase is modelled as one single plateau since transonic and low-supersonic regime are dominated by viscous effects and cannot be analysed with the current aerodynamic panel methods. From the sensitivity analysis performed on the LAPCAT A2 mission by [93], increasing the number of mission plateaux from 10 to 20 and 40 yielded near negligible differences in aircraft performance.
- Leading edge sweep is fixed at 55 degrees to ensure a low speed stable vortex generation and low drag rise in transonic/low supersonic regime. This assumption comes from the LAPCAT project which states that: “A leading edge sweep angle of 55 [deg] was chosen as roughly equivalent to the Concorde value and known to be the minimum necessary to generate a stable separated vortex at high angles of attack.” [112].
- The engine mass cannot be estimated with the current platform and is thus kept to a constant value throughout the sizing process. While hypersonic engines mass estimation correlations exist such as the ones provided by WAATs and HASA [44] [51], these correlations are dependent on the maximum air mass flow entering the engine. Since maximum air flow is expected to occur during either take-off or transonic conditions, and these flight phases cannot be analysed with the current panel codes, the engine dry mass is set to that of a similar hypersonic transport aircraft. The chosen aircraft is the HyCAT-1, a Mach 6 hypersonic 200 passenger transport configuration with an estimated take-off mass of 350 tonnes proposed by NASA and powered by a turbo-ramjet engine with a total mass of 28 tonnes [51]. According to [76], engine mass is not expected to vary significantly with changes in vehicle concept which supports this assumption.
- The canard mass is not included as part of the mass estimation calculations. The LAPCAT A2 uses a canard configuration to provide pitch control of the aircraft. As opposed to horizontal tails, the canard is not used to provide longitudinal stability. No equations could be found in literature for the preliminary sizing of hypersonic canard surfaces and thus its

mass is not taken into account. It is however believed that the canard would constitute a very small fraction of the aircraft mass, especially for the LAPCAT A2 configuration, due to the very large fuselage length (and thus long canard moment arm available).

17.2. Optimiser setup

Design variables:

The design variables used for the optimiser are given in equation 17.1. Five variables have been set to control the shape of the main wing while four are used to control the fuselage shape. For the wing, the normalised (with respect to the baseline configuration) wing planform area $F_{S_{wing}}$, Aspect ratio F_{AR_w} , taper ratio F_{λ_w} , wing tip twist angle $\epsilon_{tip,wing}$ (non-normalised) and airfoil thickness to chord ratio $F_{(t/c)_{Airf,w}}$ are set as control variables. For the fuselage on the other hand, the width, height of the upper and lower fuselage sections and overall body length are controlled. In the optimisation process, all the design variables are used as scaling factors with respect to the baseline configuration (with the exception of wing tip twist) according to equation 17.1. The bounds and initial value of these design variables are given in Table 13.

$$\vec{X} = \left[F_{S_{wing}} \quad F_{wing,AR} \quad F_{wing,\lambda} \quad \epsilon_{tip,wing} \quad F_{(t/c)_{wing,airf}} \quad F_{fus,width} \quad F_{fus,height_{up}} \quad F_{fus,height_{lo}} \quad F_{fus,length} \right] \quad (17.1)$$

The design variables used in these optimisation studies have been set such that the platform is capable of capturing the sensitivity of each of these variables in both aero-thermal analysis and mass estimations. More design variables could theoretically be used to optimise the aircraft shape, however, the mass estimation empirical equations used in this platform (Section 14) are based on a simple set of geometrical parameters. In order to ensure the effect of a change in each of the design variables can be captured by the mass estimation equations, the set of design variables for the optimisation have been constrained to the ones given by equation 17.1.

Table 13: Initial value and Bounds of optimisation problem

Design variable	Unit	Lower bound	Initial value	Upper bound
$F_{S_{wing}}$	[-]	0.2	1	3
$F_{wing,AR}$	[-]	0.2	1	2
$F_{wing,\lambda}$	[-]	0.2	1	5
$\epsilon_{tip,wing}$	[deg]	-5	0	5
$F_{(t/c)_{wing,airf}}$	[-]	0.67	1	2
$F_{fus,width}$	[-]	0.2	1	2
$F_{fus,height_{up}}$	[-]	0.3	1	2
$F_{fus,height_{lo}}$	[-]	0.3	1	2
$F_{fus,length}$	[-]	0.2	1	2

Optimisation problem:

For the optimisation, the baseline configuration is optimised for minimum take-off mass W_{TO} , subjected to fuselage fuel volume and height constraints (c). In the implementation of the optimisation code, the optimisation problem objective function and constraints are normalised

with respect to the baseline configuration values according to equation 17.2. In these equations; $W_{TO}(\vec{X}_0)$, $V_{F,req}(\vec{X}_0)$ and $H_{cylinder,fus}(\vec{X}_0)$ represent the value of the objective and constraints evaluated at the initial design point as given in Table 13.

$$\begin{aligned}
\underset{\vec{X}}{\text{minimise}} : \quad & J_{norm}(\vec{X}) = \frac{W_{TO}(\vec{X})}{W_{TO}(\vec{X}_0)} \\
& c_{1,norm}(\vec{X}) = \frac{V_{F,AV}(\vec{X}) - V_{F,req}(\vec{X})}{V_{F,AV}(\vec{X}_0) - V_{F,req}(\vec{X}_0)} \leq 0 \\
\text{st} : \quad & c_{2,norm}(\vec{X}) = \frac{H_{cylinder,fus}(\vec{X}) - H_{cylinder,min}}{H_{cylinder,fus}(\vec{X}_0) - H_{cylinder,min}} \leq 0
\end{aligned} \tag{17.2}$$

For the evaluation of the multi-discipline feasible loop of the design structure matrix (Figure 6), a tolerance of 0.5 kg is set for the take-off mass convergence process such that $|W_{i+1} - W_i| < \Delta_{tol} = 0.5kg$. The problem is bounded by two nonlinear constraints, a fuselage fuel volume and height constraint. The fuselage available volume constraint ensures that the internal volume available for fuel $V_{F,av}(\vec{X})$ in the fuselage geometry between the start and end of the tanks sections is above the fuel volume required $V_{F,req}(\vec{X})$ for the current configuration. To size the payload bay, it is necessary to compute the required length fraction $F_{L,pay}$ of the cabin in the fuselage. This length fraction is obtained by dividing the required payload volume by the cross sectional area of the payload cabin according to equation 17.3. In this equation, H_{cab} , W_{cab} and n_{cab} are the height, width and super-ellipse coefficient of the cabin cross section and Γ is the so-called gamma function [127]. The cabin is set to be positioned at equal (longitudinal) distance in between the fuel tanks. Using this method allows for fast estimation of the length required for the payload bay without the need for calling the geometry CAD modeller (ESP) multiple times. This method may however be limited if the cross section of the payload cabin varies significantly along its length.

The height of the cylinder section of the current fuselage geometry $H_{cylinder,fus}(\vec{X})$ is also constrained to not exceed a minimum height of 2.5 meters ($H_{cylinder,min}$) to ensure passengers are capable of sitting and standing in the cabins.

$$F_{L,pay} = \frac{L_{pay}}{L_{fus}} = \frac{1}{L_{fus}} \cdot \frac{V_{pay,req}}{ACS_{pay}} = \frac{1}{L_{fus}} \cdot \frac{V_{pay,req}}{4 \cdot H_{cab} \cdot W_{cab} \cdot \frac{[\Gamma(1 + \frac{1}{n_{cab}})]^2}{\Gamma(1 + \frac{2}{n_{cab}})}} \tag{17.3}$$

Optimisation algorithm:

The optimiser settings are given in Table 14. The chosen optimisation algorithm is MATLAB's *interior point* which make use of a barrier function and Newton gradient based decent to search for a local optimum. This algorithm was chosen due to its ability to solve large scale problems and it's relatively fast convergence [78]. For the gradient computations, a step size of 1% is used to ensure that a perturbation in any of the design variables leads to a noticeable change in the objective function value (and is not influenced by the MDF tolerance defined in Table 14). The

constraint violation (TolCon) is set to a very low value to prevent unfeasible designs. Finally, the objective function and design variable tolerances (TolFunc and TolX) are set to 0.1% and 0.01% respectively. The value of the objective function tolerance is set to a low value but still large enough not to be influenced by the MDF tolerance value.

Table 14: Settings for optimisation algorithm and MDF tolerance

Setting	Description
Algorithm	'interior-point'
Finite Difference Step Size	0.01
TolX	0.0001
TolCon	0.0001
TolFunc	0.001
MDF tolerance (kg)	0.5

17.3. Results and discussion

In this section, the results obtained using the optimal sizing platform developed in this thesis are given and analysed. Firstly, a mesh convergence study is performed to select the appropriate mesh size needed for sizing. A sensitivity study of the design variables on the estimated mass distribution and aerodynamic performance of the aircraft is carried out. The sizing algorithm is then applied to the baseline configuration to observe and study how the platform behaves. Next, the effects of mission range on the optimal sizing are studied. Finally, the effect of changes in mission Mach number for a fixed range on the baseline LAPCAT A2 configuration are investigated.

17.3.1. Mesh selection

In order to perform the aero-thermal computations during the optimal sizing, a computational mesh is required. To select the appropriate mesh size, a mesh convergence study is carried out in this section. For the convergence study, seven different meshes with a gradually increasing number of panels are investigated. Table 15 provides the properties of the different meshes. The total full mesh sizes (twice the half mesh size) vary from 240 to 6960 panels with the number of elements along the longitudinal and lateral mesh networks gradually increased.

The value of the objective function W_{TO} for each of the different meshes with the computational time required for the function evaluations are given in Table 15. The objective function for the baseline mission is chosen as the mesh convergence criteria as it ensures that the complete platform converges to a single objective value with increasing mesh size.

Table 15: Meshes properties for convergence study.

Property	Mesh 1	Mesh 2	Mesh 3	Mesh 4	Mesh 5	Mesh 6	Mesh 7
Wing lateral	3	4	6	10	15	18	21
Wing longitudinal	6	8	12	20	25	30	40
Fuselage circumference	6	6	8	12	14	16	20
Fuselage front section	5	6	8	12	20	25	30
Fuselage rear section	3	3	5	8	12	15	20
Half mesh size [-]	120	166	344	880	1548	2200	3480
Take off mass [tonnes]	541.88	542.22	546.08	549.94	552.58	552.16	552.16
Computational time [min]	0.82	0.86	1.12	3.13	8.62	18.99	55.85

In Figure 138, the variation of objective function value for each of the meshes under investigation is provided. As can be seen, the objective function value reaches a converged value of 552.16 tonnes for meshes 6 and 7 (2200 and 3480 half mesh sizes). In Figure 139, the computational time required for the evaluation of the objective function for increasing mesh size is also provided. As can be observed, the computational time increases quadratically with the number of mesh panels, reaching a CPU time of 55 minutes for the most refined mesh. The majority of the computational time required is a result of the time required for the higher order PANAIR subsonic code evaluations.

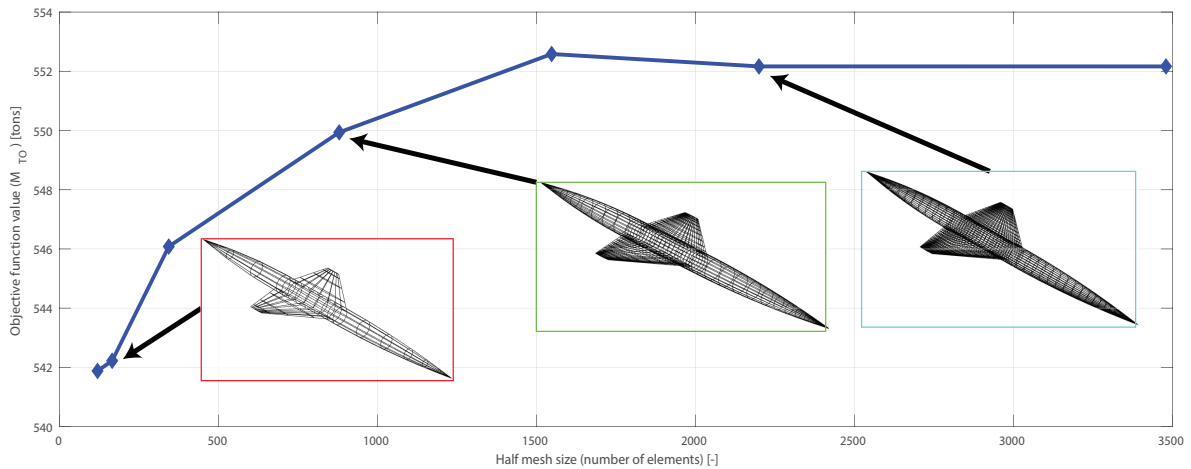


Figure 138: Mesh convergence study.

Since a single objective function evaluation time of 55 minutes would be excessively prohibitive for the optimal sizing algorithm which requires several hundreds of objective function evaluations, mesh 4 (Table 15) is selected as the computational mesh for the optimal sizer. The selected mesh provides a computational time of 3.13 minutes per evaluation making it feasible for optimisation purposes while providing an objective value close to the fully converged objective. Indeed, the difference in objective function value between mesh 4 (549.94 tonnes) and mesh 7 (552.16 tonnes) is only 0.4%.

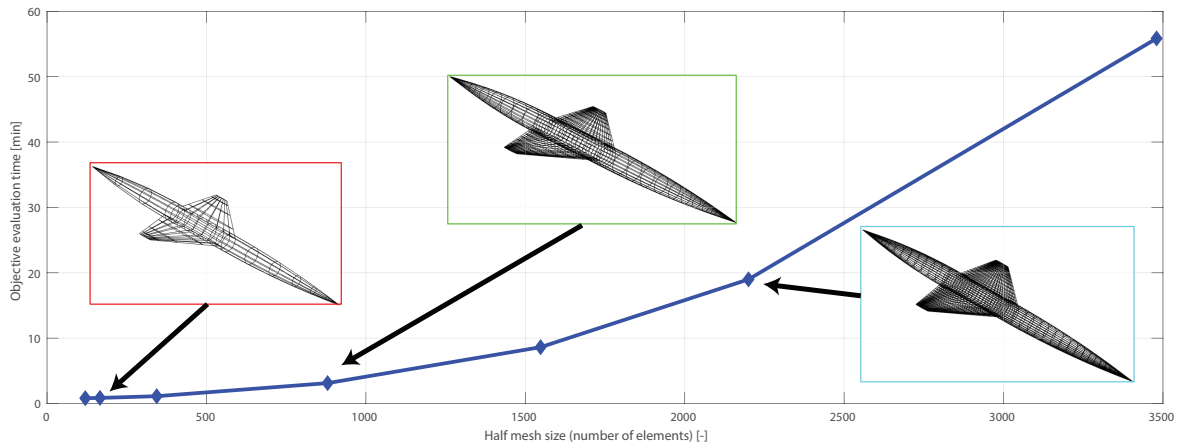


Figure 139: Mesh computational time.

The mesh chosen for the optimisation process is thus provided in Figure 140 with the generated wake networks required for the subsonic solver evaluations.

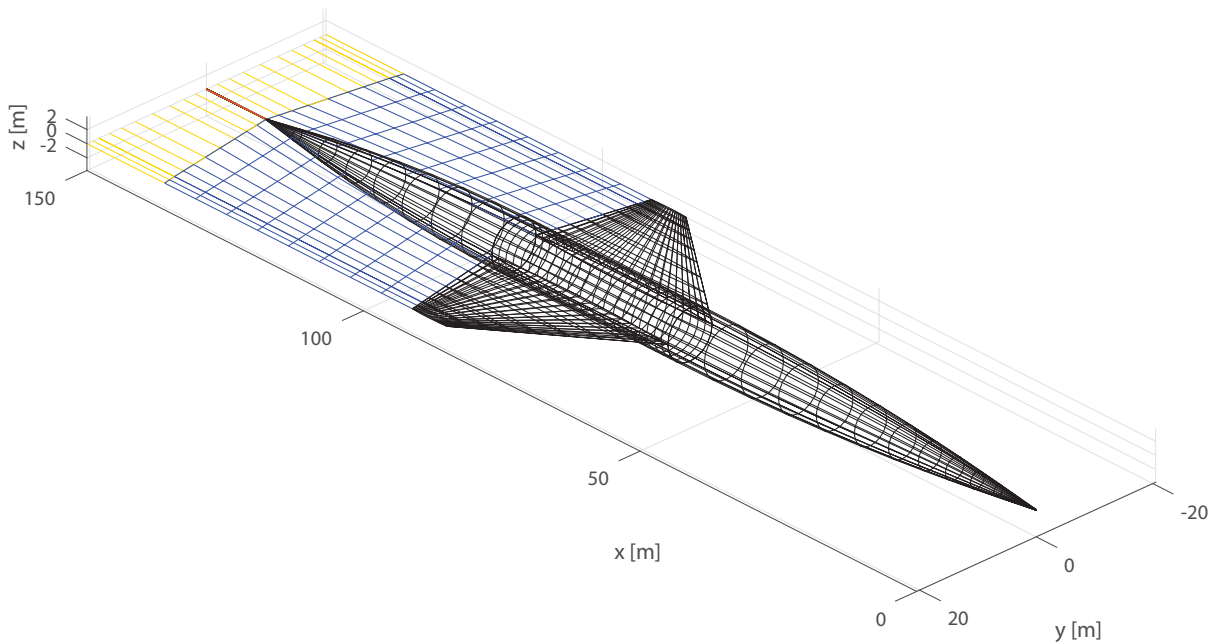


Figure 140: Mesh (4) chosen for optimisation.

17.3.2. Sensitivity of shape variables

Prior to the application of the optimal sizing algorithm, a sensitivity analysis is performed on the design variables. This is done to study the effects of the different shape parameters on the mass performance of the aircraft's main structural components and fuel mass. In addition, the effects on the subsonic and hypersonic cruise condition aerodynamic lift to drag ratios are also considered. In this study, the design variables are individually changed with respect to the baseline configuration. The parameters which have the greatest effect on the aircraft performance are summarised in this section while the effect of other parameters are given in Appendix H. Additionally, in order to support the analysis of the sensitivity of the design variable on aerodynamic performance, Appendix I provides the lift, drag and lift induced drag polars ($C_L - \alpha, C_D - \alpha$ and $C_D - C_L^2$) for each of the perturbed design variables. In this section, the sensitivity of wing

variables are first studied and followed by the sensitivity of fuselage parameters.

To understand the effects of geometrical parameters on the lift to drag ratios it is important to summarise the main sources of drag in subsonic and hypersonic flow. The drag coefficient can be decomposed into lift induced drag ($C_{D,i} = kC_L^2$) and zero lift drag ($C_{D,0}$) which can be further decomposed as the summation of viscous drag ($C_{D,visc}$) as a result of the friction caused by the flow over a surface, zero lift pressure drag ($C_{D,p0}$) and wave drag ($C_{D,wave}$) as given by equation 17.4.

$$C_D = C_{D,0} + C_{D,i} = C_{D,visc} + C_{D,p0} + C_{D,wave} + kC_L^2 \quad (17.4)$$

Wave drag occurs as a result of the pressure drag induced by the presence of shock waves on a body and is thus critical in hypersonic aircraft design. In subsonic conditions (lower than the critical Mach number), the wave drag does not play a role. The viscous drag coefficient is often related to an equivalent skin friction drag coefficient C_{fe} in the form given by equation 17.5. Since the equivalent skin friction drag coefficient is fairly constant, the total aircraft wetted area to platform area S_{wet}/S_{ref} has the most effect on the viscous drag coefficient [107]. Lift induced drag is affected by the coefficient k in equation 17.4. This coefficient is related to the wing aspect ratio AR and Oswald efficiency factor e in subsonic flow as given by equation 17.6. For hypersonic flow however, the lift induced drag is found to be inversely proportional to the lift gradient [129]. Overall, the theoretical maximum lift to drag ratio is achieved by maximizing equation 17.7.

$$C_{D,visc} = C_{fe} \frac{S_{wet}}{S_{ref}} \quad (17.5)$$

$$k_{sub} = \frac{1}{\pi e AR} \quad k_{hyp} = \frac{1}{\left(\frac{dC_L}{d\alpha}\right)} \quad (17.6)$$

$$\left(\frac{L}{D}\right)_{\max} = \frac{1}{2} \sqrt{\frac{1}{k \cdot C_{D,0}}} \quad (17.7)$$

Wing sensitivity:

For the wing, the most critical design parameters include the planform area S_{wing} , aspect ratio AR and wing thickness to chord ratio $\frac{t}{c}$. The effect of changes in the wing planform on the subsonic and hypersonic cruise lift to drag ratios as well as on the estimated mass of the fuel and primary structural components of the aircraft are given in Figures 141 to 143.

Planform area effects:

- An increase in wing area improves both subsonic and hypersonic lift to drag ratios.
- For subsonic flow, the increase in wing platform area reduces the total wetted to wing planform area ratio S_w/S_{ref} thereby decreasing the zero lift drag coefficient $C_{D,0}$ yielding to the improved aerodynamic performance.

- For hypersonic flow, the increase in wing area decreases both the zero lift drag due to viscous forces (friction) and wave drag coefficient. Since the wing produces weaker shock waves than the fuselage body (due to the use of biconvex airfoil), the overall increase in total pressure drag force due to shock waves is small relative to the increase in wing planform area.
- In terms of mass distribution, a lower surface area decreases the wing and TPS mass fractions but leads to a significant increase in fuel fraction as a result of poor aerodynamic performance. On the other hand, an excessive planform area leads to high wing and TPS mass fractions with small gains in aerodynamic efficiency, which leads to an overall increase in aircraft mass.
- The TPS mass varies as a result of changes in wing wetted area associated with the variations in planform area.
- As a result, there exists an optimum wing area which minimises the aircraft take off mass through a trade-off between fuel and wing/TPS mass.

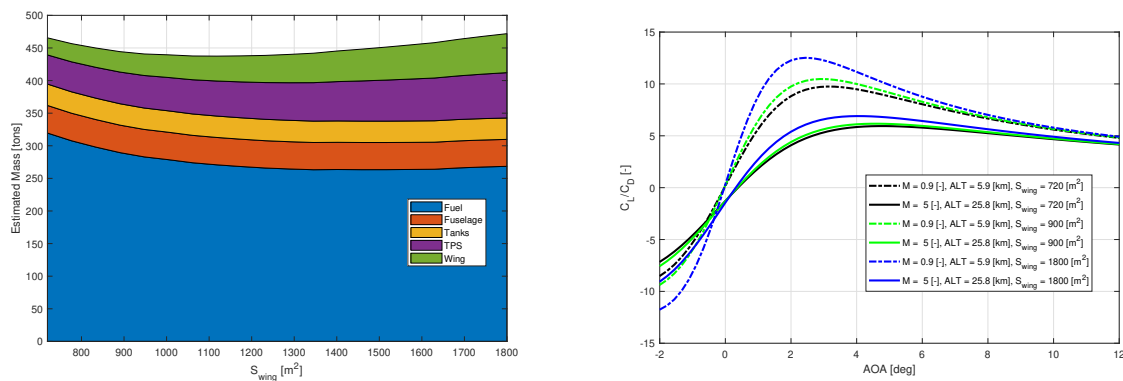


Figure 141: Sensitivity of wing surface area on mass distribution (left) and subsonic/hypersonic lift to drag ratio (right).

Aspect ratio:

- High aspect ratio wings have a high structural mass and cause a sharp rise in total mass and wing mass fraction.
- Very low aspect ratio wings perform badly in subsonic flow leading to an increase in fuel fraction at low aspect ratios as a result of an increase in induced drag. This is in line with subsonic theory whereby the induced drag coefficient is strongly affected by the aspect ratio. In addition, a lower aspect ratio strongly reduces the lift curve as shown in Appendix I, which is in line with the predictions of the DATCOM method [108].
- Hypersonic aerodynamic performance is not noticeably affected by the aspect ratio as vortex induced drag is negligible in this flow regime.
- As a result of this behaviour there exists an optimum aspect ratio which is specific to the mission type. For a trajectory mostly flown in hypersonic cruise, a decrease in aspect ratio can be expected while the opposite effect would occur for a mission with a predominant subsonic cruise phase.

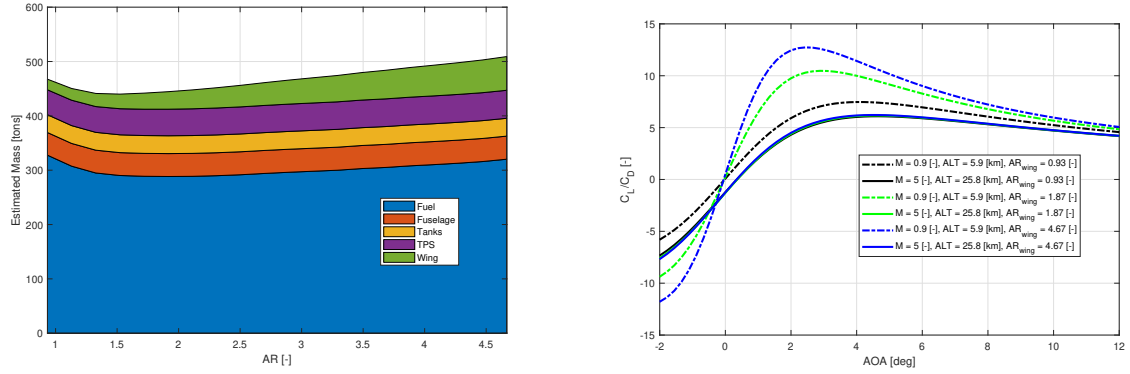


Figure 142: Sensitivity of wing aspect ratio.

Wing thickness to chord ratio:

- Higher wing thickness decreases the wing mass due to an increase in wing moment of inertia. As a result, wing mass fraction decreases with thickness. However an increased wing thickness leads to a reduced hypersonic aerodynamic performance due to the increase in flow deflection (impact angle) yielding an increase in wave drag, fuel mass fraction and thus overall increase in mass. Increases in thickness improves subsonic aerodynamics but not significantly.
- Low wing thickness increases the wing mass fraction significantly. Fuel mass decreases with a lower wing thickness as a result of improved hypersonic aerodynamic performance. However at very low wing thicknesses, the increase in wing mass is greater than the reduction in fuel mass and thus leads to an overall mass increases. As a result, an optimum exists.

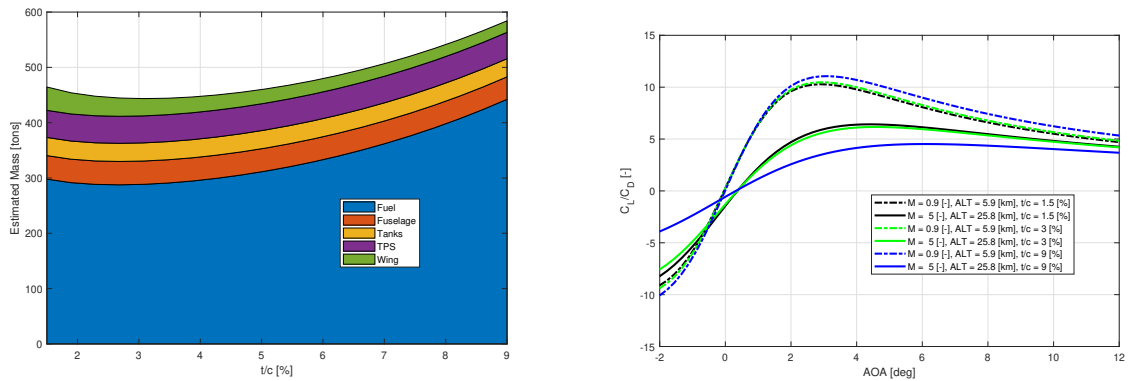


Figure 143: Sensitivity of wing thickness to chord ratio.

Fuselage sensitivity:

For the fuselage, the critical design variables identified are the height factors $F_{h_{up}}$ and $F_{h_{lo}}$ as well as the fuselage length factor $F_{fus,L}$.

Fuselage upper and lower height factors:

- A reduction in fuselage height leads to an increase in fuselage mass fraction due to a reduction in cross sectional moment of inertia of the fuselage. In addition, a decrease in fuselage height leads to a reduction in fuel tank volume and surface area leading to a reduction in fuel tank mass fraction.
- A decrease in fuselage height improves the subsonic and hypersonic aerodynamic performance. For subsonic conditions, the gain in lift to drag ratio is believed to be mainly due to the reduction in total wetted area, causing a decrease in viscous drag coefficient. In hypersonic flow, the reduction of fuselage height also decreases the frontal impact angle on the fuselage body leading to wave drag reductions.
- These aerodynamic improvements lead to a significant reduction in fuel fraction. Due to the significant reduction in both tank and fuel fractions, the wing and TPS represent a high fraction of the total mass. One significant drawback of the fuselage height reduction is the associated reduced volume available for fuel storage.
- Overall, the benefits of fuselage height reduction in terms of fuel and tank mass overcompensate for the increase in fuselage structural mass and thus yield an overall decrease in aircraft mass.

It should be noted that at very low height factors, the fuselage fraction would be expected to sharply increase, possibly leading to an overall increase in aircraft mass. However due to the nature of the equation used to estimate fuselage mass (14.4), this behaviour cannot be captured.

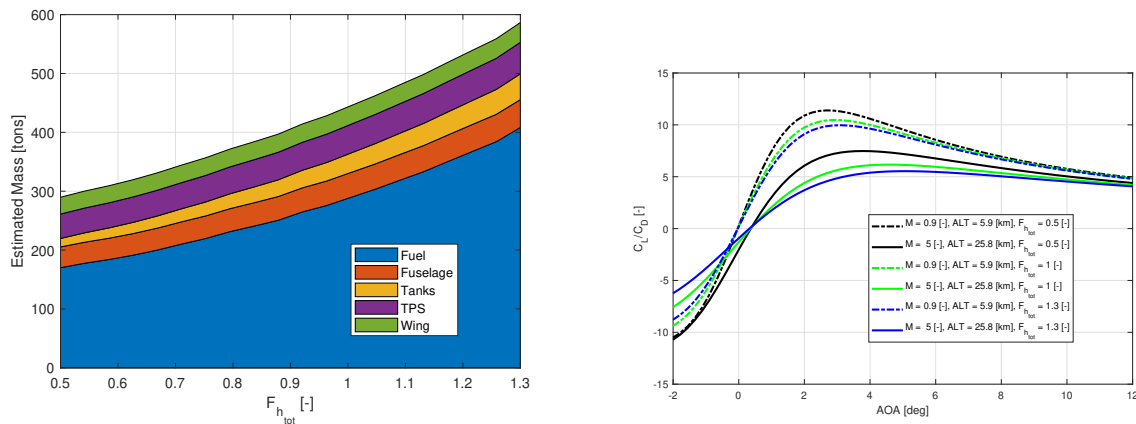


Figure 144: Sensitivity of fuselage height factor.

Fuselage length factor:

- As can be expected, a decrease in fuselage length yields a significant decrease in fuselage mass fraction due to reduction of the aerodynamic forces moment arm. The TPS and tank masses also decrease as a result of the reduced wetted area and available internal volume of the fuselage.
- Increasing the fuselage length yields a higher hypersonic lift to drag ratio as a result of the stretching of the body resulting in lower frontal flow impact angle and thus a significant reduction in wave drag. In addition, this stretching effect promotes the generation of useful pressure induced lift on the vehicle thereby increasing the lift curve slope as observed in Appendix I.

- In subsonic conditions, wave drag does not play a role on the aircraft drag and thus an increase in length causes a reduction of lift to drag ratio due to an increase in viscous drag as a result of increased total wetted area.
- As the fuselage decreases to a very low length fraction, the fuel fraction increases significantly yielding to an overall aircraft mass increase. This is due to the increase in flow impact angle with reduced fuselage length (for a fixed height) which deteriorates the hypersonic aerodynamic performance. Overall, there is an optimal length for the fuselage which minimises the aircraft's total mass.

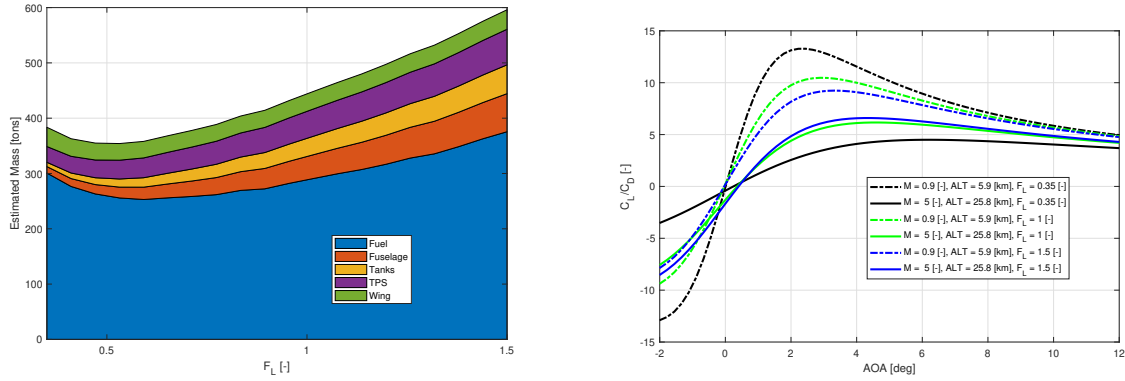


Figure 145: Sensitivity of fuselage length factor.

17.3.3. Baseline Aircraft sizing

In this section, the results of the optimal sizing of the LAPCAT A2 baseline configuration are provided for the Brussels - Sydney (alternative route) mission defined in Figures 39 and 40 reaching a range of 18771 km.

The behaviour of the objective function value and fuel volume constraint during the optimal sizing iterations are given in Figures 146 and 147. As can be seen, the objective function reaches a local optima after 12 iterations with the volume constraint satisfied. Initially the baseline configuration fuel constraint is not satisfied by a margin of $-760 m^3$. As a result, the optimiser initially ensures that the constraint is satisfied leading to an increase in the objective function value (between iterations 2 to 4). Once constraints are met, the optimiser gradually searches for an optima for which the fuel constraint is still satisfied. At the end of the optimisation process, the volume constraint is satisfied with a margin of $+5.6 m^3$. This behaviour highlights the fact that the fuel volume constraint strongly influences the available design space when liquid hydrogen is used as the source of propulsive energy.

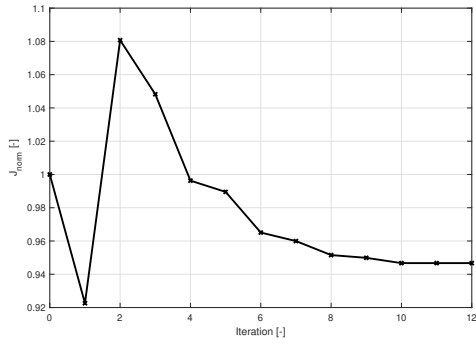


Figure 146: Value of (normalised) objective function during optimal sizing

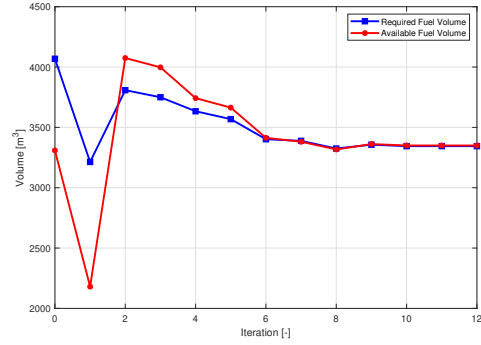


Figure 147: Behaviour of fuel volume constraint during optimal sizing.

Looking at the behaviour of the design vector (figure 148), it can be seen that the design variables start to converge to an optimum value after iteration 10. None of the variables converge to one of the bounds previously defined in Table 13 which shows that a local optima exists which is not influenced by artificial bounds.

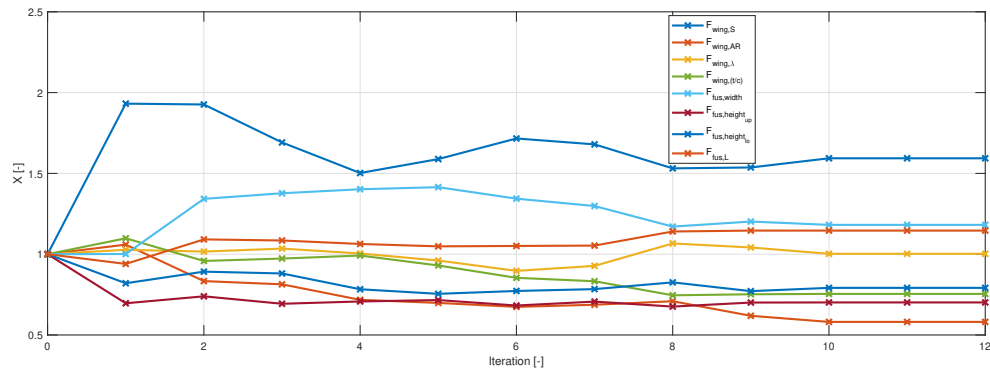


Figure 148: Design vector during optimal sizing.

In Table 16, the optimal design vector obtained at the end of the optimisation process is given. In addition, rendered views comparing the baseline and optimised configurations are given in figure 149. As can be observed, the wing platform area, fuselage width and length are increased for the optimally sized configuration. On the other hand, wing aspect ratio and thickness are reduced as well as the fuselage height. The optimal configuration thus possesses a wider and slimmer fuselage body as well as a thinner wing promoting an increased hypersonic aerodynamic efficiency.

Table 16: Baseline versus Optimal design vector.

Design Variable	Unit	Baseline	Optimised
$F_{S_{wing}}$	[-]	1	1.5935
$F_{wing,AR}$	[-]	1	0.5809
$F_{wing,\lambda}$	[-]	1	1.0023
$\epsilon_{tip,wing}$	[deg]	0	-1.0
$F_{(t/c)_{wing,airf}}$	[-]	1	0.7543
$F_{fus,width}$	[-]	1	1.1815
$F_{fus,height_{up}}$	[-]	1	0.7015
$F_{fus,height_{lo}}$	[-]	1	0.7916
$F_{fus,length}$	[-]	1	1.1461

In Table 17, the component mass breakdowns for the baseline and optimised configurations are given. Overall it can be observed that a 5.3% reduction in take-off mass is achieved by the sizer. Most of the mass improvements are achieved through a reduction of 17.8% in fuel mass while the empty mass is actually increased by 8.4% at the end of the sizing process. This can be further observed in figure 150, whereby the optimiser aims to reduce the fuel mass as much as possible while keeping the empty mass to an acceptable value. This behaviour makes sense since the fuel mass constitutes the largest proportion of the aircraft take off mass with 52% and 46% for the baseline and optimised configurations respectively.

In terms of component mass distribution it can be seen that the aerodynamic surfaces, fuselage and thermal protection system masses are all increased for the optimised configuration. This behaviour is in line with the sensitivity study carried out prior to optimal sizing. Indeed, due to the 59.4% increase in wing area and 25% decrease in thickness to chord ratio (as given in Table 16), the wing mass is expected to increase even though the aspect ratio of the optimal configuration is decreased by 42% since a change in platform area has the greatest effect on wing mass estimation as given by equation 14.1. The vertical tail mass also increases as a result of a larger vertical tail area which is directly linked to the increase in main wing planform area. The fuselage mass rises by a significant 18.5% as a result of the reduced cross sectional height and increase in length.

The 23.3% increase in thermal protection mass is explained by the larger wetted area of both the fuselage (+10.5%) and wing (+47.1%) for the optimal configuration. Wetted area is found to be the major factor of influence for the thermal protection mass since the change in vehicle shape does not significantly impact the total heat transfer distribution and thus TPS unit mass distribution, as shown in figures 164 to 167. The tank structural mass does not vary significantly as the available fuel volume changes by only +1.2% for the optimised configuration as a result of the decrease in fuel volume required as observed in Table 18. Tank insulation rises slightly due to the increase in tank surface area as a result of fuselage stretching.

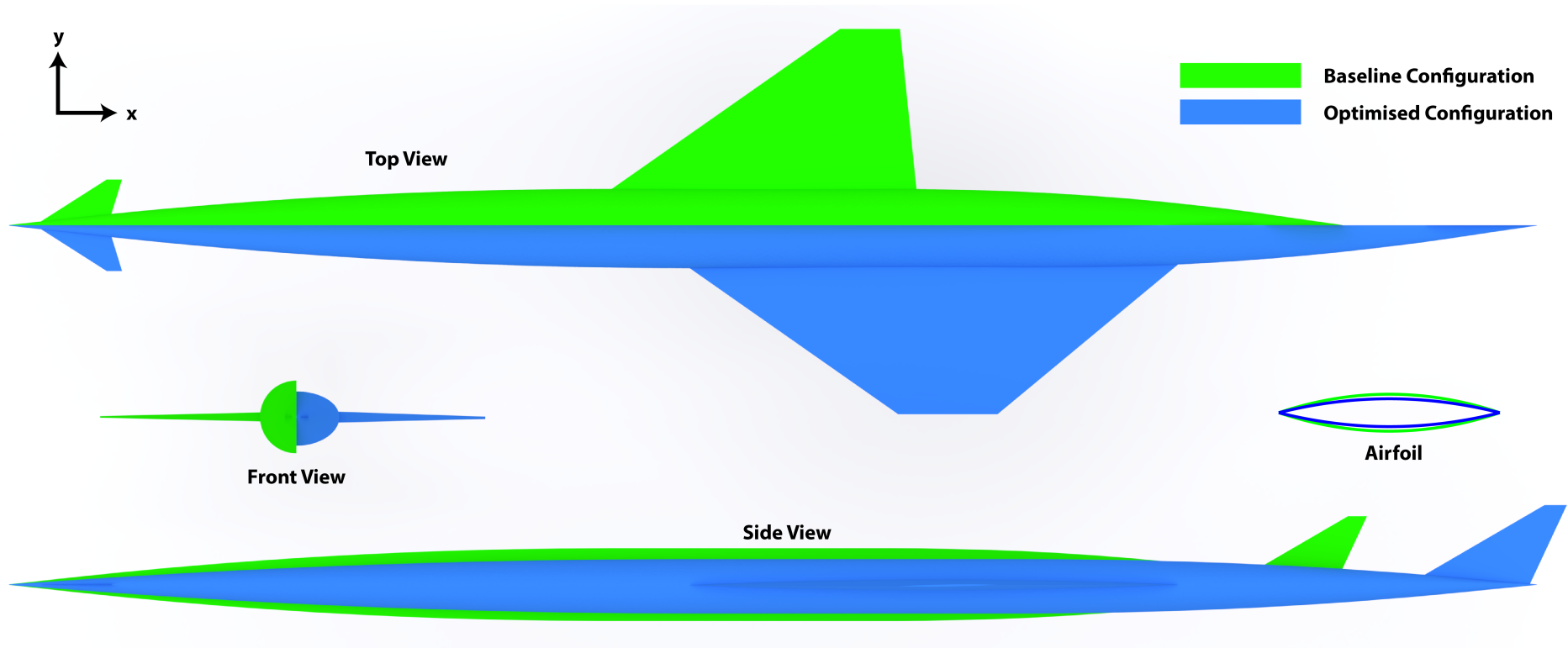


Figure 149: Geometry comparison between baseline and optimised configurations.

Table 17: Mass estimation results for baseline and optimised configurations.

Estimated Mass [tonnes]	Sub-Component	Baseline Configuration	Optimised Configuration	Percentage Difference
Payload		31.3	31.3	0.0
Aerodynamic Surfaces sub-total		31.6	35.5	+ 12.3
	<i>Main wing</i>	29.6	32.7	+ 10.6
	<i>Vertical tail</i>	2.0	2.7	+ 37.4
Fuselage mass		42.2	49.9	+ 18.5
Thermal protection system		48.8	60.1	+ 23.3
Propulsion system sub-total		60.8	61.7	+ 1.4
	<i>Fuel tank structure</i>	28.1	28.4	+ 1.2
	<i>Fuel tank insulation</i>	4.7	5.2	+ 10.8
	<i>Engine Dry</i>	28.0	28.0	0.0
Sub-system mass sub-total		18.4	18.2	- 1.0
	<i>Electric sub-systems</i>	2.7	2.7	+ 0.7
	<i>Hydro-Pneumatic sub-system</i>	0.9	1.1	+ 19.8
	<i>Avionics</i>	4.7	4.6	- 2.0
	<i>Equipment</i>	10.0	9.7	- 2.9
Landing gear		28.6	26.9	- 6.0
Operational Empty mass		261.7	283.7	+ 8.4
Fuel mass		288.2	236.9	- 17.8
Take-off mass		549.9	520.6	- 5.3

Table 18: Geometrical properties of baseline and optimised configurations.

Property	Unit	Baseline Configuration	Optimised Configuration	Percentage Difference
Required Fuel Volume ($V_{F,req}$)	$[m^3]$	4068.5	3344.5	- 17.8
Available Fuel Volume ($V_{F,av}$)	$[m^3]$	3308.8	3350.1	+ 1.2
V-Tail moment arm ($l_{vt,arm}$)	$[m]$	59.8	68.5	+ 14.5
V-Tail Area (S_{vt})	$[m^2]$	46.3	62.0	+ 33.9
Total tank surface (S_{tank})	$[m^2]$	2103.7	2330.3	+ 10.8
Fuselage wetted area ($S_{wet,fus}$)	$[m^2]$	2397.5	2649.8	+ 10.5
Wing wetted area ($S_{wet,wing}$)	$[m^2]$	1275.7	1876.0	+ 47.1

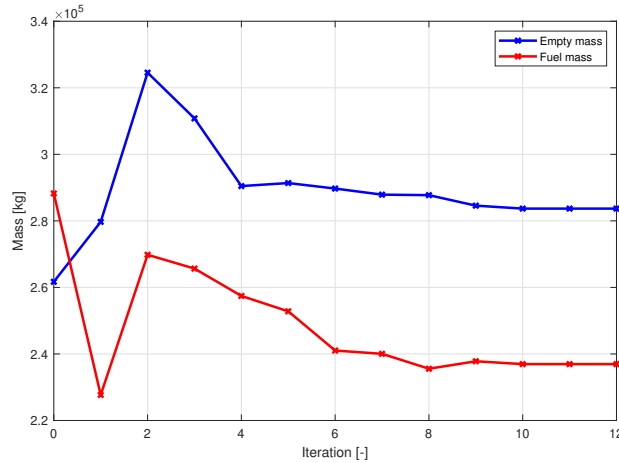


Figure 150: Variation in empty and fuel mass during optimal sizing process.

Looking at the estimated mass distributions for both baseline and optimised configurations as given in figures 151 and 152, it can be seen that the aerodynamic surfaces, fuselage body, thermal protection system and fuel tanks constitute the major portion of the configuration's structural mass, constituting total mass fractions of 29% and 35% of the aircraft take-off mass for the

baseline and optimised aircrafts respectively. NASA’s “Structural weight analysis of hypersonic aircraft” by Dr. Ardema [76] similarly estimates a total mass fraction of 35% for these four components for a liquid hydrogen fuelled hypersonic aircraft. In addition, the empty mass of the aircraft constitutes 48% and 54% of the take-off mass for the baseline and optimised configurations which is in line with the dry mass fraction of 55% estimated by [76].

The fuselage and thermal protection system constitute the largest mass fractions with 8% and 9% of the maximum take off mass respectively for the baseline aircraft and 10% and 12% for the optimised aircraft. The larger fuselage mass fraction is mainly a result of the fuel constraint which limits the minimum body dimensions. Due to the use of low density liquid hydrogen fuel, a large fuselage body is required leading to the high mass fraction. For the thermal protection system, the high duration of the mission (4.5 hours) combined with the high heat transfers encountered at a cruise Mach number of 5 lead to this high TPS mass fraction.

When looking at sub-component masses it can first be observed that the main aerodynamic surface mass contributor is the main wing in this configuration. The wing constitutes about 93% of the total aerodynamic surface mass. This is primarily due to the long fuselage of the configuration which results in a high vertical tail moment arm and thus a low tail mass. The fuel tank insulation also constitutes a significant 14.3% and 15.4% of the total tank mass. Subsystems constitute a small portion of the configuration mass amounting to approximately 3% of the take off mass for the baseline and optimised configurations.

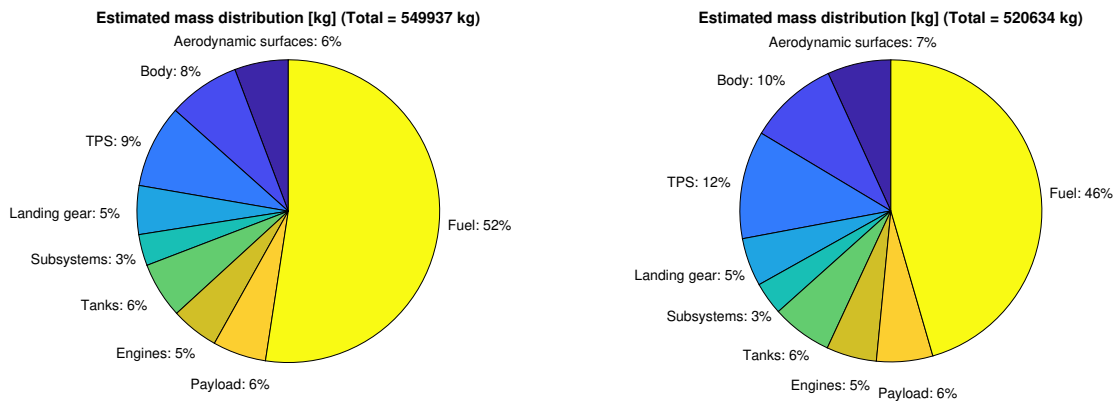


Figure 151: Baseline configuration mass distribution. Figure 152: Optimised configuration mass distribution.

In figure 153 a comparison is provided between the estimated masses for the main structural components of the LAPCAT A2 baseline configuration as obtained using the current tool and the results of the doctorate thesis research “Design Optimization and Analysis of Long-Range Hydrogen-Fuelled Hypersonic Cruise Vehicles” by Dr. Shayan Sharifzadeh [93]. The estimations of Dr. Sharifzadeh are based on RANS CFD aero-thermal analysis of the LAPCAT A2 aircraft, a thermal protection system sizer (TPSP) based on a passive concept with the same silica based thermal protection material SiO_2TiO_2 used in this research and a back wall temperature constrained to 400K [93] as well as an aluminum sub-structure. The other components are sized using empirical based methods (HAWAI, a combination of HASA and WAATs weight estimation methods [51] [44]) which are essentially the same as the ones used in this research.

When comparing the results obtained in this research to the ones obtained by Dr. Sharifzadeh,

it can be seen that for the empirical based analysis (HAWAi+TPSP), the overall structural mass difference of the combined fuselage, wing, tank and thermal protection system is small with only a 7.4% difference. This verifies the correct implementation of the mass estimation equations implemented in the current platform. In terms of component masses, the fuselage mass is in line with the results obtained by Shayan showing only a 7% difference. Fuselage mass is near identical which is expected since it is only dependent on geometrical parameters, an ultimate load factor and the modifying factor as given by equation 14.4, which should be near identical for both analyses. The fuel tank mass is predicted to be slightly higher in the current platform with a mass of 32.8 tonnes as opposed to 26.1 tonnes from the prediction of Shayan. The results from Shayan do not include the fuel tank insulation in this case which would explain the difference observed since tank insulation is predicted to account for 4.7 tonnes of the total tank mass in this research (Table 17).

The origin of the 25% difference in wing mass with the predictions from Dr. Sharifzedehe is not known, however, the current wing mass estimation is in line with the results obtained by the DLR institute who predict a 30 tonnes wing mass [93] (as compared to 29.6 tonnes for the current platform). The thermal protection system mass shows a large difference of 54% with the results from Shayan, however this is believed to be a result of the overly simplified and incorrect assumption used for the TPSP sizer in [93]. Shayan's research uses "only one position at 1.0m downstream of the stagnation point" to size the entire thermal protection system mass. On the other hand, in the current implemented platform, using the parametric heat load functions defined in Section 13.2.2, the TPS sizing method allows for the appropriate sizing of each of the panels defined on the mesh yielding a better estimate of thermal protection mass.

Overall, the take-off mass predicted by [112] for LAPCAT A2 is 400 tonnes as opposed to 549.9 tonnes with the current tool (37% difference). This difference is believed to be mostly due to the difference in specific impulse of the engine models. The LAPCAT A2 designers predict a specific impulse of 4170 [s] during the Mach 5 hypersonic cruise phase [112] as opposed to around 3800 [s] using the GHAME model in the current platform (around 10% difference). The engine specific impulse has a large impact on the fuel mass of the aircraft and thus overall maximum take-off mass. It is thus believed to be the main reason for the difference in estimated take-off mass.

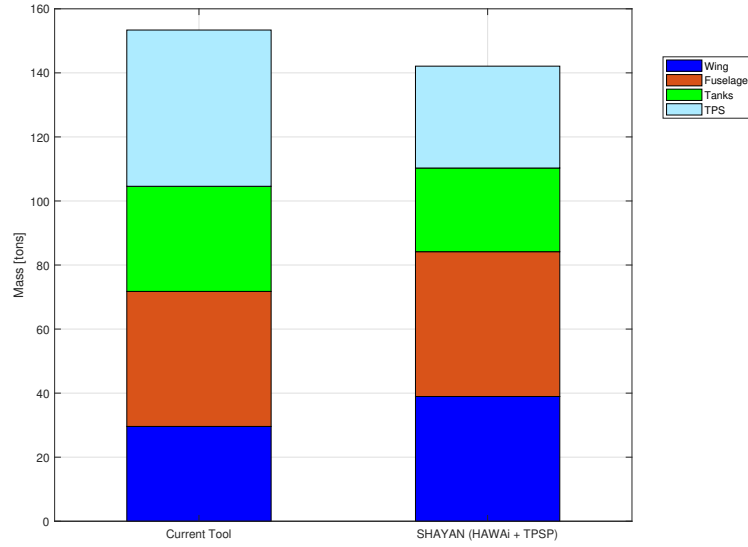


Figure 153: Comparison of estimated structural component masses for baseline LAPCAT A2 configuration with the results of Dr. Sharifzadeh [93].

Figures 154 to 158 provide the difference in lift and drag polars for the baseline and optimised configurations at subsonic and hypersonic cruise conditions. As can be observed, for the subsonic condition, the optimised configuration possesses a significantly reduced lift polar as a result of the 42% reduction in wing aspect ratio (Table 16). This reduction in aspect ratio yields a significant increase in induced drag as can be seen in figure 156, which reduces the overall subsonic maximum lift to drag ratio according to equation 17.7. On the other hand, the zero lift drag coefficient $C_{D,0}$ is slightly reduced for the optimised configuration which is believed to be due to a reduction in total wetted area to wing planform area S_{wet}/S_{ref} . According to Table 18 and 16, this ratio decreases from 4.08 to 3.16.

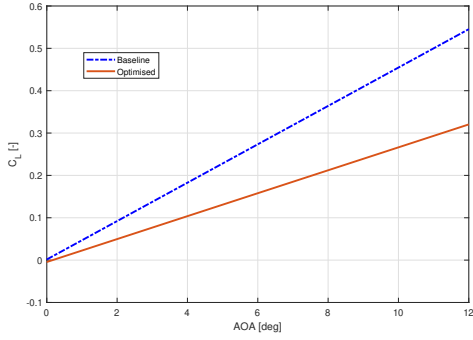


Figure 154: Lift polar comparison at subsonic cruise $M = 0.9$ [-], $ALT = 5.9$ km.

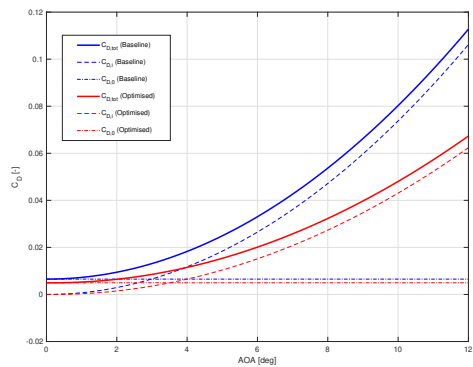


Figure 155: Drag polar comparison at subsonic cruise $M = 0.9$ [-], $ALT = 5.9$ km.

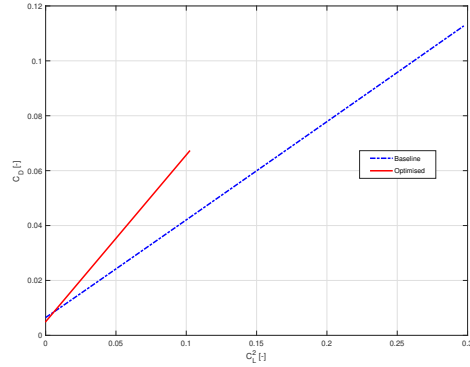


Figure 156: Drag due to lift comparison at subsonic cruise $M = 0.9$ [-], $ALT = 5.9$ km.

For the hypersonic cruise conditions, the lift curve is only slightly affected by the changes in design variables for the optimised configuration. However, the optimised aircraft shows a significant reduction in zero lift drag $C_{D,0}$. This is believed to be due to the reduction in both wing thickness and fuselage height as well as the increase in fuselage length, which, as was observed in the sensitivity analysis, all lead to a reduction in wave drag. Additionally, the decrease in wetted area to wing planform area also reduces viscous drag in hypersonic cruise condition. As was noticed in the sensitivity analysis, the aspect ratio does not have a noticeable effect on the lift induced drag for hypersonic conditions but allows for a lighter wing. Since the hypersonic cruise phase constitutes the majority of the mission, the optimiser is expected to reduce the wing aspect ratio as a means of reducing wing mass without significant penalties on overall aerodynamic performance. Overall, these combined effects lead to an increase in hypersonic cruise maximum lift to drag ratio.

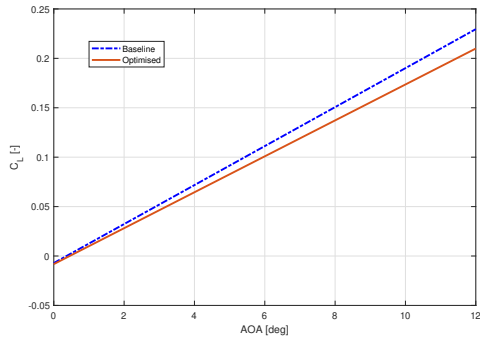


Figure 157: Lift polar comparison at hypersonic cruise $M = 5$ [-], ALT = 25.8 km.

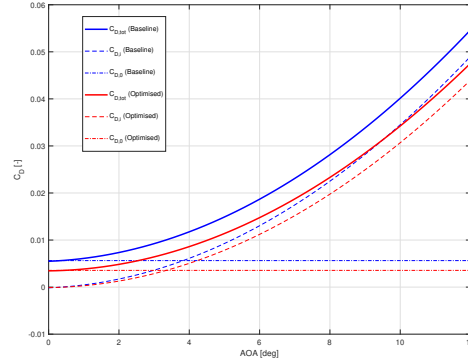


Figure 158: Drag polar comparison at hypersonic cruise $M = 5$ [-], ALT = 25.8.

The change in lift to drag ratio polars and main changes in performance of the baseline and optimised configurations during the mission are given in figures 159 to 162. In terms of lift to drag ratio, the optimised configuration has an increased hypersonic cruise performance whereby the maximum lift to drag increases from 6.16[-] at 4.7 degrees angle of attack to 7.5[-] at 4 degrees (22% increase). This improvement in hypersonic aerodynamic performance comes with a reduction in subsonic maximum lift to drag ratio from 10.47 [-] at 2.9° degrees to 9.12 [-] at 3.6°. It is worth noting that the original designers of the baseline LAPCAT configuration predict a lift to drag ratio of 11 [-] at Mach 0.9 and altitude of 5.9 km and a hypersonic L/D ratio of 5.9 [-] at Mach 5 and altitude of 25-28 km [112]. This is very close to the values predicted here for the baseline configuration (5% and 4% difference with the subsonic and hypersonic lift to drag ratios predicted by the panel codes used in this thesis).

The decrease in hypersonic drag coefficient for the optimised configuration yields a lower thrust requirement and thus reduced fuel consumption (as can be seen in figure 162), leading to an overall reduction in aircraft take-off mass. Furthermore, this reduction in aircraft mass allows the vehicle to operate at lower angles of attack to obtain steady flight during hypersonic cruise, allowing the aircraft to fly closer to its optimum lift to drag ratio which in turn reduces the fuel consumption and take off mass. Overall, through this process the aircraft is able to fly at a much higher lift to drag ratio (near 7.5 [-]) during hypersonic cruise, causing the significant fuel mass reductions previously observed in Table 17.

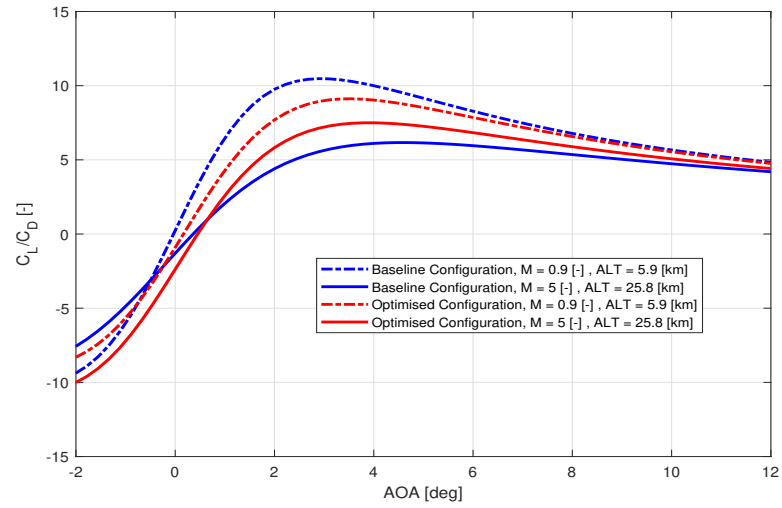


Figure 159: Lift to drag ratio comparison between baseline and optimised configurations.

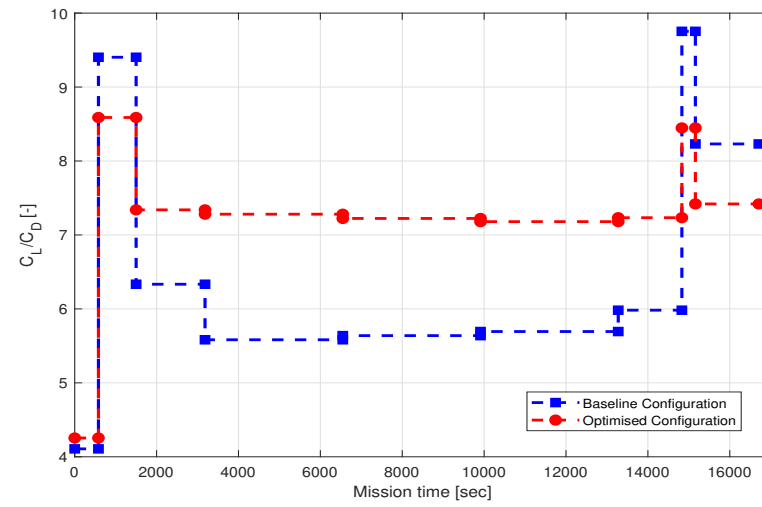


Figure 161: Aerodynamic performance during mission.

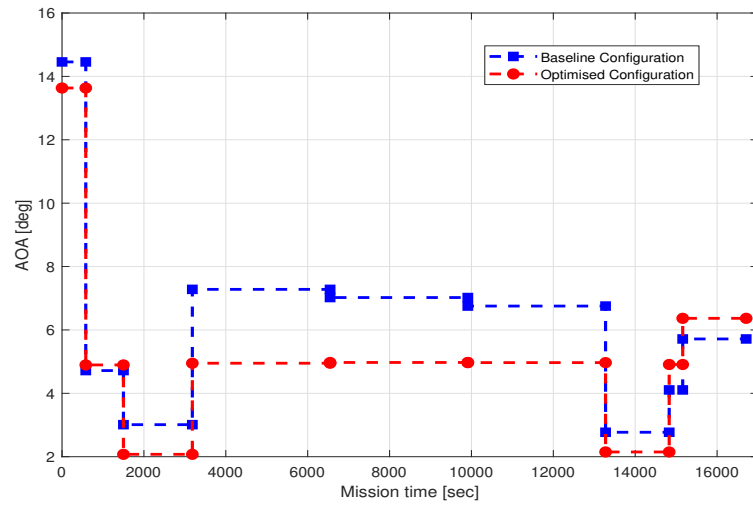


Figure 160: Angle of attack during mission.

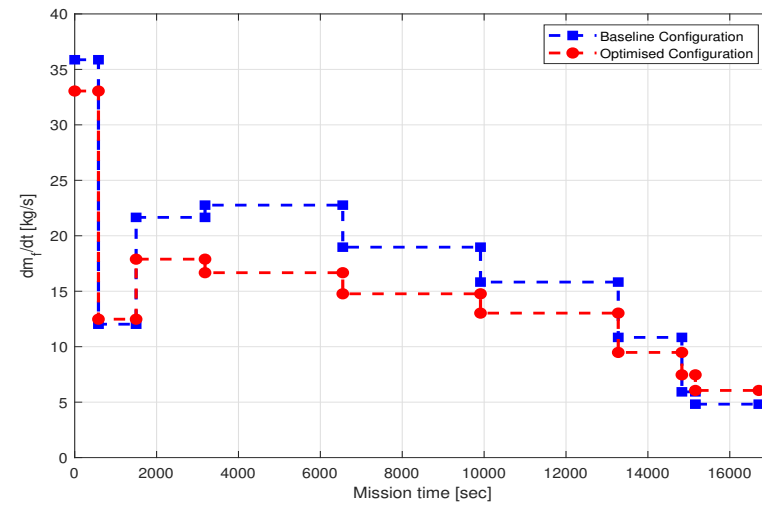


Figure 162: Fuel flow during mission.

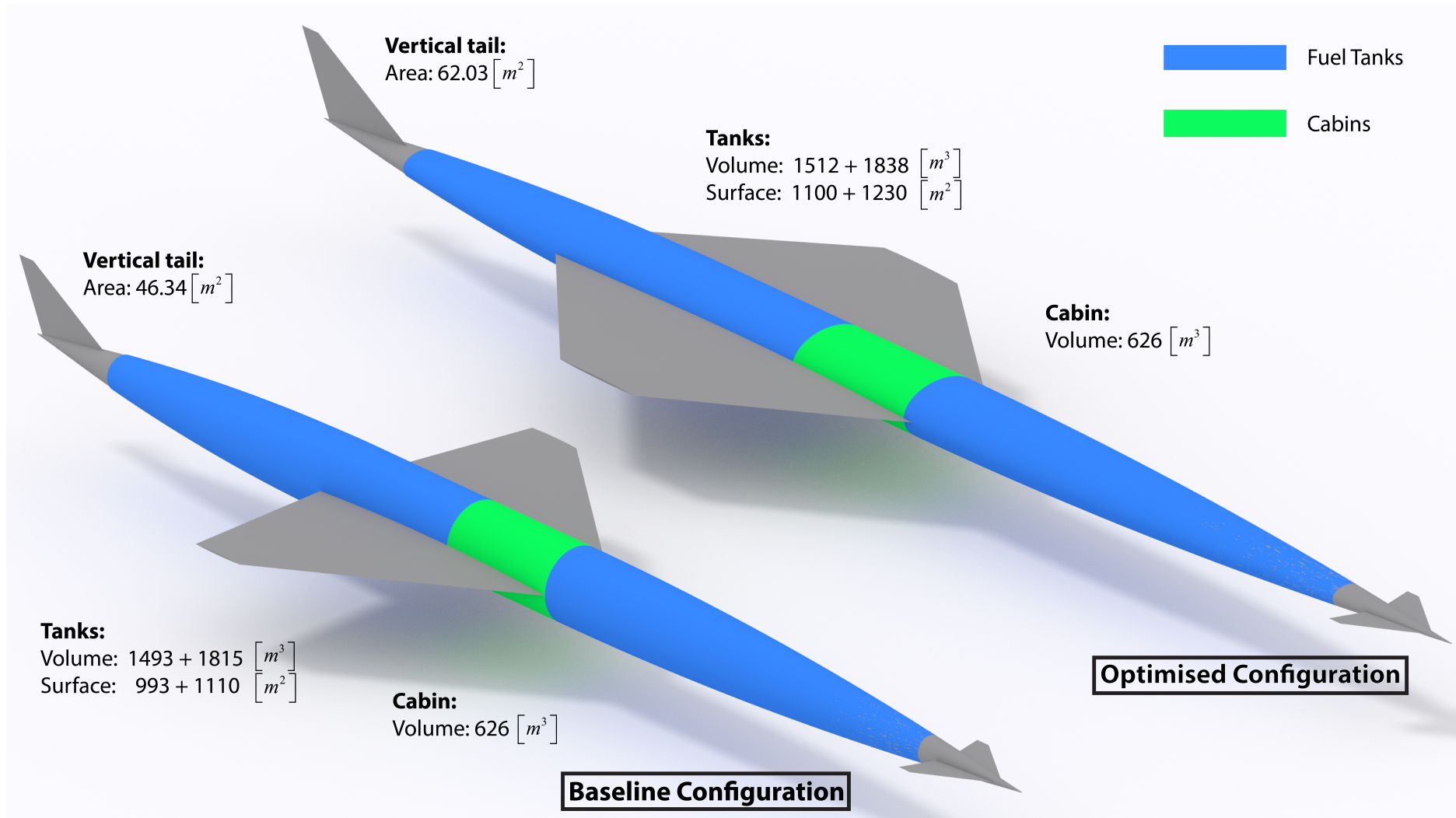


Figure 163: Geometry render comparing baseline and optimised configurations (with fuel tanks included).

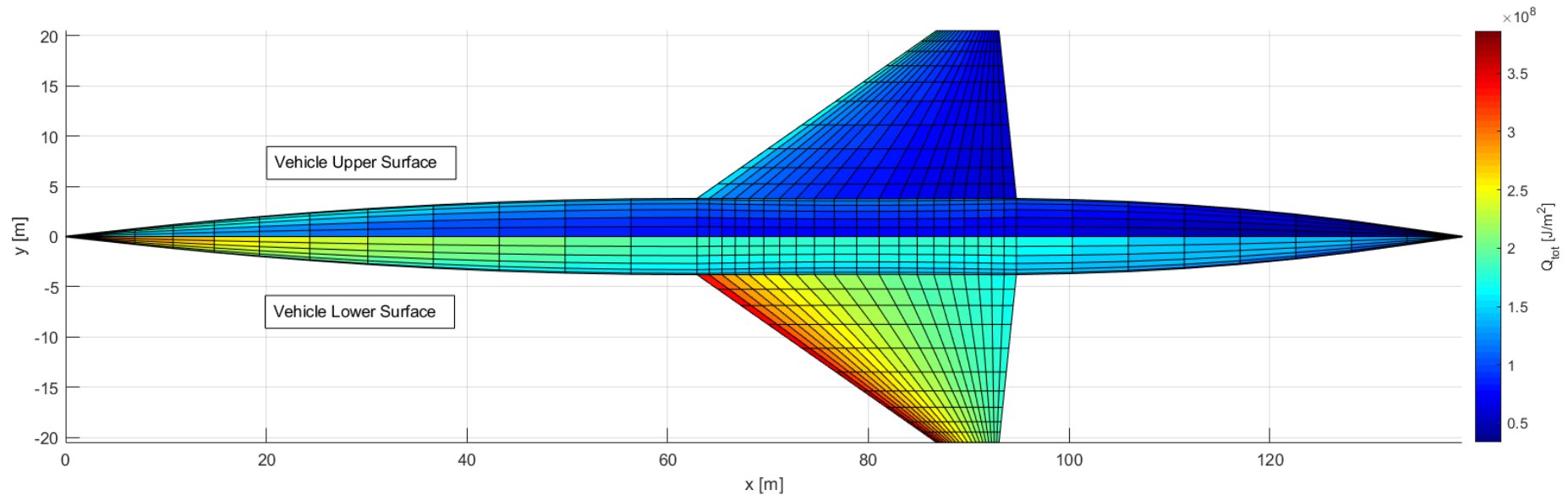


Figure 164: Total heat transfer distribution on baseline configuration.

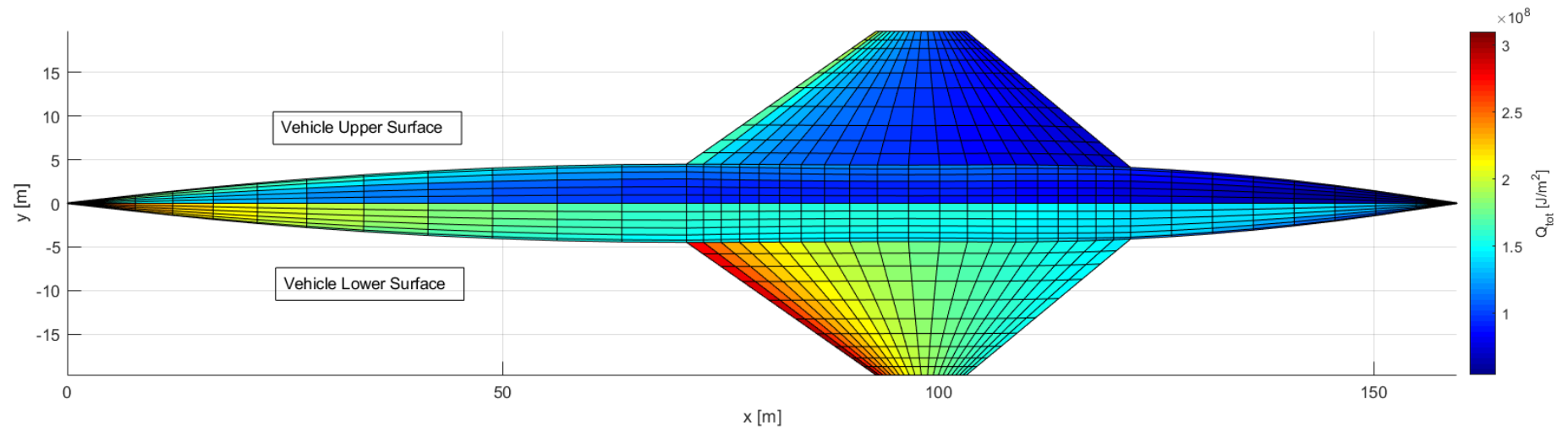


Figure 165: Total heat transfer distribution on optimised configuration.

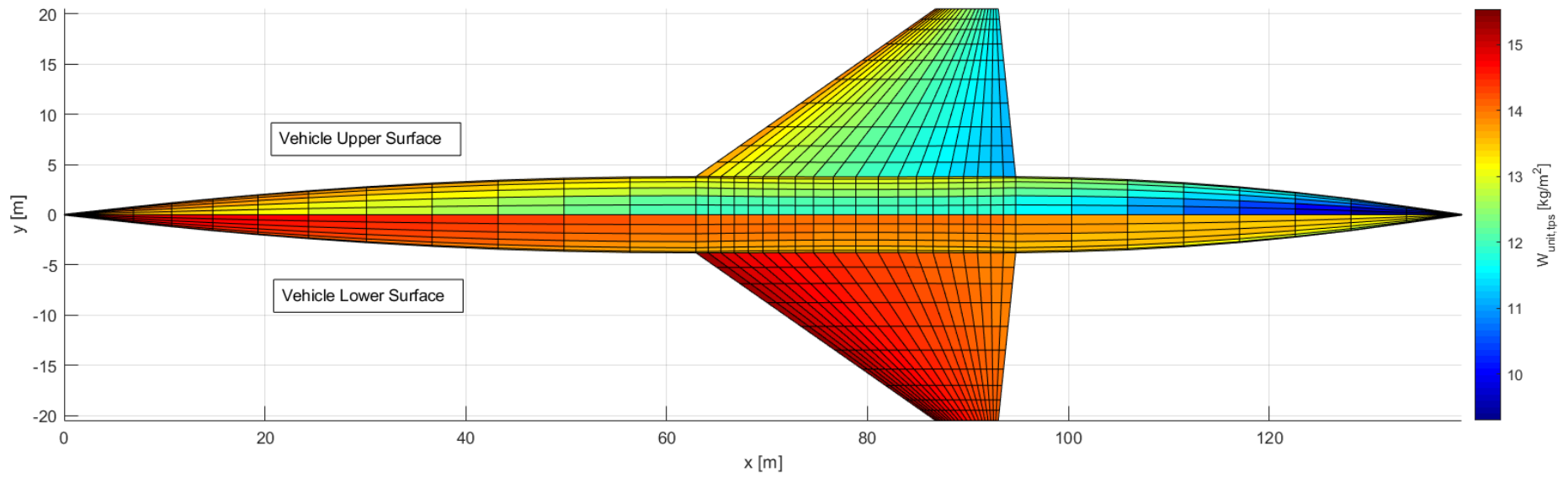


Figure 166: Thermal protection system unit mass distribution on baseline configuration.

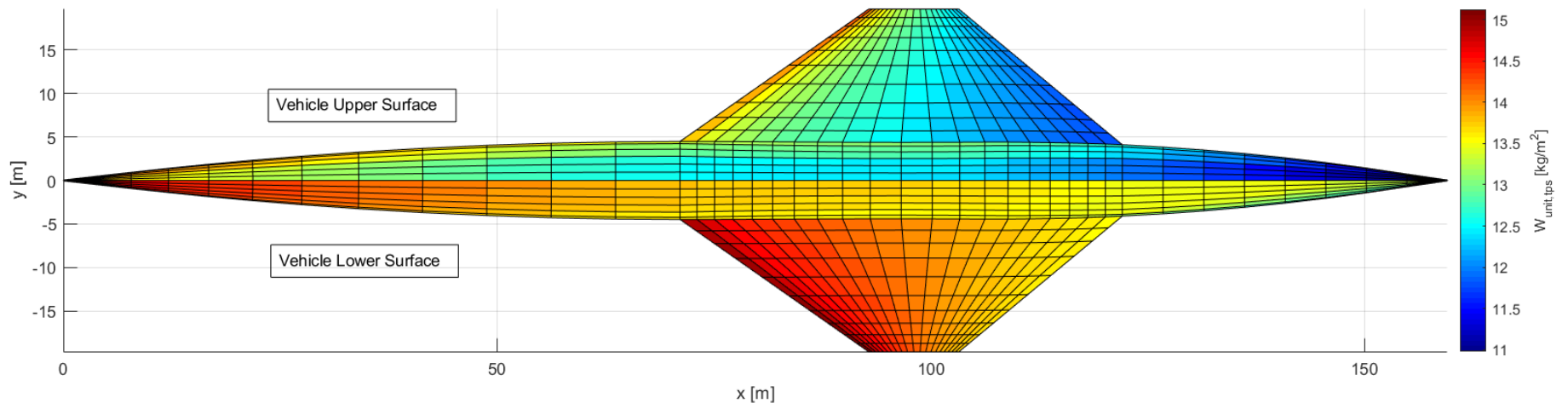


Figure 167: Thermal protection system unit mass distribution on optimised configuration.

17.3.4. Range dependence

To investigate the effect of mission range on the optimal sizing of a hypersonic transport vehicle, the LAPCAT A2 is sized for linearly increasing mission distances. To achieve this, the cruise phase of the original LAPCAT mission is scaled by a defined cruise factor CF (where the original mission is represented by $CF = 1$) such that five different missions of varying total distances are generated as shown in figure 168. By applying the optimal sizing algorithm, the configurations shown in figures 173 and 174 are obtained. In addition, the behaviour of the optimiser for each of scaled missions is provided in Appendix J.

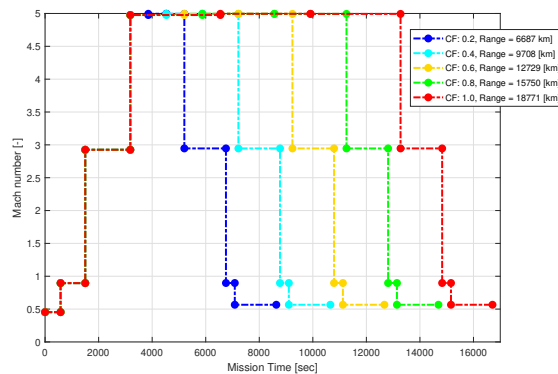


Figure 168: Scaling of LAPCAT A2 mission using a cruise factor (CF).

In Table 19, the optimal design vector for the different mission ranges is provided. Although a global minimum cannot be guaranteed since a local optimiser is used to size the configurations, some general trends can be observed in the design variables. The most noticeable change in design variable for varying cruise range is the aspect ratio which varies from a factor of 0.92 [-] at a cruise factor of 0.2 to a value of 0.58 [-] for the baseline mission ($CF = 1$). This change is believed to be due to the change in relative importance of subsonic aerodynamic performance as compared to hypersonic performance with increasing cruise factor. At a cruise factor of 0.2, subsonic conditions constitute a large portion of the mission profile (figure 168). From the sensitivity study, the aspect ratio shows the largest impact on subsonic lift to drag ratio. As a result the optimiser increases the aspect ratio at low cruise factors to ensure a good balance between subsonic and hypersonic aerodynamic performance. For higher cruise factors, the subsonic performance becomes less critical and the aspect ratio reduces to decrease the overall wing mass. The thickness to chord ratio factor on the other hand decreases with cruise factor to promote a reduction in hypersonic wave drag at the expense of an increased wing mass. The difference in optimal configuration lift to drag ratio for cruise factors of 0.2 and 1.0 is shown in figure 170. In this figure it can clearly be seen that as the cruise factor rises and the relative time spent in hypersonic cruise increases, the optimiser tries to maximise the hypersonic performance at the expense of a reduced subsonic lift to drag ratio. This behaviour clearly shows that the choice of optimal wing design is dependent on a compromise between subsonic and hypersonic flow regimes.

Other design variables such as the wing planform area increase proportionally to the increase in aircraft take-off mass (with increasing range) to ensure the configuration can generate sufficient lift. Additionally, fuselage width and length factors also increase with higher cruise factors in order to fit the fuel required for the mission while fuselage height does not vary significantly. The fuselage length factor increases the most drastically with cruise factor (from 0.67 to 1.15) as it was observed to have the most beneficial effect on the hypersonic lift to drag ratio (through

a reduction in wave drag and the generation of useful lift) from the sensitivity analysis. It is important to note that for each of the sized configurations, the fuel volume is the limiting constraint (as seen in Appendix J and Table 17.3.4), clearly confirming that the fuel volume is one of the most critical constraints in the design of liquid hydrogen hypersonic transport aircraft.

Table 19: Optimal design vector for sized aircraft at varying cruise factors.

Design Variable	Unit	CF : 0.2 [-]	CF : 0.4 [-]	CF : 0.6 [-]	CF : 0.8 [-]	CF : 1.0 [-]
		Range: 6687 [km]	Range: 9708 [km]	Range: 12729 [km]	Range: 15750 [km]	Range: 18771 [km]
$F_{S,wing}$	[-]	0.47	0.60	0.87	1.12	1.59
$F_{wing,AR}$	[-]	0.92	0.87	0.80	0.74	0.58
$F_{wing,\lambda}$	[-]	0.78	0.59	0.59	0.26	1.00
$\epsilon_{tip,wing}$	[deg]	-0.08	-0.59	-0.12	-0.39	-1.00
$F_{(t/c)wing,airf}$	[-]	0.98	0.92	0.87	0.74	0.75
$F_{fus,width}$	[-]	0.81	0.92	0.96	1.01	1.18
$F_{fus,height_{up}}$	[-]	0.59	0.52	0.60	0.84	0.70
$F_{fus,height_{lo}}$	[-]	0.71	0.67	0.70	0.68	0.79
$F_{fus,length}$	[-]	0.67	0.79	0.89	0.98	1.15

In Figure 169 and Table 20, the change in component and fuel mass for the different optimally sized configurations at varying cruise range is provided. From figure 169 it can be seen that the estimated take-off mass of the aircraft increases exponentially with linearly increasing mission range. The fuel mass has the highest growth rate with range leading to a reduction in empty to take-off mass ratio W_{emp}/W_{TO} from 72% to 54% at minimum and maximum range respectively. This fast growth in fuel mass relative to structural components is due to the combination of two factors. Firstly, as a result of the increase in distance, the fuel required to fly the additional range increases and secondly the snow ball effect further increases the fuel mass required. These effects leads to an exponential rise in fuel mass flow required to fly a further range as shown in figure 171. Associated with the exponential increase in fuel mass, the tank mass follows the same behaviour.

While the majority of structural components mass increase with respect to the aircraft mass through the snow ball effect, the thermal protection system mass mainly increases as a result of the increased heat load due to the rising exposure time of the configuration in hypersonic cruise, as well as the increase in vehicle wetted area. The fuselage is the only structural component which is not related to take-off mass according to the HASA weight estimation model (equation 14.4). Its mass still gradually increases as result of the increased length of the body required to fit the liquid hydrogen fuel, but does not follow an exponential behaviour.

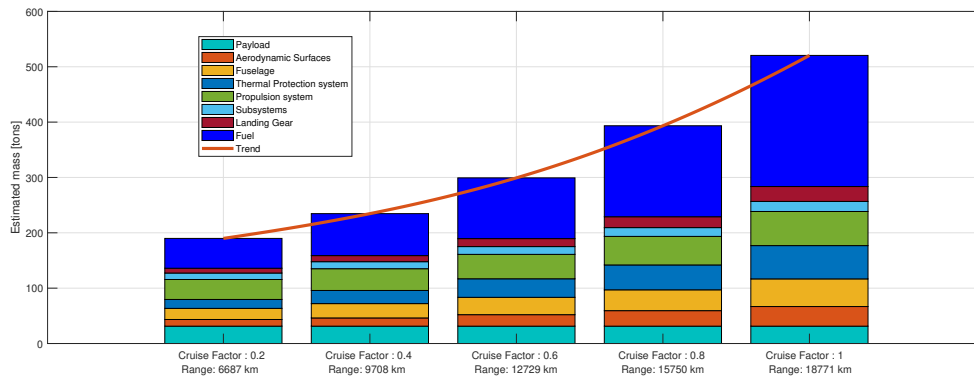


Figure 169: Change in mass distribution of sized configurations with increasing cruise range.

Table 20: Estimated mass distribution for sized aircraft at varying cruise factors.

Estimated Mass [tonnes]	Sub-Component	CF : 0.2 [-]	CF : 0.4 [-]	CF : 0.6 [-]	CF : 0.8 [-]	CF : 1.0 [-]
		Range: 6687 [km]	Range: 9708 [km]	Range: 12729 [km]	Range: 15750 [km]	Range: 18771 [km]
Payload		31.3	31.3	31.3	31.3	31.3
Aerodynamic Surfaces sub-total		12.0	14.9	20.8	28.0	35.5
	<i>Main wing</i>	11.2	13.8	19.2	25.7	32.7
	<i>Vertical tail</i>	0.8	1.0	1.6	2.3	2.7
Fuselage mass		20.1	25.9	31.3	37.6	49.9
Thermal protection system		16.1	23.7	33.5	45.0	60.1
Propulsion system sub-total		36.1	39.4	44.2	51.7	61.7
	<i>Fuel tank structure</i>	6.5	9.1	13.3	19.8	28.4
	<i>Fuel tank insulation</i>	1.6	2.2	3.0	3.9	5.2
	<i>Engine Dry</i>	28.0	28.0	28.0	28.0	28.0
Sub-system mass sub-total		11.7	12.7	14.1	15.9	18.2
	<i>Electric sub-systems</i>	1.4	1.7	1.9	2.3	2.7
	<i>Hydro-Pneumatic sub-system</i>	0.6	0.7	0.8	0.9	1.1
	<i>Avionics</i>	3.2	3.5	3.8	4.2	4.6
	<i>Equipment</i>	6.4	6.9	7.5	8.5	9.7
Landing gear		8.7	11.0	14.5	19.6	26.9
Operational Empty mass		136.0	158.9	189.7	229.2	283.7
Fuel mass		53.9	75.9	109.8	164.5	236.9
Take-off mass		190.0	234.7	299.5	393.6	520.6

Table 21: Derived properties for sized aircraft at varying cruise factors.

Property	Unit	CF : 0.2 [-]	CF : 0.4 [-]	CF : 0.6 [-]	CF : 0.8 [-]	CF : 1.0 [-]
		Range: 6687 [km]	Range: 9708 [km]	Range: 12729 [km]	Range: 15750 [km]	Range: 18771 [km]
Required Fuel Volume ($V_{F,req}$)	$[m^3]$	761.2	1070.8	1549.6	2321.5	3344.5
Available Fuel Volume ($V_{F,av}$)	$[m^3]$	766.2	1076.9	1562.9	2331.9	3350.1
V-Tail moment arm ($l_{vt,arm}$)	$[m]$	40.0	47.4	53.2	58.3	68.5
V-Tail Area (S_{vt})	$[m^2]$	21.3	25.3	38.0	53.4	62.0
Total tank surface (S_{tank})	$[m^2]$	738.9	1003.6	1321.4	1728.7	2330.3
Fuselage wetted area ($S_{wet,fus}$)	$[m^2]$	1177.1	1448.0	1725.8	2073.4	2649.8
Wing wetted area ($S_{wet,wing}$)	$[m^2]$	538.7	668.4	1025.8	1420.7	1876.0

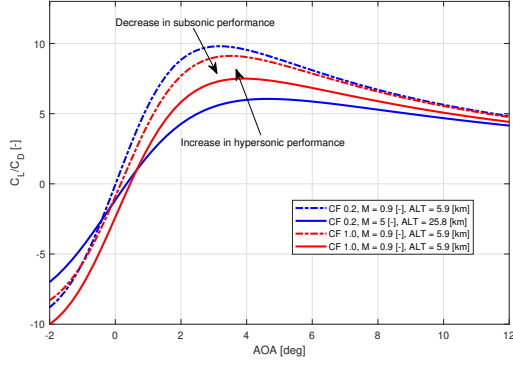


Figure 170: Lift to drag ratio of optimised configurations for two different cruise factors.

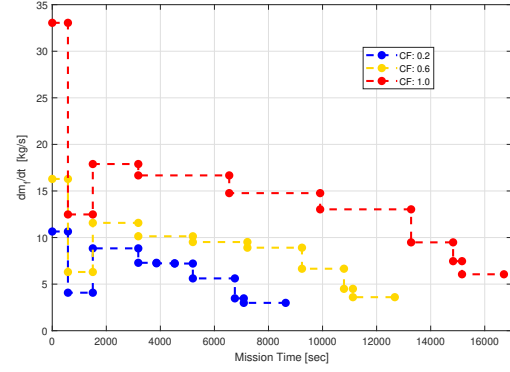


Figure 171: Exponential rise in fuel mass flow with increasing range.

In figure 172, the results obtained for the sized configurations of the LAPCAT A2 for varying mission range are compared to other types of aircraft as reported in [93]. The comparison includes three conventional subsonic kerosene based aircraft (star symbol), four kerosene supersonic aircraft (diamond), and two conceptual subsonic hydrogen transport (blue dot). For performance comparison, the Payload Range Efficiency (PRE) defined by equation 17.8 and payload to take off mass ratio (W_{pay}/W_{TO}) indicators are used. The PRE is essentially a measure of the aircraft useful work done per unit fuel mass. A high PRE indicates a low amount of fuel required for a given payload over a given range [82]. Ideally, PRE and payload mass fraction should be maximised for optimal aircraft performance (top right region of figure 172).

$$PRE = \frac{W_{pay} \cdot R}{W_F} \quad (17.8)$$

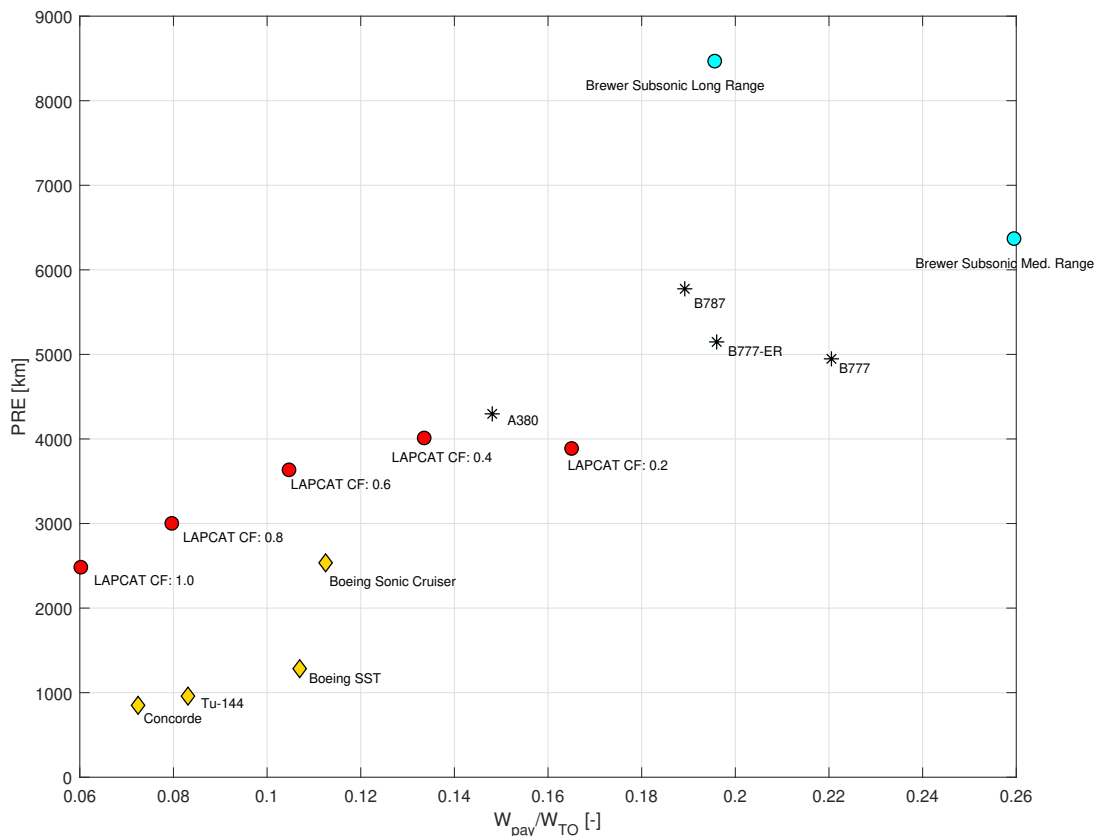


Figure 172: Comparison of optimally sized configurations of the LAPCAT A2 vehicle with other aircraft.

The first aspect which can be noticed regarding the performance estimation of the sized LAPCAT A2 configurations is that, with linearly increasing range, both PRE and payload fraction decrease significantly. The reduction in PRE with range for the LAPCAT A2 vehicle is believed to be a result of the exponential increase in fuel mass with linear increase in range which was previously observed in figure 169. Due to this exponential rise in required fuel mass, the payload mass fraction decreases proportionally as observed in figure 172. Regarding the comparison with other aircraft, the LAPCAT A2 is estimated to possess a lower PRE and payload fraction than typical kerosene subsonic aircraft (star symbol). This is mainly due to the higher lift to drag ratios which can be expected for subsonic aircraft (high fuel range efficiency) and due to the lower structural mass fraction of subsonic aircraft which do not require heavy liquid hydrogen tanks and thermal protection systems. The subsonic conceptual hydrogen aircraft are expected to perform the best in terms of PRE and payload fraction due to the combination of very high liquid hydrogen propulsive efficiency achievable at subsonic speeds and the high lift to drag ratios expected. The LAPCAT A2 is, however, estimated to perform better than supersonic kerosene aircrafts (diamond) in terms of PRE, which is mostly a result of the increased propulsive efficiency of liquid hydrogen engines at high-speeds as presented in figure 6.

Overall, while liquid hydrogen transport aircraft are not estimated to perform as well as subsonic kerosene and hydrogen aircraft in terms of PRE and payload fraction, the potential of liquid hydrogen propulsion allow such aircraft to outperform typical supersonic kerosene aircraft in terms of PRE and provide time reductions which are unachievable by subsonic aircraft.

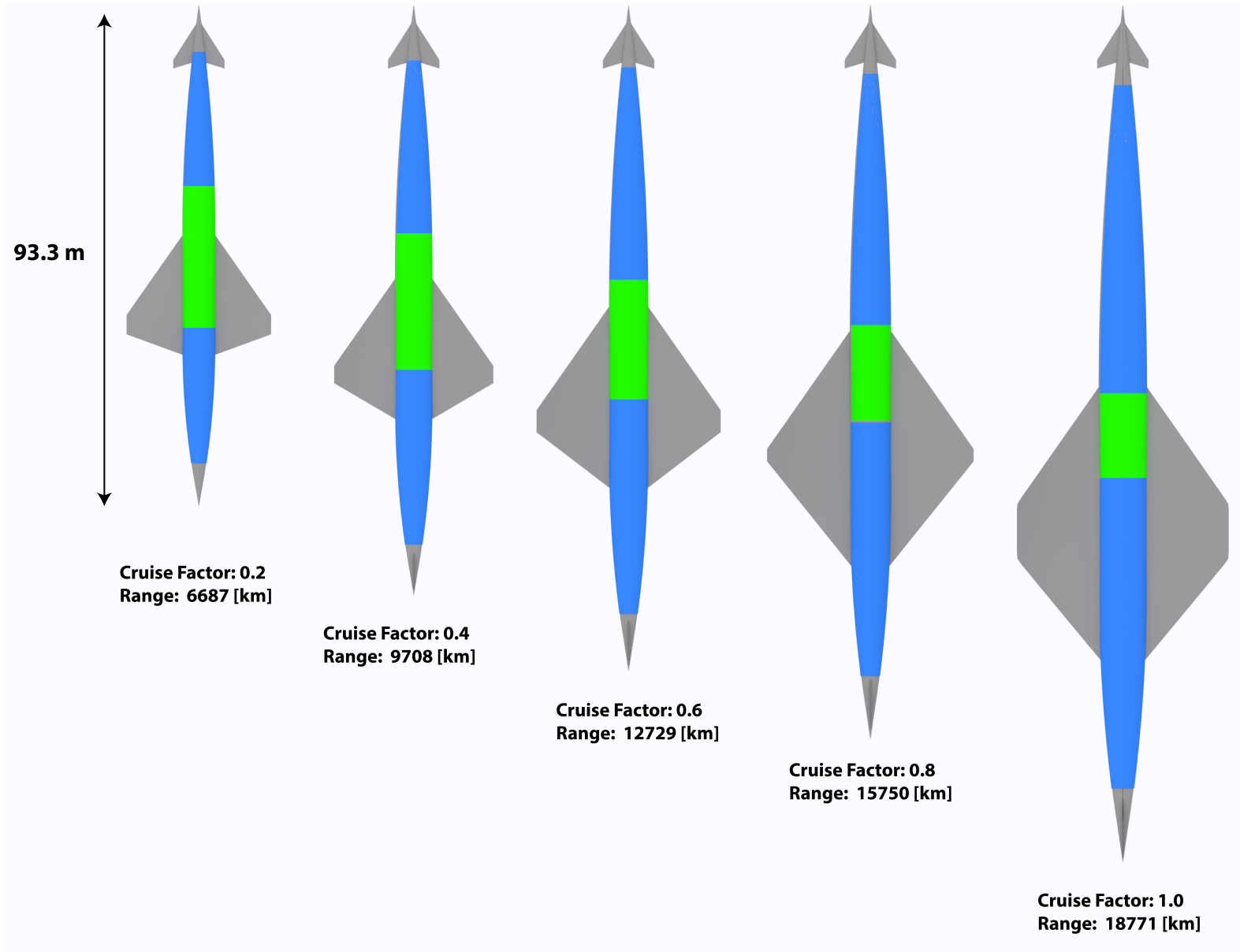


Figure 173: Optimally sized configurations for varying mission range (top view).

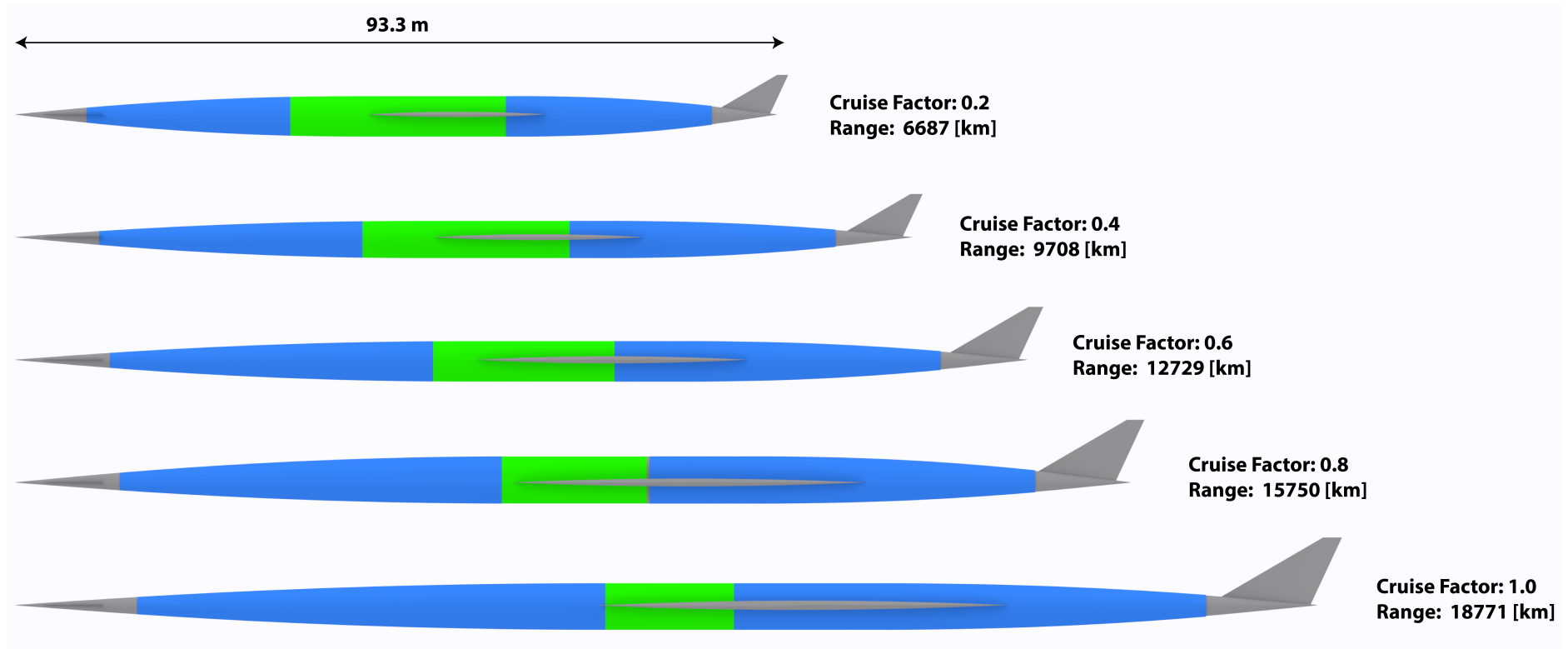


Figure 174: Optimally sized configurations for varying mission range (side view).

17.3.5. Mach number effects

As additional research, the effect of the cruise Mach number on the baseline LAPCAT A2 configuration are investigated in this section. In this analysis, the hypersonic cruise Mach number of the LAPCAT baseline mission is increased while the simulation time is scaled to match the (fixed) original mission range of 18771 km. In figure 175 the scaled missions for hypersonic cruise Mach numbers ranging from 5 to 8 are provided.

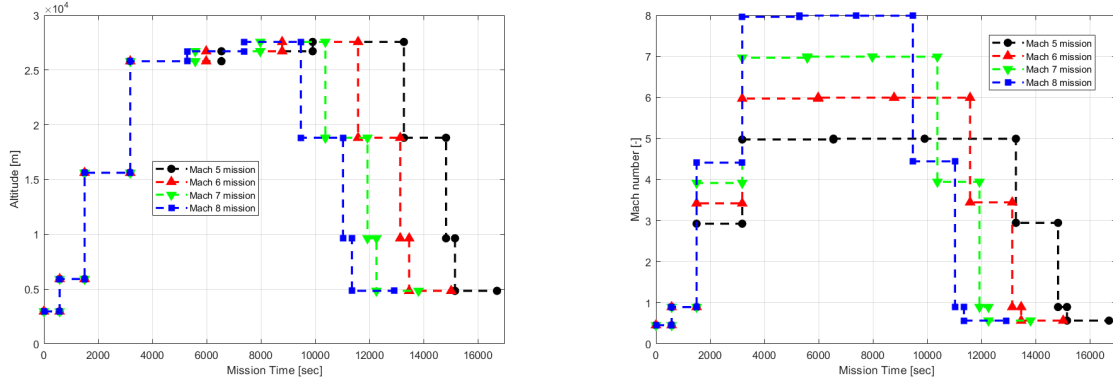


Figure 175: Scaled missions for different Mach number (fixed range of 18771 km).

In figure 176 the obtained area averaged convective heat transfer (equation 17.9) and corresponding convection-radiation equilibrium average temperature (equation 17.10 with emissivity of $\epsilon = 0.8$) throughout each of the scaled missions are provided. The average temperature computed using the methods implemented in this platform for different Mach numbers are in line with the predictions of Raymer [101], as presented in figure 23 and the predictions reported by [93].

From the computed heat properties it can be observed that with a linear increase in Mach number (from 5 to 8), the average surface temperature increases near linearly. On the other hand, the average convective heat transfer increases at near quadratic rate with a linear increase in Mach number.

$$q_{av} = \frac{\sum_P q_P A_P}{\sum_P A_P} \quad (17.9)$$

$$T_{av} = \left[\frac{q_{av}}{\sigma \epsilon} + T_{\infty, pla}^4 \right]^{\frac{1}{4}} \quad (17.10)$$

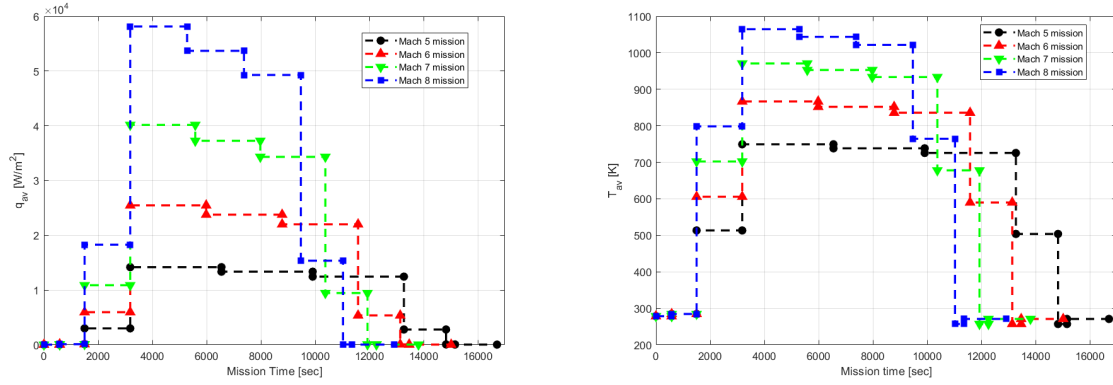


Figure 176: Average convective heat transfer (left) and conduction-radiation average surface temperature (right) throughout scaled mission profiles.

In figure 177, the change in estimated thermal protection, fuel, and take-off mass for the LAP-CAT A2 baseline configuration at varying cruise Mach numbers is provided. In addition, the change in total mission time and engine cruise specific impulse (as computed from the GHAME engine model) for the different cruise Mach number missions is shown in figure 178.

When looking at figure 177, the thermal protection system mass is predicted to gradually increase with higher cruise Mach numbers for a fixed range. This is due to the observed quadratic increase in average convective heat transfer with increasing cruise Mach numbers (figure 176). Since the convective heat transfer increases at a very high rate in comparison to the reduction in mission time that can be achieved when flying at higher cruise Mach numbers, the total heat transfer load over the vehicle increases with Mach number, thereby increasing the thermal protection system mass.

On the other hand, the decrease in mission time initially leads to a reduction in fuel mass. However at Mach number higher than 7, the decrease in mission time cannot compensate for the reduction in engine specific impulse and increasing thermal protection mass. As a result, in terms of take-off mass, an increase in cruise Mach number yields to a reduction in mass for a fixed range due to the shorter flight times that can be achieved. However, past a certain Mach number the reduction in engine specific impulse and increase in thermal protection system mass cannot be compensated by the mission time reductions which leads to an optimum cruise Mach number. In this case, for the LAPCAT A2 baseline mission, the optimal mission Mach number is estimated to be between Mach 6 and 6.5. In general, for an arbitrary configuration, the optimum cruise Mach number which minimises the aircraft take-off mass will thus be mainly dependent on a trade-off between mission time, engine specific impulse, and thermal protection system mass.

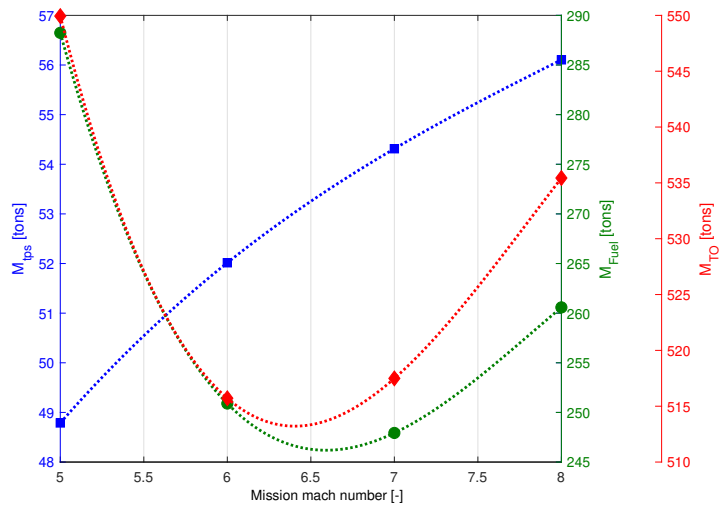


Figure 177: Change in TPS, fuel and take-off mass estimation for varying cruise Mach number of the LAPCAT A2 configuration.

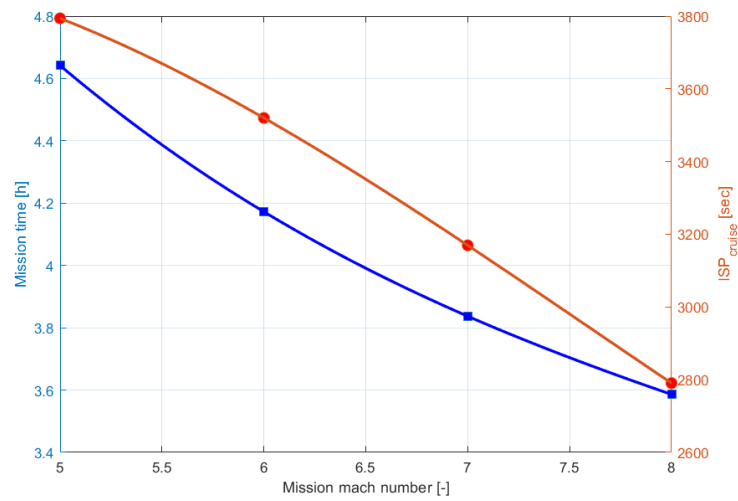


Figure 178: Change in total mission time and cruise engine specific impulse for varying Mach number.

Part V.

Conclusions and Recommendations

Based on the research carried out in this thesis different conclusions can be drawn regarding the implementation and application of the multi-disciplinary optimisation platform developed. In addition, some recommendations can be provided to tackle the limitations of the current platform and improve the models for the future.

18. Conclusions

The main goal of the current thesis was formulated as: *How can a Multi-Disciplinary Optimisation approach be used to improve the conceptual design of long-range hypersonic transport vehicles?*. In order to achieve this goal, a multi-disciplinary optimisation platform has been created to estimate the mass and aero-thermal performance of an arbitrary wing-body hypersonic configuration. A design structure matrix based on a multi-discipline feasible scheme has been incorporated to ensure consistency between aerodynamic performance and mass estimation.

The platform developed aims to minimise the take-off mass of an hypersonic aircraft using external shape variables and subjected to fuel and height constraints. Using a parametric definition of a wing-body aircraft and a discretised input mission, the MDO platform generates a three dimensional water-tight geometry using MIT Engineering SketchPAD open source software [49]. The open-source mesher, SALOME platform [34], is used to mesh the generated geometry to obtain a set of structured mesh networks by partitioning the input geometry. The meshes generated are subsequently used to generate an Aero-Thermodynamic performance matrix, A , used as input to the MDF loop and containing the lift, drag polars and heat transfers of an arbitrary configuration for each mission point.

To cover the full flow domain of a hypersonic cruise vehicle, two aerodynamic panel codes have been implemented in this platform. The panel codes integrated into the platform allow for the computation of inviscid flow over the vehicle surface. For the analysis of subsonic aerodynamics, Boeing's PANAIR higher order panel code has been integrated to the platform. For supersonic-hypersonic flow regimes, hypersonic engineering methods have been implemented based on a strip method to estimate the flow characteristics over a configuration. These include impact flow models such as the well known tangent-wedge and tangent-cone methods with prandtl expansion for shadowed flow. Viscous flow estimation are derived from the local flow properties obtained in the inviscid layer using Eckert, Van Dries and Spalding and Chi semi-empirical relations. The viscous models allow for the computation of viscous friction drag and convective heat transfers over the vehicle surface. To capture the thermal properties over the vehicle for each mission point, a Proper Orthogonal Decomposition technique was employed allowing complete convective heat transfer fields to be described as linear sets of basis functions.

Extensive validation of the aero-thermal solvers have proved their applicability to the current platform. A comparison between wind-tunnel experiments of the NACA RM L51F07 wing-body configuration and the predictions from PANAIR at Mach numbers of 0.6 and 0.8 has proven that the implemented subsonic solver matches very closely the expected local flow properties on the wing and fuselage bodies as well as being able to match closely inviscid lift and drag polars. The

main identified limitations of PANAIR include the lack of a viscous-inviscid interaction model, the small perturbation assumption, the difficulty of including leading edge vortex generation and the presence of superinclined panels at supersonic Mach numbers. As a result of these limitations, PANAIR can be used with confidence at relatively low angles of attack ($0 \leq \alpha \leq 10$ [deg]) and subsonic flow regimes ($M_\infty \leq 0.9$). For the developed hypersonic flow solver, validation performed on an ogive-cylinder body and full configurations including the X-15 research aircraft and the HyCAT hypersonic transport have confirmed the correct implementation and validity of the hypersonic engineering methods. From this set of validation, the interpolated Taylor Maccoll method has been determined to be most appropriate for estimating the lift and drag polars of fuselage bodies while the inclined wedge method should be used for lifting surfaces (wing). The limitations of implemented strip based hypersonic engineering methods include the lack of three dimensional effects such as wing-body interference, the independent panel assumption based on Newtonian flow analogy and the lack of Shock-Boundary layer interaction effects. In view of the highlighted limitation, the application of the implemented engineering methods is limited to high supersonic and hypersonic Mach numbers ($M_\infty \geq 3$) and angles of attack not exceeding 10 [deg] such that three dimensional effects are small and the strip method is applicable.

For viscous and heat transfer models, Eckert, Van Dries and Spalding and Chi models have been verified and validated using experimental results and CFD analysis for plates, wedge and cone geometries impinged in hypersonic flow conditions. From these analyses, Eckert reference enthalpy method has been determined as the most appropriate method for estimating friction coefficients and heat transfers over a wedge and cone geometry. While all methods have shown to follow the correct trend in viscous flow properties along each of the geometries investigated, the Spalding and Chi method showed considerable under-prediction for the friction coefficients, Stanton number and heat transfer computations. On the other hand, the Van Dries method was found to over-predict the viscous flow and overall, Eckert's method provides the best fit when compared to experimental and CFD data while providing conservative flow estimates. Limitations identified include the assumption of small pressure gradients, decoupling of inviscid-viscous layer, flow transition uncertainty, lack of stagnation model and the two dimensional strip flow assumption. As a result of these assumptions, the flow is modelled as fully turbulent to provide conservative heat transfer estimates and is applicable to configurations at relatively low angles of attack.

The Multi-Feasible loop incorporated in the MDO platform aims at ensuring consistency in mass estimation of a hypersonic transport aircraft whereby three modules have been implemented. The mission performance module allows for the computation of fuel mass required by assuming steady flight equilibrium of forces throughout a discretised mission. The Generic Hypersonic Aerodynamics Model Example (GHAME) engine model is used to compute the fuel flow during a mission based on a simple generic multi-cycle liquid hydrogen engine. The thermal protection system sizing module allows for the estimation of the mass of the protection system required to protect the internal load bearing substructure for the complete mission. The sizer is based on parametric curves relating TPS unit mass to total heat load during a mission for a passive TPS, allowing each mesh panel protection system thickness to be determined according to the method presented by NASA [20] for Reusable Launch Vehicles TPS. Parametric curves are generated based on the 1-D unsteady heat transfer equation with convection-radiation-conduction equilibrium and adiabatic back wall boundary conditions at the vehicle surface and sub-structure interface respectively. Among the four candidate protection materials; light silica aerogel (SiO_2TiO_2), Quartz, Saffil and Alumina Enhanced Thermal Barrier (AETB), the aerogel was found to possess the lowest unit mass as a function of heat load and would therefore be most appropriate for a hypersonic long-distance vehicle. Verification of the heat transfers and temperature distri-

butions for a similar TPS sizing platform developed by [25] on a Re-inforced Carbon-Carbon (RCC) tile under convective heat during a hypersonic decent trajectory has proved the correct implementation of the TPS model. Finally for the mass estimation module, structural component sizing is achieved through the use of the well known empirical relations from “Hypersonic Aircraft Sizing Analysis” (HASA) and “Weight Analysis of Advanced Transportation Systems” (WAATs). These correlations, although simple, allow for the sizing of each major structural component of a hypersonic aircraft and capture the vehicle mass snow-ball effect.

18.1. Case study results summary

Using the developed platform and optimiser, the LAPCAT A2 long range hypersonic transport concept by Reaction Engines [112] was used as a baseline configuration to size the aircraft for different mission scenarios. Prior to the application of the optimal sizing algorithm, a mesh convergence study and sensitivity analysis was performed on the shape variables. The optimal sizing was sub-sequentially tested on the baseline configuration and mission. Finally the effect of mission range on optimal sizing and the effect of cruise Mach number (for a fixed range) on the baseline configuration were studied. From these case studies a number of conclusions can be drawn as follows:

- **Mesh convergence study:** Using the objective function (W_{TO}) as convergence criteria for the baseline configuration, it has been shown that the developed platform is computationally efficient. Moreover, the objective function reaches a fixed value for half mesh size from 2200 to 3480 panels and the computational time increases at a quadratic rate with mesh size. The selected mesh for optimal sizing is composed of a total of 1760 panels and is within 0.4% of the fully converged objective function value with a low computational cost of 3.13 minutes. This study confirmed that the implemented platform computational cost is appropriate in the context of Multi-Disciplinary Optimisation.
- **Sensitivity Study:** The design variables were individually perturbed with respect to the baseline configuration to investigate the impact of aircraft shape parameters on the aerodynamic performance and mass distribution. In this study it was determined that regarding the wing, the platform area, aspect ratio and thickness to chord ratio have the largest impact on aircraft mass and aerodynamic performance. For each of these variables the sensitivity study shows that optimal values exist which allow for the minimisation of take off mass. Regarding the fuselage shape, a slimmer body (reduced height and width) promotes hypersonic performance through the reduction of viscous and wave drag. Also, an increase fuselage body length appears to be beneficial for hypersonic aerodynamic performance due to the associated decrease in wave drag but is detrimental for subsonic conditions due to an increase in wetted area. The fuselage body dimensions are primarily dictated by the internal volume required to store the liquid hydrogen fuel. Other design variables such as wing taper and twist have not been found to have a significant impact on aerodynamic performance and vehicle mass.
- **Baseline configuration optimal sizing:** Using the baseline mission and LAPCAT A2 configuration, the optimal sizing algorithm was applied to study the behaviour of the platform:
 - This initial study showed that the optimiser is capable of finding a local optima after 10-20 iterations and bound constraints are not active during the sizing process. This proved that an optima exists which is not influenced by artificial bound constraints but by the non-linear fuel constraint. For the baseline configuration, a 5.3% reduction in take-off mass is achieved. This is achieved through improved hypersonic aerodynamic performance, reducing the fuel mass by 17.8% at the expense of an increase

- in empty mass by 8.4%. In addition the thermal protection system is estimated to constitute the largest fraction of the vehicle structural mass, taking up about 20% of the operational empty mass. This finding highlights that one of the major priority for the success of long-range hypersonic flight is the reduction of protection system mass. Due to the long exposure time of the vehicle surface during long-range missions, passive systems may not be the optimal type of protection against convective heat transfers and semi-active cooling systems should also be investigated.
- Comparison with literature has shown that the implemented models estimations are in line with previous predictions. The main difference in mass prediction when compared to the mass estimations by Dr. Sharifzedehe thesis [93] is the thermal protection system, as a result of the overly simplified assumption by Dr. Sharifzedehe who uses a single point located at 1m from the stagnation point to estimate the entire vehicle' TPS mass. On the other hand, the parametric approach used in this thesis allows for the sizing of each of the mesh panels of the vehicle and is thus believed to provide a much more reliable prediction of TPS mass.
- **Sizing for varying mission range:** From the baseline configuration, the optimal sizing algorithm was applied to size the aircraft for increasing mission ranges:
 - The estimated take off mass of the sized configurations grows exponentially with increasing range. Fuel mass has the largest growth with range showing that a decrease in fuel consumption is one of the main key priorities to ensure the success and mass efficiency of a long-range hypersonic transport vehicle. The sized configuration dimensions increase significantly with range. The thermal protection system mass increases proportionally to the increase in mission time and vehicle wetted surface area with higher range.
 - Regarding the design variables; the wing aspect ratio has the largest impact on subsonic aerodynamic performance but its impact on hypersonic aerodynamic performance is negligible. For the wing thickness to chord ratio, the opposite is true, whereby the wing thickness has a significant impact on hypersonic aerodynamics and a small effect on subsonic conditions. As a result the optimal choice of these variables is mainly dependent on the portion of flight spent in subsonic or hypersonic flow. The optimiser attempts to reduce fuselage dimension and increase the body flatness to reduce wave drag and promote lift however, the body dimensions are mainly constrained by the liquid hydrogen fuel volume required which acts as an active constraint for each of the sized configuration.
 - Comparison of the performance of the LAPCAT A2 with other civil aviation aircraft has shown that while liquid hydrogen transport aircraft are not estimated to perform as well as subsonic kerosene and hydrogen aircraft in terms of Payload Range Efficiency and Payload mass fraction, the potential of liquid hydrogen propulsion allows such aircraft to outperform typical supersonic kerosene aircraft in terms of PRE and provide time reductions which are unachievable by subsonic aircraft.
 - **Impact of cruise Mach number on baseline configuration for a fixed range:** Using the baseline configuration, the mission cruise Mach number was gradually increased while the range was fixed to the original mission range:
 - With increasing Mach numbers, the average heat transfer on the vehicle surface increases at a near quadratic rate while temperatures vary near linearly for a fixed range. As a result even though higher cruise Mach numbers reduce mission time, the overall TPS mass is predicted to increase.

- The increase in cruise Mach number leads to a strong reduction in engine specific impulse and at high Mach numbers the mission time reduction cannot compensate for the decrease in engine performance. As a result there exist an optimum cruise Mach number for minimum take off mass which is achieved through a compromise between mission time, engine performance and thermal protection system mass.

19. Recommendations

While the current platform is believed to provide a strong basis for the application of Multi-Disciplinary Optimisation to the conceptual design of a hypersonic transport vehicles, recommendations can be provided to address the current limitations of the platform.

- **Improvement of panel codes:** Currently one of the limitations of the implemented aerodynamic solvers is the inability to compute transonic and low-supersonic flow conditions. This limitation is primarily a result of the super-inclined panel (SIP) limit of the PANAIR code. To elevate this limitation, the use of unified subsonic-transonic-hypersonic panel codes such as ZONAIR developed by ZONA Tech [133] are an attractive option but comes at a steep licencing cost. Alternatively, the PANAIR' SIP limit could be removed by applying an equivalent Mach number compressibility correction to the software according to the method presented by ZONA tech [23].
- **Use of CFD for critical flight conditions:** Another limitation of the use of inviscid panel codes is the lack of viscous-inviscid flow interaction model for predicting low speed high angle of attack stall properties and the sharp drag increase near the sound barrier. To address this limitation, the author advises the use of CFD solvers to predict the lift and drag properties of a configuration at these critical conditions. Obtaining these aerodynamic performance properties would allow for the computation of stall speed and thus required runway length as well as estimating the maximum thrust and engine air flow required to appropriately size the propulsion system. Additionally, low speed (and transonic) aerodynamic constraints could be added to the platform which could significantly impact the optimal design solutions found.
- **Improvement in structural model and stability/control:** The empirical relations used to size the hypersonic transport aircraft in the current platform are simple and allow for rapid estimation of structural component masses. However, the current relations for the wing and fuselage body only account for basic changes in planform properties and fuselage dimensions. As a result, the effect of more advanced design variables such as cranked wings and varying fuselage cross sectional shapes cannot be captured. To improve the current structural sizing while maintaining low computational costs, 1D beam element models could be implemented to size fuselage and wing components and improve the level of fidelity. The use of such model would additionally allow for the estimation of the vehicle center of gravity and allow for stability and control analysis of configurations (provided control surfaces are added to the aircraft geometry). Stability and control constraints could then also be incorporated for more realistic optimal design solutions.
- **Improvement in heat transfer and thermal protection model:** In the current platform; Eckert, Van Dries and Spalding and Chi models have been implemented to estimate viscous drag and convective heat transfers over a configuration' surface, however, the stagnation point heat is not computed. For this localised flow region, stagnation model such as Fay and Riddle [98] could be implemented. Regarding the thermal protection system sizing, currently, each of the mesh panel TPS thicknesses are sized to ensure the internal substructure does not surpass a given temperature during flight. This results in a discretised TPS thickness distribution which may not be realistically manufacturable.

To prevent this, a smooth function for TPS thickness distribution could be implemented. In addition, the TPS thickness and mass should be taken into account in the structural model as the protection system yields to a reduction in available height for the load bearing structure which could have a large impact on structural mass estimations. Finally, as was concluded from this thesis research, the protection system is predicted to constitute the largest structural mass fraction for a long-range hypersonic vehicle equipped with a passive protection system. As a result, other TPS types such as active and semi-active systems as well as more protection materials should be investigated while taking into account factors such as manufacturability and costs to determine the most appropriate system to be used.

- **Improvement in Engine model:** The engine performance model used in this thesis is the Generic Hypersonic Aerodynamics Model Example (GHAME) engine. This model is fairly basic and assumes instant changes between ideal thermodynamic cycles. Since the engine efficiency is an important aspect for predicting the total mass of a configuration, with the fuel mass constituting approximately 50% of take-off mass, higher fidelity engine models should be used in the future.

References

- [1] HYDROGEN VERSUS HYDROCARBONS A LITERATURE REVIEW OF HYPERSONIC ENGINE FUEL OPTIONS. pages 1–7.
- [2] Strength - Max. service temperature.
- [3] Hydrogen Properties. *College of the Desert*, 2001.
- [4] Hypersonic Arbitrary Body Program. *Public Domain Aeronautical Software (PDAS)*, 2002.
- [5] Aeroelastic and Aerothermoelastic Vehicle Behavior in Hypersonic Flow. *International Space Planes and Hypersonics Systems and Technologies Conference*, 46(10):1–48, 2005.
- [6] Approximate Modeling of Unsteady Aerodynamics for Hypersonic Aeroelasticity. *Journal of Aircraft*, 47(6):1932–1945, 2010.
- [7] Application of the 3D multi-block CST method to hypersonic aircraft optimization. *Aerospace Science and Technology*, 50:295–303, 2016.
- [8] Ames Aeronautical. Report 1135 - Equations, Tables and Charts for Compressible Flow. *Cartographica The International Journal for Geographic Information and Geovisualization*, 23(4):613–680, 1947.
- [9] National Aeronautics. PROPULSION FOR HYPERSONIC TRANSPORT AIRCRAFT. pages 977–999.
- [10] Airbus. Global Market Forecast 2018-2037. *Global Networks, Global Citizens*, 2018.
- [11] Airbus. Ultra Long Range A350 XWB goes the distance, 2018.
- [12] Dale Anderson, John C. Tannehill, and Richard H. Pletcher. *Computational Fluid Mechanics and Heat Transfer*. 1997.
- [13] John D. Anderson. *Hypersonic and High-Temperature Gas Dynamics, Second Edition*. AIAA Education Series, 2006.
- [14] ARC. Creep Deformation in Materials.
- [15] Michael Ashby. *Materials Selection in Mechanical Design*. 2004.
- [16] By R S Bartlett and By R S Bartlett. Tables of Supersonic Symmetrical Flow around Right Circular Cones , with and without the Addition of Heat at the Wave Tables of Supersonic Symmetrical Flow around Right Circular Cones , with and without the Addition of Heat at the Wave. 1968.
- [17] S S Benadict Bensiger and N Prasanth. Analysis of Bi-Convex Aerofoil using CFD Software at Supersonic and. 53:11695–11698, 2012.
- [18] John J Bertin. Hypersonic Aerothermodynamics.
- [19] Max Blosser and Fluids Analysis Workshop. Thermal Protection Systems for Reusable Launch Vehicles. 2003.
- [20] Max L. Blosser* and Carl C. Poteet ** , Carl J. Martin* , Kamran Daryabeigi*. REUSABLE METALLIC THERMAL PROTECTION SYSTEMS DEVELOPMENT. *NASA Langley Research Center*.

- [21] John E Bradford, John R Olds, and Technical Fellow. Thermal Protection System Sizing and Selection for RLVs Using the Sentry Code Overview : Core Competencies :. (July):1–36, 2006.
- [22] Gail Chapline, Cooper Snapp, Myron Pessin, Jim Butler, J Scott Sparks, Paul Bauer, Charles Stevenson, and Charles Stevenson. Thermal Protection Systems. *NASA*, pages 182–199.
- [23] P C Chen and D D Liu. Unified Hypersonic/Supersonic Panel Method for Aeroelastic Applications to Arbitrary Bodies. *Journal of Aircraft*, 39(3), 2002.
- [24] Kuei-Yuan Chien. HYPERSONIC, TURBULENT, COLD-WALL, SKIN-FRICTION AND HEAT-TRANSFER MEASUREMENTS ON AN AXISYMMETRIC SHARP CONE. *Naval Ordnance Laboratory*, (National Technical Information Service), 1973.
- [25] K Cowart and J Olds. AIAA 99-4806 Integrating Aeroheating and TPS Into Conceptual RLV Design Georgia Institute of Technology Atlanta , GA 9 th International Space Planes and Hypersonic Systems and Technologies Conference 3 Weakly Ionized Gases Workshop. *Aerospace*, (November), 1999.
- [26] K Cowart, J Olds, and Long Beach. AIAA 2000-5265 TCAT A Tool For Automated Thermal Protection System Design Space Systems Design Laboratory Georgia Institute of Technology Atlanta , GA AIAA Space 2000 Conference and Exposition. (September), 2000.
- [27] Lt. Kris Cowart. A Method of Integrating Reusable Design Aeroheating Launch Vehicle into Conceptual Reusable Lanch Vehicle Design. *Georgia Institute of Technology*, (June 2001), 2001.
- [28] Charlotte B. Craidon. LaWGS - A Description of the Langley Wireframe Geometry Standard Format. *NASA Technical Memorandum 85767*, 1985.
- [29] Andrew Crowell. Model Reduction of Computational Aerothermodynamics for Multi-Discipline Analysis in High Speed Flows. *PhD Thesis*, 2013.
- [30] Sebastien Defoort and Laurent Serre. ZEHST : Environmental challenges for hypersonic passenger transport ZEHST : environmental challenges for hypersonic passenger transport. (September), 2012.
- [31] Conceptual Design, Advanced Space, and Transportation Systems. Improvements in Thermal Protection Sizing Capabilities for TCAT Conceptual Design fcr Advanced Space Transportation Systems. (February 2002), 2019.
- [32] EADS. ZEHST: High-Speed Transport Concept Study, 2015.
- [33] R. G. ECKERT. SURVEY ON HEAT TRANSFER AT HIGH SPEEDS. *UNIVERSITY OF MINNESOTA*, 1962.
- [34] EDF. SALOME PLATFORM.
- [35] James C. Ellison. INVESTIGATION OF THE AERODYNAMIC CHARACTERISTICS OF A HYPERSONIC TRANSPORT MODEL AT MACH NUMBERS TO 6. *Langley Research Center*, 1997.
- [36] George Emanuel. *Analytical Fluid Dynamics, Third Edition*. 2016.
- [37] Michael A. Epton and Alfred E. Magnus. PAN AIR: A computer program for predicting subsonic or supersonic linear potential flows about arbitrary configurations using a higher

- order panel method. Volume 1: Theory document (version 3.0). *NASA Contractor Report*, (Revision 1), 1990.
- [38] Frederick Ferguson, Terry Corbett, and Haile Lindsay. THE DEVELOPMENT OF WAVERIDERS USING AN AXISYMMETRIC FLOWFIELD. pages 1–19.
- [39] Jim A. Penland Fetterman and David E. Static Longitudinal, Directional, and Lateral Stability and control data at a mach number of 6.83 of the final configuration of the X-15 research airplane. *NASA Contractor Report*, (1966), 2018.
- [40] A Gentry and D Smyth. Hypersonic Arbitrary-Body Aerodynamic Computer Program (Mark III Version). 1968.
- [41] Arvel E Gentry. Hypersonic Arbitrary-Body Aerodynamic Computer Program, Mark III Version. *McDonnell Douglas*, 1968.
- [42] Michael Joseph Gillum and Mark J Lewis. Experimental Results on a Mach 14 Waverider with Blunt Leading Edges. 34(3), 1997.
- [43] David E Glass. Ceramic Matrix Composite (CMC) Thermal Protection Systems (TPS) and Hot Structures for Hypersonic Vehicles 1. Technical Report NASA Langley Research Center, Hampton, VA 23681, 2008.
- [44] C. R. Glatt. WAATS A COMPUTER PROGRAM FOR WEIGHTS ANALYSIS OF ADVANCED TRANSPORTATION SYSTEMS. *Langley Research Center*, 2018.
- [45] C. P. GOYNE. Skin-friction measurements in high-enthalpy hypersonic boundary layers. *Journal of Fluid Mechanics* 485, 2003.
- [46] Richard Graham. *The Complete Book of the SR-71 Blackbird*. Quarto Publishing Group USA Inc., 2015.
- [47] J Grossmann. The Space Shuttle Orbiter, 2009.
- [48] IIT GUWAHATI. Module 6 : Hypersonic Viscous Interaction, 2012.
- [49] Robert Haimes. The Engineering Sketch Pad : A System for Building Parametric Geometry. (June):1–18, 2013.
- [50] Robert Haimes and John F Dannenhoffer. The Engineering Sketch Pad : System for Building Parametric Geometry. pages 1–21.
- [51] GARY J. HARLOFF and BRIAN M. BERKOWITZ. Hypersonic aerospace sizing analysis for the preliminary design of aerospace vehicles. *Journal of Aircraft*, 27(2):97–98, 1990.
- [52] J. F. Fischer Jr. Hausrath and A. H. Structural Considerations in the Design of a Liquid Hydrogen Tank for Hypersonic Vehicles. *SAE International*, Vol. 75, S, 1967.
- [53] K Higgins. Comparison of Engineering Correlations for Predicting Heat Transfer in Zero-pressure-gradient Compressible Boundary Layers with CFD and Experimental Data. *Dsto*, DSTO–TR–21, 2012.
- [54] E. Hirschel. Historical Perspective on Programs, Vehicles and Technology Issues. Number Lecture Series on Critical Technologies for Hypersonic Vehicle Development, Rhode-St-Genese,Belgium, 2004. von Karman Institute.
- [55] History NASA. Part III: THE LEAP TO SPACE : 1959-1965.
- [56] J. M. Hopkins. Ultimate Tensile Strength vs Temperature. *Hackaday*, 2016.

- [57] John Cleland Ianneti and Francesco. Thermal of the Protection Space Shuttle System. *Report, Nasa Contractor*, 1989.
- [58] By Antonella Ingenito, Stefano Gulli, and Claudio Bruno. Preliminary Sizing of an Hypersonic Airbreathing Airliner. 8:19–28, 2010.
- [59] Thomas Jazra and Michael Smart. Development of an Aerodynamics Code for the Optimisation of Hypersonic Vehicles. *47th AIAA Aerospace Sciences Meeting including The New Horizons Forum and Aerospace Exposition*, (January), 2009.
- [60] F Jivraj, R Varvill, A Bond, and G Paniagua. The Scimitar Precooled Mach 5 Engine. *2ND EUROPEAN CONFERENCE FOR AEROSPACE SCIENCES (EUCASS)*, pages 1–10.
- [61] JR JOSEPH H. KEMP. HYPERSONIC VISCOUS INTERACTION ON SHARP AND BLUNT INCLINED PLATES. *NASA Ames Research Center Moffett*, (AIAA Fluid and Plasma Dynamics Conference), 1968.
- [62] H Neale Kelly. Active Cooling From the Sixties to NASP. 1994.
- [63] David J Kinney. Aerodynamic Shape Optimization of Hypersonic Vehicles. (January):1–7, 2006.
- [64] Hiroaki Kobayashi, Hideyuki Taguchi, Exploration Agency, Takayuki Kojima, Exploration Agency, Tetsuya Sato, Senior Researcher, and Senior Researcher. Performance analysis of Mach 5 hypersonic turbojet. (September):1–9, 2012.
- [65] Takayuki Kojima, Hideyuki Taguchi, Hiroaki Kobayashi, and Atsushi Ueno. Aerodynamic heating rate evaluation of mach 5 hypersonic airplanes. 09 2012.
- [66] Alexander Kopp. Parametric Studies for the Structural Pre-Design of Hypersonic. 2012(July):20–23, 2012.
- [67] B. M. Kulfan. Universal Parametric Geometry Representation Method. *Journal of Aircraft*, 45(1):142–158, 2008.
- [68] Brenda M. Kulfan. “CST” Universal Parametric Geometry Representation Method With Applications to Supersonic Aircraft. *4th International Conference of Flow Dynamics*, pages 1–33, 2007.
- [69] Dietrich Rudolf Lampe. Thermally Perfect, Calorically Imperfect Taylor-Maccoll Flow. 9(5), 1994.
- [70] Jing Li and Weiwei Zhang. Theoretical & Applied Mechanics Letters The performance of proper orthogonal decomposition in discontinuous flows. *Theoretical & Applied Mechanics Letters*, 2016.
- [71] Marcus A Lobbia and Los Angeles. Multidisciplinary Design Optimization of Hypersonic Transport Configurations using Waveriders. pages 1–27, 2014.
- [72] J M A Longo, R Dittrich, D Banuti, M Sippel, J Klevanski, and U Atanassov. Concept Study for a Mach 6 Transport Aircraft. *American Institute of Aeronautics and Astronautic*, pages 1–16, 2003.
- [73] Chishti Maajid. Numerical Solution for Supersonic Wedge and Conical Flow. *Royal Melbourne Institute of Technology University*, pages 1–11.
- [74] Lindsay J. Lina Maglieri and Domenic J. GROUND MEASUREMENTS OF AIRPLANE SHOCK-WAVE NOISE AT MACH NUMBERS TO 2.0 AND AT ALTITUDES TO 60,000 FEET. *Langley Research Center Langley Field, Va. NATIONAL*, (March 1960), 1960.

- [75] Tariq Malik. Boeing’s Hypersonic Vision: A Sleek Passenger Plane That Can Hit Mach 5, 2018.
- [76] Nasa T N Mark D. Ardema. Structural Weight Analysis of Hypersonic Aircraft. (March 1972), 2018.
- [77] Tadeusz J. Masternak. Multi-Objective Trajectory Optimization of a Hypersonic Reconnaissance Vehicle with Temperature Constraints. page 416, 2014.
- [78] Mathworks. Choosing the Algorithm, 2018.
- [79] Yoshinori MATSUNO, Takeshi TSUCHIYA, Shunsuke IMAMURA, and Hideyuki TAGUCHI. Multidisciplinary Design Optimization of Long or Short Range Hypersonic Aircraft. *Transactions of the Japan Society for Aeronautical and Space Sciences*, 57(3):143–152, 2014.
- [80] Jack J Mcnamara. Aeroelastic and Aerothermoelastic Analysis in Hypersonic Flow : Past , Present , and Future. *AIAA Journal*, 49(6):23–26, 2013.
- [81] Peter W. Merlin. Design and Development of the Blackbird: Challenges and Lessons Learned. *NASA Dryden Flight Research Center*, (AIAA):1–38, 2009.
- [82] Li MO. *Conceptual Design Study for In-flight Refueling of Passenger Aircraft*. PhD thesis, Delft University of Technology, 2017.
- [83] STEVE H. ROWiS Moore, Frank G, MICHAEL A. ARMISTEAD. Second-order Shock-expansion Theory Extended To Include Real Gas Effects. 1992.
- [84] Benjamin J Morrell, David J Munk, Gareth A Vio, and Dries Verstraete. Development of a Hypersonic Aircraft Design Optimization Tool. *Applied Mechanics and Materials*, 553:847–852, 2014.
- [85] David J. Munk, Gareth A. Vio, and Dries Verstraete. A Hypersonic Aircraft Optimization Tool with Strong Aerothermoelastic Coupling. *Applied Mechanics and Materials*, 846:494–499, 2016.
- [86] O.J. Murillo Jr. A fast ascent trajectory optimization method for hypersonic air-breathing vehicles. *Simulation*, page 140, 2010.
- [87] K.R.A Murthy and A.G. Hammitt. Approximate Solutions for Supersonic Flow Over Wedges and Cones. pages 71–73, 1959.
- [88] David E. Myers, Carl J. Martin, Blosser, and Max L. Parametric Weight Comparison of Advanced Metallic , Ceramic Tile , and Ceramic Blanket Thermal Protection Systems. *Langley Research Center*, (June 2000), 2000.
- [89] NASA. Aerodynamic Characteristics of Supersonic-Hypersonic Flight.
- [90] NASA. X-15 Aircraft, 2006.
- [91] Hiroaki Nishikawa. Aerodynamic Heating with Turbulent Flows. pages 1–12, 1994.
- [92] Ryan Oakes. Space Shuttle Ceramic Tiles.
- [93] Design Optimization and Long-range Hydrogen-fuelled Hypersonic Cruise Vehicles. Design Optimization and Analysis of Long-Range Hydrogen-Fuelled Hypersonic Cruise Vehicles. pages 2016–2017, 2017.
- [94] PDAS. PANIN: Input Pre-Processor for PanAir. *Public Domain Aeronautical Software*.

- [95] Lin Ping, Zhang Ran, and Li Huifeng. Modeling of High Lift-drag Ratio Re-entry Vehicle Using Parameterized Configuration Approach. *Proceedings of 2012 International Conference on Modelling, Identification and Control*, (2), 2012.
- [96] Jiri Polansky. Proper Orthogonal Decomposition as a technique for identifying multiphase flow regime based on Electrical Impedance Tomography. *University of Leeds*, 2015.
- [97] Dr J. Steelant Project. LAPCAT: Long-Term Advanced Propulsion Concepts and Technologies. *ESA-ESTEC*, (2008), 2005.
- [98] Robert D Quinn and Leslie Gong. A Method for Calculating Transient Surface Temperatures and Surface Heating Rates for High-Speed Aircraft. *NASA*, 2000.
- [99] R. E. Morris and G. D. Brewer. HYPERSONIC CRUISE AIRCRAFT PROPULSION INTEGRATION STUDY. *Lockheed-California Company*, 2018.
- [100] Daniel Raymer. *Aircraft Design: A Conceptual Approach, Fifth Edition*. 2012.
- [101] Daniel P. Raymer. Aircraft Design: A Conceptual Approach. Technical report, AIAA, Reson, Viginia, 3rd Edition, 1999.
- [102] Huff R.H. Gallagher and R.D. THERMAL STRESS DETERMINATION TECHNIQUES IN SUPERSONIC TRANSPORT AIRCRAFT STRUCTURES. *Federal Aviation Agency Jointly*, (Flight Dynamics Laboratory), 1964.
- [103] Mohd Ridhwan, Bin Abu, and Bambang Basuno. The Fuselage Model of Non Circular Section. pages 5–9, 2014.
- [104] David L. Rodriguez and Peter Sturdza. A Rapid Geometry Engine for Preliminary Aircraft Design. *44th AIAA Aerospace Sciences Meeting and Exhibit*, (January):1–12, 2006.
- [105] Gary R. Saaris. A5021 User’s Manual-PAN AIR Technology Program for Solving Problems o/Potential Flow about Arbitrary Configurations. *Boeing*, 1992.
- [106] Jo Saltzmm and Darwin Jo Garringer. SUMMARY OF FULL-SCALE LIFT AND DRAG CHARACTERISTICS OF THE X-15 AIRPLANE. (March 1966), 1966.
- [107] Prof. Dr. Scholz. Aircraft Design: 13. Drag Prediction. *Hamburg University of Applied Sciences*, pages 1–16, 2015.
- [108] Prof. Dr. Scholz. Aircraft Design: 7. Wing design. *Hamburg University of Applied Sciences*, pages 1–43, 2015.
- [109] K Shimoyama and K Sagamihara. Optimal Design of Two-Stage-To-Orbit Space Planes with Airbreathing Engines. *Journal of Spacecraft and Rockets*, 42(1):90–97, 2005.
- [110] Martin Sippel, Alexander Kopp, Katalin Sinkó, and David Mattsson. Advanced Hypersonic Cryo-Tanks Research in CHATT. (September), 2012.
- [111] A K Sreekanth. *Aerodynamic Predictive Methods And Their Validation in Hypersonic Flows*. 2003.
- [112] J Steelant. LAPCAT : High-Speed Propulsion Technology. pages 1–38, 2008.
- [113] JONATHAN STRICKLAND. How the Apollo Spacecraft Worked.
- [114] Studylib. RATE OF CLIMB.
- [115] Patrick T Summers, Yanyun Chen, Christian M Rippe, Ben Allen, Adrian P Mouritz, Scott W Case, and Brian Y Lattimer. Overview of aluminum alloy mechanical properties during and after fires. *Fire Science Reviews*, 4(1):3, 2015.

- [116] T H E Mark I V Supersonic-hypersonic, E Arvel, Douglas N Smyth, and Wayne R Oliver. Mark IV SuperHypersonic Arbitrary Body Program. II, 1973.
- [117] Atsushi UENO TAGUCHI and Hideyuki. Aero-thermodynamic design of JAXA’s hypersonic passenger aircraft. In *1st International Symposium: “Hypersonic flight: from 100.000 to 400.000 ft”*, Rome, Italy. Japan Aerospace Exploration Agency.
- [118] Hideyuki Taguchi, Hiroaki Kobayashi, Takayuki Kojima, Atsushi Ueno, Shunsuke Imamura, Motoyuki Hongoh, and Kenya Harada. Research on hypersonic aircraft using pre-cooled turbojet engines. *Acta Astronautica*, 73:164–172, 2012.
- [119] Ilias G Tapeinos, Sotiris Koussios, Roger M Groves, Structural Integrity, and Composites Group. Design and Analysis of a Multi-Cell Subscale Tank for. (July):19–24, 2015.
- [120] C. Terhes. PRELIMINARY STRUCTURAL DESIGN FOR A HYPERSONIC UAV. *Glass*, (April):453–463, 2014.
- [121] The Telegraph. Qantas promises 20-hour direct flights from London to Sydney by 2022 – but where’s next?
- [122] Takeshi Tsuchiya, Yoichi Takenaka, and Hideyuki Taguchi. Multidisciplinary Design Optimization for Hypersonic Experimental Vehicle. *AIAA Journal*, 45(7):1655–1662, 2007.
- [123] G Tulapurkara. Chapter 6 Fuselage and tail sizing - 4 Lecture 26 Topics. *Airplane design (Aerodynamic)*, pages 1–10.
- [124] Atsushi Ueno and Kojiro Suzuki. Two-Dimensional Shape Optimization of Hypersonic Vehicles Considering Transonic Aerodynamic Performance. *Transactions of the Japan Society for Aeronautical and Space Sciences*, 52(176):65–73, 2009.
- [125] Dries Verstraete. The Potential of Liquid Hydrogen for long range aircraft propulsion. *PhD Thesis*, (CRANFIELD UNIVERSITY), 2009.
- [126] Dries Verstraete, Shayan Sharifzadeh, Patrick Hendrick, and Mechatronic Engineering. DEFINITION AND AERO-ELASTIC OPTIMISATION OF THE STRUCTURE OF THE LAPCAT A2 MACH 5 AIRLINER. 2006.
- [127] Eric W Weisstein. Super Ellipse.
- [128] Frank M. White. *Viscous Fluid Flow*. 1974.
- [129] Louis J. Williams. ESTIMATED AERODYNAMICS OF ALL-BODY HYPERSONIC AIRCRAFT CONFIGURATIONS. *NASA, Office of Advanced Research and Technology*, (March 1971), 1971.
- [130] R D Witcofski. HYDROGEN FUELED HYPERSONIC TRANSPORTS. *NASA Langley Research Center*.
- [131] Tian-tian Zhang, Zhen-guo Wang, Wei Huang, and Li Yan. Parameterization and optimization of hypersonic-gliding vehicle configurations during conceptual design. *Aerospace Science and Technology*, 58(September):225–234, 2016.
- [132] ZONA. ZONAIR Applications Manual. *ZONA TECHNOLOGY INC*, 2016.
- [133] ZONA. ZONAIR User’s Manual: Engineering Software for Aerodynamics and Flight Loads. *Zona Technology Inc*, 2016.

A. Dimensionalisation of subsonic inviscid results (PANAIR)

To dimensionalise the results of the subsonic analysis (PANAIR), the inviscid flow velocity is first evaluated by multiplying equation 11.37 by the freestream velocity $V_\infty = M_\infty \sqrt{\gamma RT_\infty}$. Then using the definition of the pressure coefficient ($c_p = \frac{P - P_\infty}{q_\infty}$), the local inviscid layer pressure can be computed using equation A.1. Now using the isentropic relations and the speed of sound definition $a = \sqrt{\gamma RT}$, the temperature is defined in equation A.2 and can be re-arranged according to equation A.3. Finally the inviscid layer density can be derived from the equation of state using equation A.4.

$$P_{inv} = \frac{1}{2} \rho_\infty V_\infty^2 c_{p,2nd} + P_\infty \quad (\text{A.1})$$

$$\frac{T_{inv}}{T_\infty} = \frac{1 + \frac{\gamma-1}{2} M_\infty^2}{1 + \frac{\gamma-1}{2} M_{inv}^2} = \frac{1 + \frac{\gamma-1}{2} M_\infty^2}{1 + \frac{\gamma-1}{2} \left(\frac{V_{inv}^2}{\gamma RT_{inv}} \right)} \quad (\text{A.2})$$

$$T_{inv} = T_\infty \left(1 + \frac{\gamma-1}{2} M_\infty^2 \right) - \frac{\gamma-1}{2} \frac{V_{inv}^2}{\gamma R} \quad (\text{A.3})$$

$$\rho_{inv} = \frac{P_{inv}}{RT_{inv}} \quad (\text{A.4})$$

B. Real gas equations for air

Real gas effects are taken into account using Sutherland's law [93] [12] to compute the flow dynamic viscosity μ and the thermal conductivity k as a function of the gas temperature. For the specific heat at constant pressure c_{spe} , thermally perfect gas is assumed and evaluated using equation B.3 from [8]. In equation B.3, the perfect gas specific heat $c_{spe,perf}$ is equal to 1005 J/kg.K and the perfect specific ratio is set to $\gamma_{perf} = 1.4$ [-]. The correction factor is set to $\Theta = 3311$ Kelvins as recommended by [8] for engineering analysis.

$$\mu(T) = \frac{1.458 \cdot 10^{-6} \cdot T^{3/2}}{T + 110.4} \quad (\text{B.1})$$

$$k(T) = \frac{2.495 \cdot 10^{-3} \cdot T^{3/2}}{T + 194} \quad (\text{B.2})$$

$$c_{spe}(T) = c_{spe,perf} \left[1 + \frac{\gamma_{perf} - 1}{\gamma_{perf}} \left[\left(\frac{\Theta}{T} \right)^2 \frac{e^{\frac{\Theta}{T}}}{\left(e^{\frac{\Theta}{T}} - 1 \right)^2} \right] \right] \quad (\text{B.3})$$

C. Additional flow diagrams

C.1. Viscous thermal analysis computations

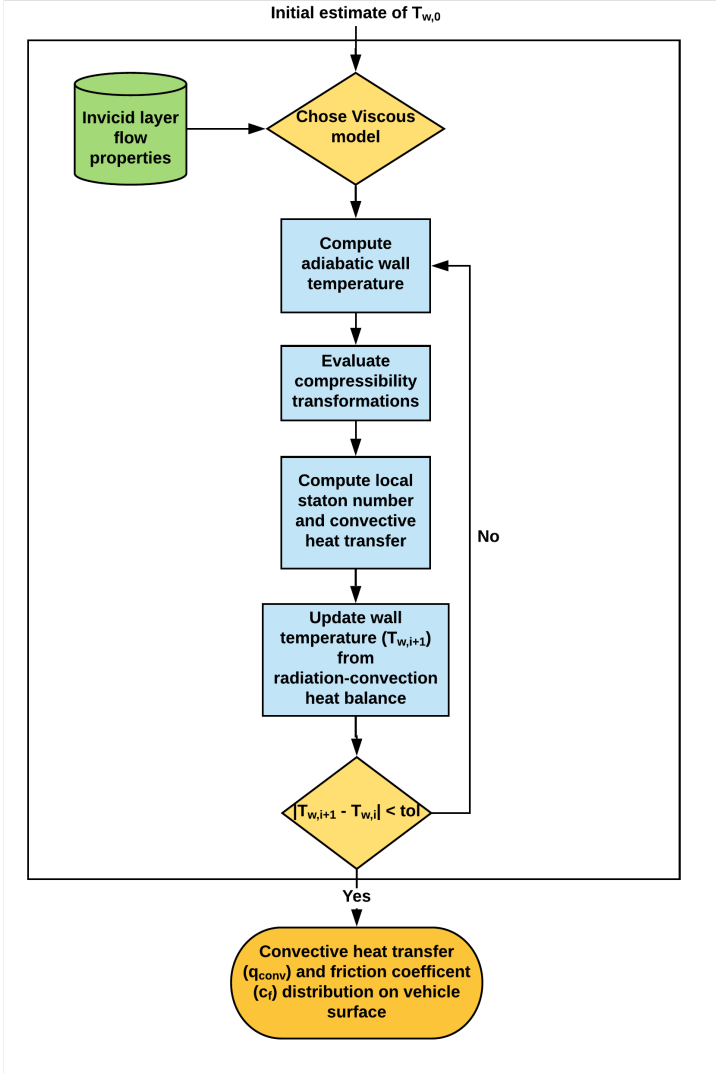


Figure 179: Viscous-Thermal computations flow diagram.

C.2. Thermal Protection System sizing

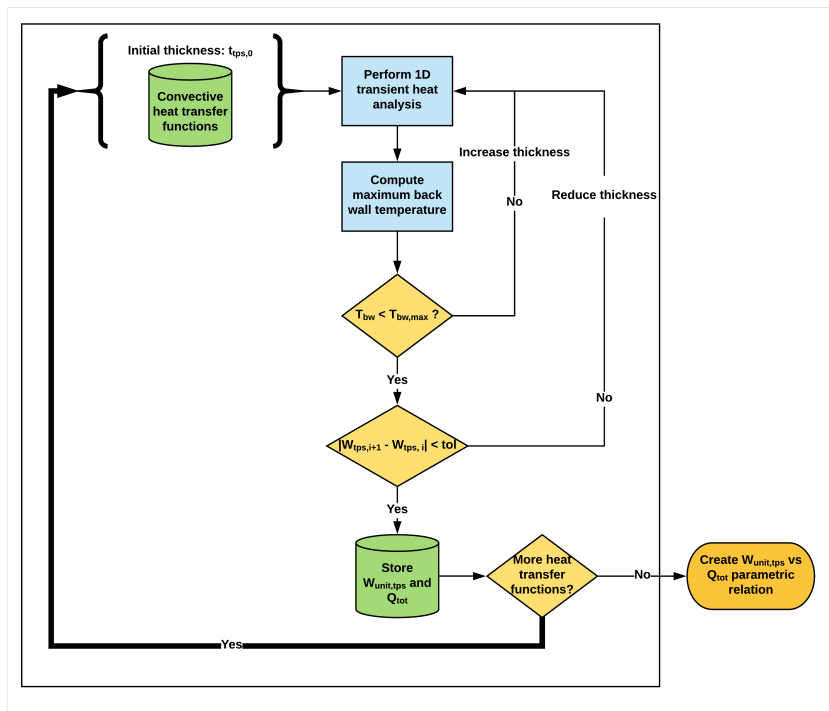


Figure 180: TPS sizing flow diagram.

C.3. Component mass estimation

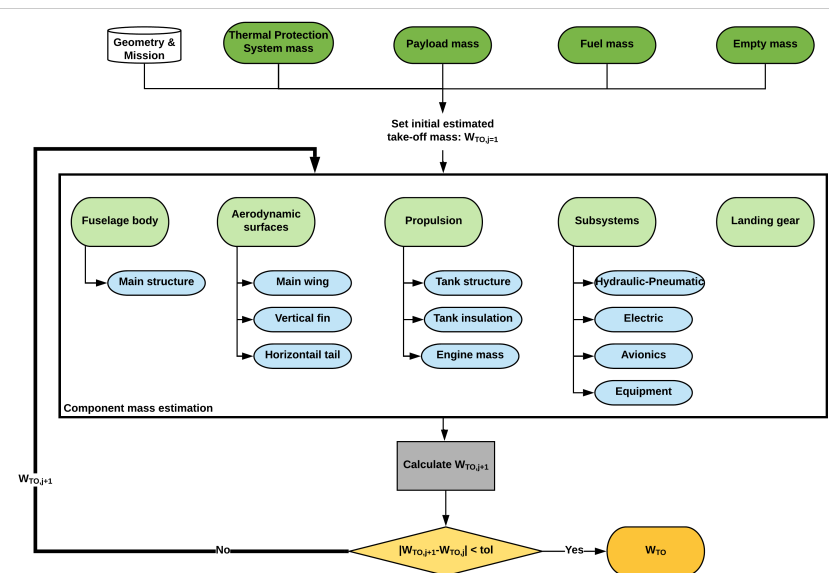


Figure 181: Structural component mass estimation flow diagram.

D. Hypersonic solver solution examples

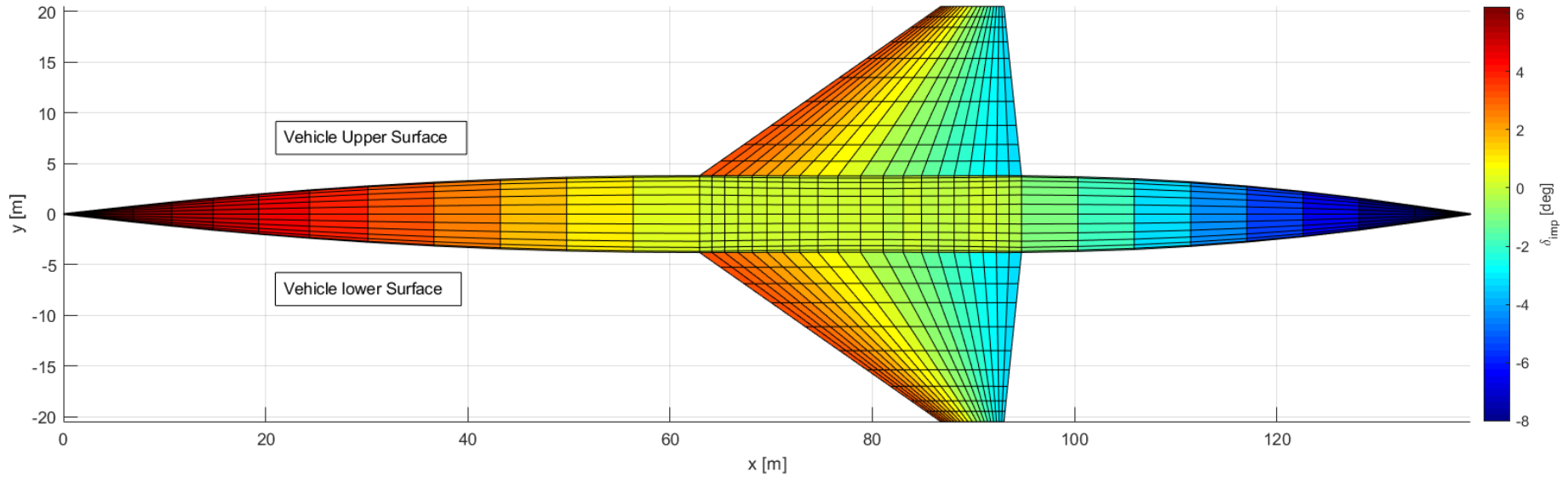


Figure 182: Impact angles over LAPCAT A2 baseline configuration at AOA = 0 [deg], M = 5 [-] and ALT = 25.8 [km].

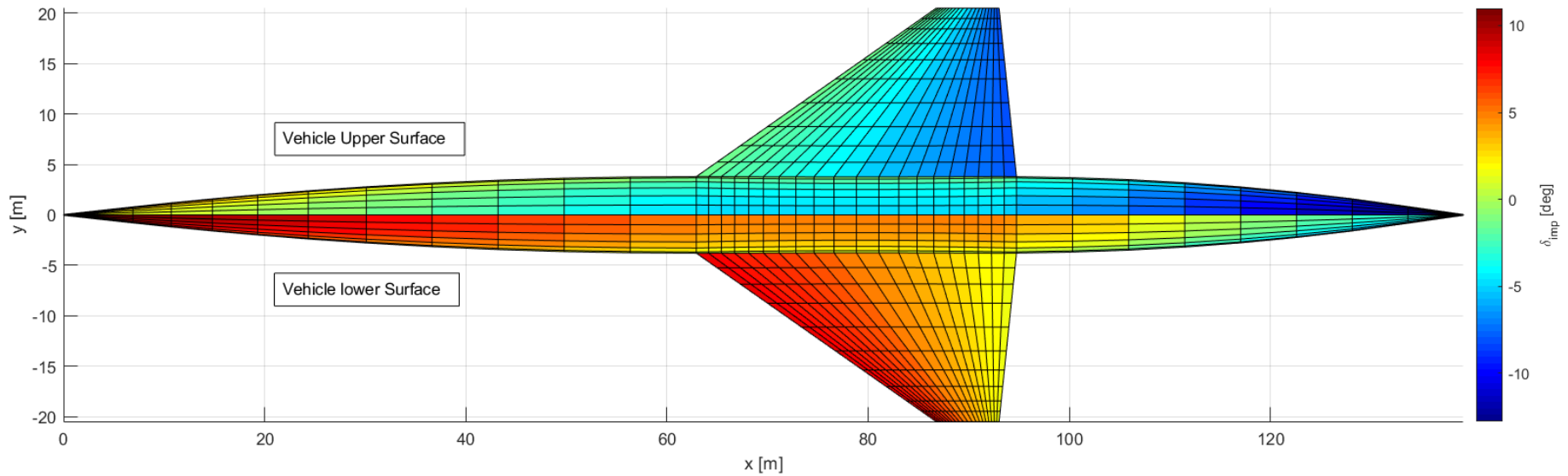


Figure 183: Impact angles over LAPCAT A2 baseline configuration at AOA = 5 [deg], M = 5 [-] and ALT = 25.8 [km].

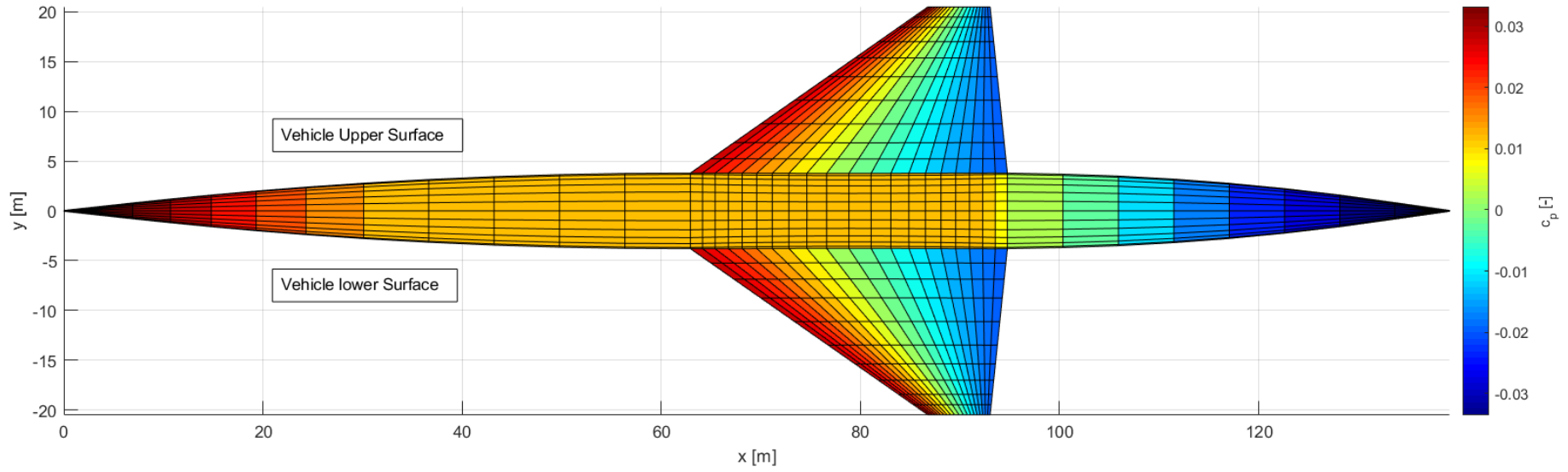


Figure 184: Pressure coefficient distribution over LAPCAT A2 baseline configuration at AOA = 0 [deg], M = 5 [-] and ALT = 25.8 [km].

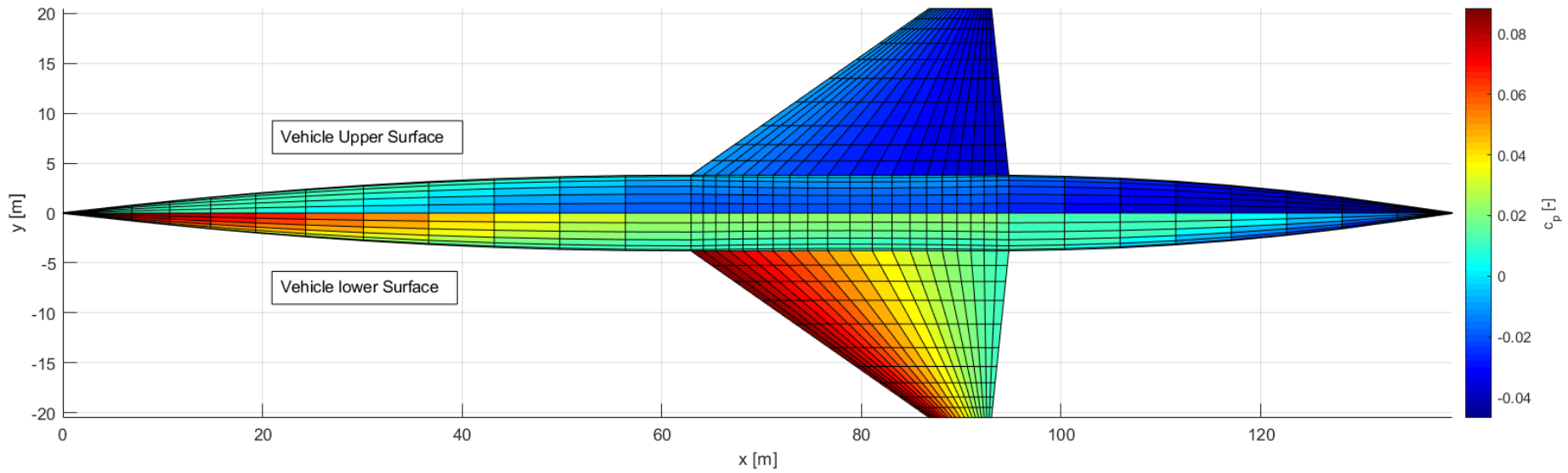


Figure 185: Pressure coefficient distribution over LAPCAT A2 baseline configuration at AOA = 5 [deg], M = 5 [-] and ALT = 25.8 [km].

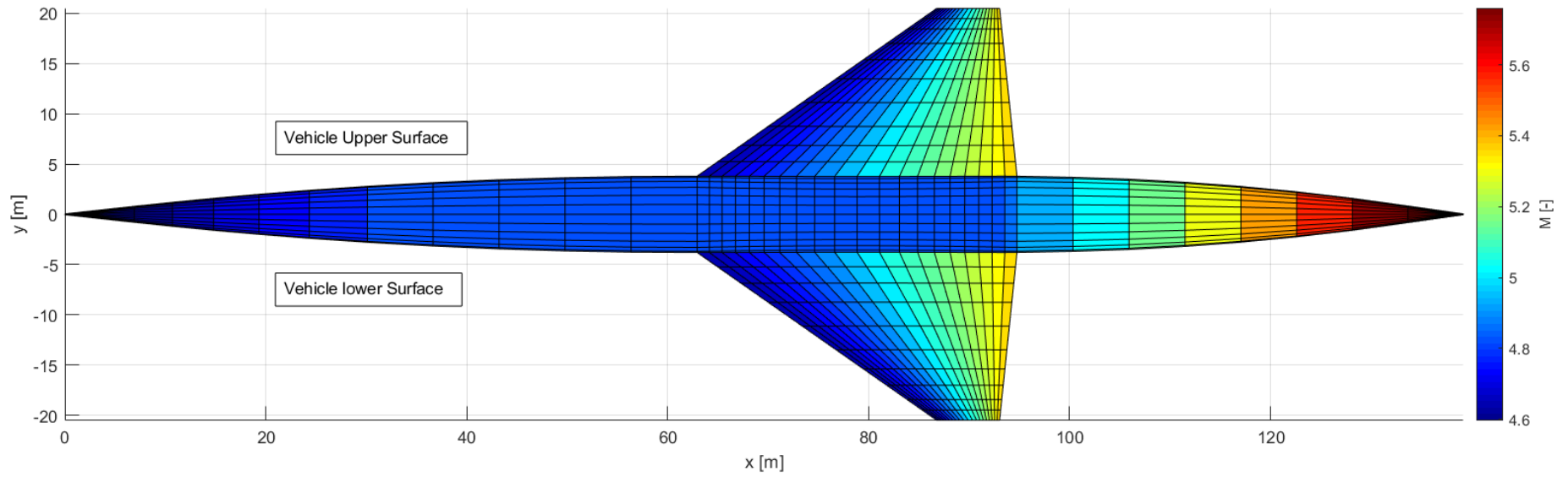


Figure 186: Mach number distribution over LAPCAT A2 baseline configuration at AOA = 0 [deg], M = 5 [-] and ALT = 25.8 [km].

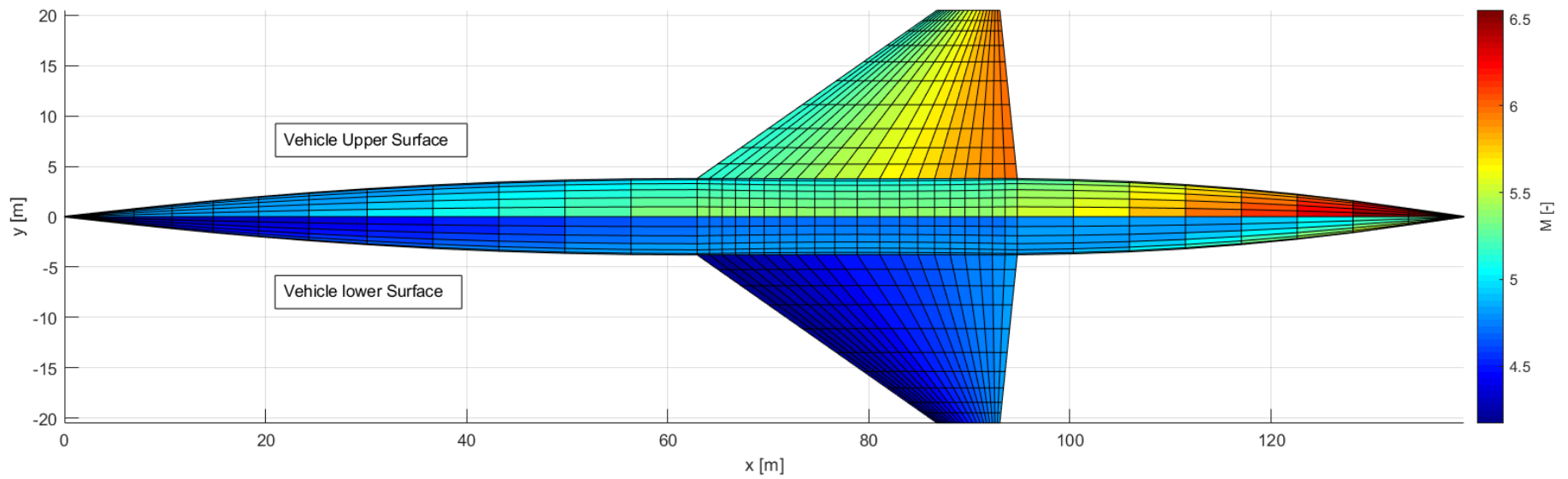


Figure 187: Mach number distribution over LAPCAT A2 baseline configuration at AOA = 5 [deg], M = 5 [-] and ALT = 25.8 [km].

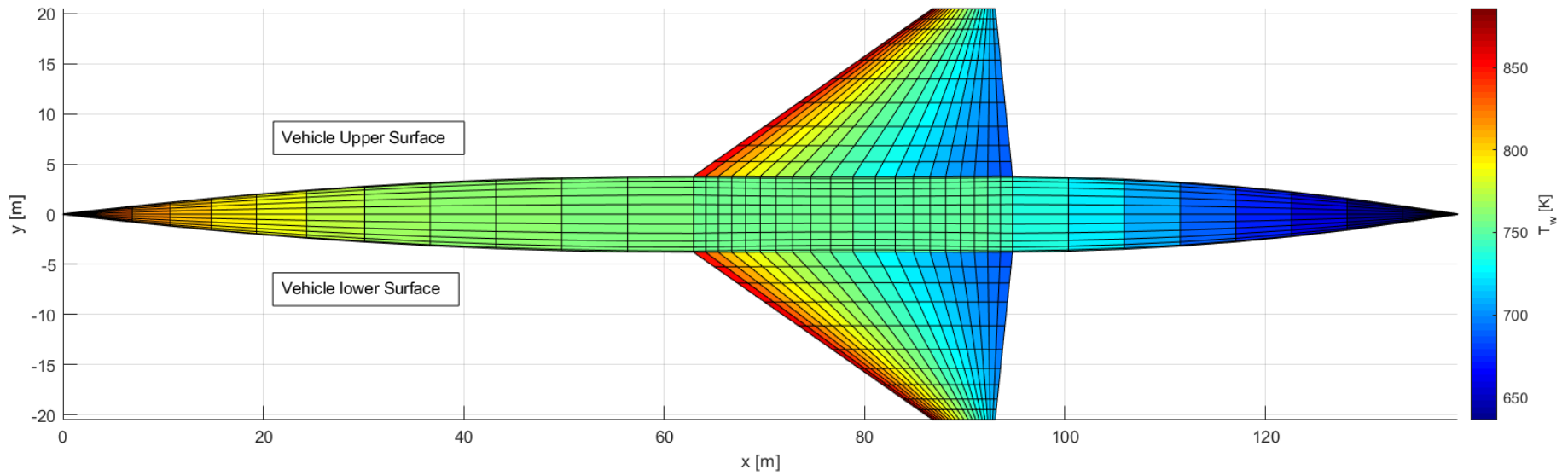


Figure 188: Convection-Radiation equilibrium wall temperature distribution over LAPCAT A2 baseline configuration at AOA = 0 [deg], M = 5 [-] and ALT = 25.8 [km].

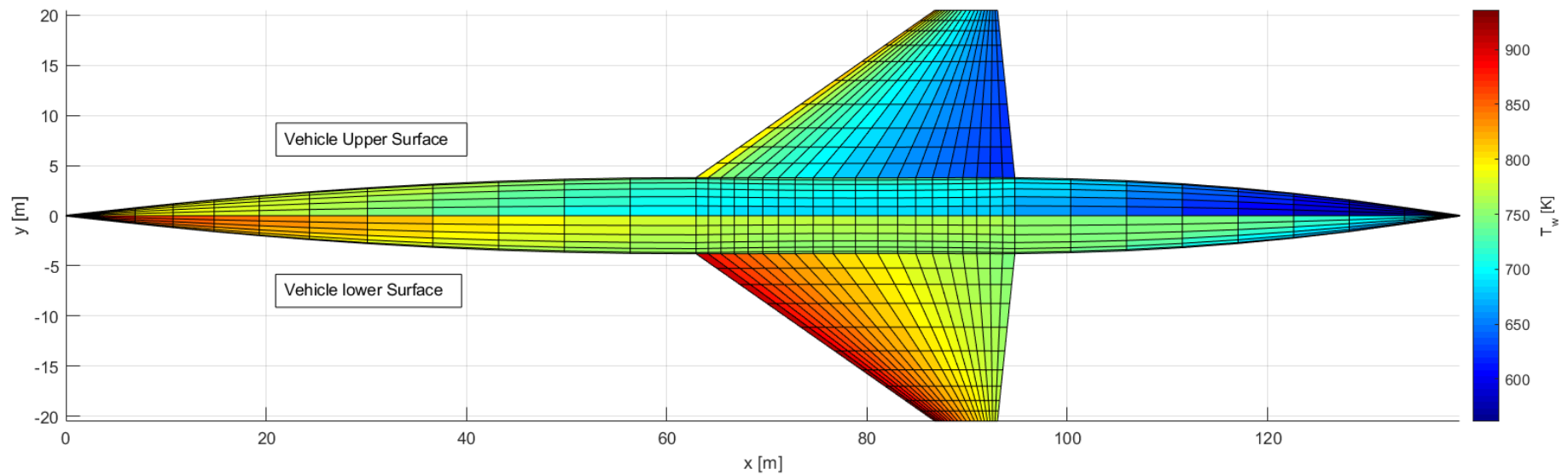


Figure 189: Convection-Radiation equilibrium wall temperature distribution over LAPCAT A2 baseline configuration at AOA = 5 [deg], M = 5 [-] and ALT = 25.8 [km].

E. PANAIR pressure validation along wing span at $M = 0.6$ [-]

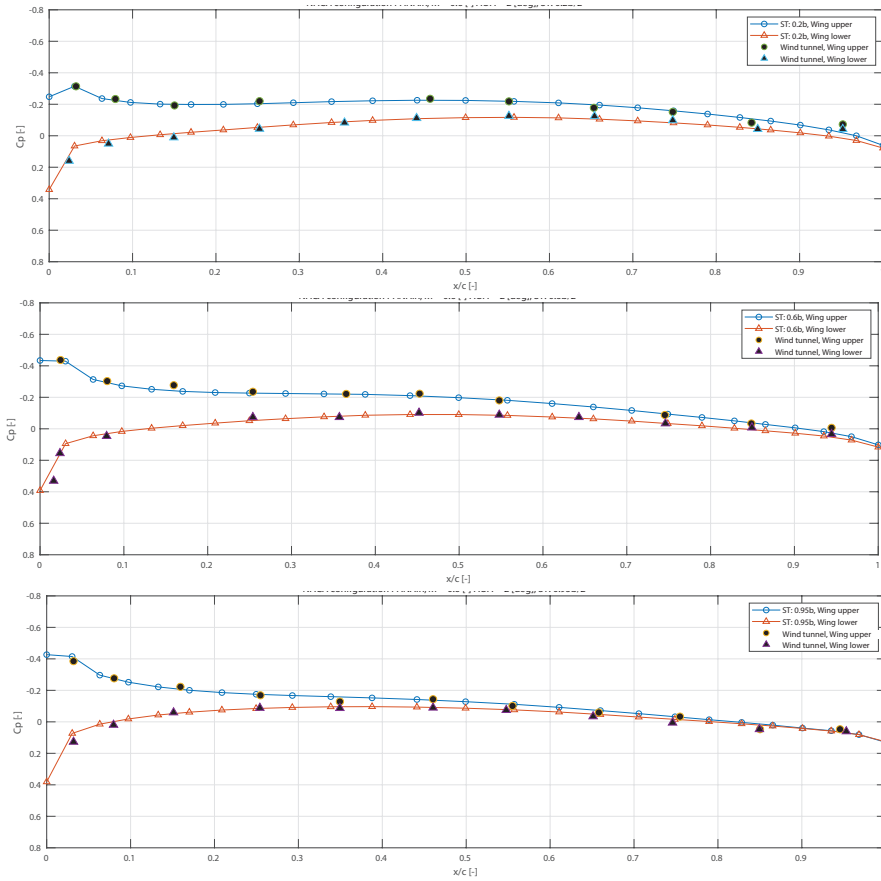


Figure 190: Pressure distribution along wing span at $M = 0.6$ and $AOA = 2$ [deg], $ST = 0.2b_s, 0.6b_s, 0.95b_s$ (top to bottom).

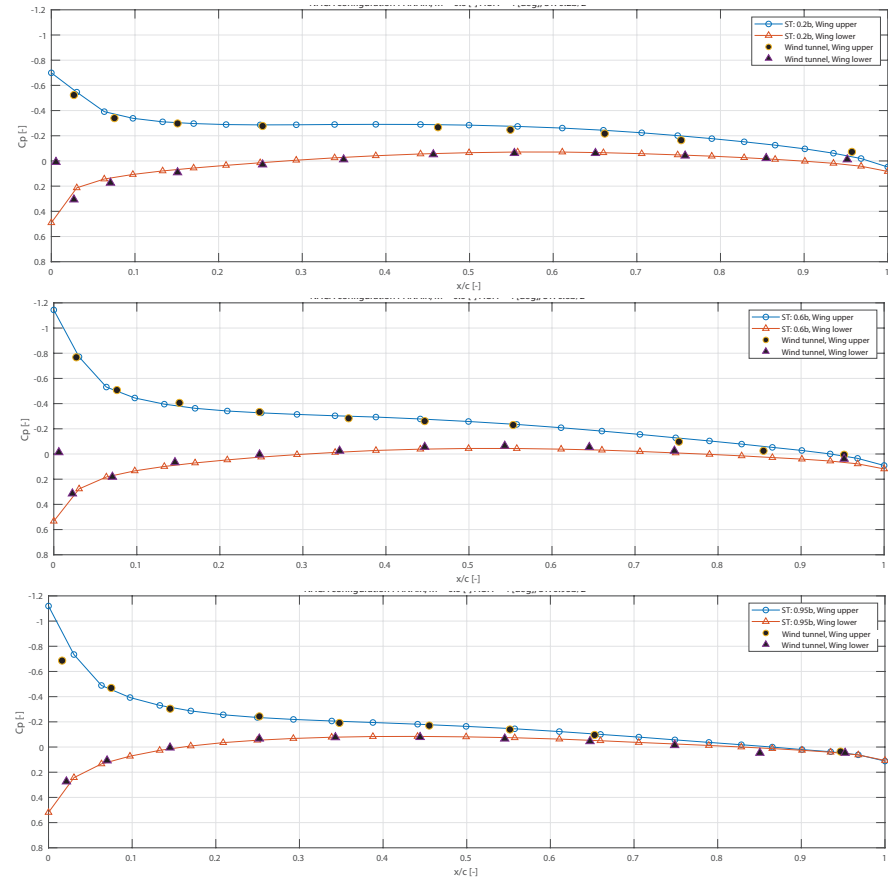


Figure 191: Pressure distribution along wing span at $M = 0.6$ and $AOA = 4$ [deg], $ST = 0.2b_s, 0.6b_s, 0.95b_s$ (top to bottom).

F. Additional viscous flow validation

Experiments performed by Goyne et al. and Chien are conducted under various freestream flow conditions over a flat plate (Goyne) and cone (Chien) in hypersonic flow [45] [24]. These experiments sample the Stanton number C_H and local friction coefficients c_f along the length a flat plate and cone [45] [24]. These experimental result have been used over the years to verify and validate the results of CFD and semi-empirical methods to determine the flow properties in a hypersonic viscous boundary layer [93].

In this section, the various viscous flow semi-empirical models of Eckert, Van Dries and Spalding and Chi presented in Section 11 and implemented in the current platform to predict vehicle viscous drag $C_{D,v}$ and convective heat transfers q_{conv} are compared to the validation data presented by Goyne and Chien.

The flat plate hypersonic experiments reported by Goyne consist of three different sets of laminar/turbulent boundary layer conditions described in Table 193. In addition, the experiments are performed on a 1 meter long plate with the wall temperature fixed to $T_w = 300K$. For the semi-empirical models, the freestream conditions are reproduced for each of the experimental set described by Goyne on a flat plate mesh model containing 100 elements along the 1 meter plate length. In addition, for the semi-empirical models, a reynolds analogy of $R_f = 1.1[-]$ is selected for the turbulent flow and the inviscid flow conditions over the flat plate are equal to the freestream conditions (no flow deflection over a flat plate). The comparison of the different experimental datasets of Goyne and the results obtained from the semi-empirical viscous flow models is given in figure 194. The results of the Stanton number C_H as a function of the local reynolds number Re are reported. The local friction coefficient c_f can be related to the local Stanton number by equation 11.40.

Set	T[K]	P[kPa]	ρ [kgm ⁻³]	h_0 [MJkg ⁻¹]	u [ms ⁻¹]	M	Re [m ⁻¹]
Laminar 1	486	0.87	0.0063	4.4	2800	6.4	0.669×10^6
Laminar 2	772	1.03	0.0045	7.8	3460	6.2	0.434×10^6
Laminar 3	1010	2.70	0.0090	9.1	3740	5.9	0.789×10^6
Turbulent 1	336	8.14	0.0842	3.2	2425	6.6	10.1×10^6
Turbulent 2	741	10.90	0.0499	6.2	3240	6.0	4.65×10^6
Turbulent 3	1147	10.10	0.0294	9.0	3783	5.7	2.45×10^6

Figure 192: Goyne et al. average test conditions on a hypersonic flat plate [45] [93].

The hypersonic cone experiments reported by Chien also consist of three different sets of freestream flow conditions given in Table 193. The model for this experiment is a 1 meter long sharp cone with $5[deg]$ semi-apex angle. The wall temperature is varied for the three different experimental sets but is kept constant over the cone surface. Once again a reynolds analogy of $R_f = 1.1[-]$ is selected for the turbulent flow with 100 panels distributed along the cone length. For the inviscid flow conditions, the interpolated taylor maccoll (tangent-cone) impact model from Section 11.1 is used. The experimental local Stanton number C_H results from Chien for the different set conditions are compared to the implemented semi-empirical models in figure 195.

Set	Chien (1974)		
	1	2	3
r_n [m]	Sharp	Sharp	Sharp
Half-angle [°]	5	5	5
M	7.9	7.9	7.9
Chord [m]	0.5977	0.5977	0.5977
Re_u [m^{-1}]	30.7×10^6	25.8×10^6	35.5×10^6
T_∞ [K]	60.38	59.93	60.23
P_∞ [kPa]	1.459	1.675	1.677
T_w [K]	288	158	88
Flow Type	Transition	Transition	Transition

Figure 193: Chien average test conditions on a hypersonic sharp cone [24] [93].

Firstly, observing the comparison of the semi-empirical methods with the validation data over the flat plate model (figure 194) it can be seen that the Eckert laminar flow model fits the validation data well over the three datasets. For turbulent flow, the spalding and chi model underestimates the Stanton number in all three validation sets thereby also underestimating the local friction coefficient. The turbulent Eckert and Van dries methods on the other hand correlate much better with the validation data over the three different sets. For sets 2 and 3, the difference between the Stanton number predicted by both method is very small. However for set 1, at higher freestream Mach number, the Van Dries method best approximates the validation data.

Secondly, observing the comparison over the conical model (figure 195), it can be seen once again that the laminar flow model from Eckert is able to correctly predict the local Stanton number at lower reynolds number ($0 < Re_x < 0.4 \cdot 10^7$). Transition to turbulent flow over the cone occurs for reynolds number between (approximately) $0.4 \cdot 10^7 < Re_x < 1 \cdot 10^7$ for all three validation datasets. Overall, once again, the results estimated by the spalding and chi method underestimate the local Stanton number over the cone length for all three datasets. Eckert turbulent flow model underestimates the Stanton number for set 1, gives a good fit for set 2 while overestimating the validation data in set 3. Overall, once again the Van Dries method provides the best overall fit of the validation data for turbulent boundary layers.

The primary conclusion from this validation study is that Eckert and Van Dries models are judged to be the most appropriate semi-empirical viscous flow models for flat plates and conical flow. The Van dries model performs slightly better than the Eckert model in turbulent flow, however the advantage of Eckert model is that it is applicable to both laminar and turbulent flows.

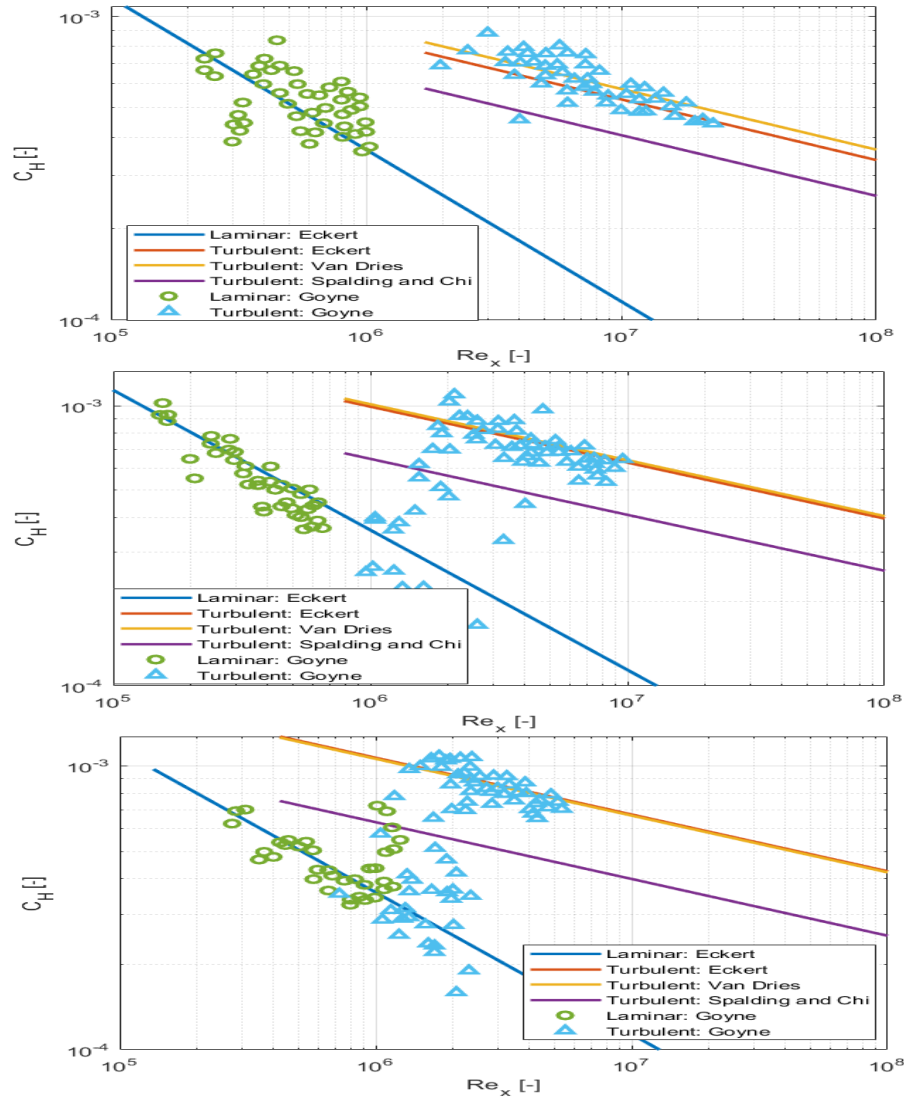


Figure 194: Stanton number comparison for a flat plate under conditions described by Goyne in Table 192, sets : 1,2,3 (top to bottom).

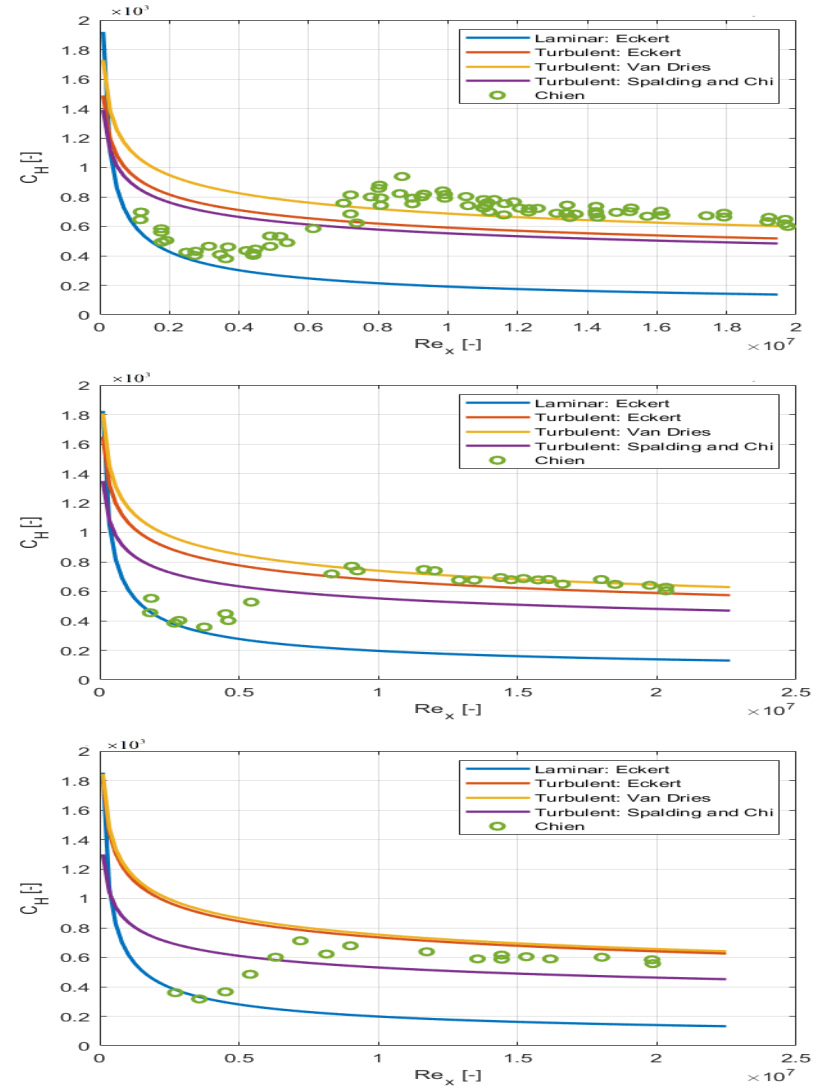


Figure 195: Stanton number comparison for a 5 [deg] sharp cone under conditions described by Chien in Table 193, sets : 1,2,3 (top to bottom).

G. Vertical Tail sizing

For the vertical tail sizing, the methodology employed here is the classical volume ratio method [123], whereby the vertical tail area is sized based on the ratio of similar aircraft. In the volume ratio method, the vertical tail area is sized according to the volume ratio $C_{vt,ref}$ defined by equation G.1. The reference moment arm of the vertical tail $l_{arm,vt,ref}$ is obtained as the longitudinal distance between the quarter mean aerodynamic chord (MAC) of the reference wing (where the center of gravity of the aircraft is assumed to be located) and the quarter MAC of the reference vertical tail. The subscript *ref* stands for the reference values as defined by the baseline aircraft (table 10).

$$C_{vt,ref} = \frac{l_{arm,vt,ref} \cdot S_{vt,ref}}{b_{w,ref} \cdot S_{w,ref}} \quad (G.1)$$

Now in order to resize the vertical tail surface area, the reference volume coefficient $C_{vt,ref}$ and the planform shape parameters ($AR_{vt,ref}$; $\lambda_{vt,ref}$; $\Lambda_{vt,LE,ref}$) of the vertical tail are kept constant. Throughout the optimisation process, a change in main wing area S_w , wing span b_w or vertical tail moment arm $l_{arm,vt}$ require a re-sizing of the vertical tail. The new vertical tail area is given by solving equation G.2. However, as can be seen, this equation is implicit since the vertical tail moment arm is itself dependent on the new vertical tail area such that $l_{arm,vt} = f(S_{vt})$. Therefore to solve for the vertical tail area, the non linear MATLAB solver *fsolve* is used to find the tail area which satisfies equation G.2 where the moment arm of the vertical tail is computed using equations G.3.

$$S_{vt} - \frac{C_{vt,ref} \cdot S_w \cdot b_w}{l_{arm,vt}} = 0 \quad (G.2)$$

$$\begin{aligned} h_{vt} &= \sqrt{S_{vt} \cdot AR_{ref}} \\ c_{r,vt} &= \frac{2 \cdot S_{vt}}{(1 + \lambda_{ref}) \cdot h_{vt}} \\ MAC_{vt} &= \frac{2}{3} \cdot c_{r,vt} \cdot \frac{1 + \lambda_{vt,ref} + \lambda_{vt,ref}^2}{1 + \lambda_{vt,ref}} \\ z_{MAC,vt} &= h_{vt} \cdot \frac{(MAC_{vt} - c_{r,vt})}{c_{r,vt} \cdot (\lambda_{vt,ref} - 1)} \\ l_{arm,vt} &= L_{fus} - c_{r,vt} + \tan(\Lambda_{vt,LE,ref}) \cdot z_{MAC,vt} + 0.25 \cdot MAC_{vt} - cg_w \end{aligned} \quad (G.3)$$

H. Additional results: Design variable sensitivities

In this Appendix, the sensitivities of the estimated aircraft mass distribution and subsonic/hypersonic lift to drag ratio with respect to the remaining design variables (figure 196) are summarised.

Taper ratio:

- An increase in taper ratio leads to an increase in wing mass according to equation 14.1. Overall the effect of taper ratio on estimated mass are very small.
- Taper ratio appears to have a negligible effect on both subsonic and hypersonic aerodynamic performance.

Wing tip twist angle:

- The wing tip twist angle leads to a shift in lift to drag polars. The twist angle must be chosen to allow the aircraft to fly at an angle of attack which maximises the lift to drag ratio to reduce fuel mass.
- Twist does not influence the structural mass fraction of the wing in this model due to the lack of twist effects on the wing mass semi-empirical formula employed in equation 14.1. Although twist would have an effect on wing structural mass, this effect is expected to be small.

Fuselage width factor:

- An increase in fuselage width increases the amount of effective lifting surface by making the fuselage a lifting body, thereby increasing the lift curve and decreasing the lift induced drag coefficient. However with increased width, the wave drag drastically increases as a result of stronger impact angles on the fuselage forebody. Additionally the increase in width is associated with an increase in wetted to platform area ratio leading to an higher viscous drag contribution. Overall as a result, increasing the fuselage width reduces the lift to drag ratio of the aircraft.
- In addition, increasing the fuselage width also results in a higher fuel tank volume and surface area leading to an increased tank mass fraction.

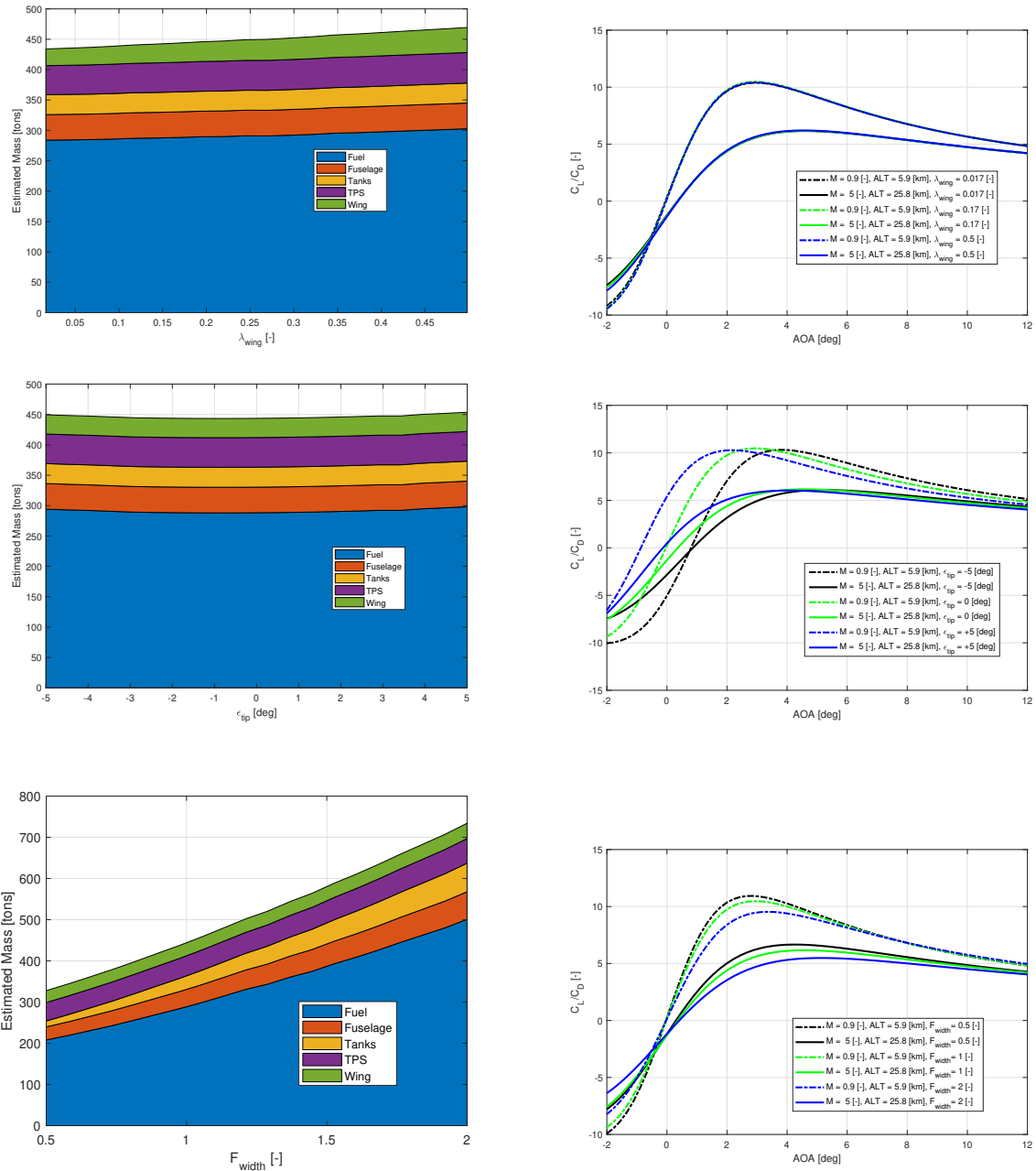


Figure 196: Effect of changes in wing taper ratio (top), wing tip twist angle (middle) and fuselage width factor (bottom) on estimated mass distribution and subsonic/hypersonic lift to drag polars.

I. Additional sensitivities: Lift, Drag and Drag due to lift polar

In this Appendix the sensitivities of the subsonic and hypersonic lift (C_L vs α), drag (C_D vs α) and drag due to lift polars (C_D vs C_L^2) with respect to the different design variables are provided.

Wing planform area effects:

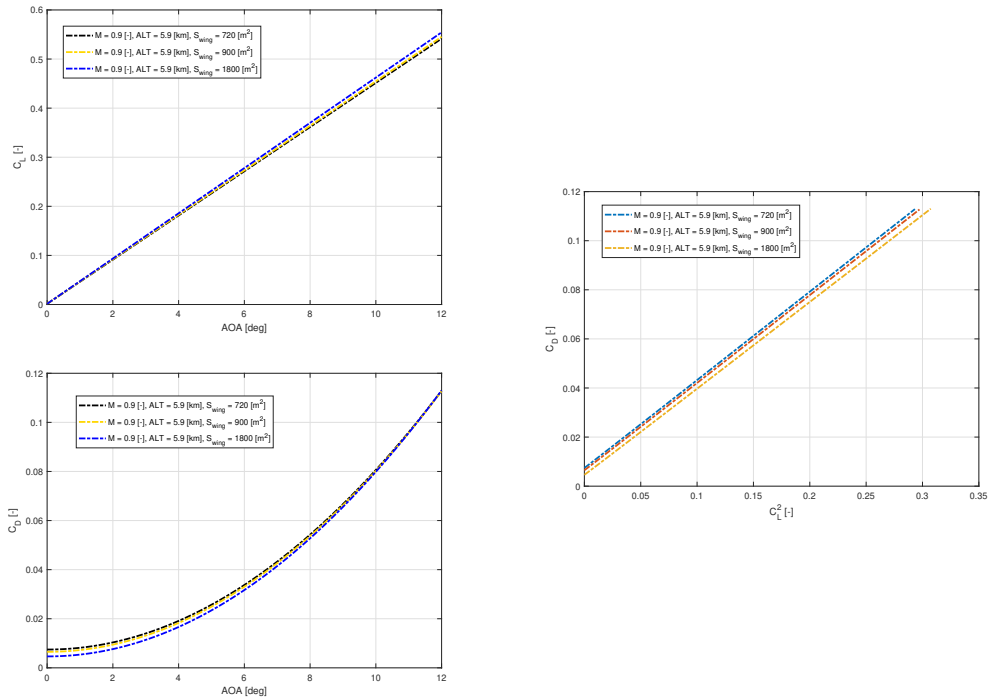


Figure 197: Effect of wing planform area on Subsonic lift (top left), drag (bottom left) and drag due to lift (right) polars.

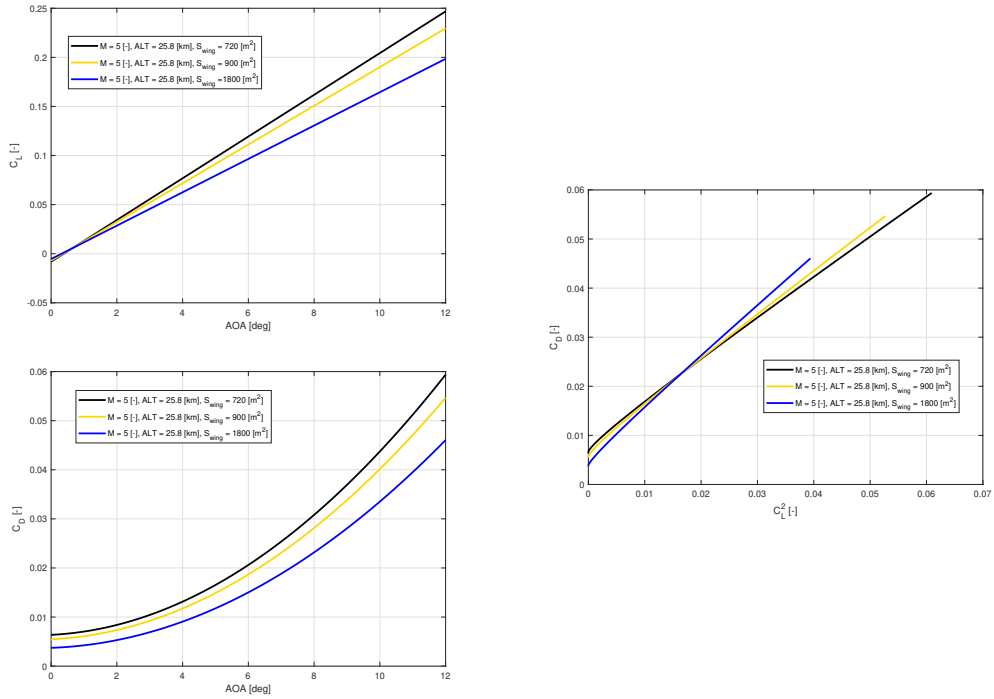


Figure 198: Effect of wing platform area on Hypersonic lift (top left), drag (bottom left) and drag due to lift (right) polars.

Wing aspect ratio effects:

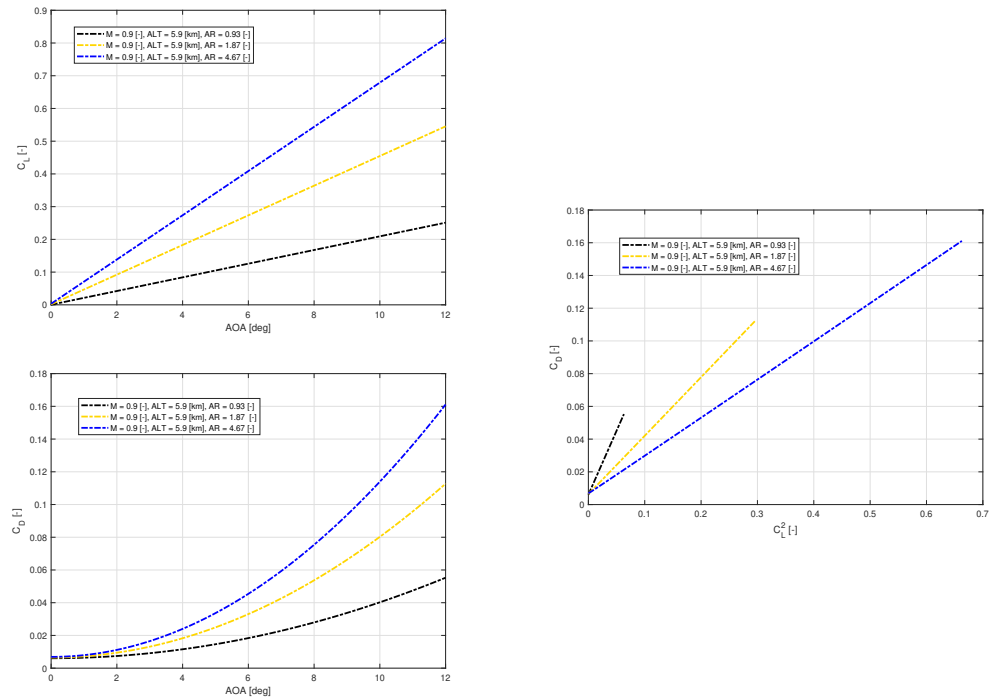


Figure 199: Effect of wing aspect ratio on Subsonic lift (top left), drag (bottom left) and drag due to lift (right) polars.

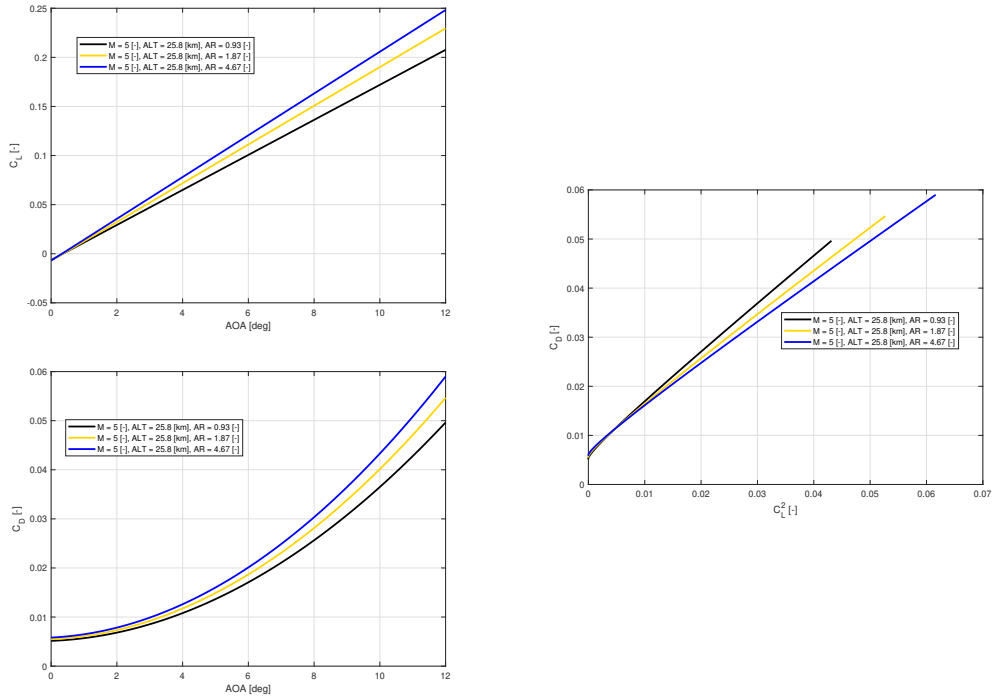


Figure 200: Effect of wing aspect ratio on Hypersonic lift (top left), drag (bottom left) and drag due to lift (right) polars.

Wing taper ratio effects:

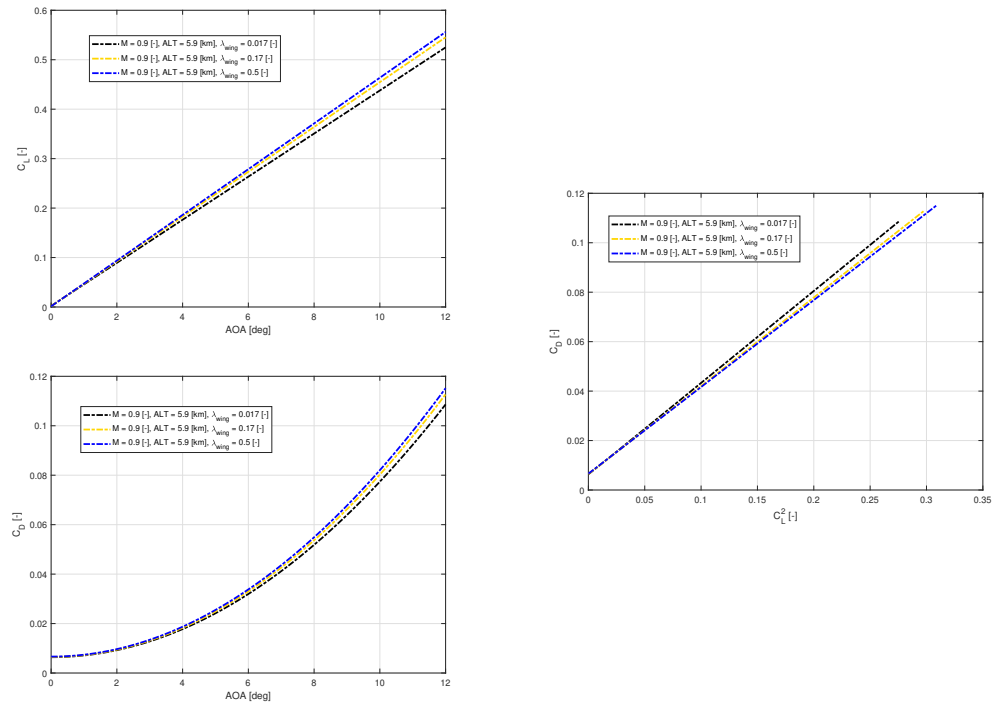


Figure 201: Effect of wing taper ratio on Subsonic lift (top left), drag (bottom left) and drag due to lift (right) polars.

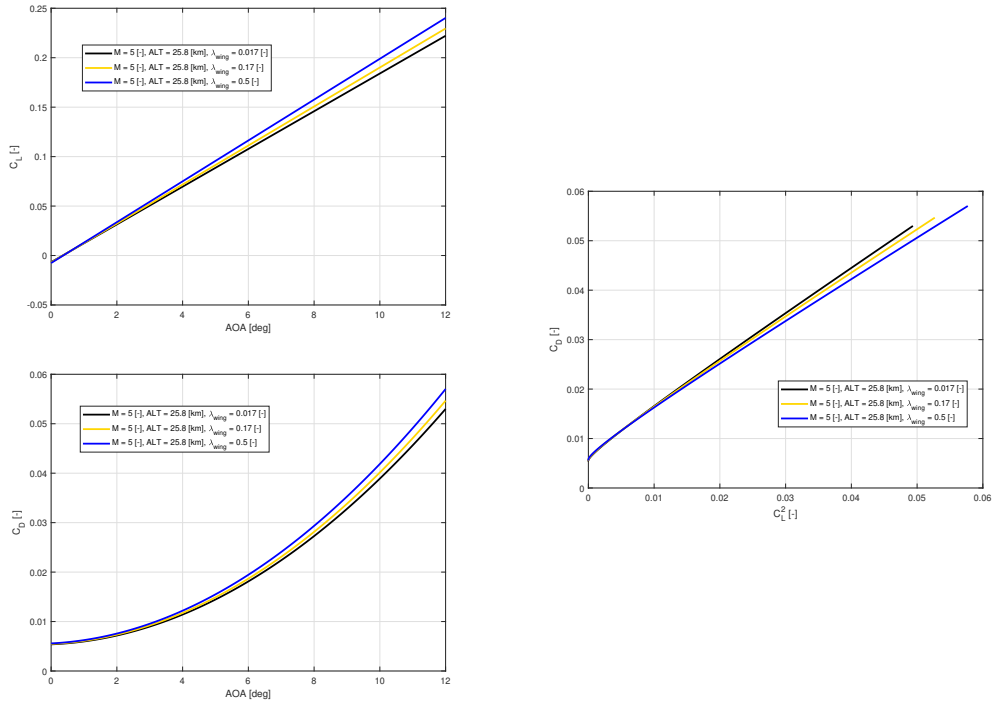


Figure 202: Effect of wing taper ratio on Hypersonic lift (top left), drag (bottom left) and drag due to lift (right) polars.

Wing tip twist effects:

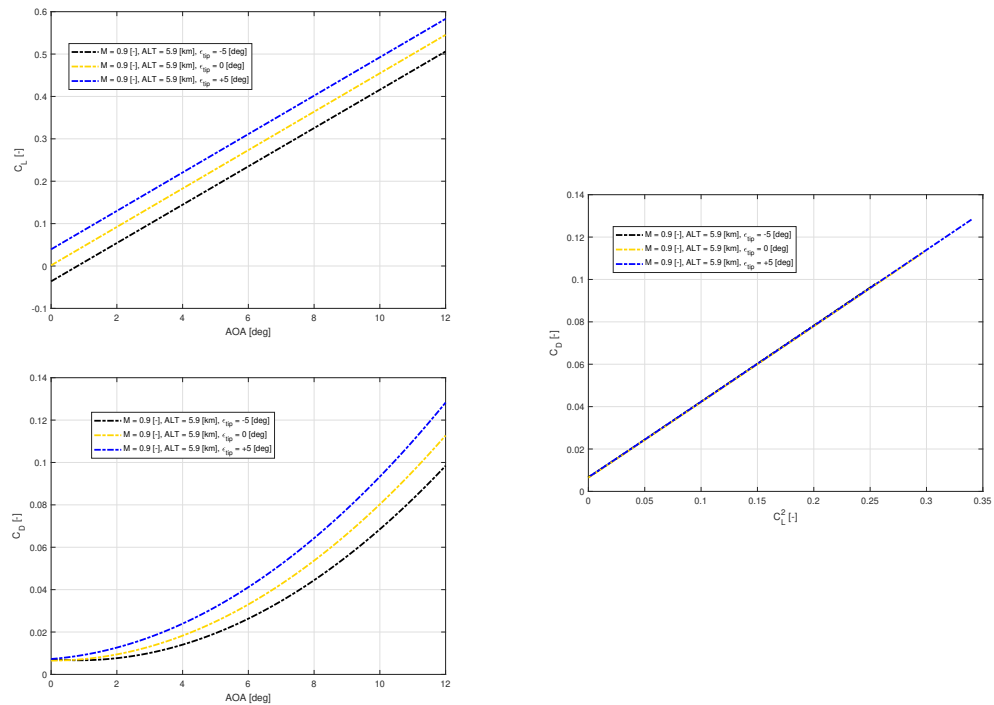


Figure 203: Effect of wing tip twist on Subsonic lift (top left), drag (bottom left) and drag due to lift (right) polars.

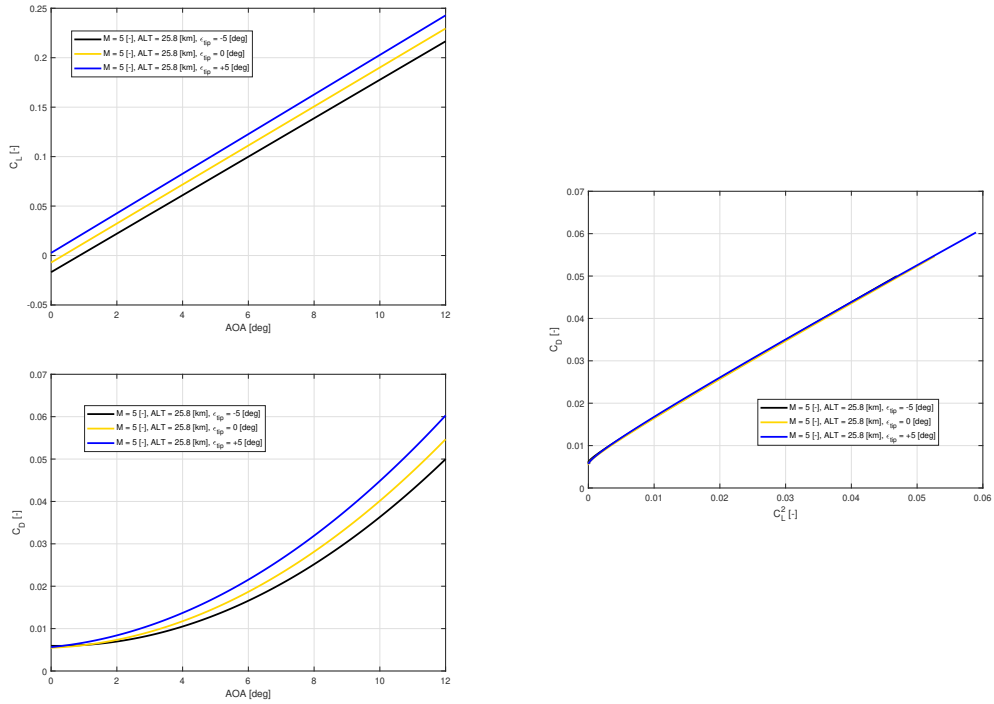


Figure 204: Effect of wing tip twist on Hypersonic lift (top left), drag (bottom left) and drag due to lift (right) polars.

Wing thickness to chord ratio effects:

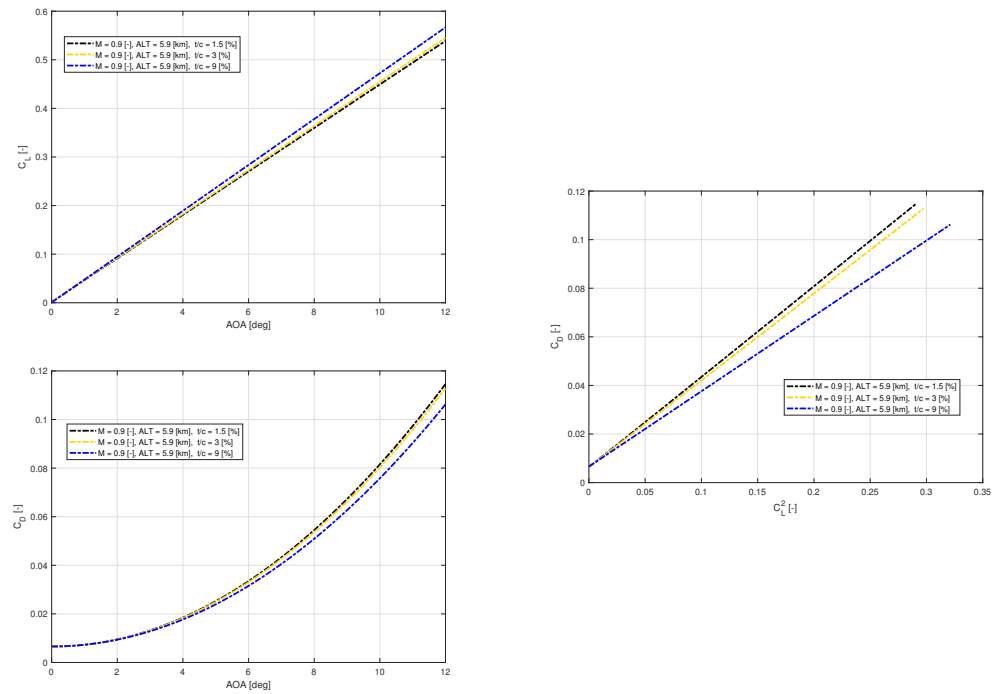


Figure 205: Effect of wing thickness to chord ratio on Subsonic lift (top left), drag (bottom left) and drag due to lift (right) polars.

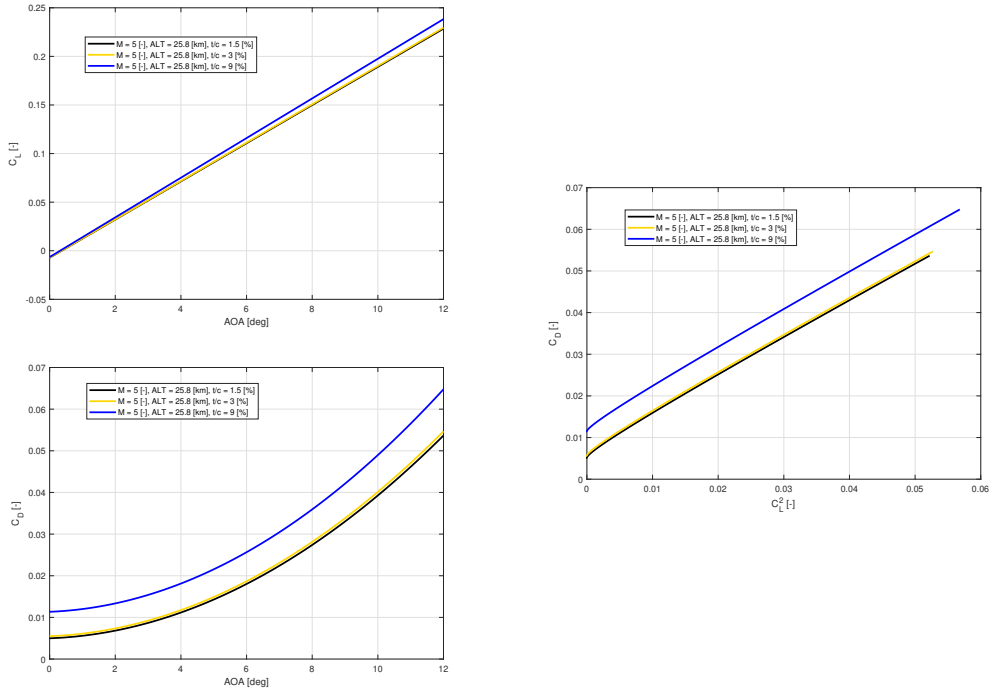


Figure 206: Effect of thickness to chord ratio on Hypersonic lift (top left), drag (bottom left) and drag due to lift (right) polars.

Fuselage width factor effects:

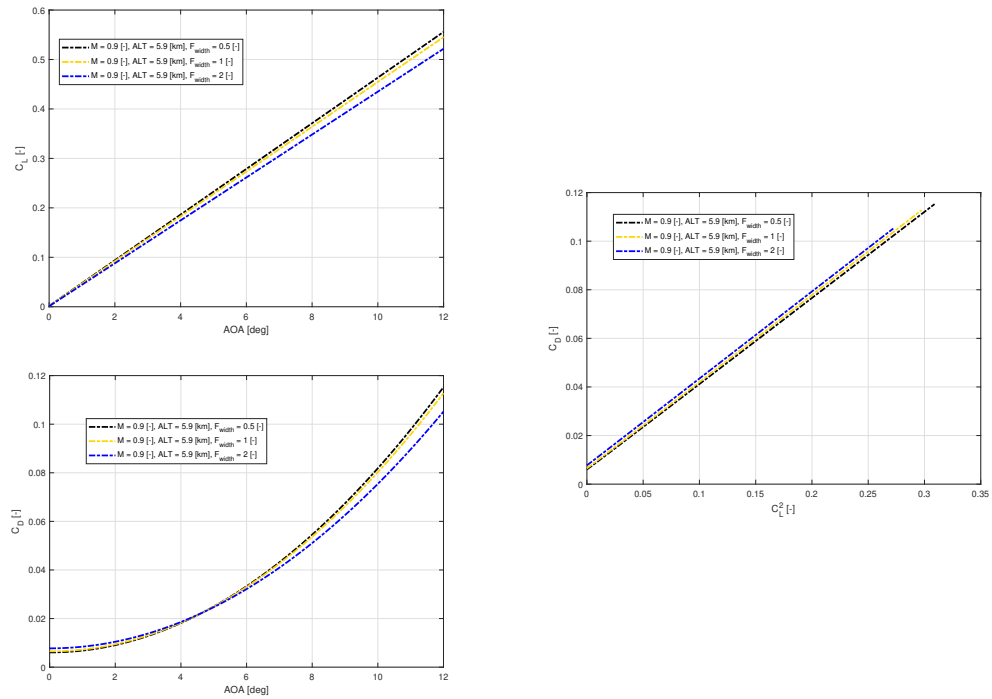


Figure 207: Effect of fuselage width factor on Subsonic lift (top left), drag (bottom left) and drag due to lift (right) polars.

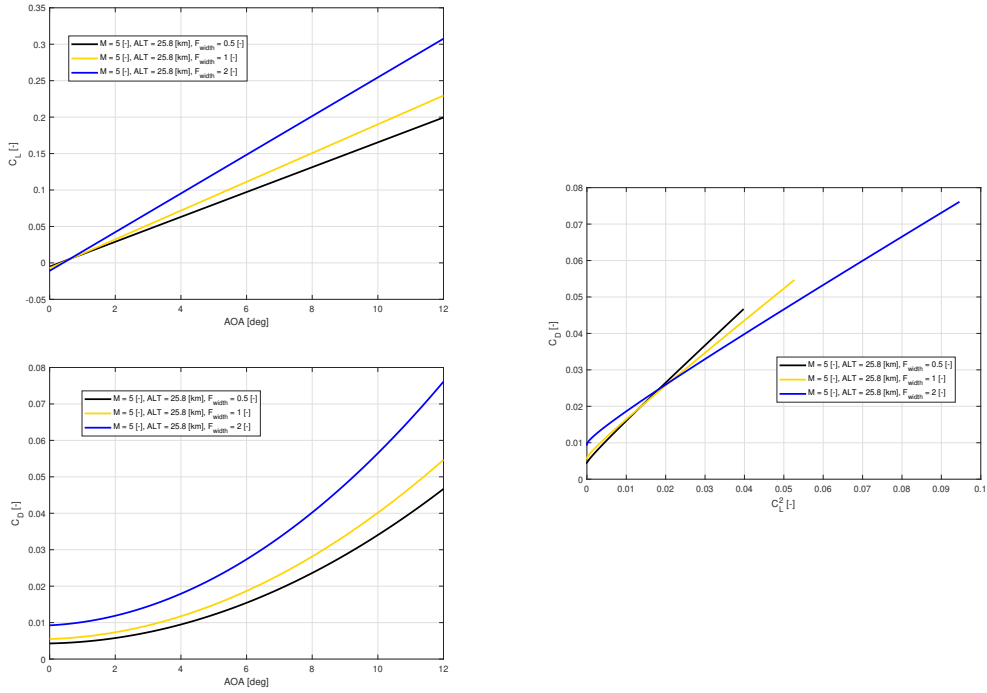


Figure 208: Effect of fuselage width factor on Hypersonic lift (top left), drag (bottom left) and drag due to lift (right) polars.

Fuselage height factor effects:

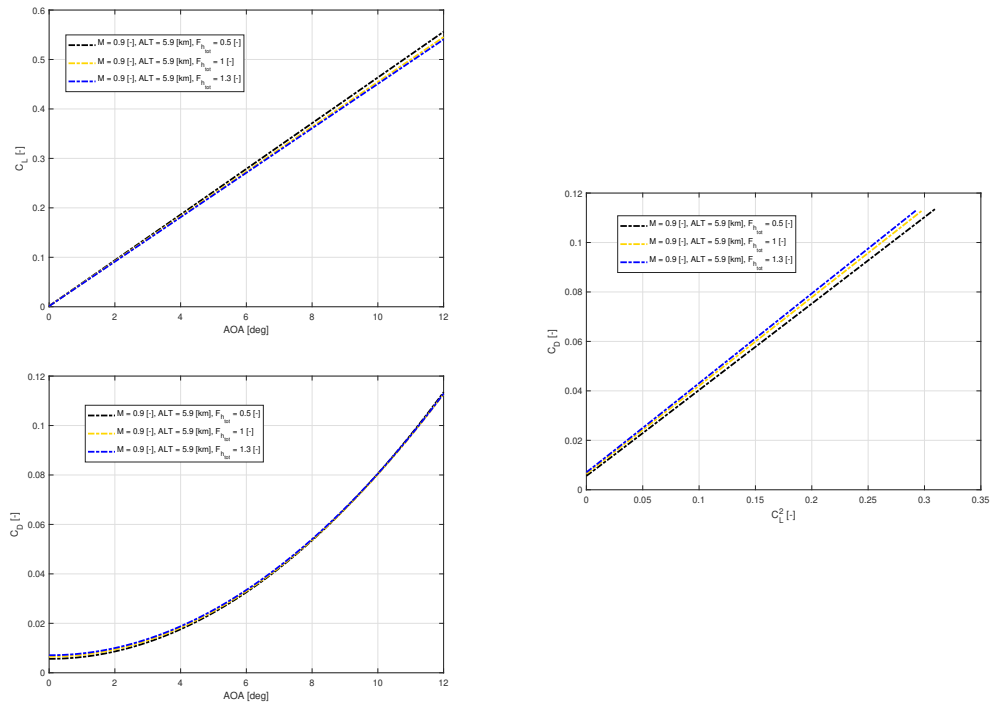


Figure 209: Effect of fuselage height factor on Subsonic lift (top left), drag (bottom left) and drag due to lift (right) polars.

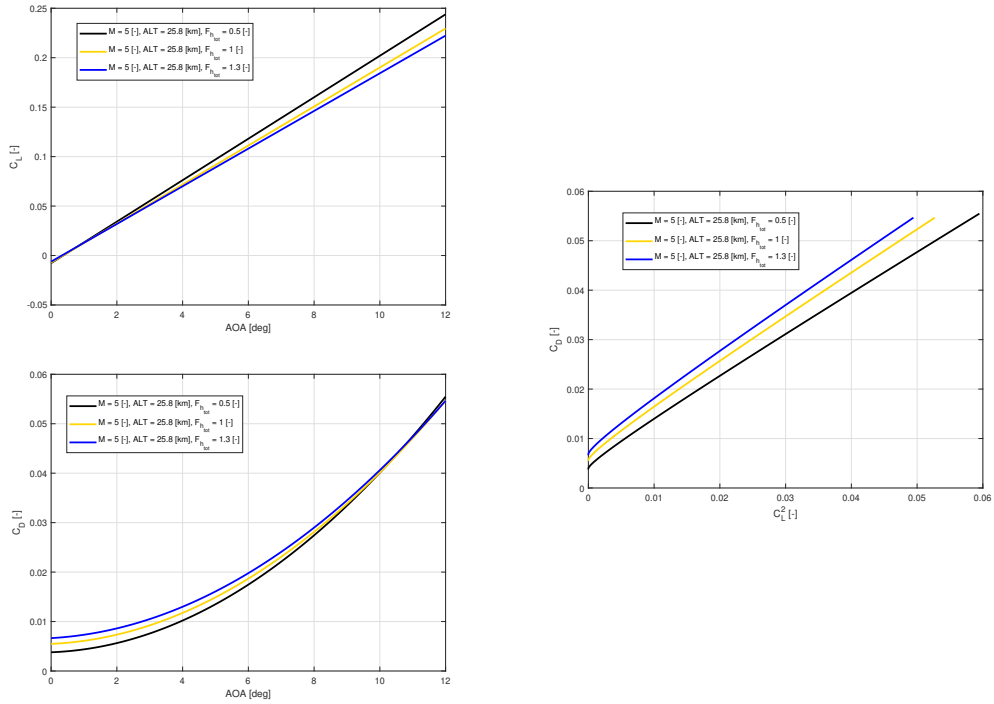


Figure 210: Effect of fuselage height factor on Hypersonic lift (top left), drag (bottom left) and drag due to lift (right) polars.

Fuselage length factor effects:

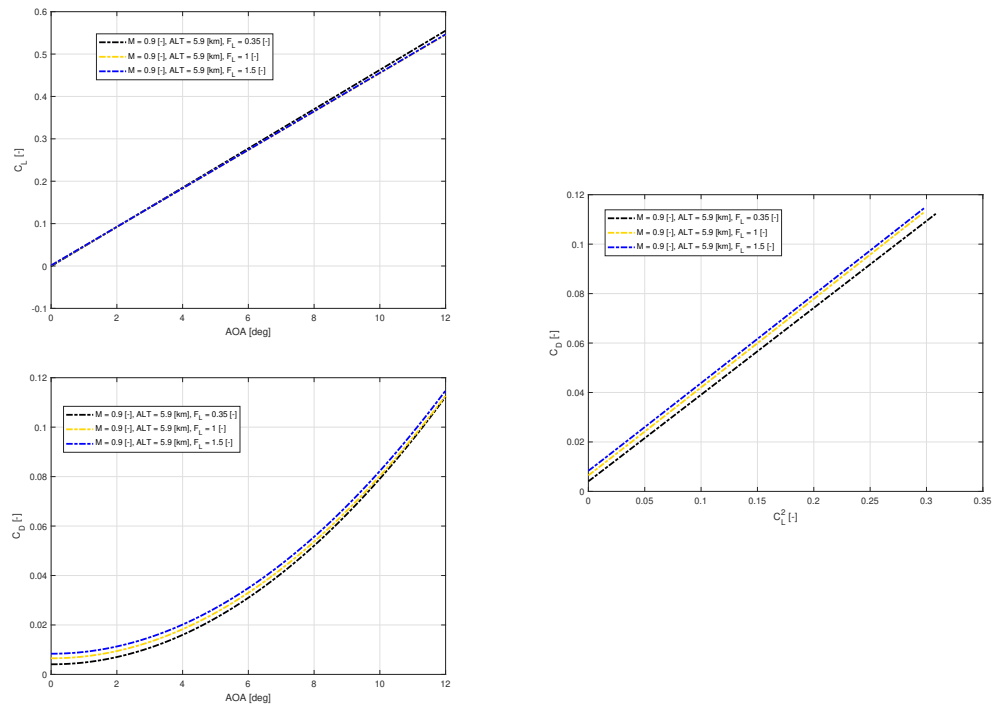


Figure 211: Effect of fuselage length factor on Subsonic lift (top left), drag (bottom left) and drag due to lift (right) polars.

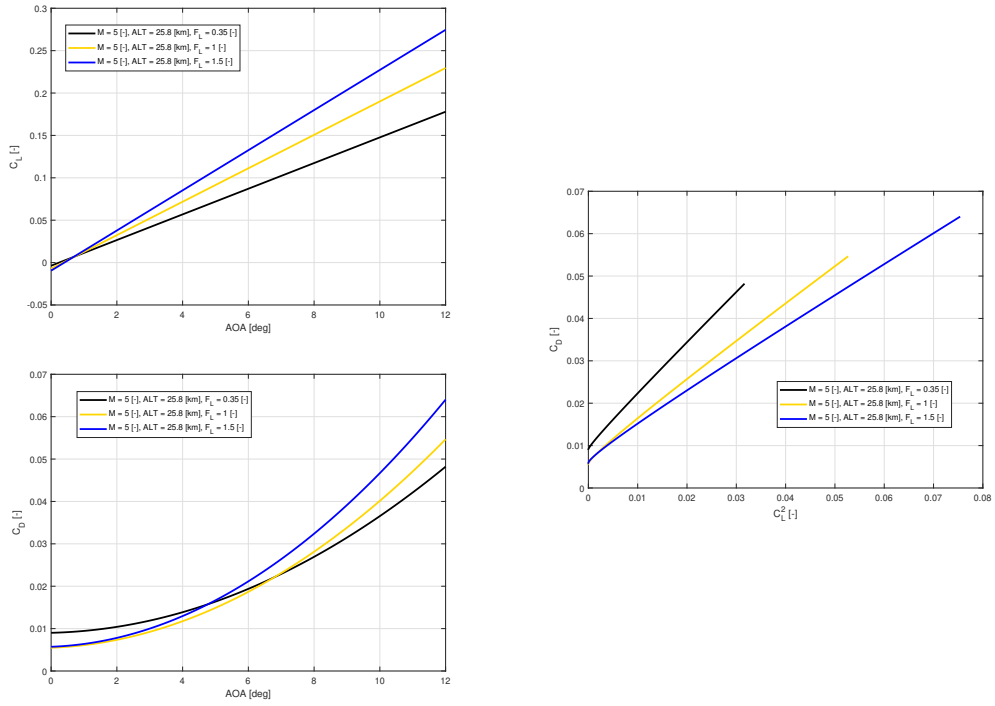


Figure 212: Effect of fuselage length factor on Hypersonic lift (top left), drag (bottom left) and drag due to lift (right) polars.

J. Additional results: Range effects

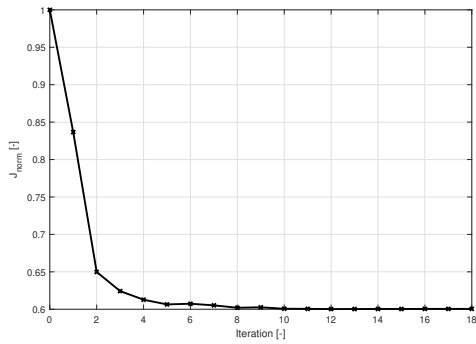


Figure 213: Normalised objective function value at Cruise Factor = 0.2 [-].

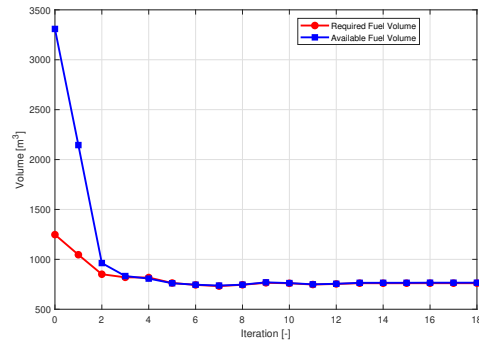


Figure 214: Fuel constraint during optimal sizing, CF = 0.2 [-].

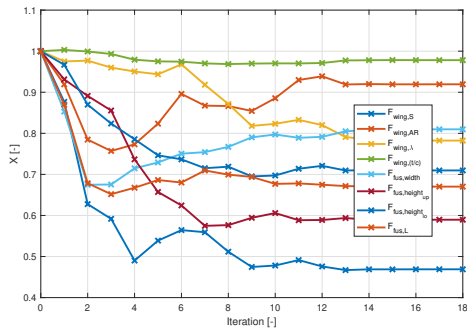


Figure 215: Design vector during optimal sizing, CF = 0.2 [-].

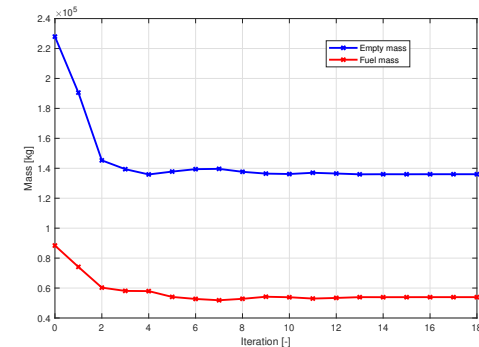


Figure 216: Empty and Fuel mass during optimal sizing, CF = 0.2 [-].

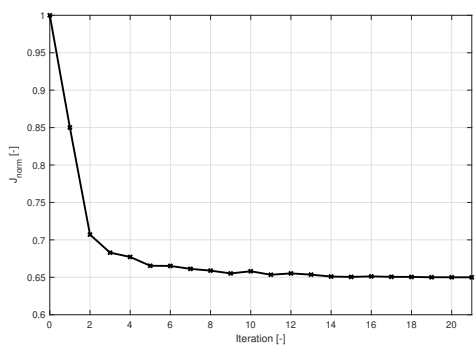


Figure 217: Normalised objective function value at Cruise Factor = 0.4 [-].

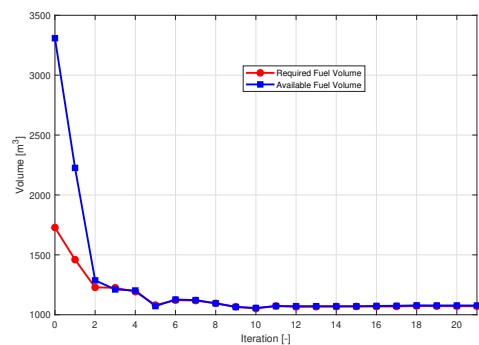


Figure 218: Fuel constraint during optimal sizing, CF = 0.4 [-].

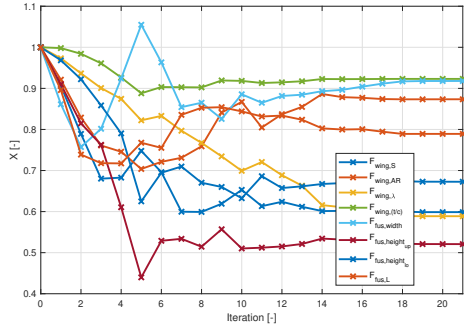


Figure 219: Design vector during optimal sizing, $CF = 0.4 [-]$.

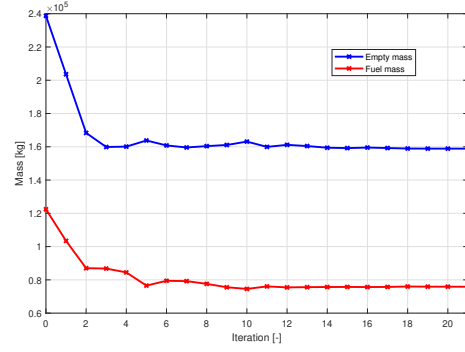


Figure 220: Empty and Fuel mass during optimal sizing, $CF = 0.4 [-]$.

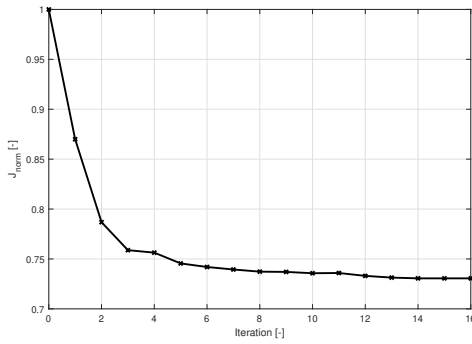


Figure 221: Normalised objective function value at Cruise Factor = 0.6 [-].

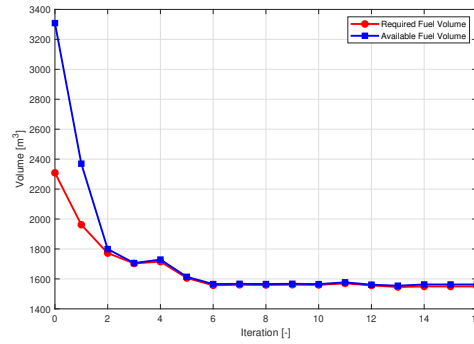


Figure 222: Fuel constraint during optimal sizing, $CF = 0.6 [-]$.

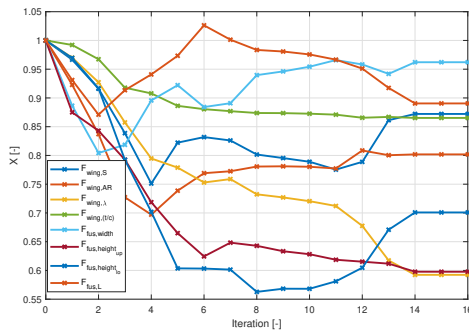


Figure 223: Design vector during optimal sizing, $CF = 0.6 [-]$.

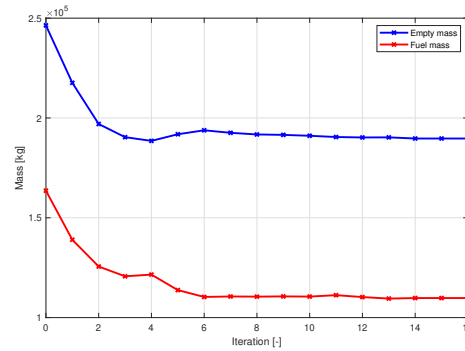


Figure 224: Empty and Fuel mass during optimal sizing, $CF = 0.6 [-]$.

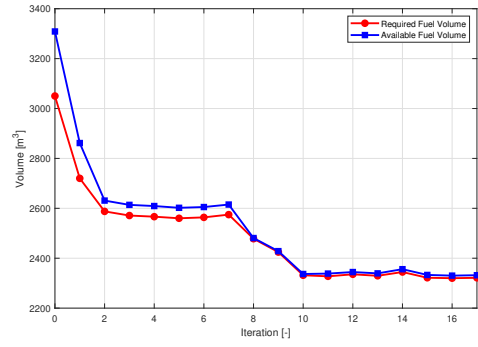
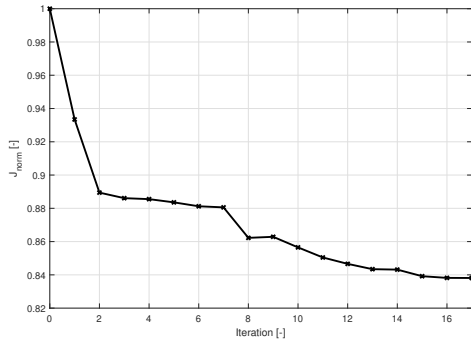


Figure 225: Normalised objective function value at Cruise Factor = 0.8 [-]. Figure 226: Fuel constraint during optimal sizing, CF = 0.8 [-].

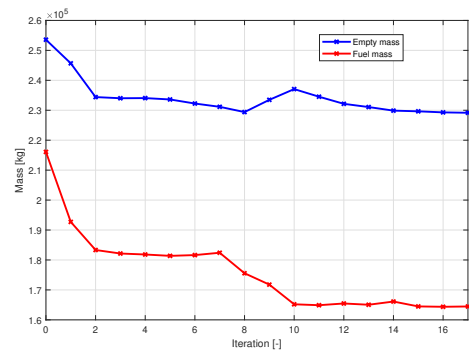
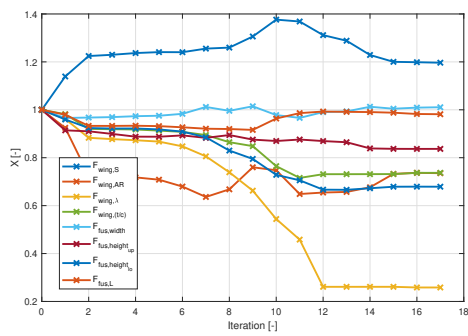


Figure 227: Design vector during optimal sizing, CF = 0.8 [-]. Figure 228: Empty and Fuel mass during optimal sizing, CF = 0.8 [-].